

DEPARTMENT OF PHYSICS
UNIVERSITY OF JYVÄSKYLÄ
RESEARCH REPORT No. 11/2018

DEVELOPMENT OF MICROFLUIDICS FOR SORTING OF CARBON NANOTUBES

BY
JÁN BOROVSÝ

Academic Dissertation
for the Degree of
Doctor of Philosophy

*To be presented, by permission of the
Faculty of Mathematics and Science
of the University of Jyväskylä,
for public examination in Auditorium FYS1 of the
University of Jyväskylä on December 13th, 2018
at 12 o'clock noon*



Jyväskylä, Finland
December 2018

Preface

The work reviewed in this thesis has been carried out during the years 2012 & 2014-2018 at the Department of Physics and Nanoscience Center in the University of Jyväskylä.

First and foremost, I would like to thank my supervisor Doc. Andreas Johansson for his guidance during my Erasmus internship and consequent Ph.D. studies. I am very grateful for his willingness to share both the professional competence and personal wisdom. Equal gratitude belongs to Prof. Mika Pettersson, without whom this project would never exist. His ability to see the big picture, his interesting insights, and genuine joy from the beauty of the microworld were a true motivation for me.

It has been a great experience to work in the Nanoscience Center for all these years. I would like to express my gratitude to the whole staff for being supportive, sharing good ideas, or just having fun meaningful conversations. A special thanks goes to Prof. Janne Ihalainen for providing me access to the facilities of the Department of Biology. I humbly acknowledge the irreplaceable help of our technical staff, namely Dr. Kimmo Kinnunen, Mr. Tarmo Suppula, Dr. Pasi Myllyperkiö, Dr. Alli Liukkonen, and Dr. Petri Papponen. Their help and ability to guide me together with their readiness to keep things running were vital to this work. The patient support from the office staff of both Nanoscience Center and the Department of Physics is greatly acknowledged. In particular, I would like to mention Riitta-Liisa Kuittinen, who made me to feel like home.

I would like to thank my officemates, flatmates, and friends. Heli, Saara, Elena, Heikki, Andrey, Vesa-Matti, Jyrki, Simon, Yaro, and Juraj. Without you, my life would certainly not be so lively and vivid. I owe unmeasurable gratitude to my parents, Milan and Anna, for bringing me up and shaping me to who I am. Similarly, I thank my sisters, Marta and Tereza, for being supportive and always willing to help.

Lastly, I wish to thank my lovely wife Nunu for her limitless patience, support, and love, especially during the moments when we were separated by distance or by me working at nights.

Financial support from the Academy of Finland and Department of Physics, University of Jyväskylä are gratefully acknowledged.

Omina ad maiorem Dei gloriam.

Jyväskylä, November 2018

Ján Borovský

Abstract

Borovský Ján

Development of Microfluidics for Sorting of Carbon Nanotubes

Jyväskylä: University of Jyväskylä, 2018, 199 p.

(Research report/Department of Physics, University of Jyväskylä

ISSN 0075-465X; 11/2018)

ISBN 978-951-39-7634-7 (paper copy)

ISBN 978-951-39-7635-4 (e-print)

diss.

Sorting of carbon nanotubes by their chirality is the current bottleneck in the way to their broad employment based on their exceptional electronic and optical properties. Despite the extensive effort, there is no known method, which would result in really pure chirality ensembles. Previously reported sorting protocols result in enrichment rather than in sorting, alter electronic structure, and suffer from low yield. This is mostly due to the statistical approach, where the nanotubes with mixed chiralities are treated as a set. In this thesis, we propose a new sorting technique based on nanotube-by-nanotube compartmentalization, characterization, and sorting in a continuously running droplet-based microfluidic device.

A new microfluidic platform for droplet-based experiments in femtoliter scale has been fully developed in this work. We report manufacture of full-glass spectroscopy-friendly microfluidic chips with the characteristic length of channels below 3 μm . A novel procedure for immersed planar metallic electrodes suitable for the harsh glass processing is introduced. Selective treatment of the channels with a hydrophobic self-assembled monolayer is implemented for stable water-in-oil droplet microfluidics.

Several unique properties of the system: the size, the unorthodox capacity of low droplet formation frequency, effective trap system, and tailored fluorescence detection system, were developed with the aim of lowering the detection limit down to single nanotube level. The automated processing of fluorescence spectra triggers the dielectrophoretic sorting valve deflecting the nanotube carrying droplets to either the reservoir or to the waste. Besides the primary goal, this microfluidic platform represents a powerful experimental tool to be employed in various fields of research.

A method of individualization of carbon nanotubes in an aqueous dispersion based on sonication and centrifugation is systematically addressed in this thesis. The purity, level of individualization, quality of individualized nanotubes, and long-term stability are found to be critically dependent on the sonication parameters, mainly the sonication power. For the purpose of water-in-oil droplet

microfluidics, a unique protocol for depletion of the surfactant at unaltered level of individualization is reported.

The development described in this thesis brought the project to the very doorstep of automated carbon nanotubes sorting, one nanotube at the time. We believe that successful realization of the sorting would allow a major breakthrough in small-scale applications of single nanotube devices with precise chirality requirements for achieving the desired behavior.

Keywords carbon nanotubes, sorting, individualization, dispersion, SDBS, sonication, centrifugation, long-term stability, near-infrared fluorescence, microfluidics, glass microfabrication, wet etching, metallic electrodes, TADB, silinization, droplet-based, water-in-oil, decane, Span 80, low droplet formation frequency, passive trapping, dielectrophoresis, sorting, droplet stability, surface tension, interfacial tension

Author's address	Ján Borovský Department of Physics University of Jyväskylä Finland
Supervisors	Senior Researcher Doc. Andreas Johansson Nanoscience Center Department of Physics University of Jyväskylä Finland Professor Mika Pettersson Nanoscience Center Department of Chemistry University of Jyväskylä Finland
Reviewers	Head of Work Group Dr. Thomas Henkel Department of Nanobiophotonics Leibniz Institute of Photonic Technology Germany Professor Yuri Svirko Institute of Photonics University of Eastern Finland Finland
Opponent	Professor Sami Franssila Department of Chemistry and Materials Science Aalto University Finland

Contents

Preface

Abstract

Contents

1	Introduction.....	13
1.1	Carbon nanotubes.....	13
1.2	Microfluidics.....	14
1.3	The aim and content of the thesis.....	14
2	Carbon nanotubes - A review.....	19
2.1	Introduction.....	19
2.2	Atomic structure	20
2.3	Electronic structure.....	21
2.4	Band structure	23
2.5	CNT characterization	25
2.5.1	Direct characterization	25
2.5.2	Indirect characterization	26
2.6	CNT manufacture	30
2.7	Application issues.....	31
2.7.1	Sorting.....	32
2.7.2	Individualization.....	36
2.8	Aqueous dispersions of SWCNTs	38
2.8.1	Choice of surfactant	38
2.8.2	Concentration of nanotubes.....	38
2.8.3	Amount of SDBS.....	39
2.8.4	Sonication	39
2.8.5	Centrifugation.....	41
3	Carbon nanotubes - The dispersion.....	43
3.1	Reagents	43
3.2	Instrumentation.....	46
3.2.1	Preparation of CNT dispersion	46
3.2.2	Characterization	46
3.2.3	Remark on spectra acquisition	47
3.2.4	Processing the spectra	51
3.3	Parameters of the process	51

3.3.1	Amount of surfactant.....	52
3.3.2	Amount of nanotubes.....	52
3.3.3	Sonication.....	52
3.3.4	Centrifugation.....	57
3.3.5	Filtration.....	60
3.3.6	Properties of the CNT dispersion.....	60
3.4	Conclusion.....	66
4	Theory of microfluidics.....	69
4.1	Definition.....	69
4.2	Applications of droplet-based microfluidics.....	71
4.3	Theoretical background.....	71
4.3.1	Characteristic dimensions.....	71
4.3.2	Dimensionless numbers.....	73
4.3.3	Navier-Stokes equations.....	74
4.3.4	Poiseuille flow.....	75
4.3.5	Hydraulic resistance.....	75
4.3.6	Flow of confined droplets.....	76
4.4	Basic operations in droplet-based microfluidics.....	78
4.4.1	Droplet formation in open and confined systems.....	78
4.4.2	Droplet formation in confined regime.....	78
4.4.3	Compartmentalization.....	80
4.4.4	Droplet trapping.....	81
4.4.5	Droplet content characterization.....	81
4.4.6	Droplet sorting.....	82
4.4.7	Droplet stability.....	82
5	Manufacture of a microfluidic system.....	85
5.1	The material.....	85
5.2	Inlets and Outlets.....	86
5.3	Lithography technique.....	87
5.4	Instrumentation.....	88
5.5	General description of the process.....	88
5.6	Substrate cleaning.....	89
5.7	Etching.....	89
5.7.1	Dry etching.....	90
5.7.2	Wet etching.....	95
5.7.3	Combined etching.....	99
5.7.4	3D channels.....	100
5.7.5	Conclusion on etching methods.....	102
5.8	Bonding.....	103
5.9	Electrodes.....	106
6	Operation of a microfluidic system.....	111
6.1	World-to-chip interface.....	111
6.2	Surface properties of the channels.....	113
6.2.1	Hydrophobic treatment of the glass surface.....	114

6.2.2	Silinization in enclosed channels	116
6.3	Instrumentation.....	120
6.4	Reagents	120
6.5	Operations on the microfluidic chip	121
6.5.1	General description.....	122
6.5.2	Droplet formation	122
6.5.3	Droplet trapping.....	131
6.5.4	Droplet sorting.....	134
6.5.5	Droplet stability	143
7	Conclusion on microfluidics manufacture and operation	149
8	Microfluidics for carbon nanotubes spectroscopy and sorting.....	153
8.1	Introduction to SMS and FADS	153
8.1.1	Brief history of SMS and FADS.....	153
8.1.2	Current situation in SMS and FADS	154
8.1.3	SMS and FADS for SWCNT sorting	155
8.2	Instrumentation and automation	156
8.3	Ambient considerations	159
8.3.1	Glass contribution	159
8.3.2	Decane contribution.....	160
8.4	CNT dispersion in microfluidic system.....	160
8.4.1	CNT dispersion in microfluidic channel	160
8.4.2	CNT dispersion in droplets	161
8.4.3	Continuous droplet formation with CNT dispersion.....	163
8.4.4	CNT dispersion post-processing.....	165
8.4.5	Low SDBS disperse phase for droplet formation	170
9	Summary and perspectives	173
9.1	Summary	173
9.2	Perspectives	174

Appendixes

1 Introduction

The miniaturization has been the driving force for the Third Industrial Revolution, an unprecedented raise of information technology, user electronics, and connectivity in the digital world of today. The technology, which is largely based on the transistor effect – an effect inherently existent only in microscale – triggered the boom of development, wealth, and well-being as we know it in nowadays society. Furthermore, the miniaturization is an inevitable prerequisite for the already present Fourth Industrial Revolution as an era, where the fusion of technologies blurs the borders between the physical, biological, and digital worlds.

For decades, the performance of digital electronics was steadily growing as a result of denser integration of components in integrated circuits, following the famous Moore's law [1]. This was possible mainly by progressing miniaturization of circuit's components. However, the pace is slowing down as the aggressively scaled-down components starts to hit the physical limits of conventionally used materials.

1.1 Carbon nanotubes

Since their discovery in 1993 [2], the single-walled carbon nanotubes have attracted attention as promising candidates to overcome the scaling limitations of silicon-based electronics [3]. With excellent thermal and mechanical stability, these hollow cylinders made out of a planar hexagonal carbon matrix offer a wide set of properties uniquely suitable for implementation to integrated circuits. The main lure, besides the nanometer-scaled dimensions, is the geometry dependent conductivity ranging from fully metallic to semiconducting behavior with bandgap up to 1.8 eV [4]. The utilization of semiconducting properties of carbon nanotubes is especially tempting, as the wide selection of bandgaps would allow to replace virtually any conventional semiconductor with nanotubes. This fact makes the application of nanotubes essentially limitless, spanning from sensors and probes to solar cells and displays [5].

Unfortunately, the strict relationship between the geometry and the bandgap of a nanotube is both a blessing and a curse. The methods of carbon nanotubes production are inherently incapable of manufacturing nanotubes with a single arbitrarily chosen bandgap [6]. This remains, despite certain progress in bandgap specific synthesis [7] and post-synthesis sorting [8], the main bottleneck hindering a broader deployment of carbon nanotubes to everyday life.

1.2 Microfluidics

The drive towards miniaturization has also positively affected the fields of biology and chemistry. The advancements in the fields of microanalytical methods, *in situ* diagnostics, and genomics would not be possible without the development of high-throughput screening, reduction of sample volumes, and reaction times [9]. These became possible in large scale by down-scaling of the processed volumes, eventually leading to the manipulation of fluids in micrometer scales. The boom of microfluidics is directly linked to the miniaturization in the electronics, as the silicon processing technology allowed the manufacture of precise yet complex capillaries. The full potential of microfluidics got under way with introduction of droplet-based microfluidics [10]. The elaborate manipulation with discrete droplets in continuous phase brought the possibility to conventionally work with unprecedentedly small volumes [11].

The state-of-the-art microfluidic systems work with droplets ranging from 2 pL to 4 nL (15 to 200 μm in diameter) [12]. Nevertheless, further miniaturization of microfluidic systems is needed for highly sensitive detection and high-throughput sorting techniques based on confocal fluorescence microscopy [13,14]. A droplet volume matching the fluorescence microscope excitation volume not only allows to exploit the capabilities of the system to its fullness, but the smaller droplets also generally result in a higher signal-to-noise ratio [15].

1.3 The aim and content of the thesis

The envisioned mass utilization of single-walled, single-bandgap carbon nanotubes and even more single nanotube devices does not seem to be anywhere in sight. Nevertheless, the new protocols for chirality-selective synthesis and sorting have been growing dramatically in the last couple of years [8]. The goal of this work is to contribute to this effort with a new sorting protocol, which does not necessarily provide high yields but aims for 100 % purity and eased manipulation of individual nanotubes. The secondary goal is to develop a previously non-existing universal microfluidic platform for the further enrichment of in-house experimental techniques.

The scheme of the envisioned sorting protocol is visualized in FIGURE 1.1. The aqueous dispersion of individualized carbon nanotubes is injected to a microfluidic channel. In the moment of contact with an immiscible fluid, small droplets are created. The tailored concentration of carbon nanotubes in the dispersion and known size of the droplets can lead to a single nanotube in every droplet on average. As the droplets proceed forward in the channel, their content is characterized by the means of fluorescence spectroscopy. The spectroscopy result further triggers the sorting, deflecting the droplets with the desired content to the reservoir while letting all the others to pass to the waste channel.

The research described in this thesis is based on pioneering work of three master students, who explored the possibilities in microfluidic chip manufacture [16,17] and light spectroscopy in microfluidic channels [18]. Further

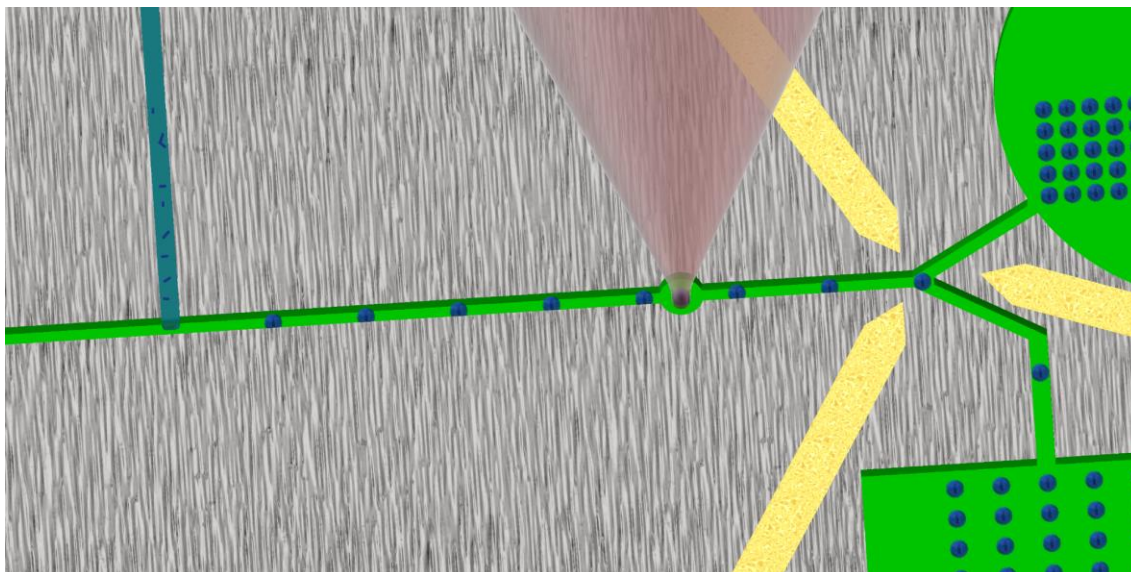


FIGURE 1.1: An illustrative scheme of the microfluidic system for spectroscopy and sorting of carbon nanotubes.

miniaturization, deepening the understanding of many related processes, the dynamics of microfluidic systems scaled down to the largely unexplored femtoliter regime and confidence levels in operations are among the issues addressed in this work. The thesis is naturally divided into three books.

1. BOOK I - Carbon nanotubes
2. BOOK II - Microfluidics
3. BOOK III - Carbon nanotubes in microfluidic system

In its first part, BOOK I address the topic of carbon nanotubes with a review-like approach. General properties of carbon nanotubes are discussed together with the obstacles inhibiting their massive deployment. The reported approaches for overcoming these obstacles are discussed in detail. In the second part, the preparation of an aqueous dispersion of carbon nanotubes is investigated both theoretically and experimentally.

BOOK II describes in its first part the basic theory of microfluidics with focus on the behavior of systems scaled down to the femtoliter regime. Since no essential discrepancy in the functionality of the femtoliter system compared to conventional system was found, the second and third part of the book experimentally address the manufacture and operation of a femtoliter microfluidic system.

BOOK III merges the knowledge gained in the previous books and reports the work on introducing the carbon nanotubes to the microfluidic system. Relevant results, challenges, and strategies how to overcome them are extensively discussed.

BOOK I - CARBON NANOTUBES

2 Carbon nanotubes - A review

2.1 Introduction

The physics of one-dimensional (1D) systems has been theoretically studied already for several decades. The results were predicting exciting new physics originating from the specific properties of quantum-restricted electron gas. Despite the fact that reduction of dimensionality appears almost in every solid-state physics textbook as an approximate approach to analytical calculation of electronic structure, the lack of instrumentation as well as computational resources postponed the experimental verification till late 1970s. With the development of methods for both production and characterization of predicted systems, the era of conductive polymers, engineered DNA¹, nanowires, nanorods and nanotubes has begun.

The first observation and characterization of carbon nanotubes (CNT, *pl.* CNTs), a tubular form of 1D carbon sheet, is often attributed to the work of S. Iijima from 1991 [19], even though the observation of tubular graphitic objects can be documented back to early 1950s [20]. The observed objects were concentric tubes placed one within the other with the spacing of 3.4 Å, a typical value for the distance between single carbon layers in graphite. The first synthesis of single-walled CNTs (SWCNTs) broadly noticed by the scientific community followed in 1993 [2], although their history reaches at least back to 1976 [21]. SWCNTs with diameters in units of nanometers have become very popular in the field of 1D nanostructures. With their stability and clearly defined crystallographic structure, they started to be considered an ideal candidate for practically exploitable 1D carbon system [22].

The interest in SWCNTs is not based only on their extraordinary mechanical properties but mainly on excellent conductivity of metallic and controllable bandgap of semiconducting nanotubes. While some properties can be easily explained macroscopically, *e.g.* the elasticity by the model of a homogeneous cylinder, most of them crucially depend on atomic configuration. For example, the band structure or density of states and associated electronic and optical properties are directly defined by the diameter and chirality of the nanotube (see FIGURE 2.1). This straightforward dependence of geometrical properties on atomic configuration is rather unique in solid-state physics and it brings motivation for the development of new production methods. Novel manufacture processes could allow use of such objects in devices where exactly defined (electronic) properties of nanotubes are required. One of the examples could be a complex

¹ deoxyribonucleic acid

manufacture of logical circuits with components in nanometric scale. And indeed, the first computer with logical units constructed from CNTs was reported in 2013 [23] and new applications keep coming.

Despite stormy development in the field of carbon nanotubes since their discovery, most of the applications are at the stage of prototypes - or even worse - only ideas [3,5]. Commercially available solutions are only known in applications where bulk properties of CNTs can be utilized, such as composites, transparent electrodes (replacement for ITO²), microwave shielding, and nanotube based mode locks. Possible future applications, however, lie in the areas with huge technological impact as scanning microscope tips, semiconductor technology (integrated circuits [23], thin film transistors [24], and single nanotube transistors [25]), and electron and photon sources [7] promising improvements for many applications, from electron microscopes and medical imaging [26] to screens and lighting systems. In energetics, the concept of solar cells [8], hydrogen storage inside of the CNTs and large surface area used for improvement of lithium accumulators and supercapacitors are very promising. One should also remember, that since CNTs already significantly entered the commercial sphere it is difficult if not impossible to follow the newest applications as the newest technologies often become the subject of a trade secret.

2.2 Atomic structure

The SWCNTs are formed by one-layer hexagonal carbon lattice rolled to hollow cylinder of diameter in units of nanometers and large length to diameter ratio (FIGURE 2.1). According to the aim of the research or particular application, one can describe CNTs as single molecules or quasi 1D crystals with translational symmetry along their axis. Because of basically infinite number of ways how to roll a sheet into a cylinder there is a large ensemble of nanotubes differing in chiral geometry, or in other words, in diameter and microscopic structure.

For clarity, the SWCNTs are defined with the use of nomenclature, which is customary for graphene lattice. The descriptive geometrical idea how the nanotube is formed by rolling a graphene sheet is plotted in FIGURE 2.1. Its structure is defined by *chiral vector* \vec{c}_h , which connects two crystallographically equivalent points A and A' and represents the circumference of the nanotube. Consequently, the geometry of a CNT is fully defined by a pair of integers (n,m) denoting the relative position of two atoms on the graphene surface, which overlap when the graphene sheet is 'rolled' to the shape of a cylinder. The chiral vector is then defined:

$$\vec{c}_h = n\vec{a}_1 + m\vec{a}_2, \quad (2.1)$$

where \vec{a}_1 and \vec{a}_2 are the basis vectors of a hexagonal graphene sheet.

Whereas the chiral vector represents the circumference of the nanotube, its diameter can be formulated as

² indium tin oxide

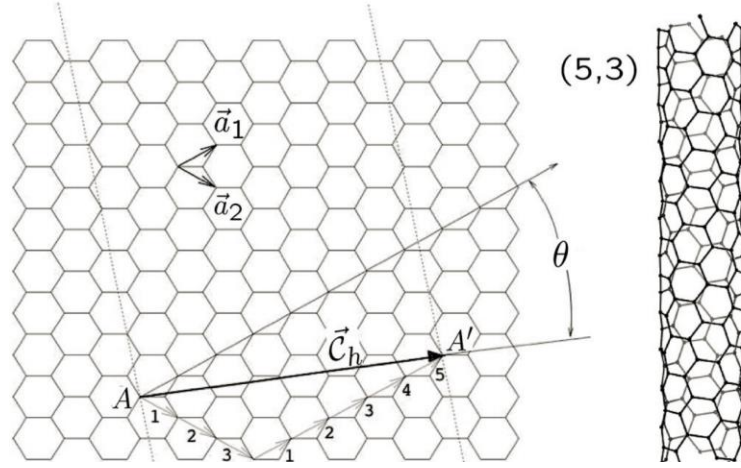


FIGURE 2.1: Graphene hexagonal structure with lattice vectors \vec{a}_1 and \vec{a}_2 . The chiral vector $\vec{c}_h = 5 \cdot \vec{a}_1 + 3 \cdot \vec{a}_2$ represents one of the possible rollings of 2D lattice to 1D cylindrical form. Reprinted with permission from [22]. Copyright 2007 by the American Physical Society.

$$d = \frac{|\vec{c}_h|}{\pi} = \frac{a}{\pi} \sqrt{n^2 + nm + m^2}, \quad (2.2)$$

where a is the lattice parameter of a hexagonal structure: $a = \sqrt{3} \cdot a_{C-C}$ and $a_{C-C} \cong 1.44 \text{ \AA}$, corresponding to the bond length between two carbon atoms.

The nanotube can be also defined by *chiral angle* θ situated between \vec{c}_h and \vec{a}_1 (so-called 'zig-zag' direction, FIGURE 2.1). The θ and \vec{a}_1 are related by

$$\cos \theta = \frac{\vec{c}_h \cdot \vec{a}_1}{|\vec{c}_h| \cdot |\vec{a}_1|} = \frac{2n + m}{2\sqrt{n^2 + nm + m^2}}. \quad (2.3)$$

The value of the chiral angle is within interval $0 \leq |\theta| \leq 30^\circ$, which arises from the hexagonal graphene structure. Accordingly, this angle determines the rotation of hexagons in relation to the nanotube axis.

The SWCNTs are sorted to three basic groups according to their geometry. The nanotubes with indices $(n,0)$ ($\theta = 0^\circ$) are called *zigzag* nanotubes, because of the zigzag pattern of carbon atoms along their circumference (vertical edges of graphene lattice in FIGURE 2.1). Zigzag nanotubes have carbon bonds parallel to the CNT axis. On the other hand, the nanotubes $(n,m = n)$ ($\theta = 30^\circ$) are called *armchair* nanotubes, because of the armchair pattern of carbon atoms along their circumference (horizontal edges of graphene lattice in FIGURE 2.1). Their carbon bonds are perpendicular to the CNT axis. Both zigzag and armchair nanotubes are *achiral* in contrast to all the other $(n,m \neq n \neq 0)$ *chiral* nanotubes (FIGURE 2.2).

2.3 Electronic structure

Similarly to graphene, CNTs are characterized by two types of chemical bonds, which show so called planar sp^2 hybridization [22,27,28]. First three out of four carbon valence orbitals ($2s$, $2p_x$, $2p_y$ and $2p_z$, where z is perpendicular to the plane of the lattice) form *localized* bonding and antibonding orbitals in the plane of 2D

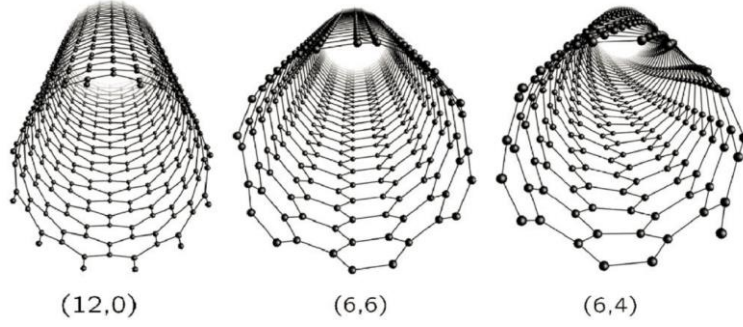


FIGURE 2.2: The structure of (12,0) zigzag, (6,6) armchair, and (6,4) chiral CNT. Reprinted with permission from [22]. Copyright 2007 by the American Physical Society.

hexagonal lattice, σ and σ^* respectively. σ orbitals form strong covalent bonds, which are responsible for most of the bonding energy and the mechanical properties of the honeycomb lattice. The $2p_z$ orbital – pointing out of the lattice plane – cannot bond with the σ states considering the symmetry of the system. Lateral bonding between adjacent $2p_z$ orbitals form *delocalized* bonding and antibonding orbitals, π and π^* respectively. π bonds are normal to the surface and they are responsible for the weak van der Waals interactions between SWCNTs, similar to the interaction of single graphene sheets in graphite. In terms of energy, the energy levels related to σ bonding are far away from the Fermi level (> 10 eV at Γ , FIGURE 2.3(a)), therefore their contribution to electronic properties is negligible. On the other hand, bonding and antibonding π bands cross Fermi level exactly at the K point of the first Brillouin zone of hexagonal carbon lattice (FIGURE 2.3(b)), virtually defining the electronic properties of carbon nanotubes.

Allowed 1D quantum states of a carbon nanotube defined by chiral vector \vec{c}_h can be determined from periodic boundary conditions

$$\vec{c}_h \cdot \vec{k} = 2\pi q, \quad (2.4)$$

where q is an integer. For the meaning of \vec{k} , see FIGURE 2.4. As long as one of the allowed states crosses one of the K points, the nanotube is metallic along its axis (zero bandgap), otherwise semiconducting (non-zero bandgap). The graphical interpretation for metallic (9,0) and semiconducting (10,0) nanotubes is plotted in FIGURE 2.4. The condition for metallic nanotubes takes the form

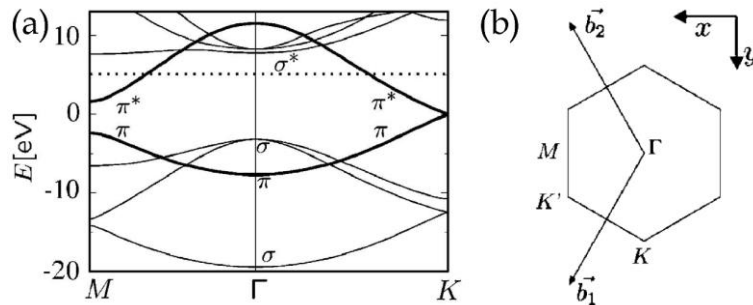


FIGURE 2.3: Band structure (a) and first Brillouin zone (b) of hexagonal carbon lattice. There is always wide bandgap between σ and σ^* , while π and π^* meet at the K point of Brillouin zone. Reprinted with permission from [22]. Copyright 2007 by the American Physical Society.

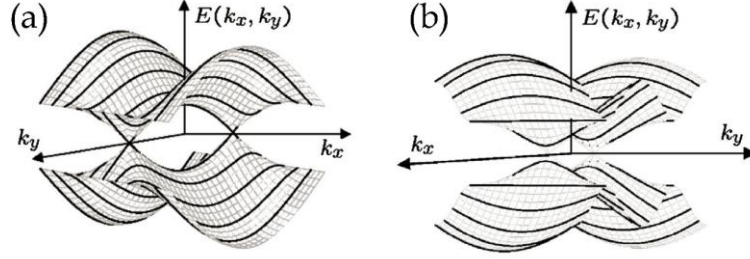


FIGURE 2.4: Allowed states on the π/π^* carbon lattice. (a) Allowed states for metallic (9,0) CNT, crossing the K point. (b) Allowed states for semiconducting (10,0) CNT, not crossing the K point. Reprinted with permission from [22]. Copyright 2007 by the American Physical Society.

$$\vec{c}_h \cdot \vec{k}_F = 2\pi q. \quad (2.5)$$

In this approximation, all the nanotubes where $(n - m)/3$ is an integer are metallic. All the other nanotubes are moderate semiconductors (< 2 eV) and their bandgaps decrease with increasing nanotube diameter not depending on its chirality.

In reality, the chirality of the nanotube partially influences the bandgap by an effect called trigonal warping [29]. In addition, the curvature of the CNTs leads to mixing of carbon π/σ bonding and π^*/σ^* antibonding orbitals. This results in a slight shift of the degenerate point out of the K point and thus in opening of a narrow bandgap in some of the metallic nanotubes. The width of this very small bandgap (\sim meV) drops with growing nanotube diameter [30]. This applies to all metallic SWCNTs except armchair nanotubes, which are always truly metallic because the σ and σ^* orbitals are too far in energy from the π and π^* orbitals and cannot influence the position of the allowed states. Hence, an improvement to the rule is made. If $(n - m)/3$ is an integer for chiral or zigzag nanotubes the nanotubes are *quasi-metallic* with tiny bandgap, otherwise semiconducting with bandgap dependent on diameter/chirality.

2.4 Band structure

The allowed electronic states in solid-state matter create band structure and related *density of states* (DoS). DoS describes the number of available electronic states in certain interval of energies. In contrast to isolated systems (atoms, molecules), the DoS of macroscopic systems is continuous. A high DoS then means there are many available states to be occupied, while zero DoS conversely means, there is no electronic state available for certain energy. With reduced dimensionality of a macroscopic system, the DoS gradually reduces from continuous to (semi)discrete one. For 1D structures, like CNTs, the $\text{DoS}(E) \sim \sqrt{E}$ with sharp change with every new electronic state (FIGURE 2.5).

The simple model of a pure 1D quantum system holds very well for SWCNTs [4]. Computations using tight-binding [27,31] and zone-folding [22] approximations result in band structure and $\text{DoS}(E)$ plot expected for a 1D system

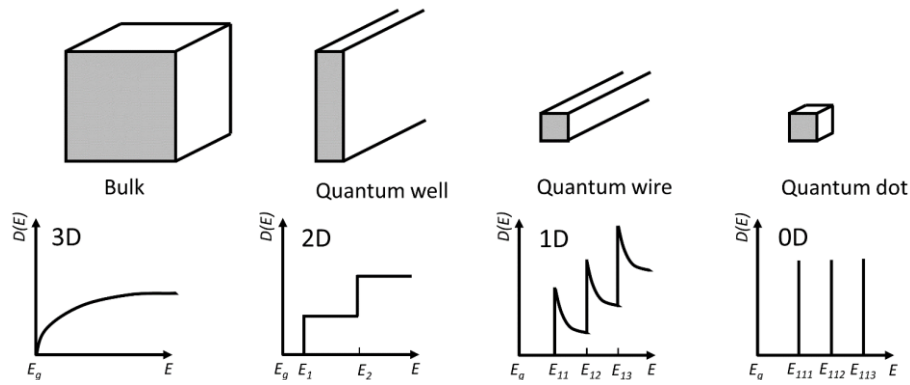


FIGURE 2.5: Comparison of DoS(E) for 3D - 0D structures.

(FIGURE 2.6). However, these approximations, similarly to the discussion above, are not able to recognize the existence of quasi-metallic CNTs. The presence of their meV bandgap was later successfully verified by *ab initio* calculations [30,32]. Obviously, this small bandgap can be observed only at very low temperatures, where the bandgap is not blurred by thermal broadening.

The previous discussion of electronic and band structure of SWCNTs considers idealized model of individual, defect-free, infinitely long nanotube, not affected by the material environment or physical fields. Actual CNTs have, naturally, finite length and their end caps act as defects in the crystallographic structure. Similarly, defects in the hexagonal lattice may be formed during the manufacture process. Due to van der Waals interactions, the nanotubes bundle together or create bonds with molecules in their surroundings. In addition, electric

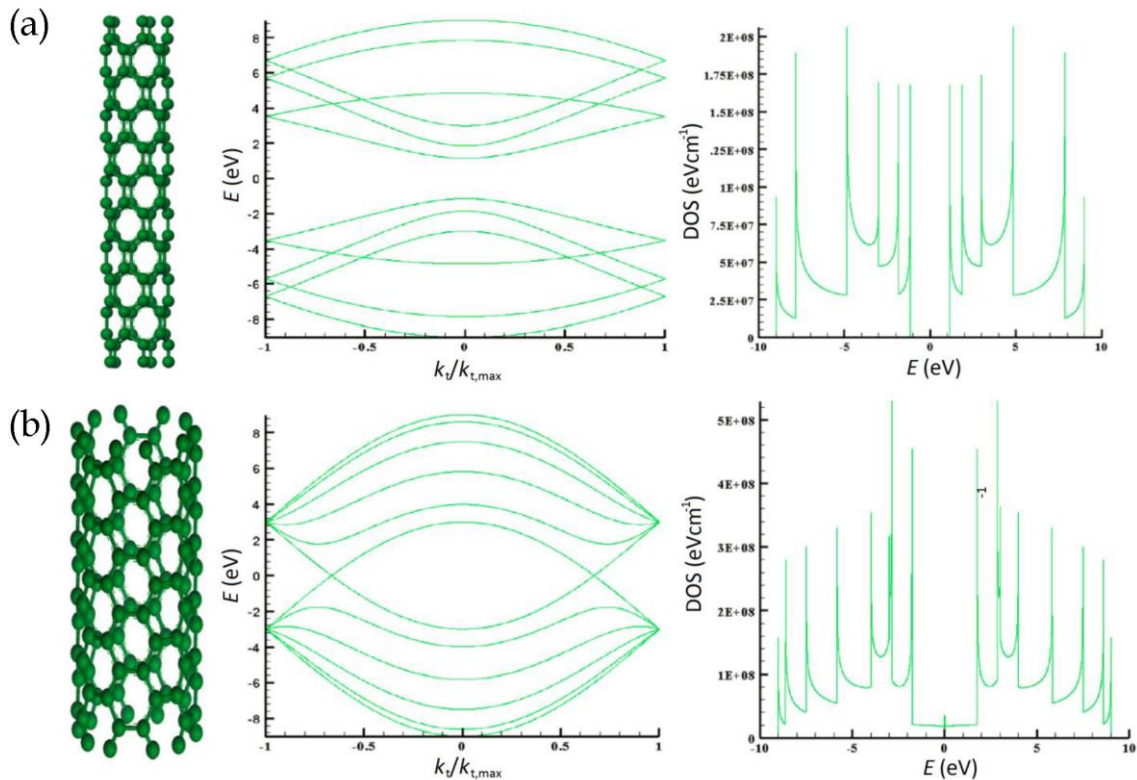


FIGURE 2.6: Atomic structure, band structure and DoS of (a) semiconducting (5,0) and (b) metallic (5,5) nanotube. Fermi level is located at 0 eV. Reprinted from Open Access [31].

and magnetic fields are often present to some extent. All of these effects more or less influence electronic and related optical properties of nanotubes. A comprehensive description of many possible factors influencing electronic structure can be found in [22]. It must be also mentioned, that previous considerations, except the case of *ab initio* calculations, fail in the case of nanotubes with very small diameter, where the curvature effect starts to dominate over the properties of a plain carbon sheet.

2.5 CNT characterization

2.5.1 Direct characterization

The experimental characterization of individual CNTs is a complicated task mainly due to their dimensions and related challenges with manipulation. Direct observation of the atomic structure of a nanotube is possible via some scanning probe microscopy techniques. Atomic Force Microscopy (AFM) [33,34] similar to state-of-the-art Scanning Electron Microscopy [27] can only provide information about nanotube diameter (FIGURE 2.7(a) and FIGURE 2.7(b), respectively). Scanning Tunneling Microscopy or Scanning Tunneling Spectroscopy [27,28] are able

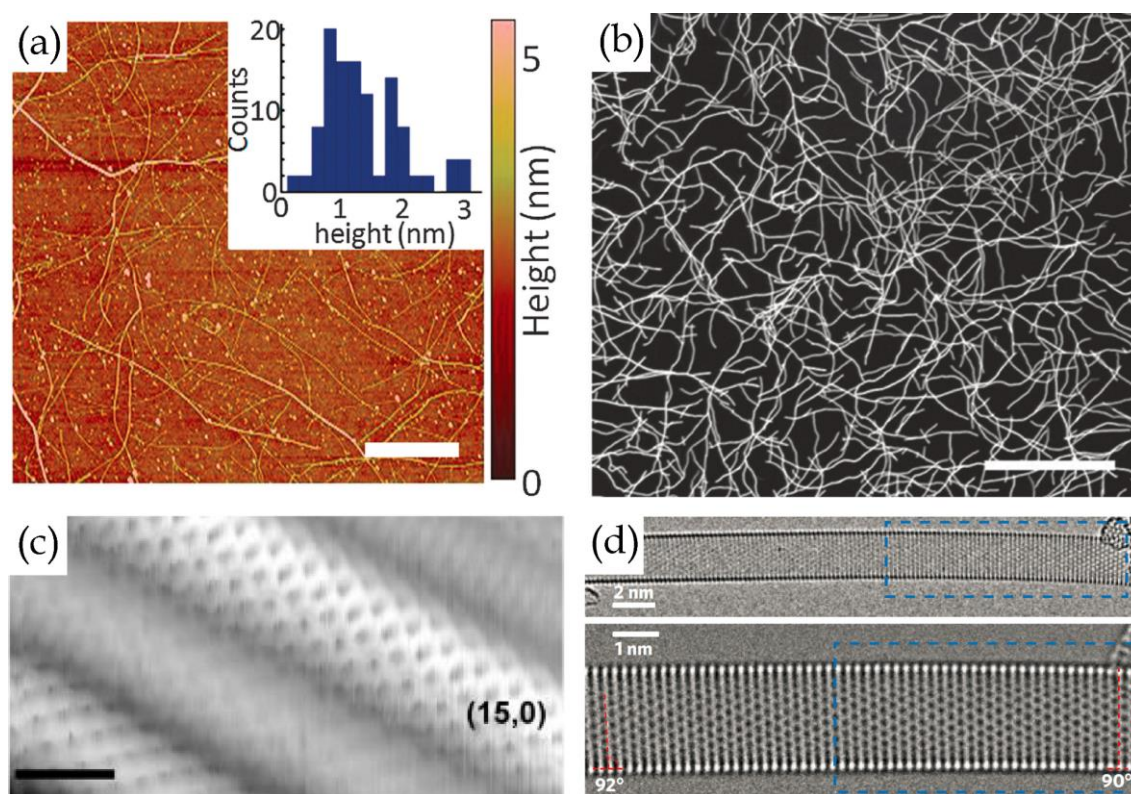


FIGURE 2.7: Direct imaging of CNTs. (a) Atomic Force Microscopy. The scale bar is 1 μm . (b) Scanning Electron Microscopy. The scale bar is 6 μm . (c) Scanning Tunneling Microscopy. The scale bar is 1 nm. (d) Transmission Electron Microscopy. Figures (a) and (b) reproduced from [34] with permission from the PCCP Owner Societies. Figure (c) reprinted from [32] with permission from AAAS. Figure (d) reprinted by permission from [36]. Copyright Springer Nature, 2011.

to provide full atomic resolution (FIGURE 2.7(c)) together with partial information about the electronic structure. Electron Diffraction [35] and aberration corrected Transmission Electron Microscopy [36] (FIGURE 2.7(d)) are able to provide exact structural information routinely.

2.5.2 Indirect characterization

Indirect characterization of carbon nanotubes utilizes their geometry-dependent optical or electronic properties. This enables to link the measured values to particular (n,m) indices. While measurement of Ohmic behavior alone is not able to provide any information except the metallicity/semiconductivity of the nanotube, the optical methods allow direct determination of structural indices. Moreover, optical methods are non-invasive, can be done in short time, require minimal sample preparation, and make use of common, relatively inexpensive equipment. A description of commonly used optical methods for characterization of CNTs follows below.

Raman spectroscopy

In general, Raman spectroscopy measures the energy difference between vibrational states. In the case of SWCNTs, the geometry-dependent vibration unique for nanotubes is the so-called *radial breathing mode* (RBM) (FIGURE 2.8(a)). This mode is diameter-dependent, which is described by the empirical equation [37]:

$$\omega_{\text{RBM}} = \frac{227}{d} \sqrt{1 + C d^2}, \quad (2.6)$$

where ω_{RBM} is the RBM frequency in cm^{-1} , d is the diameter of the nanotube in nm, and $C = 0.05786 \text{ nm}^{-2}$ is a correction constant, which takes into account the effect of the CNT curvature on RBM position. Employing resonance Raman effect, the signal from individual SWCNTs is readily achievable [38]. A comprehensive theoretical and experimental review on Raman spectroscopy of SWCNTs can be found in [39].

Absorption spectroscopy

Absorption spectroscopy measures the energy of photons absorbed by the system. For a quantum system, the energy of an absorbed photon must exactly match the energy difference between allowed electronic states. This difference is unique for a given system and therefore allows to characterize it. For individual SWCNTs, the highest probability of transition is between the valence and conduction bands from the van Hove singularities (FIGURE 2.6), mirrored across the Fermi level. This is due the symmetry of the system. The transitions are usually denoted $E_{11}^S, E_{22}^S, E_{11}^M, \dots$ with index ^S for semiconducting and ^M for metallic nanotubes ($S_{11}, S_{22}, M_{11}, \dots$ in some sources). Since this energy difference is chirality dependent, the peaks in absorption spectra allow to determine the presence of a nanotube with certain chirality. The direct link between the chirality and the position of the absorption peak was first time observed by Kataura *et al.* [40], leading to the well-known Kataura plot in both graphical (FIGURE 2.8(b)) and tabulated [4] form. The absorbance spectrum is then a true fingerprint for particular chirality (FIGURE 2.9).

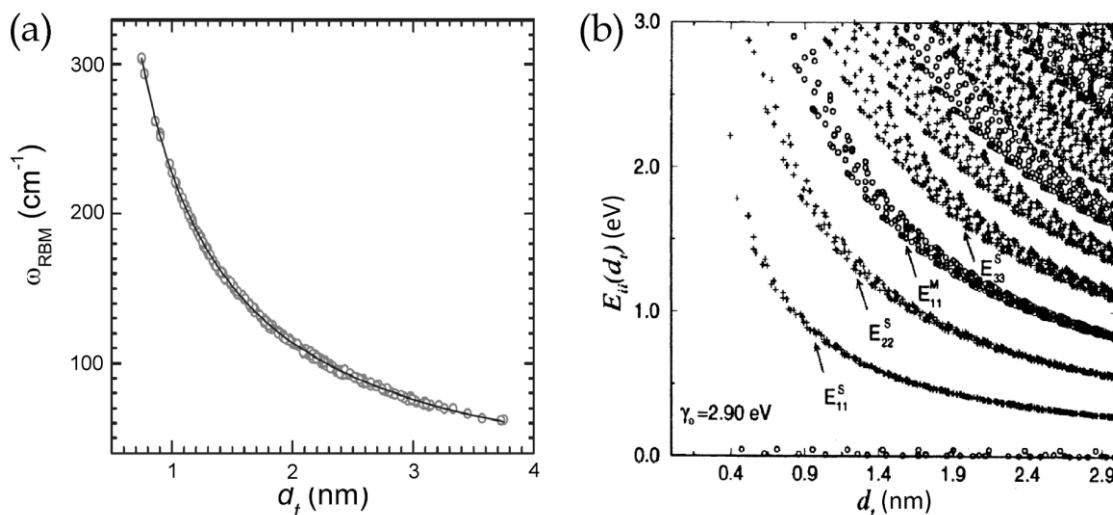


FIGURE 2.8: (a) Experimental radial breathing mode frequency as a function of tube diameter. (b) Calculated energy separations between van Hove singularities in the 1D electronic density of states of the conduction and valence bands for all (n, m) values versus nanotube diameter $0.4 < d_t < 3.0$ nm. Figure (a) reprinted with permission from [37]. Copyright 2008 by the American Physical Society. Figure (b) reprinted from [39]. Copyright 2002, with permission from Elsevier.

Fluorescence spectroscopy

The last indirect characterization method to be mentioned is fluorescence spectroscopy. Fluorescence occurs when a system absorb energy in the form of a photon and an electron-hole pair (*exciton*) is formed. The system is then trying to return to its ground state. In certain systems, radiative transition is the deexcitation pathway with the highest probability and the system in question returns to the ground state via emitting a photon.

The fluorescence pathway for SWCNTs goes as follows: an exciton is formed in a nanotube by absorbing a photon via E_{22}^s (or higher) transition. Both electron and hole rapidly relax via non-radiative transitions to LUMO and HOMO, respectively. Since in this situation no other competing pathway exists in individual semiconducting SWCNT, the hole and electron recombine across the bandgap emitting a photon with the energy of the band-gap. The energy of an emitted photon directly points out the presence of a nanotube with certain chirality. The efficiency of this process is naturally strongly enhanced if the excitation wavelength exactly matches the energy of the E_{22}^s transition (FIGURE 2.9(a)). This results in an excitation/emission plot, which allows clear assignment of the chiralities present in the sample (FIGURE 2.9(b)) [41]. On the other hand, no excitonic fluorescence can be observed from metallic nanotubes. The electron can be excited via absorption of a photon, but the resulting hole is immediately filled by another electron from the electron gas and radiative transition is not possible.

The basics of fluorescence spectroscopy characterization of SWCNTs were published in the early 2000s. The first individual nanotube fluorescence spectrum [42] was rapidly followed by structure-assigned fluorescence spectra [43] and later by experimental observation and empirical relationships (2.7) - (2.10)

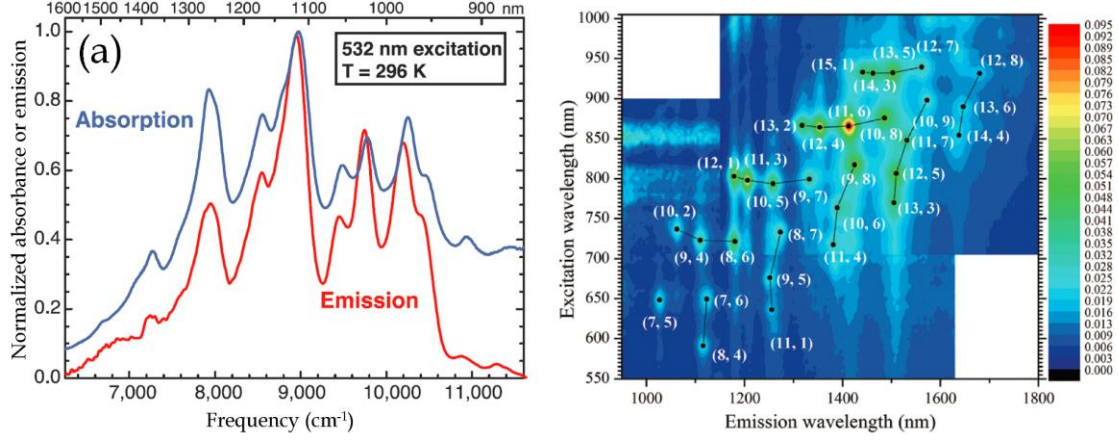


FIGURE 2.9: (a) Absorption and fluorescence spectra of HiPco™ nanotubes. (b) Near-infrared fluorescence map of SWCNTs. Figure (a) from [42]. Reprinted with permission from AAAS. Figure (b) reproduced from [41] with permission of the Royal Society of Chemistry.

for the first and second van Hove transition of a wide range of semiconducting SWCNTs [4]. They have form

$$\bar{\nu}_{11}(\text{mod1}) = \frac{1 \cdot 10^7 \text{ cm}^{-1}}{157.5 + 1066.9d} - 771 \text{ cm}^{-1} \frac{[\cos(3\theta)]^{1.374}}{d^{2.272}} \quad (2.7)$$

$$\bar{\nu}_{11}(\text{mod2}) = \frac{1 \cdot 10^7 \text{ cm}^{-1}}{157.5 + 1066.9d} + 347 \text{ cm}^{-1} \frac{[\cos(3\theta)]^{0.886}}{d^{2.129}} \quad (2.8)$$

$$\bar{\nu}_{22}(\text{mod1}) = \frac{1 \cdot 10^7 \text{ cm}^{-1}}{145.6 + 575.7d} + 1326 \text{ cm}^{-1} \frac{[\cos(3\theta)]^{0.828}}{d^{1.809}} \quad (2.9)$$

$$\bar{\nu}_{22}(\text{mod2}) = \frac{1 \cdot 10^7 \text{ cm}^{-1}}{145.6 + 575.5d} - 1421 \text{ cm}^{-1} \frac{[\cos(3\theta)]^{1.110}}{d^{2.497}}, \quad (2.10)$$

where ν_{11} and ν_{22} are the energy differences for first and second van Hove transition, respectively. The mod1 and mod2 are modulus of $(n - m)/3$ where n and m are indices of the chiral vector. The equations (2.7) - (2.10) clearly show the chirality dependent nature of the transition energies with both diameter d and chiral angle θ influencing the resulting value. These equations are conventionally used for identification of nanotubes till these days.

One of the crucial parameters, when it comes to optical detection of individual nanotubes is the *quantum yield*. The first reported values were very low, showing yields of only about 0.01 % [44]. Later on, the quality of the nanotubes as well as the degree of interactions with the environment, especially with another nanotubes and substrate, were shown to be the main limiting factors when it comes to the fluorescence efficiency. As it was shown, the excitons are delocalized over the bundle [45] and the presence of a single metallic nanotube will provide a faster non-radiative deexcitation pathway [42], similarly to a nanotube in contact with the substrate [46]. By improving both the manufacturing methods and individualization of nanotubes, the quantum yield was reported to be ~ 1 % [47] using gradient centrifugation, ~ 3 % [48] using ultracentrifugation, ~ 8 % [49] using ultralow sonication doses, and the highest value of ~ 20 % [50]

using special surfactant restricting contact with oxygen. The improvements in the individualization together with the advent of superresolution microscopy allowed direct fluorescent observation of individual nanotubes [49,51-53].

There has been a lot of effort in further understanding how environment, nanotube length, presence of defects, and mechanical strain influence the fluorescence spectra. While bundling to semiconducting nanotubes or contact with semiconducting substrate results in shift of emission peaks [45,46], the bundling with metallic nanotubes or close proximity of a substrate leads to significant quenching of the emission [42,46,53]. The fluorescence intensity is generally increasing with the length of the nanotube, however, the published relationship varies from exponential [54] to linear [52,55], with latter results supporting the linear dependence. This implies a nearly constant fluorescence quantum yield and constant absorption cross section per carbon atom. The defects in SWCNT structure (both deviations from hexagonal lattice and nanotube ends) are known to decrease the fluorescence intensity [52,53], while the strain was measured to have little to no influence on fluorescence intensity [53].

Conclusion on indirect characterization methods

Direct characterization methods of SWCNTs allow straightforward determination of the atomic properties of a nanotube. The indirect methods, on the other hand, rely on secondary properties, which are direct consequence of the atomic structure. Nevertheless, the indirect methods are able to reliably determine the chirality of the investigated nanotube. All the above mentioned indirect characterization methods of SWCNTs - Raman, absorption and fluorescence spectroscopy - have indisputable advantage over direct characterization methods in their simplicity. They usually do not require complicated sample preparation and are significantly less time-consuming and less costly. However, these methods are not equally suitable in every situation as their different properties may favor or disqualify them for certain applications.

The common property of all three spectroscopies is the alignment of transition dipole moment along the nanotube axis [39]. It means that only light polarized along the nanotube axis can be absorbed or cause Raman scattering. It results in a situation, where many nanotubes, especially in a 3D scenario, will pass the characterization process unnoticed. In the same way, the inelastically scattered photons and fluorescence emission are linearly polarized in the direction of the nanotube axis. In some cases, this can be utilized for determination of the orientation of the nanotube.

Absorption spectroscopy suffers from several serious drawbacks. Firstly, the always-present background makes it difficult to distinguish the real contribution of SWCNTs to the absorption. Secondly, the absorption spectroscopy is not a very sensitive technique, considering the challenges of numerical comparison of two very close values - reference and sample. From the nature of the experiment it is not common to perform microscopy and thus the examination is limited to relatively large volumes. This favors absorption spectroscopy for bulk characterization and experiments with larger volumes.

Both Raman and fluorescence spectroscopy are conveniently used in microscope configuration, which allows high spatial resolution and thus favors these

techniques for single nanotube experiments. Employing the resonance process [56], single molecule detection and characterization is achievable. With the combination of RBM position and used excitation wavelength one can reliably determine the chirality of the excited nanotubes. However, this is possible only for a limited subset of nanotubes, for which electronic transition energy exactly matches the excitation wavelength. In addition, Raman spectroscopy inherently suffers from low sensitivity compared to fluorescence spectroscopy due to low efficiency of inelastic scattering.

The only serious drawback of fluorescence spectroscopy is its inherent incapability of detecting metallic nanotubes [7] compared to Raman [39] and absorption [57,58] spectroscopy, as these do not discriminate nanotubes by being metallic or semiconducting. The single fluorescence spectrum is less congested compared to absorption spectrum due to the enhanced emission of SWCNTs nearly resonant with the excitation wavelength. At the same time, the fluorescence spectroscopy is not as 'picky' as Raman spectroscopy, because the resonant spectral window for fluorescence excitation is much broader. The sideband and off-resonant absorption together with wide fluorescence dynamic range and spectral separation then allows minor emitting species to be distinguished from dominant emitters and a relatively wide subset of (n,m) can be detected [59]. Since the fluorescence signal is directly linked with nanotube atomic structure, the fluorescence spectroscopy is particularly useful for characterization of isolated individual semiconducting SWCNTs. In another words, it is a useful tool when it comes to determination of whether the examined nanotube is truly not bundled (at least with metallic nanotube) or in contact with substrate. Due to its great sensitivity, it is possible to reach single-nanotube detection limit.

2.6 CNT manufacture

Various production methods have been systematically developed and improved since the discovery of SWCNTs [3,5,60,61]. In majority, nanotubes are grown on metallic catalyst particles with a suitable source of atomic carbon (FIGURE 2.10) [62]. The most used method is CVD³, where a carbon-containing gas is thermally decomposed, and the carbon adsorbs on edges of metallic nanoparticles

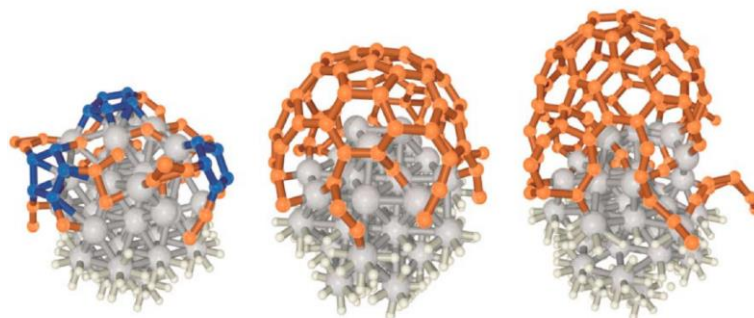


FIGURE 2.10: Snapshots of the growth process of a SWCNT on a 1 nm Fe nanoparticle (55 atoms), as observed in *ab initio* molecular dynamics simulations. Reprinted with permission from [62]. Copyright 2005 by the American Physical Society.

forming the nanotubes. Another approach utilizes chemical-based methods as catalytic decomposition of hydrocarbons, electrolysis, thermal decomposition of polymers, low temperature pyrolysis, and CCVD⁴. This approach uses catalysts to speed up the reaction rate as compared to conventional CVD. Also, more rare methods like synthesis in plasma flame, by electric arc in controlled atmosphere or in water, by pulsed or continuous laser radiation, and growth in microgravitational environment should be mentioned. All these methods vary in cost, quality and purity of produced nanotubes, and in the level in which the properties of nanotubes can be controlled.

One manufacture methods should be highlighted for the purpose of this manuscript. The *high pressure carbon monoxide* (HiPco™) method [63,64] uses a flow of Fe(CO)₅ mixed with CO through heated reactor at high pressures. Both precursors thermally decompose with iron pentacarbonyl providing iron for formation of nucleation clusters and carbon monoxide supplying carbon for the growth of nanotubes. With properly tuned parameters, a production of SWCNTs with purity up to 99.9 % is achievable. The HiPco™ nanotubes are nowadays commercially available with diameter within interval 0.8 – 1.2 nm and length 100 – 1 000 nm. While nanotubes manufactured by this method are generally too short for applications exploiting the mechanical properties of CNTs, the high quality HiPco™ nanotubes are often considered a quality standard in studies dealing with electronic and optical properties of SWCNTs.

2.7 Application issues

Despite the enthusiasm started after SWCNTs discovery and peaking with every reported application, the nanotubes are not a part of our everyday life even 27 years later. The main challenge impeding their broad application lies in the heterogeneity of the produced nanotubes. Every current production method, except cloning, produces nanotubes mixed with various crystalline and amorphous impurities as graphitic nanoparticles, amorphous carbon, and catalyst particles. The degree and nature of impurities varies with growth method. The presence of such impurities makes as-produced SWCNTs basically impossible to use as it generally leads from erroneous behavior to total failure of a nanotube-based device. The process of removal impurities from as-grown product is called *purification*. Purification usually consist of a combination of steps [6]:

- dispersion – to access impurities inside of the bundles
- dry oxidation OR
- rapid thermal annealing [65] – to remove carbonaceous catalyst encapsulation
- wet oxidation – to etch away the catalysts
- filtration – to remove the etching products
- vacuum annealing – to restore possible damages in CNT structure

⁴ catalytic CVD

The obvious harsh treatment of SWCNTs during purification necessarily damages also the nanotubes themselves. Therefore, some milder protocols were reported, including magnetic or electrophoretic purification and centrifugation [6]. Nowadays, the purification process of as-grown nanotubes is well established even in large scale and products with less than one weight percent of metal catalyst impurity are commercially available [66].

Besides the impurities, as-manufactured SWCNTs inherently contain a mixture of different chiralities/diameters. These geometry variations result in changes of their electronic and optical behaviors of the ensemble. The close proximity of other nanotubes leads to shifts in electronic spectra and thus to change of required properties for given application. This brings inevitable decrease of the performance of as-designed device due to the bandgap position and width variation whether it comes to electronic, optical, biomedical, solar cell, or sensing applications [8]. The process of separation of nanotube mixture into different grades is called *sorting*.

Moreover, the nanotubes readily form bundles due the surface van der Waals force [67]. Since the nanotubes bundle randomly with other chiralities, every successful sorting procedure must be preceded by debundling - *individualization*. This step, along with another challenging task, manipulation of individual nanotubes, has to be mastered on the way towards the realization of SWCNTs potential, the single nanotube devices.

While the outstanding properties of many single SWCNT devices have been experimentally proven (single nanotube FET⁵ [25], single nanotube memory [68], single photon source [7], single metallic nanotube interconnects [69], just to name a few), the way of obtaining nanotube with appropriate properties is everything but easy and straightforward. Even nowadays, the way how to build a single SWCNT device goes as follows: a small number of nanotubes are grown directly on a substrate, or a mixture of purified and individualized nanotubes are dispersed on a substrate. Consequently, all the nanotubes are characterized. If a nanotube with needed properties/chirality is found (which is far from a rule), the rest of a device is actually build around it. This complicated, time-consuming, and difficult to scale-up process is the main bottleneck in broader deployment of single SWCNT based technology.

2.7.1 Sorting

Nanotubes can be sorted according to several parameters, namely the length, electronic type, diameter and chirality. Two major approaches exist in the community. The first focuses on property selective synthesis and consequent purification while the second one works on sorting from ensemble of purified nanotubes with varying properties [6-8,70,71].

The length of the nanotube is important when it comes to its application. While shorter nanotubes are needed for nanoelectronic devices, long ones are a necessity for structural applications and composites. The length of nanotubes can be controlled by tuning the synthesis parameters, however the purification and

⁵ field-effect transistor

individualization often results in breaking of the SWCNTs. Therefore, the post-purification sorting is usually used for length sorting. The field-flow fractionation, capillary electrophoresis, and size-exclusion chromatography are just some of the techniques used with the last one resulting in length variation less than ten percent [6].

Sorting by electronic type is needed especially when pure fractions of metallic nanotubes are needed for application utilizing their mechanical and optical properties together with high conductivity. A pure fraction of semiconducting nanotubes is used in applications, where the performance of the device is not significantly affected by mixture of bandgaps present in the sample. Highly selective sorting protocols, relying mostly on *in situ* selective etching were reported for both enriched metallic (>88 %) [72] and enriched semiconducting (>97 %) [7,62] SWCNTs. From the sorting methods, electronic type selective surface interaction leading to change of density, AC dielectrophoresis, DNA assisted separation, and surface discriminating surfactant should be mentioned [6,8,70]. All of these methods, however, result rather in enrichment than in real separation.

Chirality-selective synthesis

Due to the outstanding knowledge of the properties of SWCNTs with particular chirality and related simplicity and repeatability of devices based on such nanotubes, a remarkable effort has been made in the field of exact chirality selective synthesis or chirality selective sorting. The chirality of a nanotube is believed to be set at the nucleation step on the catalyst particle, therefore, controlling the nucleation step at the beginning of nanotube growth is crucial [7]. There are many parameters, which control the nucleation and consequently the chirality including catalyst types, sources of carbon, system temperature and pressure, carrier gas composition, growth time, and so forth. From the results reported so far, the catalysts have the most deterministic role on the chirality of as-grown SWCNTs [73,74]. Highly sophisticated metallic nanoparticles were used for producing carbon nanotubes with very narrow diameter distribution [64,75]. Development in this field led to CoMoCAT method [76], which is able to synthesize a mixture of SWCNTs with 55 % share of (6,5) nanotubes. It was a big challenge to engineer catalysts for nanotubes with larger diameters, but recent research has resulted in bimetallic atomic cluster catalysts able of selective synthesis of (12,6) (>92 % purity) and (16,0) (>79 % purity) [7]. This concept provides nearly single chirality nanotubes in industrial scales, but it still suffers from insufficient selectivity, limited choice of chiralities and post-purification caused damage, which decrease the quality of this product.

Another sub-field of the chirality selective synthesis is so-called cloning. In this method a short piece of nanotube is used as a precursor for further growth by vapour-phase epitaxy [77] (FIGURE 2.11(a)). It was shown, that nanotubes synthesized in this way keep the chirality of a seed along its axis and thus very long nanotubes with known chirality can be prepared. Since then, other ways to prepare suitable growth templates were reported, including one hexagon wide ring for production of armchair SWCNTs and self-closing end caps [78] synthesized via organic chemistry methods (FIGURE 2.11(b)). The effectivity and yield

of this method, capable of producing single chirality nanotubes is, unfortunately, still very low [7,8].

Chirality selective sorting

The post-production chirality selective sorting of as-grown SWCNTs is another approach for obtaining nanotubes with single chirality. Many different protocols were developed in last two decades. Their common feature is individualization of the SWCNTs in a dispersion prior to the separation. Five successful methods have established in the field of sorting to this day [7,8,70].

- *DGU*: In density gradient ultracentrifugation method, SWCNTs with different structure have different densities due to the selective adsorption of surfactants onto them. In the environment of competing buoyant and centrifugal forces, nanotubes with specific chirality move towards the place with matching density in a medium with linear change of density. More than 97 % purity of nanotubes in 0.02 nm interval of diameters was achieved by this method [79].
- *IEX (DNA wrapping)*: Ion exchange chromatography is a method separating ions and polar molecules based on their affinity to the ion exchanger. Usually DNA molecules are used to wrap around the SWCNTs and their mutual structure-dependent affinity results in different adsorption onto the exchanger. In the newest update of this method, single-stranded DNA sequences were tailored to selectively wrap around nanotubes with specific chirality. In this way, all 12 semiconducting species from HiPco™ nanotubes were separated with purity varying from 60 % to 90 % and yield 0.1 % [57,80] (FIGURE 2.11(c)).
- *Gel chromatography*: Compared to traditional use of gel chromatography in molecular biology for sorting of molecules by size, gel chromatography for carbon nanotubes sorting uses selective affinity of surfactant molecules to nanotubes with different chirality and minimal interaction of well-wrapped nanotubes with gel medium. By this method >93 % pure fraction of (9,4) and >96 % pure fraction of (10,3) nanotubes in significant amounts (1.2 mg·day⁻¹) were sorted [81,82] (FIGURE 2.11(d)).
- *(Co)polymer isolation*: In this method, tailored polymers selectively wrap around different-structure SWCNTs, making them soluble in organic solvents, while nanotubes not being wrapped remain insoluble. Different polymers have been proposed. The best work using this method reported 60 % purity of (7,5) chirality [70]. DNA was also used as a highly tailorable polymer for this type of sorting [8]. This method benefits from its simplicity, however, the cost of tailoring polymers for selective wrapping limits its broad deployment.
- *ATPE*: Aqueous two-phase extraction is the latest technique successfully used for SWCNTs sorting. It utilizes spontaneous separation of aqueous solutions of polyethylene glycol and dextran when mixed together. The difference in hydrophilicity of these two separated phases and fine tuning of the surfactant concentration, which influence the structure-dependent

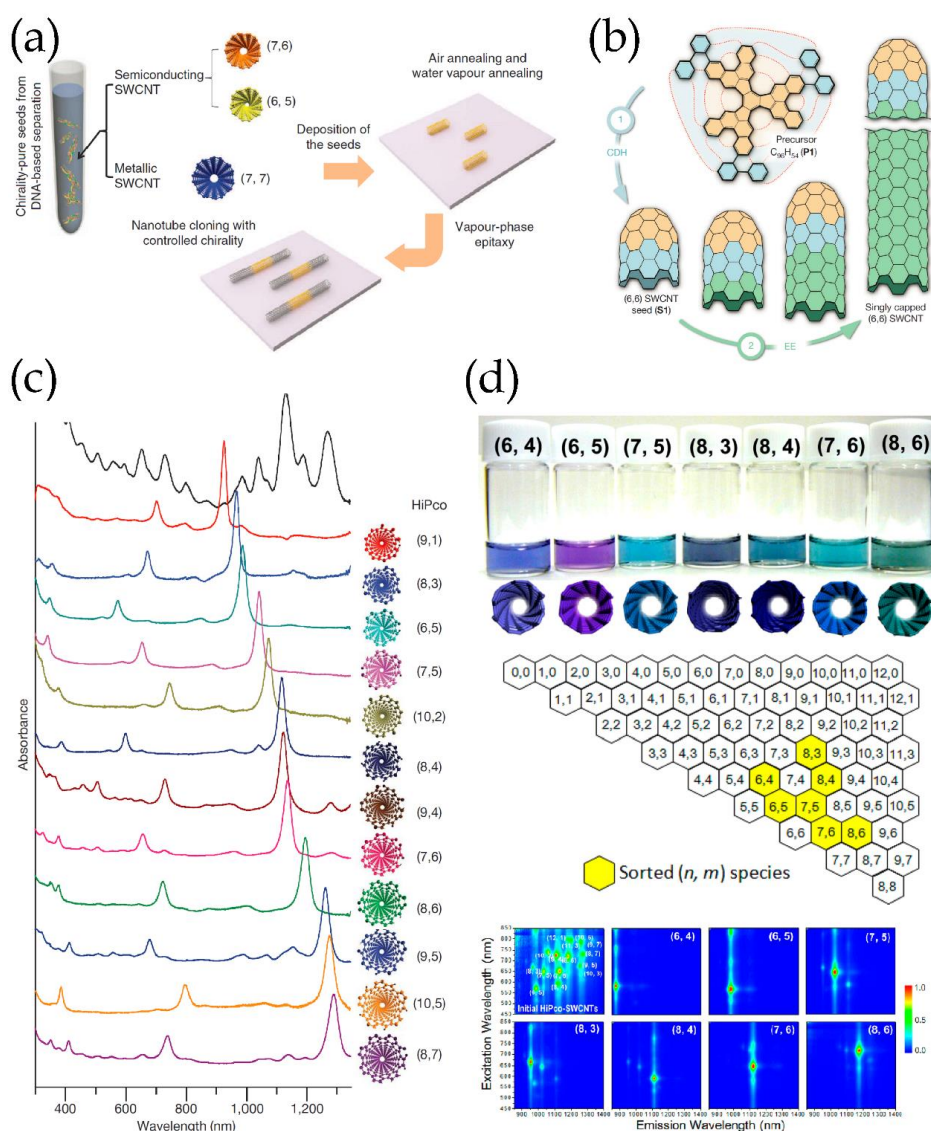


FIGURE 2.11: (a) Vapour-phase epitaxy cloning of SWCNT seeds. (b) Chirality specific growth from self-closing nanotube end cap. (c) UV-VIS-NIR absorption spectra of sorted semiconducting SWCNTs. In some tubes (8,3), (9,4), (7,6), (8,6) and (8,7) even E_{44}^S transition can be seen at the highest energies. (d) Single chirality CNT dispersions sorted by gel chromatography. Figures (a), (b), and (c) reprinted by permission from [77], [78], and [57]. Copyright Springer Nature, 2012, 2014, and 2009. Figure (d) re printed with permission from [82]. Copyright 2013 American Chemical Society.

hydrophilicity of the SWCNTs leads to distribution of nanotubes to the different aqueous phases. More than 84 % purity of (9,8) SWCNTs were achieved by this method. The ATPE seems to be very promising in terms of efficiency, tunability, scalability and low cost. However, there are some obstacles to overcome, mainly the sensitivity to experimental conditions and difficulties with removal of the used chemicals from the surface of the nanotubes [70].

The chirality-selective sorting methods offer better results compared to chirality-selective synthesis so far. While 90 % purity is easily achievable by sorting, it stays elusive for synthesis. The main difference lies in the active length of the

reaction. While in synthesis, the chirality is defined on the size of a catalyst nanoparticle, the region for dispersant molecule to wrap around the nanotube is along the whole nanotube. A small difference in binding energy per unit length can be amplified to a large difference on the whole length of the nanotube resulting in high selectivity of the separation [7]. However, all the sorting processes inherently suffer from low yield, mainly due to the iterative process, which is needed to reach reasonable purity of the chosen chirality. On the other hand, SWCNTs prepared in this way usually possess less internal damage as the sorting process is usually capable of removing damaged nanotubes. Nevertheless, the ultimate goal of pure chirality SWCNTs is still too far away to grab even when considering all the methods known to date.

2.7.2 Individualization

Prior to basically any kind of handling of nanomaterials including SWCNTs, they are usually dispersed in liquid phase. This allows safer and easier manipulation, handling and processing. It can be seen *e.g.* from the previous section, where all the sorting methods utilize nanotubes dispersed in the liquid phase. However, two fundamental challenges arise when it comes to dispersing SWCNTs in any kind of solvent.

- Carbon nanotubes naturally come entangled in bundles and ropes.
- All carbon materials (except fullerenes) are inherently hydrophobic and insoluble [83].

Due to the negative influence bundling has on electronic and optical properties, most applications require full individualization, if they aim to take full advantage of SWCNT's potential [84]. Hence, some energy has to be delivered to the system in order to separate the bundles. In addition, pristine nanotubes can be only dispersed in solvent, never truly dissolved [85], with the fundamental unit to disperse being one nanotube. There are very few exceptions to this rule, *e.g.* bile salt surfactants [86] or electrically charged systems [87,88], which do not need energy from outside to individualize nanotubes from bundles, or special synthesis processes producing individual nanotubes rather than bundles [75].

The SWCNTs are tightly bound in bundles by van der Waals attraction energy of about $500 \text{ eV} \cdot \mu\text{m}^{-1}$ of nanotube-nanotube contact [89]. Therefore, rather vigorous mechanical actuation has to be performed to individualize the nanotubes. Sonication followed by centrifugation is the most widespread method, but also other ways to deliver energy to the system were reported [85]. It is commonly accepted that debundling happens via process, where the energy delivered from outside frays the end of the bundle, allowing adsorption of surfactant molecules in the open cleavage and continue in so-called *unzipping* [90] (FIGURE 2.13(a)).

Although insoluble, SWCNTs can be relatively well dispersed in several organic solvents. 1,2-dichlorobenzene, chloroform, or 1-methylnaphthalene were shown to have the best affinity to graphenic nanotube surface [91]. However, the concentrations of dispersed nanotubes are very low ($\sim 10 \mu\text{g} \cdot \text{mL}^{-1}$) and the

rebundling happens relatively fast ($\sim 4 - 72$ hours). To increase the concentration and prevent reaggregation, a system which makes them repel each other or at least prevents them from coming in contact with each other, has to be introduced. The most straightforward way is to introduce some charge to the nanotube either via reduction or oxidation. The resulting charged macromolecules are soluble in some organic solvents or acids, respectively. It must be noted here, that this treatment fundamentally changes the electronic structure of the nanotube (in the language of physics, reduction results in n-doping and oxidation/protonation in p-doping). Although it allows the formation of a true thermodynamically stable solution with high degree of individualization, the electronic properties are different from pristine SWCNTs and thus of limited use. A typical example of a reduction is the formation of a lithium salt of carbon nanotubes and dissolving in tetrahydrofuran [87]. On the other side, an oxidative treatment or protonation in strong acids leads to good solution of SWCNTs [88,90]

The most used systems, however, are aqueous dispersions. Safe and easy manipulation, low cost, achievable high concentrations, and plenty of interesting ready-to-be-used biological techniques developed for water-based solutions are very attractive. Due to the intrinsic hydrophobicity of the SWCNTs, the surface of the nanotubes must be functionalized, and the nanotubes must be protected from rebundling. Both covalent or noncovalent functionalization are used but the noncovalent systems are generally preferred. The reason is the typical low surface functionalization, irreversibility and modification of the electronic structure of covalently functionalized nanotubes [85]. On the contrary, it was shown that noncovalent functionalization have little effect on the electronic properties of SWCNTs [92] and can form dispersions which are stable for more than a year [85]. The vast family of materials used to disperse SWCNTs are shown in FIGURE 2.12.

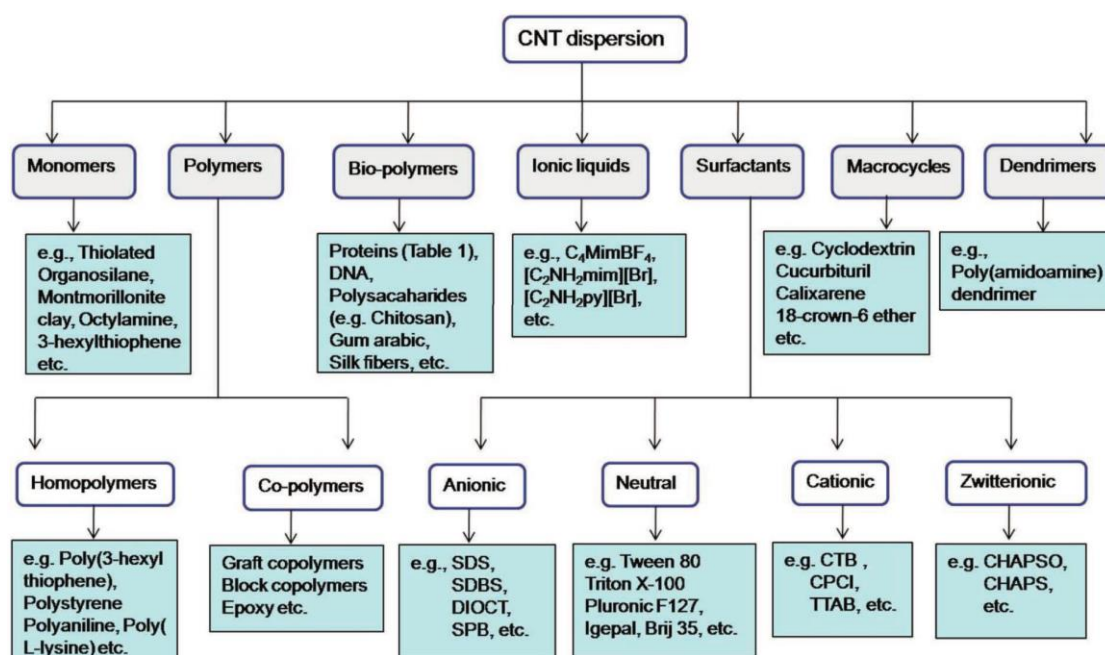


FIGURE 2.12: Various types of materials used for the aqueous dispersions of CNTs. Figure reprinted with the permission from [85]. Copyright John Wiley and Sons, 2012.

2.8 Aqueous dispersions of SWCNTs

The aqueous dispersions of SWCNTs are very popular, especially for spectroscopic investigation of carbon nanotubes. In addition, the systems water-surfactant-nanoparticle are widely used and well understood. Due to the intrinsic hydrophobicity of SWCNTs, amphiphilic nature of surfactants is considered an advantage, as the hydrophobic side adheres on the nanotube surface and hydrophilic side orients itself towards the water. This situation not only allows the water phase to wet the nanotube covered with surfactant but also prevents the re-bundling of once individualized nanotube. Since SWCNTs with larger diameters are active further in near-infrared (NIR) region, where water strongly absorbs, some papers report use of heavy water D₂O to avoid this obstacle [48,93-95]. Nevertheless, both systems (H₂O and D₂O) are addressed as aqueous solutions.

2.8.1 Choice of surfactant

Surfactants are traditionally divided to four groups according to the charge on their hydrophilic head (FIGURE 2.12). Some representatives from every group were found to support the dispersion of SWCNTs but generally, ionic surfactants are preferred for aqueous dispersions of SWCNTs. Interestingly, there is not a clear conclusion on superiority of either cationic or anionic surfactants [96]. This is an important observation, since it implies the fact that the surface charge of an individual nanotube, which interacts with the surfactant tail, is defined during the purification and wall-functionalization process rather than by the nature of the nanotube [83]. Despite this fact, the most commonly used surfactants in the (fluorescence) spectroscopy field, sodium dodecylbenzene sulfonate (SDBS) [93-95,97,98] and sodium dodecyl sulfate (SDS) [97,99,100] are from the group of anionic surfactants having negative charge on their head. More systematic studies [97,101,102] revealed superior performance of SDBS among all the other commonly used ionic surfactants with the best surface coverage and with the highest mass of nanotubes dispersed in the water. The benzene ring in the SDBS structure was proposed to be the main reason for superior behavior of SDBS due to the π - π interaction between the CNT surface and the ring [96,97]. The surfactant self-assembly was thought to play critical role during individualization and consequent stability of the SWCNT dispersion (FIGURE 2.13(b)&(c)). It seems, however, that the surfactants adsorb on the surface of the nanotube in a more or less random way [103] (FIGURE 2.13(d)). This conclusion further supports the contribution of the benzene ring in the SDBS structure to the final stability of the dispersion.

2.8.2 Concentration of nanotubes

The amount of the nanotubes at the beginning of the individualization process does not significantly affect the resulting dispersion. The only condition is to supply enough nanotubes to cover the needs of the process before the concentration of dispersed nanotubes reaches saturation. The usual amounts of as-produced SWCNTs added to the water vary in different studies (0.1 mg·mL⁻¹ [101], 0.4 mg·mL⁻¹ [100], 0.006 to 5.0 mg·mL⁻¹ [94], and 0.2 to 0.6 mg·mL⁻¹ [95]) but the

general conclusion is that 0.1 to 0.5 mg·mL⁻¹ is a reasonable amount. The dispersion will not reach its full potential below these values and it is a wasting of SWCNTs above these values. The more important value, however, is the amount of nanotubes, which can be *well individualized and dispersed* in the aqueous surfactant solution. The reported values are in the interval of 0.025 mg·mL⁻¹ [42] – 0.07 mg·mL⁻¹ [94] with an outstanding record of 3.35 mg·mL⁻¹ when using sucrose as viscosity modifier [93].

2.8.3 Amount of SDBS

The critical micellar concentration (CMC) is an important characteristic of every surfactant. When surfactant is added to the water, it is automatically driven to the surface and interfaces. When the created layer saturates, the free surfactant molecules start to self-assemble to micelles – spheres with hydrophobic tails hidden inside and hydrophilic heads heading outside⁶. The concentration of SDBS does not seem to play a role in the quality of dispersion with >1xCMC⁷, and the micelles are expected to act as reservoirs supplying surfactant molecules. However, at too high surfactant concentrations depletion-driven aggregation significantly decreases the SWCNTs dispersibility. The top limit for SDBS was reported to be ≥10xCMC [97] or >2 % (w/w) [102]. Accordingly, the amount of SDBS reported throughout the literature varies within these borders (0.1 % [104], 0.5 % [102,104], 0.7 % [98], 1 % [49,51,52,94,105], and 2 % [93], all (w/w)), with the 1 % (w/w) considered as a standard value.

2.8.4 Sonication

Sonication is the usual procedure when it comes to individualization of SWCNTs from the bundles and the kinetically stable colloidal dispersion is formed (FIGURE 2.13(a)) [90,97]. Three types of sonicators are used; bath-type [97], horn-cup [42], and finger-type [52]. Unfortunately, the main parameter of a sonicator, the sonication power, has different meaning and effect in all three sonicator types. In general, finger-type sonicators are preferred as they usually work at lower frequency of ~20 kHz, compared to ~40 kHz for the other types. Lower sonication frequency creates larger cavitation bubbles – the main driving force of unzipping – and thus greater forces as they collapse [95]. However, there is one noteworthy disadvantage of finger-type sonicators. The cavitation bubbles driving the individualization also cause damage to the sonication tip and the efficiency of the debundling decreases with time [95]. Therefore, the tip has to be regularly polished to obtain comparable results.

The sonication parameters using finger-type sonicators vary vastly among the reported protocols. In addition, important parameters are often missing, causing the comparison of results close to impossible. However, a general agreement exists among authors of sonication parametric studies [95,104]:

⁶ This happens in reverse order when surfactants are added to oil-based solvent.

⁷ CMC for SDBS in water is 0.05 % (w/w).

- Increasing the power density and sonication time creates dispersions with higher SWCNTs concentrations, reduced bundle sizes and higher fraction of individual tubes.
- Increasing the power density and sonication time causes shortening of the SWCNTs and introduction of structural defects.
- The mechanical energy introduced to the system via sonication is partially converted into heat. The heat must be allowed to dissipate quickly out of the system as increase of the temperature over 30 °C causes the SDBS to lapse and prevents proper coverage of the nanotubes [95].

The clear contradiction in first two conclusions results in a trade-off, where the amount of individual tubes has to be balanced with acceptable amount of defects [95,97,100]. In order to properly classify the sonication process, several parameters have to be defined:

- Sonicator power (W): The highest power a finger-type sonicator is able to deliver to sample at optimal conditions.
- Sonotrode diameter (mm): The diameter of the end of the probe, which delivers mechanical waves to the sample.
- Sonotrode end: Flattened tip of the electrode, perpendicular to the sonotrode axis. All the power is delivered to the sample via sonotrode end.
- Amplitude (μm): Vertical displacement of the sonotrode end, equal to the amplitude of acoustic waves in the sonotrode material. A parameter provided by manufacturer. Besides the sonication time, this is often the only tunable parameter of the sonication process.
- Sonication time (s): The duty time of sonication. Since the sonicators often offer the possibility of cycling, the sonication time includes only the time, when the sonicator is on.
- Acoustic power density ($\text{W}\cdot\text{cm}^{-2}$) The power delivered through the surface of the sonotrode end. A parameter equal to intensity, provided by manufacturer. Since intensity and amplitude are linearly dependent, the acoustic power density changes proportionally to the amplitude.
- Delivered power (W): Acoustic power density divided by the sonotrode end surface. It represents the real power delivered to the sample.
- Delivered energy (J): Delivered power multiplied by sonication time.
- Proportional delivered power ($\text{W}\cdot\text{mL}^{-1}$) Delivered power divided by sample volume.
- Proportional delivered energy ($\text{J}\cdot\text{mL}^{-1}$) Delivered energy divided by sample volume.

At least two papers, investigating the influence of sonication on resulting SWCNT dispersion conclude that the crucial parameter is the proportional delivered energy. For finger-type sonicator, the optimal value was found to be $530 \text{ J}\cdot\text{mL}^{-1}$ [97] and $450 \text{ J}\cdot\text{mL}^{-1}$ [95] with recommended proportional delivered power $<0.5 \text{ W}\cdot\text{mL}^{-1}$ in order to prevent structural damage of the SWCNTs [95], while for bath-type sonicator the optimal value was found to be $2\ 250 \text{ J}\cdot\text{mL}^{-1}$ [104].

Despite these conclusion, some authors argue, that shorter sonication at high acoustic power density causes more structural defects than longer sonication time at low acoustic power density [93,95,97,98]. The latter approach takes place mainly when high(er) concentration of SWCNTs in dispersion is requested. Conversely, when concentration does not play a role and only a few high quality nanotubes are needed, mostly for fluorescence spectroscopy, the high acoustic power density and ultrashort sonication times with thorough consequent centrifugation is preferred [49,52,94,102].

2.8.5 Centrifugation

Centrifugation commonly follows the sonication process. The centrifugation utilizes the difference in density between individualized nanotubes and bundles, both covered by surfactant molecules. The centrifugation force applied on the sample effectively accelerates the natural process of sedimentation with components denser than the environment migrating away from the axis of the centrifuge, while components less dense than the environment migrate towards the axis. For a spherical particle, the sedimentation rate can be derived from the Stokes equation as

$$R = \frac{d^2(\rho_P - \rho_M)g}{18\eta}, \quad (2.11)$$

where R is the sedimentation rate, d the diameter of the particle, ρ_P the density of the particle, ρ_M the density of the medium, g is the gravitational acceleration, and η is the dynamic viscosity of the medium. The gravitational acceleration depends on angular velocity expressed as revolutions per minute (RPM). The effective centrifugal force, however, depends on the radius of the rotor. The *centrifugal field* is therefore better value to compare results from different centrifuges. The centrifugal field is commonly expressed in multiples of g , where $1g$ is regular gravitational acceleration. The term ultracentrifugation is often used in available literature. The ultracentrifugation, however, only addresses high centrifugation forces applied and therefore, the term *centrifugation* with specified field will be used from here.

The SWCNTs dispersion after sonication still contains significant amount of small bundles and other impurities, mainly remaining metal catalyst particles. The density of surfactant-wrapped individual nanotubes differs from bundles or catalyst particles. While the density of individual tubes wrapped by SDS surfactant was reported to be $\sim 1.0 \text{ g}\cdot\text{cm}^{-3}$, the typical 7-tube bundle has a density of $\sim 1.2 \text{ g}\cdot\text{cm}^{-3}$, and catalyst particle $\sim 2 - 3 \text{ g}\cdot\text{cm}^{-3}$ [42] (FIGURE 2.13(e)). Individual SWCNTs in Sodium cholate system shows a density of $\sim 1.06 \text{ g}\cdot\text{cm}^{-3}$ versus $\sim 1.15 \text{ g}\cdot\text{cm}^{-3}$ for bundles [45]. The values reported for SDBS surfactant system are $1.07 \text{ g}\cdot\text{cm}^{-3}$ for individual SWCNT and decreasing from 1.65 to $1.20 \text{ g}\cdot\text{cm}^{-3}$ with decreasing bundle size [98]. Since the settling velocity of a particle is a complex function of its shape, size, centrifugal field, the *density difference* between the particle and the environment, viscosity of the environment, and volume fraction of the particles, the separation of bundles and individual SWCNTs can be conveniently done by proper choice of centrifugal field and time. This will result in a

precipitate (pellet, sediment) formed mainly from bundles and other impurities, while the supernatant will be highly enriched in individual SWCNTs.

Similarly to sonication, the parameters of centrifugation significantly vary across the literature. It is difficult to find any optimal values, with the reported centrifugal field varying from 1 700g [94] to 300 000g [26] and time from 3 minutes [98] to 4 hours [42,93]. Nevertheless, one interesting correlation can be found. The works utilizing absorption spectroscopy, Raman spectroscopy, and/or AFM analysis generally conclude that low centrifugal fields (thousands of g) and relatively short times (minutes) are sufficient to separate individual nanotubes from the bundles [94,97,102,104], while studies utilizing fluorescent emission report both much higher fields (>100 000g) and times (hours) [26,42,93,98]. It seems, as Raman spectroscopy, absorption spectroscopy, and AFM are not very sensitive when it comes to distinguishing between individual nanotubes and small bundles, the works using weak centrifugation include also solutions containing small bundles to the category of well individualized dispersions. There are naturally some exceptions, *e.g.* [95,102] using strong centrifugation and characterization of the dispersion using only absorption and Raman spectroscopy. This approach, however, does not interfere with the previous statement. On the other hand, studies [49,52] use only weak centrifugation for dispersions investigated by fluorescence spectroscopy. Both of them, however, apply only very short sonication, which may suggest that there are only a few individual nanotubes and plenty of relatively large bundles. Therefore, even weak centrifugation can be sufficient to prepare dispersion of well individualized SWCNTs. For the samples investigated by fluorescence spectroscopy, one set of parameters is particularly popular: the centrifugal field 122 000g and time from 1 to 4 hours [42,93,95,102]. However, it is difficult to conclude if this particular set of values was found to be the best, simply sufficient, or it was an instrumental limit.

There are two more noteworthy details. As reported in [95], too long centrifugation time removes longer individual nanotubes preferentially over the short ones. It also seems, that centrifugation followed by filtration with a fine membrane can further improve the fluorescent quality of SWCNT dispersion [95].

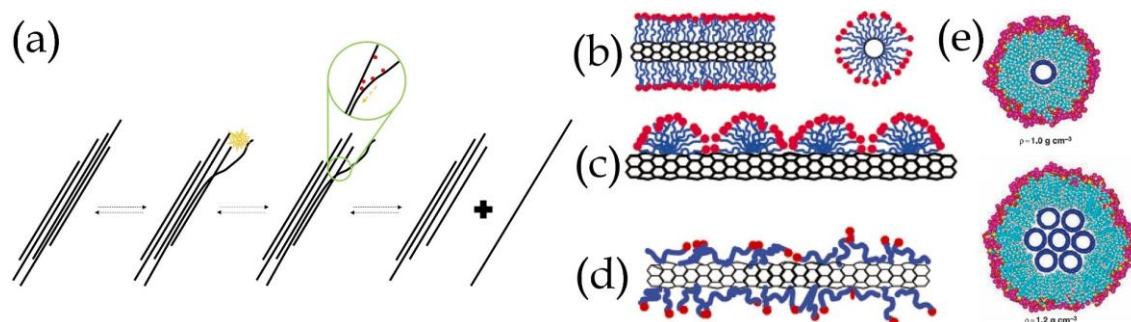


FIGURE 2.13: (a) Proposed unzipping mechanism [90] during sonication process. (b) - (d). Possible mechanisms of surfactants wrapping a nanotube. (e) Comparison of a density of the surfactant wrapped individual nanotube and the nanotube bundle. Figures (b) - (d) reprinted with permission from [103]. Copyright 2004 American Chemical Society. Figure (e) from [42]. Reprinted with permission from AAAS.

3 Carbon nanotubes - The dispersion

The goal of the experimental part was to develop a protocol, which will fit the needs of single SWCNT spectroscopy in the femtoliter-sized droplets. In other words, a step-by-step guide for preparation of concentrated SWCNT dispersion with nanotubes of unaltered properties and minimum contaminants was needed. In order to achieve a dispersion of required properties, all reagents and parameters of the process had to be carefully considered.

An aqueous system was more or less a necessity due to the aim for water-in-oil droplet-based system and SDBS was the surfactant of choice for its superior qualities in dispersing the SWCNTs in water and preventing them from re-bundling. In addition, there was already some history of using this system at the Nanoscience Center [17,18,106]. The characterization of the samples was performed using Raman and UV-VIS-NIR absorption spectroscopy in the beginning of the project. After the NIR fluorescence setup was build, it became the main instrument for characterization of the nanotube dispersions and the UV-VIS-NIR absorption and Raman spectroscopy were used only as complementary methods. The NIR fluorescence was chosen as the main technique for its inherent sensitivity, lower sensitivity to exact excitation wavelength, capability to detect individual nanotubes (or very small semiconducting bundles) and sensitivity for presence of bundles via quenching.

3.1 Reagents

Only three reagents are needed in preparation of aqueous dispersions of SWCNTs: water, surfactants, and nanotubes. The water used in this work was Type II purified water from Millipore Elix UV 3 system with resistivity $>10 \text{ M}\Omega\cdot\text{cm}$ and $\text{TOC}^8 <30 \text{ ppb}$ without any further treatment. The SDBS was purchased from Sigma-Aldrich and used as received. The chosen nanotubes were Purified HiPco™ SWCNTs purchased from NanoIntegris Technologies. According to the product datasheet [107], the diameter of individual HiPco™ nanotubes lies in the interval 0.8 – 1.2 nm with the mean diameter 1.0 nm and their length is between 100 – 1000 nm. The properties of SWCNTs in this range are plotted in FIGURE 3.1 and TABLE 3.1 and TABLE 3.2.

⁸ total organic carbon

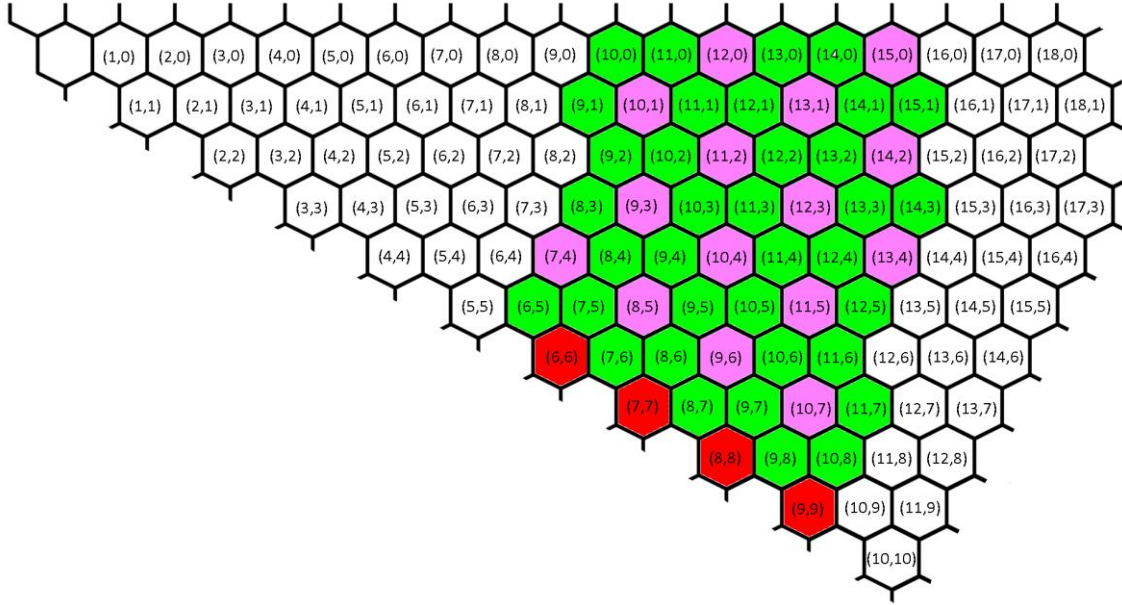


FIGURE 3.1: Chiral vector indices of SWCNTs with diameters from 0.75 nm to 1.25 nm, covering HiPco™ nanotubes. The red hexagons highlight the positions of metallic nanotubes, green hexagons highlight the positions of semiconducting nanotubes, and pink hexagons highlight the positions of quasi-metallic nanotubes. The quasi-metallic nanotubes behave like metallic at room temperature.

TABLE 3.1: Calculated electronic and optical properties of metallic HiPco™ nanotubes. QM states quasi-metallic and M metallic CNT. Diameter from eq. (2.2), RBM from eq. (2.6), E_{11}^M from [108].

(n,m)	Type	d (nm)	RBM (cm^{-1})	E_{11}^M (eV)	E_{11}^M (nm)
(7,4)	QM	0.766	303.0	2.98	416.3
(6,6)	M	0.825	281.6	2.90	427.8
(10,1)	QM	0.836	277.9	2.69	461.2
(9,3)	QM	0.859	270.8	2.66	466.4
(8,5)	QM	0.902	258.2	2.60	477.2
(12,0)	QM	0.953	244.8	2.40	517.0
(7,7)	M	0.963	242.3	2.51	494.3
(11,2)	QM	0.963	242.3	2.38	521.3
(10,4)	QM	0.992	235.4	2.35	528.0
(9,6)	QM	1.038	225.1	2.29	541.8
(13,1)	QM	1.074	217.8	2.15	577.1
(12,3)	QM	1.091	214.4	2.13	582.5
(8,8)	M	1.100	212.8	2.21	561.4
(11,5)	QM	1.126	208.1	2.10	590.8
(10,7)	QM	1.175	199.7	2.04	608.2
(15,0)	QM	1.191	197.1	1.96	633.0
(14,2)	QM	1.199	195.8	1.95	636.3
(13,4)	QM	1.222	192.2	1.93	642.8
(9,9)	M	1.238	189.9	1.98	626.6

TABLE 3.2: Calculated electronic and optical properties of semiconducting HiPco™ nanotubes. Diameter from eq. (2.2), RBM from eq. (2.6), E_{11}^S and E_{22}^S from eq. (2.7) – (2.10).

(n,m)	d (nm)	RBM (cm^{-1})	E_{11}^S (eV)	E_{11}^S (nm)	E_{22}^S (eV)	E_{22}^S (nm)
(6,5)	0.757	306.2	1.27	976.2	2.19	566.1
(9,1)	0.757	306.2	1.36	912.1	1.79	691.3
(8,3)	0.782	296.8	1.30	951.6	1.86	665.4
(10,0)	0.794	292.4	1.07	1155.7	2.31	537.5
(9,2)	0.806	288.2	1.09	1137.6	2.25	550.8
(7,5)	0.829	280.4	1.21	1023.7	1.92	645.3
(8,4)	0.840	276.7	1.12	1111.4	2.11	588.9
(11,0)	0.873	266.4	1.20	1036.9	1.67	744.6
(10,2)	0.884	263.3	1.18	1053.4	1.68	736.7
(7,6)	0.895	260.2	1.11	1119.8	1.92	647.6
(9,4)	0.916	254.4	1.13	1100.6	1.72	722.4
(11,1)	0.916	254.4	0.98	1264.8	2.03	610.2
(10,3)	0.936	249.0	0.99	1249.1	1.96	631.5
(8,6)	0.966	241.5	1.06	1173.0	1.73	718.0
(9,5)	0.976	239.2	1.00	1241.5	1.85	671.9
(12,1)	0.995	234.7	1.06	1169.7	1.55	798.9
(11,3)	1.014	230.4	1.04	1197.1	1.57	792.6
(8,7)	1.032	226.4	0.98	1264.5	1.70	728.5
(13,0)	1.032	226.4	0.90	1383.6	1.83	677.0
(12,2)	1.041	224.5	0.90	1378.4	1.81	686.1
(10,5)	1.050	222.6	0.99	1249.1	1.58	787.7
(11,4)	1.068	219.0	0.91	1370.8	1.74	712.5
(9,7)	1.103	212.3	0.94	1321.5	1.56	793.0
(10,6)	1.111	210.7	0.90	1377.1	1.65	754.0
(14,0)	1.111	210.7	0.96	1295.1	1.44	859.1
(13,2)	1.120	209.2	0.95	1307.1	1.45	857.5
(12,4)	1.145	204.7	0.92	1341.9	1.45	855.2
(14,1)	1.153	203.3	0.83	1501.6	1.66	748.3
(9,8)	1.170	200.6	0.88	1409.9	1.53	808.9
(13,3)	1.170	200.6	0.83	1497.9	1.62	763.7
(11,6)	1.186	197.9	0.89	1397.2	1.45	857.6
(12,5)	1.201	195.4	0.83	1499.2	1.56	793.3
(15,1)	1.232	190.6	0.87	1426.3	1.35	920.5
(10,8)	1.240	189.5	0.84	1469.6	1.43	869.4
(11,7)	1.248	188.4	0.82	1515.9	1.48	835.5
(14,3)	1.248	188.4	0.86	1447.1	1.35	920.2

The semiconducting nanotubes naturally attract more interest than the metallic ones due to their anticipated impact on semiconducting industry. In addition, only the semiconducting SWCNTs can be characterized with fluorescence microscopy. It would seem advantageous to use SWCNTs enriched in semiconducting tubes. Despite these facts, the presence of metallic nanotubes is actually very beneficial, at least it was in the early stages of this work. During the development of the protocol for preparation of SWCNT dispersion, the rate of rebundling after the individualization is an important parameter determining the stability of prepared dispersion. One third of metallic or quasi-metallic nanotubes in HiPco™ gives significant possibility of bundling previously individual and fluorescently

active SWCNT with nanotube with metallic behavior. In such a bundle, the de-excitation would proceed in non-radiative way. The drop in fluorescent activity of a well individualized sample therefore confirms ongoing rebundling and decreasing quality of the dispersion.

3.2 Instrumentation

3.2.1 Preparation of CNT dispersion

The finger-type sonicator (dr. Hielscher UP200S ultrasonic processor with 3 mm titanium tip) was used for SWCNT individualization. The tip was re-polished in regular intervals to prevent decrease of its performance due to cavitation. To prevent surfactant degradation during the sonication, the glass vial with sample was always submerged in icy cold water ~ 0 °C. The characteristics of the sonicator are summarized in TABLE 3.3. For some special treatments in the processing of SWCNT dispersion also bath-type sonicator was used. The finger-type sonicator was used for all experiments and it will be further addressed simply as a sonicator. If the bath-type sonicator was used, it will be highlighted in the text.

TABLE 3.3: Characteristics of the dr. Hielscher UP200S sonicator with S3 sonotrode [109].

Working frequency (kHz)	Sonicator power (W)	Sonotrode diameter (mm)	Amplitude (μm)	Amplitude control (%)	Acoustic power density ($\text{W}\cdot\text{cm}^{-2}$)	Delivered power (W)
24	200	3	210	20 - 100	92 - 460	6.5 - 32.5

The Beckman-Coulter Optima L-90K Ultracentrifuge was used to remove the bundles and other impurities from the sample. The Thinwall polyallomer tubes were placed in Type 70.1 Ti Rotor [110]. The centrifugations were performed at room temperature (~ 20 °C) with maximum acceleration (~ 300 RPM $\cdot\text{s}^{-1}$) and slow braking at the beginning and end of the process, respectively.

3.2.2 Characterization

A home-build Raman table-top setup with back-scattering geometry was used for Raman spectroscopy. The setup is equipped with a 532 nm Alphalas MLL-532 laser. The 532 nm edge filter reflects the laser beam to the Olympus Plan N 10x/0.25 NA microscope objective and the cuvette is placed in the focal point of the objective. The laser power in the sample space is ~ 18 mW. The inelastically scattered photons were collected by a microscope objective and passed through the edge filter to a spectrometer. The spectrometer was Acton SP2500i with 600 $\text{l}\cdot\text{mm}^{-1}$ or 1200 $\text{l}\cdot\text{mm}^{-1}$ grating and Andor Newton 940N CCD camera. The absorption measurements in NIR region were performed with FTIR Nicolet Magna-IR 760 ESP Spectrometer and in UV-VIS region with Perkin Elmer Lambda 850 spectrometer.

A home-build NIR fluorescence microscope was used for the fluorescence measurements. The setup was constantly developed from the beginning of the

project according to the needs of the microfluidic part of the project. Most of the optical elements were upgraded and the whole optical layout was changed several times. Therefore, recorded intensities cannot be compared between different sample batches. The most recent setup is based on an inverted Nikon Eclipse TE2000-U microscope, which serves as a base for further optical components. The excitation branch starts with a 632.8 nm continuous Thorlabs HRP120 laser and the laser power in the sample space is 5.42 mW. The setup is equipped with Acton SP2150i spectrometer with $150 \text{ l}\cdot\text{mm}^{-1}$ grating. The Andor iDus 1.7 μm camera with InGaAs linear detector is designed to be used in the spectral region from 600 to 1700 nm, ideal for observing fluorescence from E_{11}^S transition of SWCNTs with small diameters. The detector was always cooled down to $-50 \text{ }^\circ\text{C}$. The optical branch with OV2710 sensor (OmniVision, 30 fps at 1080p, 120 fps at 480p) together with a light source is designed to allow direct observation and computer image processing even with the tightly focused laser beam in the focal plane. This allows real-time observation of processes in the microfluidic chip while measuring the content of the droplets. The optical layout of the microscope is plotted in FIGURE 3.2.

3.2.3 Remark on spectra acquisition

For all absorption techniques, a reference spectrum was subtracted from the spectrum of dispersed SWCNTs. The reference spectrum was measured from aqueous SDBS solution with the same concentration of SDBS as in the SWCNT sample. Neither water nor SDBS are significantly Raman active in RBM or G band regions,

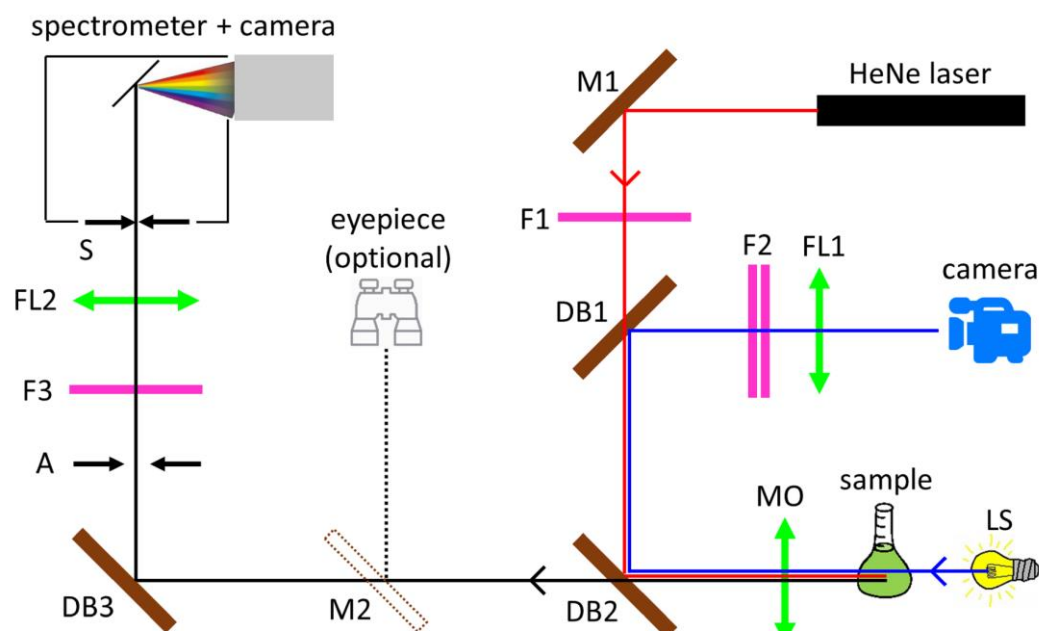


FIGURE 3.2: Optical layout of the NIR fluorescence setup. M1 & M2 – broadband mirrors, F1 – Thorlabs FGS900 filter, F2 – C3C20 & C3C9 laserline filters, F3 – HKC7 laserline filter, DB1 – longpass dichroic beamsplitter Semrock FF605, DB2 – longpass dichroic beamsplitter Semrock FF685, DB3 – shortpass dichroic beamsplitter Thorlabs DMSP805, FL1 – focusing lens $f = 100 \text{ mm}$, FL2 – focusing lens $f = 25 \text{ mm}$, MO – microscope objective Nikon LU Plan 50x/0.55 NA, LS – blue LED light source, a – aperture, S – slit.

therefore, Raman spectra were acquired without background subtraction. Since neither water nor SDBS show any emission in the interval of E_{11}^S transitions of HiPco™ nanotubes, only dark current background spectrum was subtracted from the fluorescence measurement. Typical spectra of HiPco™ aqueous dispersion obtained by various techniques are plotted in FIGURE 3.3 – FIGURE 3.7.

Deconvolution of the obtained spectra is an important step towards determination of presence of SWCNTs with particular chirality. The fluorescence peaks have Voigt profile [59], which is a convolution of Gaussian and Lorentzian profile originating from inhomogeneous and homogeneous broadening mechanisms, respectively. Due to the high computational requirements for deconvolution of a spectrum to Voigt functions, the simpler deconvolution to Gaussian functions was used in FIGURE 3.3 and FIGURE 3.7.

FIGURE 3.7 represents the fluorescence spectrum obtained upon excitation with a HeNe laser. The fluorescence of nanotubes, for which electronic transitions are in resonance with the excitation laser wavelength are strongly enhanced. The complete spectrum of all semiconducting nanotubes in the sample can be obtained either by scanning the excitation wavelength across the E_{22}^S interval (see FIGURE 2.9(b)) or by white light excitation, which would cover all the possible excitation transitions. It would be indisputably beneficial to see all the semiconducting nanotubes in the sample for the sake of the sorting, however, there are several technical drawbacks compared to single laser excitation. Scanning through the excitation wavelengths is very time-consuming and not suitable for microfluidic detection. On the other hand, the conventional white light sources are generally non-coherent and thus they cannot be focused tightly enough to illuminate individual femtoliter droplets and excite solely their content. In addition, they usually exhibit relatively strong activity in NIR region (halogen, LED⁹), which interferes with the fluorescence signal. The broad-band coherent light sources overcome these limitations, but their power density is low compared to conventional lasers. This limitation is even exacerbated by the power distribution of broad-band light sources over the wavelength spectrum. Therefore, the power density per particular wavelength is hardly sufficient for efficient and fast excitation of the SWCNT sample. In addition, the spectrum excited by white light is rather congested and way more complicated for both visual and automated evaluation.

Therefore, all the fluorescence spectra in this work were measured using HeNe laser excitation. Since the resonant nanotubes are from relatively wide interval of diameters, the fluorescence spectra measured upon HeNe excitation can be considered representative for the whole sample and it does not restrict the development of the protocol for preparation of carbon nanotube dispersion or first trials in microfluidic sorting. In addition, one or two extra lasers in the setup, together with the knowledge of the nanotube sample chirality distribution is sufficient for fast and full characterization even of trace amounts of SWCNTs in aqueous dispersions [59].

⁹ light emitting diode

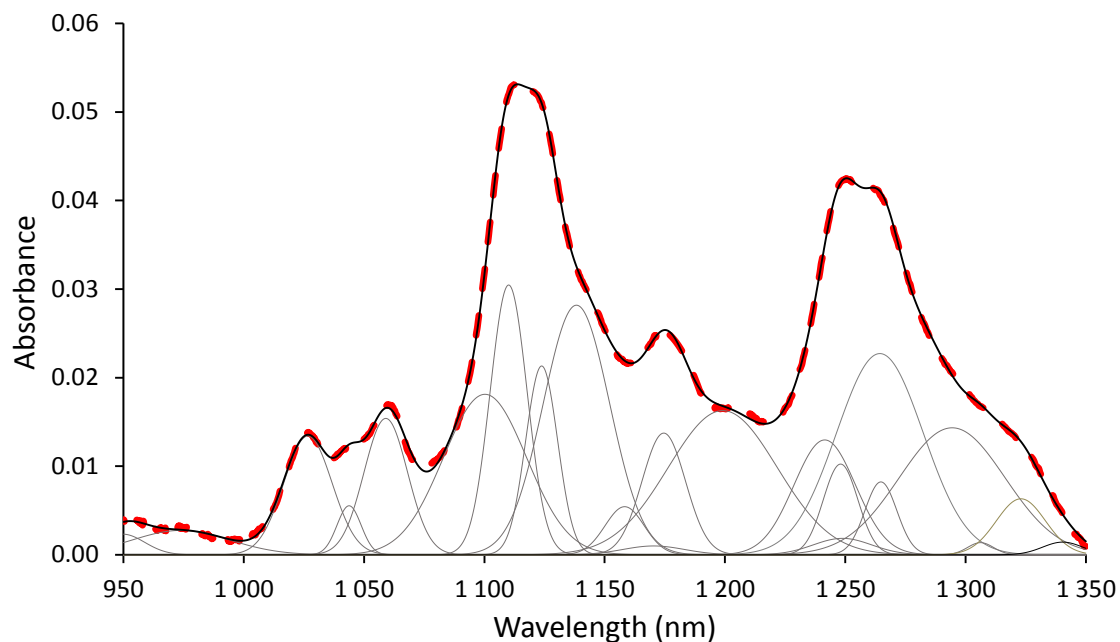


FIGURE 3.3: Absorption of aqueous HiPco™ dispersion in NIR region (sample A). The red dashed line is from experiment (non-resonant background was subtracted) and black line is the sum of deconvoluted contributions from individual nanotubes via absorption across E_{11}^S transition. The position of the transitions is slightly red-shifted (~ 0.005 eV) from expected absorption energy [4], which may point at presence of surfactant [92] or, together with broadening of some features, suggests presence of small bundles [96].

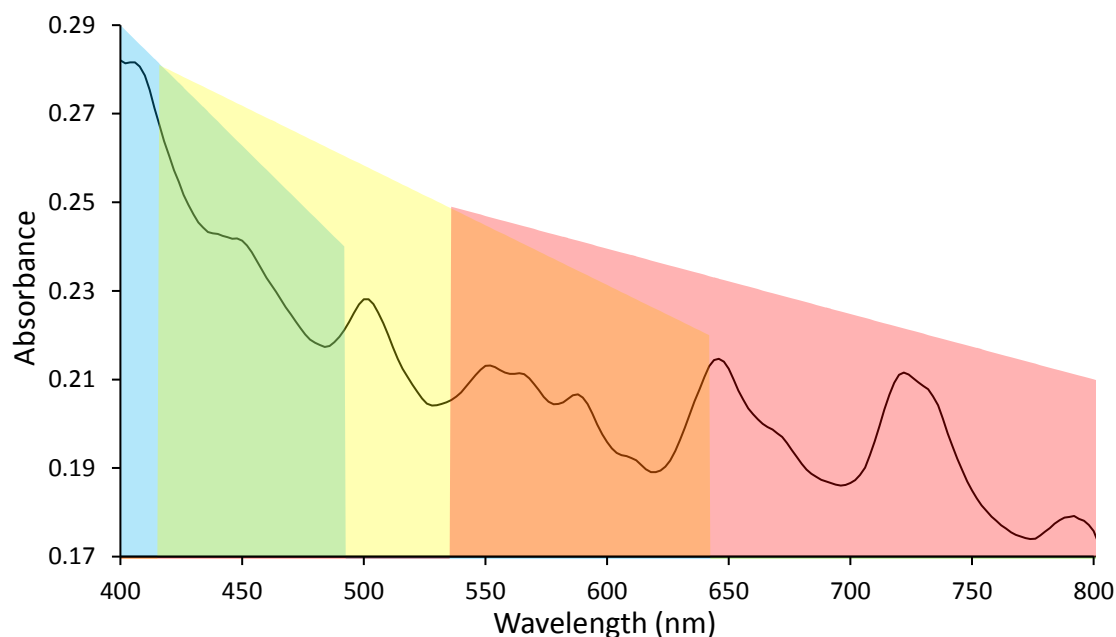


FIGURE 3.4: Absorption of aqueous HiPco™ dispersion in visible region. The blue-green area highlights the interval of E_{33}^S transitions, green-yellow-orange area highlights the interval of E_{11}^M transitions, and orange-red area highlights the interval of E_{22}^S transitions. Altogether 71 transitions belonging to HiPco™ SWCNTs are located in this area.

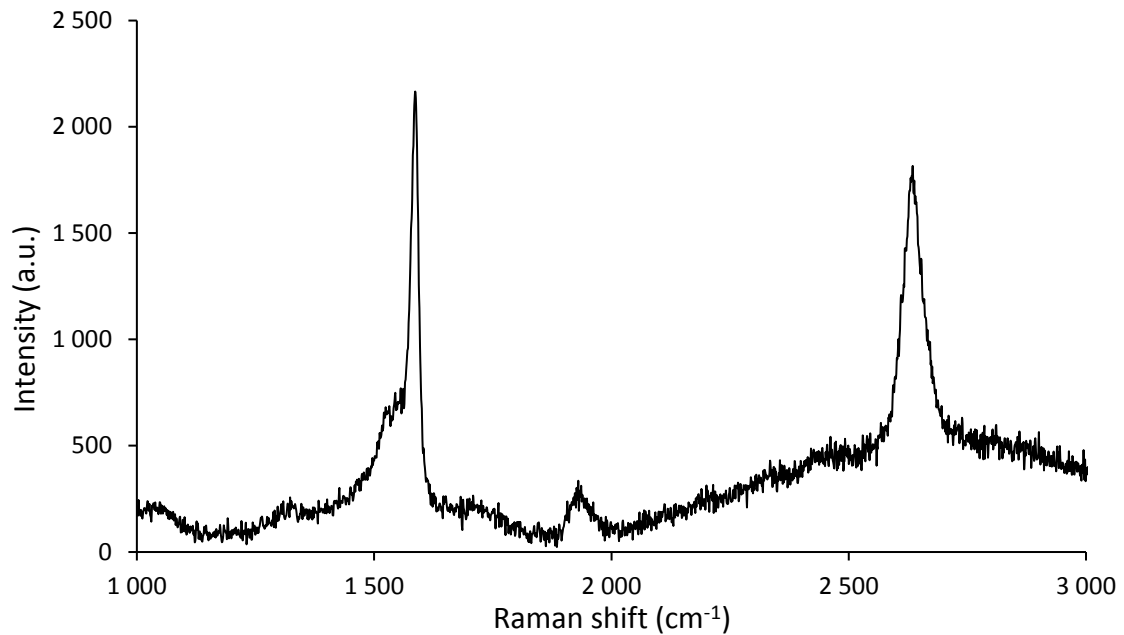


FIGURE 3.5: Raman spectrum of aqueous HiPco™ dispersion (sample B). A straight baseline was subtracted from the spectra. Very weak D band ($\sim 1300 \text{ cm}^{-1}$) confirms good structural quality of the sample. G band ($\sim 1590 \text{ cm}^{-1}$), iTOLA band ($\sim 1930 \text{ cm}^{-1}$), and G' band ($\sim 2630 \text{ cm}^{-1}$) are clearly visible.

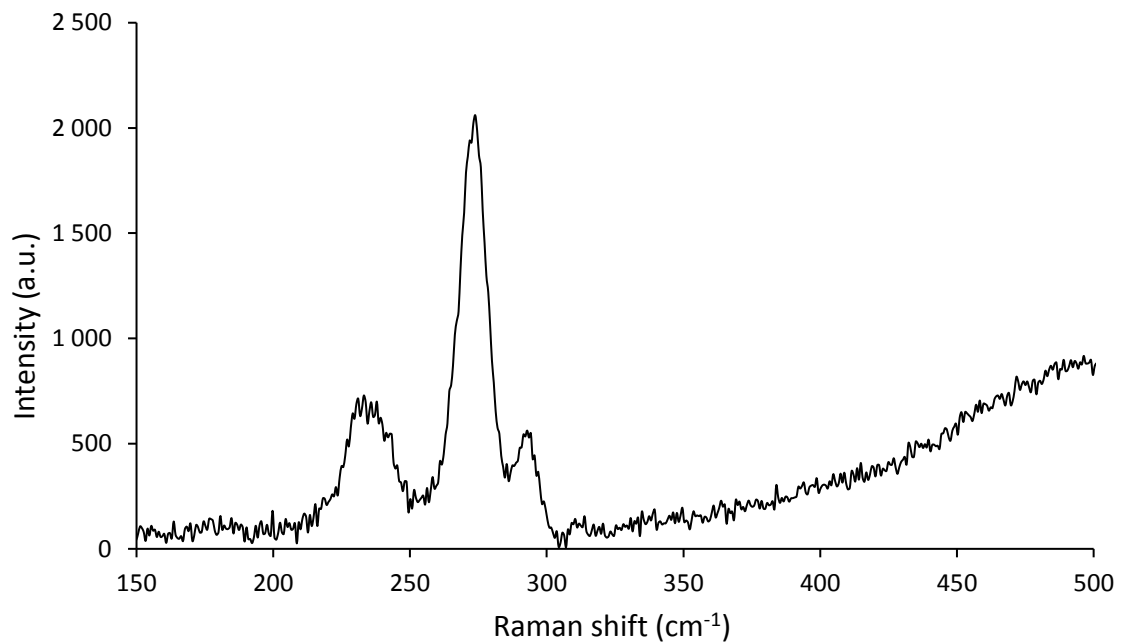


FIGURE 3.6: Raman spectrum of aqueous HiPco™ dispersion (sample B). A straight baseline was subtracted from the spectra. The (9,6) quasi-metallic ($\sim 225.1 \text{ cm}^{-1}$), (10,4) metallic ($\sim 235.4 \text{ cm}^{-1}$), (8,4) semiconducting ($\sim 276.7 \text{ cm}^{-1}$), and (10,0) semiconducting ($\sim 292.4 \text{ cm}^{-1}$) SWCNTs can be recognized by combining the RBM position and resonant energies of electronic transitions.

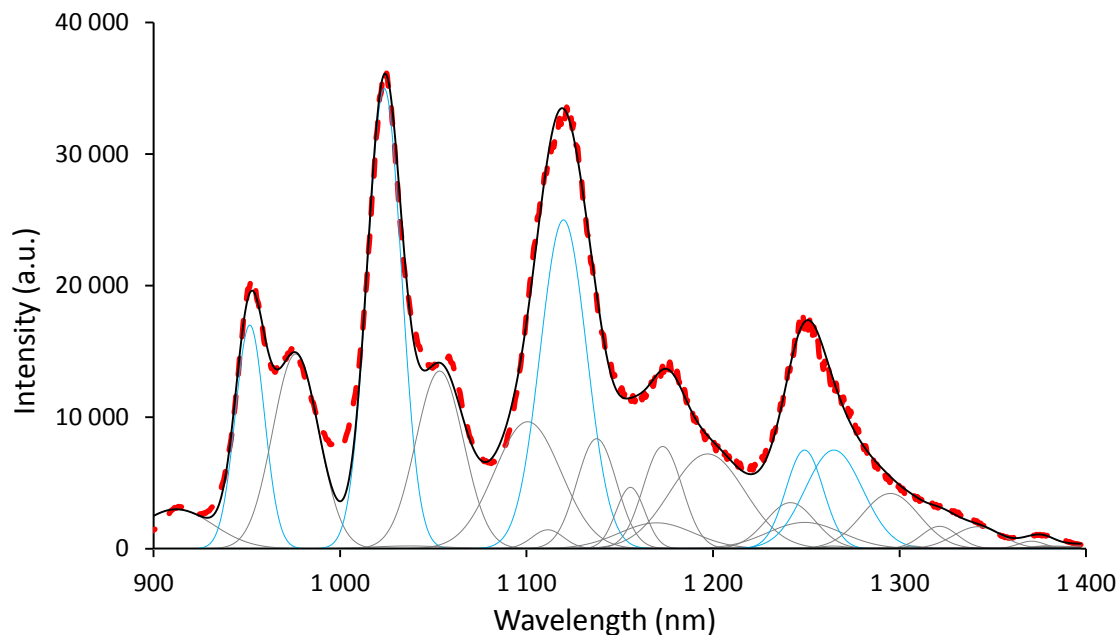


FIGURE 3.7: Fluorescence spectrum of aqueous HiPco™ dispersion excited by HeNe laser (sample C). Red dashed line is the experimental measurement, the thin black line is a sum of deconvoluted contributions. The deconvolution reveals strong fluorescence of (8,3), (7,5), (7,6), (10,3), and (11,1) semiconducting nanotubes (highlighted blue) with E_{22}^S transition resonant with excitation wavelength. Compared to Raman spectroscopy, fluorescence of SWCNTs with non-resonant electronic transitions is also possible via sideband and off-resonant excitation pathways and higher number of present chiralities can be reliably identified.

3.2.4 Processing the spectra

The fluorescence spectra of aqueous HiPco™ dispersion obtained upon HeNe laser excitation always have the same shape. This is due to the fluorescence activity of individualized nanotubes and virtually no background. Naturally, some simple parameter describing the fluorescence activity was needed for easier and more clear quality evaluation of the prepared dispersion, while varying parameters of the preparation protocol. The integrated surface area of the fluorescence spectrum was found to be a reliable parameter, depending linearly on the height of the main peaks in the spectrum for particular development stage of the optical setup (for a certain set of experiments). The dependency for the last modification of the optical setup (FIGURE 3.2) is plotted in FIGURE 3.8(left). It also means that the single parameter describing the surface area underneath the curve can be easily used to reconstruct the fluorescence spectrum. Only exception to this rule comes with too extensive sonication, where debundling selectivity towards certain chiralities starts to play a role and the ratios slightly change.

3.3 Parameters of the process

A set of experiments for investigating the influence of procedural parameters on quality of SWCNT aqueous dispersions is described in this section. All the

parameters describing the amount of SDBS surfactant or HiPco™ nanotubes are given in weight by weight (w/w) proportions.

3.3.1 Amount of surfactant

Several aqueous dispersions of SWCNTs were prepared to investigate the influence of SDBS concentration on the quality of the final dispersion, while other parameters were not altered. 0.1 - 0.5 % with 0.1 % increment of SDBS was added in the water together with 0.04 % of HiPco™ nanotubes. The samples were sonicated with delivered power of 6.5 W for 3 or 60 minutes leading to proportional delivered energy of 234 J·mL⁻¹ or 4,680 J·mL⁻¹, respectively. Consequent sonication took 70 minutes at 3 000g, 20 000g, and 126 000g. All prepared samples showed the same quantitative relationship within the increasing surfactant concentration sets, independently on other preparation parameters. An illustrative example is plotted in FIGURE 3.9.

Too low surfactant concentration is not able to sufficiently stabilize the dispersed SWCNTs, even at relatively high proportional delivered power. The ability to disperse nanotubes increases with increasing SDBS concentration, however, for the price of extensive growth of the non-resonant background, most likely originating from bigger dispersed bundles and non-nanotube carbon. Since the background can be effectively reduced with the proper settings of centrifugation process, with respect to the literature and further experiments, the concentration of SDBS was set to be 1 % and used so for further development of HiPco™ dispersion protocol.

3.3.2 Amount of nanotubes

With the set concentration of surfactant and at steady parameters of the dispersion process, the concentration of nanotubes possible to disperse in certain amount of water was investigated. 1 % of SDBS was added in the water together with 0.05, 0.10, and 0.15 % of HiPco™ nanotubes. The samples were sonicated with delivered power of 6.5 W for 12 hours leading to proportional delivered energy of 28.1 kJ·mL⁻¹. Consequent centrifugation took 60 minutes at 12 000g. The integrated fluorescence intensity is plotted in FIGURE 3.8(right). The fluorescence intensity does not grow proportionally with increasing concentration of nanotubes, which was also observed in other samples (e.g. sample D). The amount of well-dispersed nanotubes saturates at the concentration above 0.1 % but even that concentration does not fully utilize the HiPco™ product. According to this finding, the search for processing parameters were done with 0.05 % SWCNT powder. In absolute numbers, 10 mL of water was mixed with 100 mg of SDBS and 5 mg of HiPco™ powder for further processing.

3.3.3 Sonication

Delivered sonication power

The effect of delivered sonication power on the quality of resulting SWCNT dispersion was investigated. High power is expected to significantly speed up the

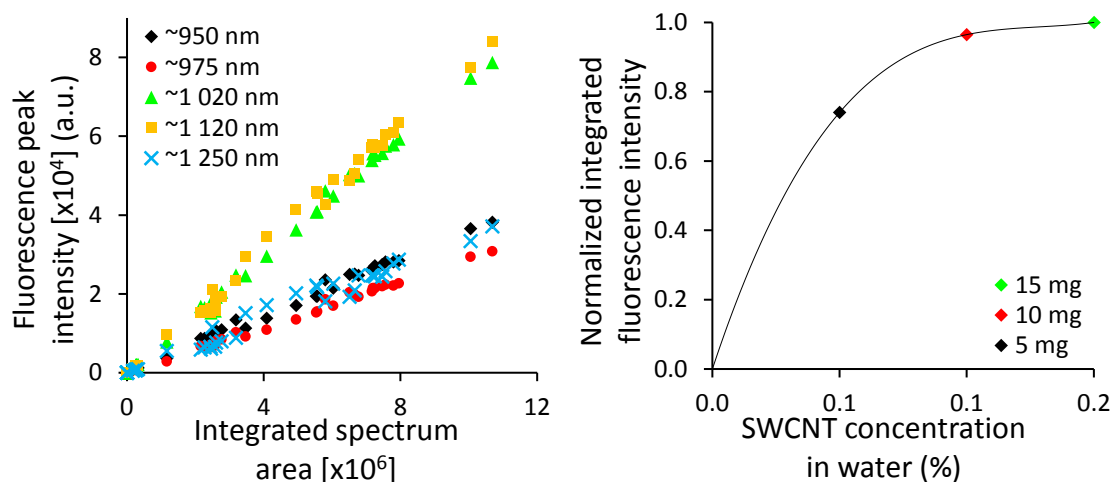


FIGURE 3.8: (left) A ratio of the intensity of the main peaks present in fluorescent spectrum and integrated area under the curve of many independently prepared samples. (right) The effect of increasing nanotube concentration on the integrated fluorescence intensity (sample E1 – E3). The black line is a least squares fit of a logarithmic function.

unzipping process, however, for the price of shortening of the nanotubes and possible generation of structural defects. The effect of delivered sonication power was investigated throughout the range of settings of the used sonicator. The samples were sonicated with delivered power of 13 W, 19.5 W, and 26 W keeping the proportional delivered energy at constant $2,6 \text{ kJ mL}^{-1}$ by varying the sonication time. The samples were subsequently centrifuged for 1 hour at 14 000g and 4 hours at 122 000g. The resonant part of the NIR absorption and integrated fluorescence intensity are plotted in FIGURE 3.10.

The data in FIGURE 3.10(right) show that sonication with lower power for longer time gives stronger fluorescence than sonication with higher power for shorter time. The lower sonication power presumably supports debundling process more efficiently, while sonication with higher powers may lead to structural damage of the nanotubes. Interestingly, the sonication at lower power also causes

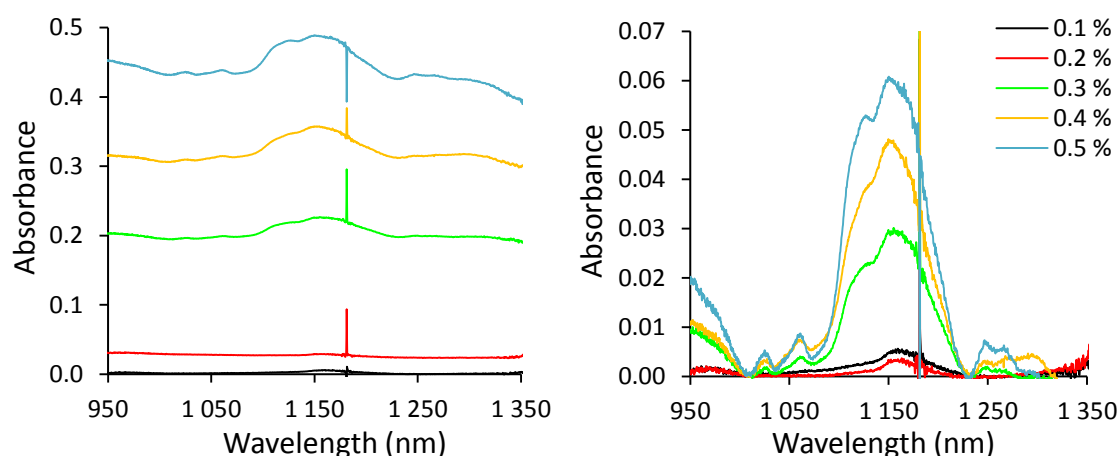


FIGURE 3.9: (left) NIR absorbance of samples with increasing surfactant concentration (sample F1 – F5) sonicated with proportional delivered energy 4.68 kJ mL^{-1} and centrifuged for 70 minutes at 3 000g. (right) NIR absorbance of the same samples with subtracted non-resonant background. The peak at 1 182 nm is an instrumental error.

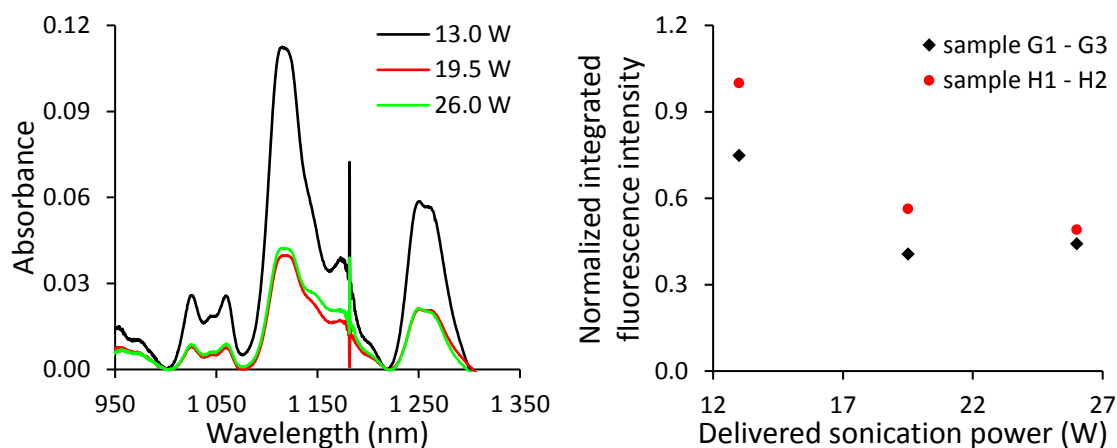


FIGURE 3.10: (left) NIR absorbance of samples (sample G1 - G3) sonicated with different sonication power with subtracted non-resonant background. The peak at 1182 nm is an instrumental error. (right) The effect of increasing delivered sonication power to the integrated fluorescence intensity of two independently processed set of samples (sample G1 - G3) and (sample H1 - H2).

significant increase of the non-resonant background in NIR absorption. This is probably due to the good dispersing capability of these settings, when also small bundles are well dispersed in the water. Further experiments showed even better dispersing capability of sonication performed at lowest possible power allowed by the sonicator. This result is in agreement with the findings of the sonicator manufacturer, reporting optimal amplitude for dispersing to be in the range 10 - 30 μm , while for particle size reduction the optimum is in the range 40 - 120 μm [111]. For the sonicator and sonotrode used in this experiment, these amplitudes correspond to delivered power of 1.5 - 4.6 W and 6.2 - 18.6 W, respectively. That explains lower non-resonant background for samples sonicated at high powers, where significant structural defects and shortening were introduced to the nanotubes during the debundling process and those were removed in the centrifugation process. In conclusion, the lowest possible delivered sonication power (~ 6.5 W) was found to be the most effective for the debundling process, while preserving the quality of the nanotubes. Therefore, the following experiments were performed at sonication power of 6.5 W.

Proportional delivered energy

The time of sonication of known amount of liquid at known power is possible to state in the form of proportional delivered energy. Prolonged time of sonication allows more SWCNTs to get debundled, however, it increases the risk of unwanted structural damage and above certain value becomes nonconstructive. The effect of increasing proportional delivered energy on NIR fluorescence intensity was investigated. The sample was sonicated for 24 hours with a measurement of fluorescence intensity every hour for the first 12 hours and then at the end of the sonication cycle FIGURE 3.11(left). The data plotted in FIGURE 3.11(left) were measured *without* usual centrifugation and therefore may not fully reflect the effect of delivered energy on fluorescence intensity of samples cleaned by centrifugation. Therefore, another set of samples was prepared, where the

centrifugation sequence of 1 hour at 12 000g and 4 hours at 113 000g was performed. The fluorescence spectra from these samples are plotted in FIGURE 3.11(right).

The data in FIGURE 3.11(left) shows that the amount of nanotubes and therefore the fluorescence intensity saturates with proportional delivered energy of about 25 kJ mL^{-1} . However, the centrifuged samples show linear growth of fluorescence intensity at least up to 28 kJ mL^{-1} and probably even further. This is probably caused by the competitive increase of non-nanotube particles in the dispersion and some kind of equilibrium is reached between the increasing number of well dispersed SWCNTs and possible quenchers [112]. Those are selectively removed during the centrifugation and the growth of fluorescence intensity may continue. Nevertheless, the proportional delivered energy 28 kJ mL^{-1} was found sufficient for preparation of SWCNT aqueous dispersion and was used for the experiments described in BOOK III.

Remarks on sonication process

Two important effects related to the sonication process should be mentioned here. The experiment with increasing proportional delivered energy reveals certain selectivity of sonication based on nanotube diameter. FIGURE 3.12(left) shows the ratio of the leftmost and rightmost peaks in the NIR fluorescence spectra located at about 950 nm and 1250 nm, respectively. The rise of the peak at 1250 nm is very fast compared to the peak placed at 950 nm at the beginning of the sonication. However, at delivered energy of about 15 kJ mL^{-1} the rate of the 1250 nm peak growth is outperformed by the growth rate of the 950 nm peak. At energy of about 23 kJ mL^{-1} , the growth of the 1250 nm peak reaches its maximum and from this moment, its intensity starts to decrease, while the intensity of the 950 nm peak keeps steadily growing with the increasing energy up to the end of the experiment. This is due the fact that van der Waals forces acting on the surface of

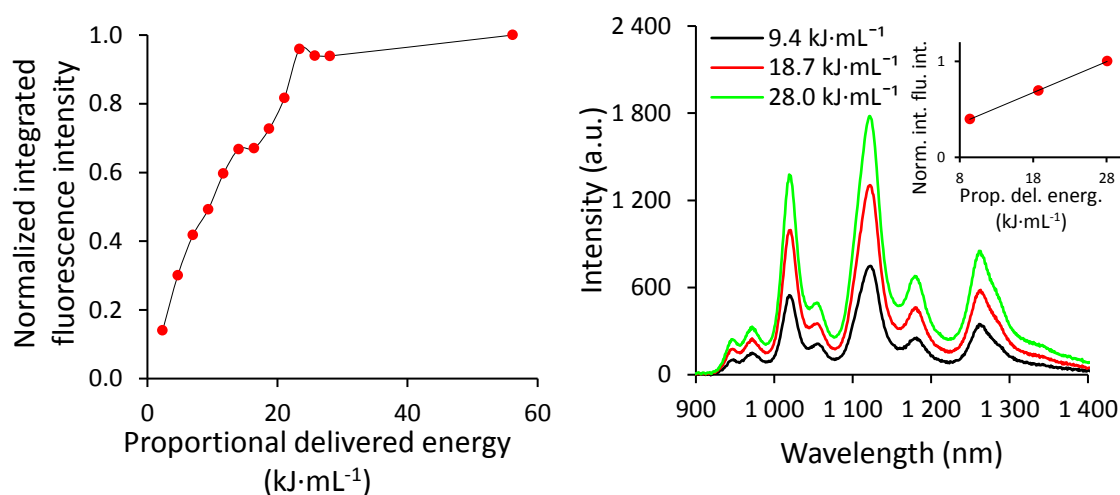


FIGURE 3.11: (left) The effect of proportional delivered energy to the integrated fluorescence intensity of sonicated samples (sample I). The solid line is an aid to guide the eye. (right) Fluorescence intensity of samples (sample J1 – J3) sonicated at various proportional delivered energies and consequently centrifuged. (inset) The effect of proportional delivered energy (x-axis) to the integrated fluorescence intensity (y-axis) of sonicated and centrifuged samples. The black solid line is least squares linear fit.

the nanotubes are not constant [89] but vary with the nanotube diameter [67,104]. Generally, the smaller diameter means larger interaction energy. The peaks at 950 and 1250 nm can be identified with (8,3) and (10,3) nanotubes, respectively. A plausible explanation is that at certain energy all (10,3) nanotubes (and other bigger diameter nanotubes) are debundled and the fluorescence intensity starts to drop due the induced structural defects, while (8,3) nanotubes (and other smaller diameter nanotubes) keeps debundling and increase their part of the fluorescence spectrum.

After the sonication, the transition to the next processing step, centrifugation, should be immediate as relatively fast decay of the fluorescence activity takes place right after the sonication as depicted in FIGURE 3.12(right). Here, the sample was sonicated for 5 hours leading to proportional delivered energy of 11.7 kJ mL^{-1} with fluorescence spectrum taken every hour. The sonication was then interrupted for 13 hours and the spectrum taken afterwards shows steep natural decay of the fluorescence intensity. The sample was sonicated again for seven more hours leading to delivered energy 28.1 kJ mL^{-1} with fluorescence spectrum taken every hour. The fluorescence intensity rapidly reached its previous values and the growth continued as expected. Another 12 hours of waiting showed similar decay as in the previous case. Last 4 hours of sonication brought the fluorescence intensity to its maximum, similarly to the case from FIGURE 3.11(left), with the overall proportional delivered energy of 37.4 kJ mL^{-1} . The integrated fluorescence intensity started to decay immediately but obvious growth of intensity was measured in long term observation. This suggests some kind of time-dependent dynamics in the SWCNT dispersion. This observation is in agreement with decay of fluorescence intensity of only sonicated samples reported in [99]. Interestingly, a detailed look on the fluorescence spectra shows that fluorescence from nanotubes emitting at longer wavelengths decays faster than fluorescence from nanotubes emitting at shorter wavelengths. This is contradictory to the assumption of smaller nanotubes having higher van der Waals energy and thus rebundling faster. Obviously, also some other process besides

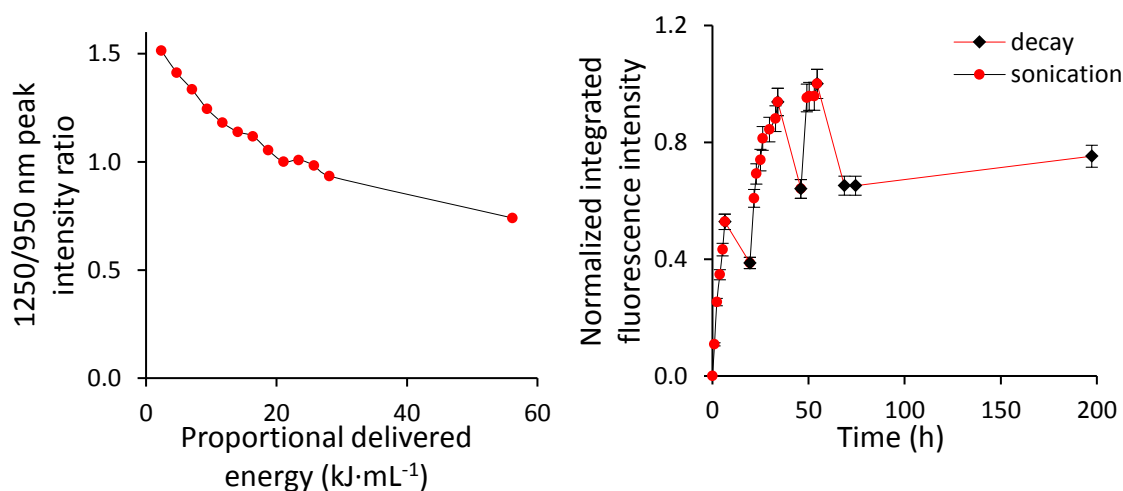


FIGURE 3.12: (left) A ratio of the fluorescence peak intensities of (10,3) and (8,3) nanotubes during sonication process (sample I). (right) Natural decay of fluorescent intensity of sonicated SWCNT dispersion (sample K). The solid lines are an aid to guide the eye.

rebundling must play a role in the decay of the fluorescence intensity. We speculate that some diameter related selectivity in the attachment of the surfactant on the nanotube surface may play a role here. Last but not least, there is a striking variability in fluorescence intensity (over 3-times) of samples sonicated with the very same parameters. This points towards inhomogeneity in the HiPco™ material and the fluorescence activity of the dispersion must always be evaluated even with well-established preparation protocol.

3.3.4 Centrifugation

Centrifugal field

The SWCNT bundles, metal catalyst particles and non-nanotube carbon particles have higher density than the well individualized nanotubes and therefore sediment in the aqueous dispersion. This sedimentation is significantly accelerated by applying a centrifugal field on the sample. It is crucial not to disturb the precipitate while pipetting the supernatant after the centrifugation, as the supernatant contains well individualized SWCNTs needed for further experiments. Therefore, a two-phase centrifugation was always used. In the first phase, 1-hour centrifugation at low centrifugal field was used to remove the major part of the unwanted content. Consequently, a second centrifugation took place with much less precipitate formed and easier manipulation while handling the supernatant. FIGURE 3.13(left) shows the evolution of the integrated fluorescence activity of several samples sonicated under various parameters as a function of the centrifugal field. The starting point at 0 centrifugal field represents as-sonicated dispersion. The pre-centrifugation step was done at 13 200g for 1 hour (FIGURE 3.13(right(a))) and the supernatant was consequently centrifuged for 4 hours at either 28 100g (FIGURE 3.13(right(b))), 36 700g (FIGURE 3.13(right(c))), 57 400g, 82 700g, 113 000g, or 147 000g.

The data shows that pre-centrifugation and centrifugation up to the fields 36 700g does not significantly affect the fluorescence activity of a dispersion and, actually, the fluorescence intensity increases in the majority of the cases. This happens together with removal of significant amount of material from the dispersion as can be seen in FIGURE 3.13(right(a)-(c)). The fluorescently inactive or fluorescence quenching material is therefore preferentially removed at these low centrifugal fields. This was confirmed also by examining the precipitate diluted with water, which was found to have zero fluorescence for the precipitate formed during pre-centrifugation and nearly zero for precipitates formed during centrifugation at less than 36 700g. Higher centrifugal fields already cause significant drop in fluorescence activity, which is an evidence for fluorescent active and thus well individualized SWCNTs being removed from the dispersion. In extreme cases, with centrifugal fields over 147 000g nearly all nanotubes are removed from the supernatant. The decrease of the fluorescent activity happens side by side with constant drop of non-resonant background found in NIR and VIS absorption spectra. The fluorescence spectra taken from water diluted precipitates from high field centrifugations confirm the presence of a vast amount of fluorescent active nanotubes. The shape of the fluorescent spectra from both supernatants and precipitates does not change and thus, no structure-related selectivity

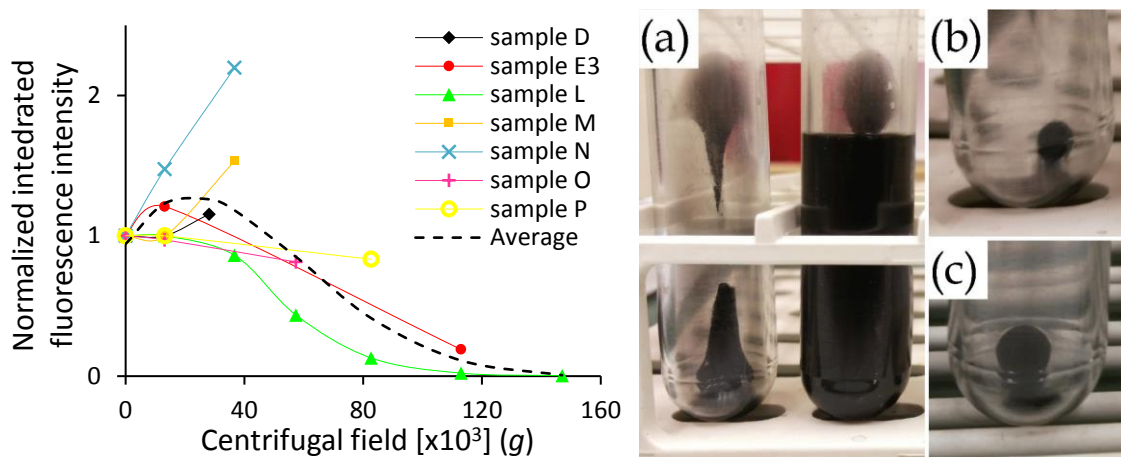


FIGURE 3.13: (left) Evolution of fluorescence activity of samples undergoing centrifugation at different centrifugal fields. Data points at 0g represent as-sonicated dispersion and the black line is a polynomial fit to the averaged values at every centrifugal field. (right(a)) Precipitate formed during pre-centrifugation (sample D). (right(b)) and (right(c)) Precipitate formed from pre-centrifuged samples, centrifuged at 28 100g (sample D) and 36 700g (sample Q), respectively.

is found in the centrifugation process. The parameters used for preparation of the final dispersion used for further experiments are a trade-off between removing the fluorescent inactive components of the dispersion happening side by side with the removing of fluorescent active components. The reasonable value used in further experiments was found to be 82 700g.

Time of centrifugation

A particle with given size and density moves in the solvent with given density and viscosity with a constant sedimentation rate under constant centrifugal field. The time of the centrifugation then determines how small particles with certain density will be given enough time to move along the vial to create the precipitate. The time evolution of absorbance and fluorescence intensity of various samples is plotted in FIGURE 3.14.

FIGURE 3.14(top left) shows that the majority of the not individualized absorbing material, causing the presence of the non-resonant background, is removed within the first hour of centrifugation. However, FIGURE 3.14(top right) and FIGURE 3.14(bottom left) present constant drop of the non-resonant background but on much slower rate. The resonant features remain conserved within the first 3 hours of centrifugation, later a small drop can be observed suggesting the beginning of removal of well individualized nanotubes. After 4 hours of centrifugation, the non-resonant background starts to decrease at much lower rate and there is not much difference between the absorbances of the samples centrifuged for 4 and 20 hours. The fluorescence intensity usually slightly raises after the first hour of centrifugation. Centrifugation time over one hour has only little effect on the fluorescence intensity (FIGURE 3.14(bottom right)), where only a subtle drop can be observed. To conclude, the first hour of centrifugation is responsible for the substantial removal of the vast majority of the non-individualized nanotubes and non-nanotube material.

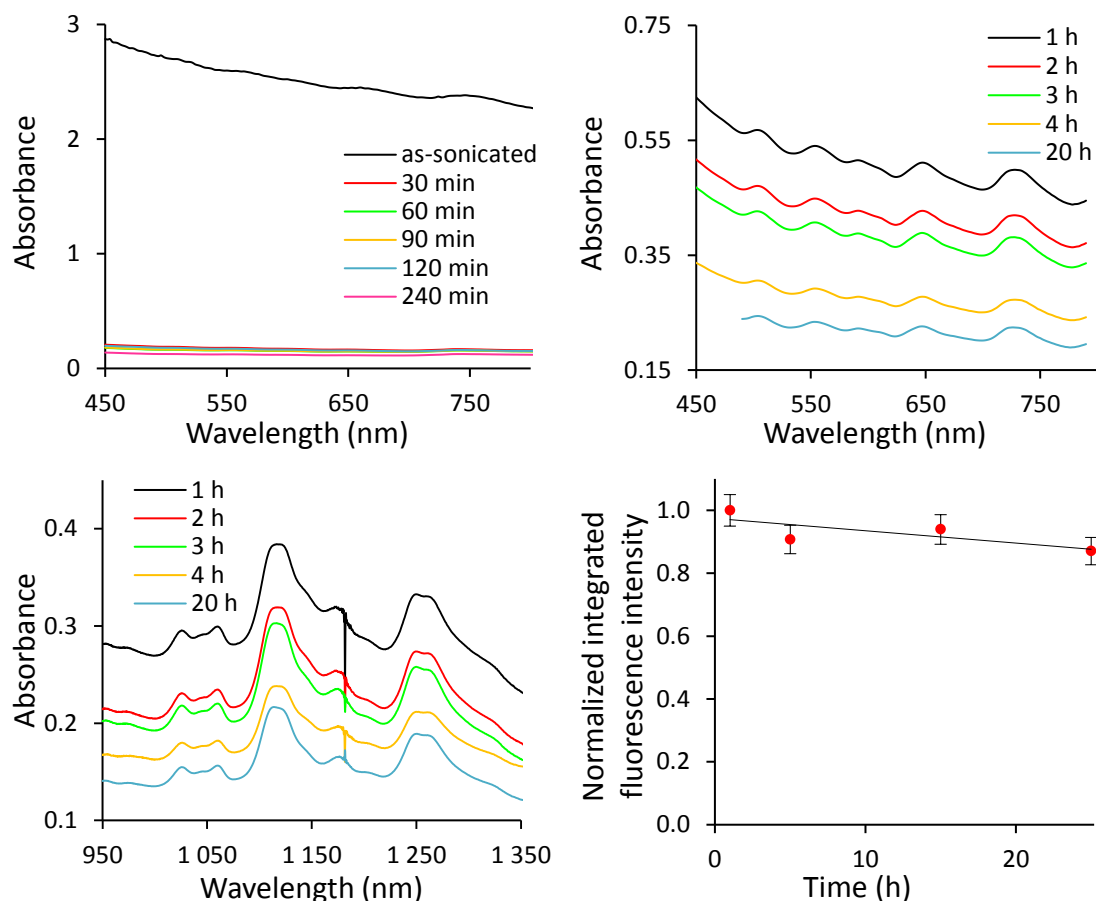


FIGURE 3.14: (top left) Time evolution of VIS absorbance (samples R1 - R6) centrifuged at 122 000g. (top right) Time evolution of VIS absorbance (samples S, T1 - T3, U) centrifuged at 122 000g. (bottom left) Time evolution of NIR absorbance (samples S, T1 - T3, U) centrifuged at 122 000g. (bottom right) Time evolution of integrated fluorescence intensity (sample H1) centrifuged at 122 000g, black line represents least squares linear fit.

The first hour essentially sets the fluorescence activity of the ready SWCNT dispersion. Centrifugation up to 4 hours still brings some benefit in lowering the non-resonant background but centrifugation over 4 hours appears to be redundant. A note has to be done here. As centrifugation at about 120 000g is widely popular for SWCNT dispersions used for fluorescence spectroscopy [42,93,95,102], these observations had been made for samples centrifuged in centrifugal field of 122 000g. Indeed, this value gives samples with excellent fluorescent properties, as was confirmed also in our experiments. However, later experiments showed the drawback of this value - the unwanted removal of fluorescently active and thus well individualized nanotubes FIGURE 3.13(left). For the deep understanding of the properties of SWCNT dispersion prepared at optimal 82 700g centrifugal field, a similar set of time-dependent centrifugation experiments would be beneficial. However, there is no obvious reason to suspect the samples centrifuged in this field would show significantly different behavior.

3.3.5 Filtration

Besides centrifugation, filtration can be used to remove bigger particles from the SWCNT dispersion and improve its quality. Two types of membrane filters were used considering the planned dimension of microfluidic system: Chromafil® 1.2 μm PET 25 mm syringe filter and Acrodisc® 0.45 μm PVDF 13 mm syringe filter. As-sonicated nanotube dispersions must be pre-centrifuged prior to the use of the filter as the undispersed particles (FIGURE 3.13(right(a))) cause immediate clogging even of the more coarse filter and the material caught in the filter further removes also well dispersed nanotubes.

The filtration of pre-centrifuged and up to some extent centrifuged samples always brings increase of the fluorescence intensity (FIGURE 3.15(left)). A pattern can be observed in the improvement of the fluorescence intensity, where the samples centrifuged at lower centrifugal fields show higher improvement of the fluorescence signal compared to samples centrifuged at higher fields. This agrees with the premise of higher centrifugal fields being able to remove smaller and smaller unwanted particles (bundles), which quench the fluorescence, leaving less and less particles big enough to be filtered. Interestingly, the 0.45 μm filter seems to exceed the performance of the 1.2 μm filter, which means that the quenchers are bigger than 450 nm in contrary to fluorescently active SWCNTs. It is obvious that filtration cannot replace the centrifugation process. However, it is useful to know the ability of membrane filters to further clean the nanotube dispersion. This is very handy especially for performing microfluidic experiments where any bigger particles could cause troubles as well as time saving, since the filtration takes only a fraction of time of centrifugation.

3.3.6 Properties of the CNT dispersion

Long-term stability

The knowledge of time-dependent behavior of the SWCNT dispersions is interesting from both scientific and practical point of view. The time-dependent changes in fluorescence intensity point out the dynamics of nanotube-nanotube, nanotube-surfactant, surfactant-surfactant and surfactant-water interactions. The understanding of ongoing processes is helpful in order to improve the preparation protocol, while the simple knowledge of shelf-life of SWCNT dispersion determines, how often the new dispersion has to be prepared to ensure the highest quality.

FIGURE 3.15(right) shows exponential decay of the integrated fluorescence activity towards ~60 % of the original intensity within first two months. Then the intensity remains stable for at least two more months. This could be attributed to slow rebundling, confirming the metastability of this system. The data from both NIR and VIS absorption spectroscopy show overall drop of the absorbance together with the drop of resonant features. This observation also supports the assumption of ongoing rebundling and slow sedimentation of bigger bundles. Nevertheless, it can be concluded that even highly concentrated SWCNT dispersion is a relatively stable system, ready to be used for months, especially when filtered before the immediate use.

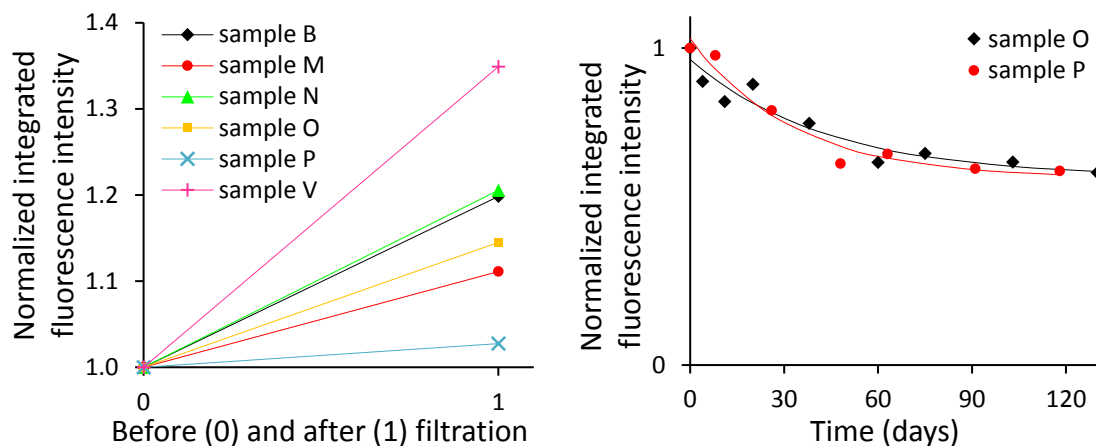


FIGURE 3.15: (left) The effect of filtration on integrated fluorescence intensity of samples prepared in different ways, in different stages of the preparation process. (right) The integrated fluorescence intensity as a function of time. The solid lines are least squares fits of an exponential function.

Concentration of the nanotubes

The concentration of SWCNTs in the aqueous dispersion is a crucial parameter for its further processing. The knowledge of the concentration is especially important in composite materials science, where the concentration determines the degree of the composite strength improvement [113]. Nevertheless, the concentration is a key parameter when it comes to nanotube-by-nanotube sorting from the dispersion. Despite its importance, no universal, fast, and reliable protocol is known. This is mostly due to the way how nanotube dispersions are prepared and the nature of the SWCNTs. Upon surfactant assisted debundling, nanotubes are divided between the supernatant and the precipitate together with the surfactant in non-proportional way [113]. In addition, the SWCNTs dispersed in the precipitate consist from both individual and bundled nanotubes. Since only the individual nanotubes are interesting for the sorting, not only the absolute concentration of the SWCNTs in the dispersion has to be determined, but also the quality of their individualization.

Several different approaches to this challenging task can be found in the literature. An interesting approach is mentioned in [114], where the fluorescence intensity is computed for every nanotube type. The computed intensities are compared to experimental values and their ratios determines the relative concentration or abundance of SWCNTs in the particular dispersion. Emission intensity is found to be inversely proportional to the square of the SWCNT diameter, leading to much more effective absorption - relaxation - emission process for the smaller nanotubes. This method is not straightforward to use for determination of nanotube concentration, nevertheless, it gives important insight to the fluorescence process. The intensity of the fluorescence itself is found to be a reliable parameter for determination of concentration of the SWCNT dispersion [112]. It inherently works only with semiconducting individual nanotubes, which are in the focus of this project. The proportionality of the fluorescence intensity to the concentration strongly depends on the mean nanotube dimensions (mainly length). The linear dependence fails above the concentration, when the size of unit cell of

water attributed to one nanotube drops below the length of the nanotube [112]. At this point, inter-cross quenching starts to take place and the fluorescence intensity starts to drop with increasing concentration.

This observation could interfere with the results taken during the development of the SWCNT dispersion preparation protocol. However, a drop in the fluorescence intensity was not observed at any of the parameters, which could potentially increase the nanotube concentration (amount of nanotubes, sonication power, sonication energy). Therefore, a conclusion can be made that the critical concentration was not exceeded in any of the preparation steps. With the assumption of one nanotube per one droplet in the femtoliter scale, this concentration is much below the critical value. Therefore, the fluorescence intensity could be used as a reliable tool for determination of SWCNT concentration in diluted dispersions. For quantitative results, however, a calibration curve must be constructed by different means.

The absorption is reported to be a good parameter for measuring the SWCNT concentration in the dispersion. While the absorption in NIR region is not a reliable parameter because the signal interferes with fluorescence emission, the absorption in VIS region is used for determination of the concentration [113,115]. This protocol is suitable for measurement of the total SWCNT concentration [113], as well as the ratio of individual and bundled nanotubes [115]. This is done by comparing the area of non-resonant background to the area of the resonant features in absorption spectrum of (6,5) enriched CoMoCAT SWCNT dispersion. This confirms the assumption from previous paragraphs that lower non-resonant background with unchanged resonant features means better SWCNT dispersion. Unfortunately, the VIS spectrum, especially its resonant features, are dependent on the distribution of nanotube diameters in the used SWCNTs. The VIS absorption spectrum of HiPco™ nanotubes is cluttered (see FIGURE 3.4) with overlapping contributions from different electronic transitions, which makes it challenging to distinguish the contributions from resonant and non-resonant part.

The absorption spectrum of the SWCNT dispersion in UV region shows two characteristic features, both originating from π -plasmon resonance. This π -plasmon originates purely from grapheneous structures and thus is a good parameter for measuring the concentration of the SWCNTs in the dispersion. The peak, usually found at around 270 nm can be linked to surface π -plasmon, while peak around 225 nm originates from bulk π -plasmon. In theory, both of them can be used for determination of the concentration. However, the bulk π -plasmon absorbance is usually not used as it may interfere with absorbance from other carbonaceous components [112] as well as for its interference with absorbance of several popular surfactants (SDBS strongly absorbs at 225 nm [105]). The absorption by surface π -plasmon does not suffer from these effects, however, its position depends on the diameter of the used nanotubes [116]. Nevertheless, if the surface π -plasmon can be distinguished from the absorption spectrum, it can be used for exact determination of the concentration of nanotubes in the dispersion. Similarly to the fluorescence, the linear dependence of the concentration holds only within a limited interval. The absolute value of absorbance should not be under 0.1,

where the error of the measurement grows too large and not above 2.0, where the linear dependence from eq. (3.1) does not hold anymore [105,113].

The absorbance of the SWCNT dispersion follows Beer-Lambert law [105,116]:

$$A = \varepsilon \cdot c \cdot l, \quad (3.1)$$

where A is absorbance, ε molar absorption coefficient, c the concentration, and l the pathlength. The molar absorption coefficient of the SWCNTs can be defined by understanding the nanotubes as individual molecules. The molar absorption coefficient is particularly useful for the purpose of the sorting project as the concentration in eq. (3.1) straightforwardly leads to a number of SWCNTs per unit volume. The absorbance, however, depends on the amount of carbon atoms in the right form, not on the amount of nanotubes, dimensions of which may significantly vary. Other absorption 'coefficients', which lead to concentration related to mass or unit length of the dispersed SWCNTs are therefore also used. The number and dimensions of the nanotubes are evaluated either by AFM [112,117] or the mass of the nanotubes is determined by TGA¹⁰ [105,116]. The comparison of absorption coefficients from different references are listed in TABLE 3.4.

TABLE 3.4: Absorption coefficients of HiPco™ nanotubes in aqueous dispersion for surface π -plasmon peak. The data in bright yellow cells are missing in the references and are only estimated for comparison. The pale yellow cells are calculated using values from bright yellow cells.

Ref.	Calibr. method	Mean length (nm)	Mean d (nm)	Abs. coeff. per nanotube (mL·NT ⁻¹ ·cm ⁻¹)	Molar abs. coefficient (mL·mol ⁻¹ ·cm ⁻¹)	Abs. coeff. per mass (mL·mg ⁻¹ ·cm ⁻¹)	Abs. coeff. per nm (mL·nm ⁻¹ ·cm ⁻¹)
[105]	TGA	400	1	1.8·10 ⁻¹³	1.1·10 ¹¹	184.6	4.5·10 ⁻¹⁶
[116]	TGA	400	1	4.9·10 ⁻¹⁴	3.0·10 ¹⁰	50.0	1.2·10 ⁻¹⁶
[112]	AFM	600	1	3.1·10 ⁻¹⁴	1.9·10 ¹⁰	21.0	5.2·10 ⁻¹⁷
[117]	AFM	180	1	6.0·10 ⁻¹⁵	3.6·10 ⁰⁹	13.5	3.3·10 ⁻¹⁷

The absorption coefficient per mass differs more than an order of magnitude from case to case. Compared to AFM calibration, TGA generally produces large measurement error and important data from papers using this method are missing. In addition, the preparation of the SWCNT dispersion is closest to the method reported in [112], while [117] already uses too harsh sonication, which possibly induces non-negligible amount of structural defects. Therefore, the value of 20 mL mg⁻¹ cm⁻¹ is used to estimate the concentration of samples in this project. Since the absorbance of as-prepared SWCNT dispersions in UV region is generally too high, the absorbance in acceptable interval is achieved by dilution and consequent recalculation of the concentration according to the dilution ratio. A typical absorption spectrum is plotted in FIGURE 3.16(top). The spectrum is deconvoluted similarly to the protocol reported in [112] to an exponential function representing the general background and three Gaussian functions representing the absorption peaks. The centers of the peaks lie at ~223 nm (bulk π -

¹⁰ thermogravimetric analysis

plasmon), ~ 261 nm (surface π -plasmon – shift in agreement with [116] for HiPco™ nanotubes) and very small peak at ~ 295 nm of unknown origin. The absorbance of surface π -plasmon is then used to construct a calibration curve (FIGURE 3.16(bottom)). Despite the different preparation parameters, and dilution ratios, the relation of surface π -plasmon absorbance and nanotube concentration is strictly linear. This straight line allows reverse calculation of the SWCNT concentration in undiluted dispersion.

The estimation of SWCNT concentration in the dispersion from the surface π -plasmon absorption is found to be reliable and repeatable. However, it requires more time and sample preparation than fluorescence spectroscopy, which is zero-preparation, one-click measurement. Therefore, a calibration curve was constructed, by using the known concentration from UV absorption measurement and total fluorescence signal. The new calibration curve is loaded with higher measurement error (FIGURE 3.17(left)), nevertheless it is sufficient for quick estimation of the concentration of the nanotubes in a dispersion.

The comparison (FIGURE 3.17(right)) of the calculated concentration of the undiluted dispersions versus the total measured signal shows several

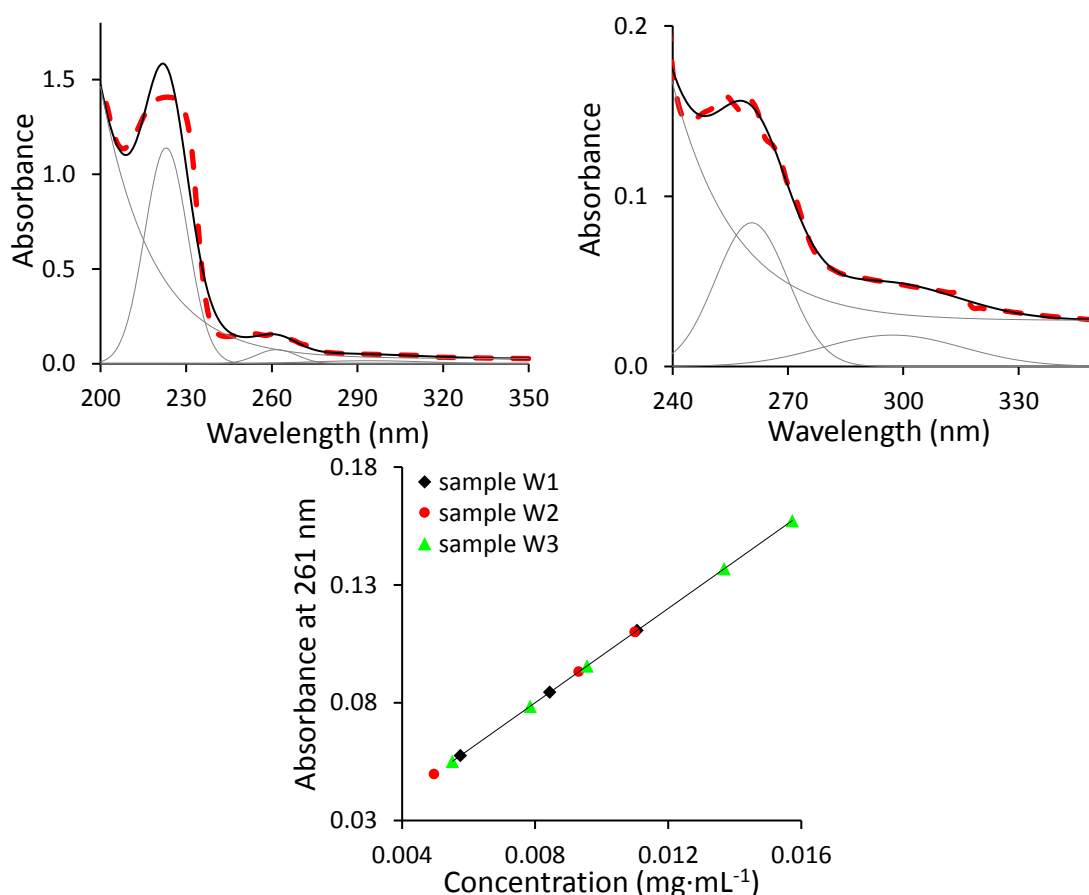


FIGURE 3.16: (top left) A typical absorption spectrum of highly diluted aqueous SWCNT dispersion in UV region (sample W1–1:50). The red dashed line is the measured value, the black solid line represents a sum of individual deconvoluted functions (grey solid lines). (top right) Zoomed area of the surface π -plasmon absorption peak. (bottom) Calibration curve constructed from values measured from several samples with different dilution ratios (sample W1 – W3). The calibration curve is a least squares fit of a linear function.

noteworthy effects. The samples W1 and W2 were prepared with the same parameters, except the sonication power, which was much higher for the W1 sample. The fluorescence intensity is much lower than expected for the given concentration, which could be contributed to structural damage caused by the extensive sonication power, or by higher concentration of non-fluorescent grapheneous particles. They would not affect the fluorescence intensity at high dilution ratios, however, they can cause serious inter-cross quenching at original concentration. The samples W2 and W3 were prepared with the same parameters, except the centrifugal field, which was much higher for the sample W3. The lower fluorescence intensity of sample W2 could be contributed to a higher number of non-fluorescent bundles or quenchers not removed by the centrifugation. The inter-cross quenching can then alter the measured fluorescence intensity similarly to previous case. It seems that the integrated fluorescence intensity could be a sufficient parameter for estimation of the concentration. This is valid only for the well centrifuged samples, where the presence of non-fluorescent bundles and other possible quenchers is eliminated. Since the development of the SWCNT dispersion preparation protocol leads to high centrifugal fields anyway, this is not an obstacle for this method.

The samples J3 and B are prepared under conditions, which should work well with the calibration curve (FIGURE 3.17(right)). The fluorescence spectra were, however, obtained in different stages of the development of the home-build NIR fluorescence setup. Understandably, as the efficiency of the signal collection changes, this method requires a new calibration curve for every rebuild of the fluorescence setup. The position of the new data point obtained from UV absorption and fluorescence intensity of the new setup compared to the calibration curve measured with the previous setup can serve as a quality indicator for the new NIR fluorescence setup. The signal collection quality for sample J3 was

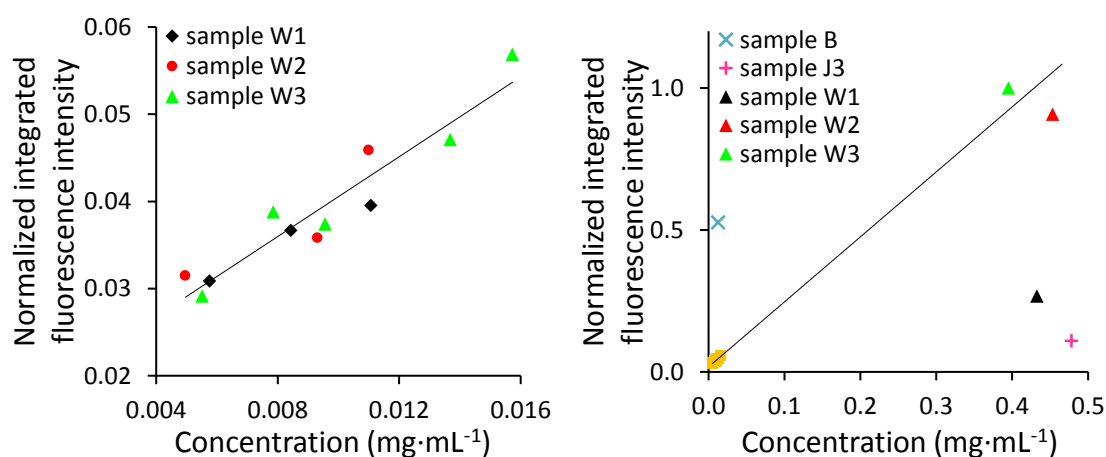


FIGURE 3.17: (left) The calibration curve for estimation of the concentration of the SWCNTs in the dispersion from integrated fluorescence signal. (right) The same calibration curve extended for calculated concentrations of undiluted samples and its agreement with measured fluorescence intensity. Data points from the left graph are plotted in orange, triangular data points are measured on NIR fluorescence setup, for which the calibration curve was constructed, and round data points were measured on altered setup.

poor compared to the original calibration curve, while the setup used for measurement of sample B had superior collection efficiency.

The surface π -plasmon, a cornerstone for all the methods described above, does not carry any information about the level of individualization [105]. Comparison of the nonresonant background and resonant features in VIS spectrum is hardly of any use as the HiPco dispersion contains many overlapping absorption bands here (FIGURE 3.4). However, the estimation of concentration by NIR fluorescent spectroscopy shows reasonable agreement with the calibration curve for samples, which undergo harsh centrifugation under conditions described in previous paragraph. Since only individual semiconducting nanotubes exhibit fluorescent behavior, this agreement is an indirect evidence for high level of individualization and purity of the dispersion. In addition, the harsh centrifugation is generally used for preparation of high quality SWCNT dispersions and the amount of non-nanotube material and bundles can be considered negligible. Hence, the concentration determined on the basis of NIR fluorescence is the concentration of individual nanotubes in the dispersion if the preparation was done under the right conditions. Specifying of the molar concentration, and therefore the real number of nanotubes in the unit volume would require the knowledge of mean dimensions of the nanotubes, namely the length, after the preparation process. Nevertheless, the method described above is sufficient for approximate estimation of the SWCNT concentration in aqueous dispersions.

3.4 Conclusion

A protocol for preparation of SWCNT dispersions suitable for microfluidic sorting has been developed. The prepared dispersions have high concentration of well individualized nanotubes, very low non-resonant background in absorption and long shelf-life. Dispersions prepared by this protocol are suitable for any kind of application where aqueous dispersions of individual SWCNTs are needed. After deposition and washing [112,117], the nanotubes are ready for AFM measurements or electro-optical experiments. The detailed protocol for the preparation of SWCNT dispersion is attached at the end of this manuscript as Appendix A.

BOOK II - MICROFLUIDICS

4 Theory of microfluidics

The rapid growth of technology nowadays is largely based on miniaturization. Decreasing size of basic building blocks allowed integration of higher number of elements and made (mainly) electronics an inseparable part of our everyday life. This includes not only smartphones, computers and displays but also fields like meteorology, space research, medicine and pharmacology, just to name a few. Likewise, instruments working with fluids, especially with moving fluids, often benefit from miniaturization in similar way. The downscaling brings higher speed, lower reagent consumption, unprecedented precision, possibility of automation, and high-throughput screening; all resulting in significant reduction of the cost. The branch of technology dealing with miniaturized fluidic devices is called *microfluidics*. The gradual development of this field over the last 40 years, propelled by emerging fields of molecular analysis, biodefense, molecular biology and microelectronics, lead from simple straight channels to overwhelmingly complex devices often referred as *micro total analysis systems* (μ TAS) [9].

4.1 Definition

The term microfluidics is used to name both the field of science which studies the behavior of fluids confined in the micro-channels and the field of technology and manufacturing devices for confined flow of fluids in micro-scale. The word *micro* usually refers to either small size of the channels, very small volumes (μ L to fL), or to prevailing effects characteristic for microdomain.

The microfluidic science deals with precise control and manipulation of fluids in geometrical conditions which causes the fluid behavior to be different from everyday life. The surface and interfacial tension, hydraulic resistance, and energy dissipation start to dominate the system and some interesting and often un-intuitive properties appear. They are the key for innovations and experiments either significantly improving the capabilities of conventional methods or bringing absolutely new possibilities, unknown before the advent of microfluidics.

The microfluidic technology utilizes various microfabrication techniques for manufacture of the desired structures. New applications of microfluidics come almost on daily basis requiring more and more complex devices. The microfluidic devices nowadays allow much wider possibilities besides simple flow: two- and multi-phase flow, droplet formation, sorting, on-chip characterization, droplet trapping, splitting and merging, on-chip incubation, *etc.* are commonly used in modern microfluidics. The systems integrating several functions to a

single chip are known as *microelectromechanical systems* (MEMS). A subset of MEMS operating with fluids is often called *lab-on-a-chip* (LOC).

The manufacture of complex structures, 3D profiles, implementation of active elements and electrodes uses similar techniques to micromachining technology known from semiconductor industry. Since the dimensions of the microfluidic device can vary from 500 μm down to 100 nm, the manufacture is usually simpler than manufacture of cutting-edge nanodevices and top-down¹¹ approaches are usually used. Nevertheless, the manufacture of microfluidic devices brings its own set of challenges originating from different materials, requirements for surface quality and structure, and implementation of moving components.

The whole concept of microfluidics is a highly multidisciplinary field at the intersection of physics, chemistry, nanotechnology, biochemistry, and engineering. The small size of the systems and high requirements for cleanliness and precision often demand cleanroom environment for manufacture. Despite these challenges, microfluidics has allowed new achievements with obvious impact on everyday life with technology like LOC in medical diagnostics, DNA microarrays, and inkjet printheads. The impact on laboratory instrumentation is even larger with a broad palette of commercial suppliers offering complex microfluidic systems for numerous applications.

The broad field of microfluidics can be categorized according to several criteria. Plenty of applications use passive control of fluids, either capillary based or with contribution of rotary actuation. They are used mainly in point-of-care testing, drug screening, etc. where a sample enters the system via capillary force, reacts with reagent inside and shows a result. More complex systems, however, requires *active* control of the fluid flows. Here, various types of pumps and valves are used to drive and influence the behavior of the fluids in real time. The active microfluidics offers two different approaches of handling the fluids. Well-defined and simple operations are often performed in continuous-flow systems; however, their utilization is rather limited for more complex tasks.

Unlike the continuous-flow systems, the *droplet-based* microfluidics is based on creating discrete *droplets* utilizing mutually immiscible fluids. The continuously flowing fluid is referred as *continuous* phase, while the fluid creating droplets is called *disperse* phase. The droplet-based microfluidics, after the droplet generation, allows for complex operation like droplet sensing and sorting, droplet merging and breakup, encapsulation of particles and driven mixing of reagents within the droplets. It even allows performing Boolean logical functions and forming logical 'circuits'.

¹¹ The type of manufacture, where larger devices and substrates are used to direct the creation of a smaller ones.

4.2 Applications of droplet-based microfluidics

The droplets in a droplet-based microfluidic system offer several novel features, which has led to a boom of new applications. Namely [118]:

- The droplet provides an isolated compartment for different species or for a reaction.
- The droplets are highly monodisperse (variation $<1\%$ in diameter [10,119]) and thus suitable for quantitative experiments.
- The size of the droplets allows downscaling to single cell or molecule level.
- The fast generation of droplets allows to perform large amount of experiments in short time with minimal reagent consumption.

Droplet-based microfluidics proves its utility and viability in numerous applications across the experimental science and laboratory research. The application of microfluidics significantly improved the efficiency of PCR¹² [12,118], single cell encapsulation and sorting [120], synthetic biology, screening and delivery of new drugs, assaying of cells and microorganisms and synthesis of functional micro- and nanoparticles, and many more [10,11,118,121]. The rapid development of microfluidic technology, however, starts to be impeded by the lack of operating and support systems, the development of which is not able to keep the pace. The development of detection methods, novel materials for microfluidic chips, and deeper understanding of complex and multiphase fluid-fluid and fluid-solid interfaces in a confined dynamic regime is needed for further miniaturization and improvement of the microfluidic systems.

4.3 Theoretical background

The vast majority of microfluidic devices have found practical utilization in cell biology applications and naturally, with the remarkable boom of this field in the last two decades, the dimensions adapt to the size of the basic biological unit – the cell. The eukaryotic cells may vary in size from $100\ \mu\text{m}$ to $10\ \mu\text{m}$ corresponding to spherical volume from picoliters to nanoliters [12] (FIGURE 4.1). One can easily find a plethora of both theoretical and experimental knowledge about the microfluidic system in this range of sizes and the majority of physical phenomenon are relatively well described and understood.

4.3.1 Characteristic dimensions

One of the descriptive properties of a physical system is its *characteristic length*. The characteristic length is a dimension which defines the scale of a physical system. In the microfluidic domain, the only characteristic length that matters is the dimension of the system L [14]. The characteristic lengths considered in this work

¹² polymerase chain reaction

are the shortest dimensions of the microfluidic channel - its width and depth. The hydraulic radius

$$r_H = 2 \frac{S}{P}, \quad (4.1)$$

where S is the cross section and P is the wetted perimeter of a rectangular channel, can be used as the characteristic length

$$L = r_H = \frac{wd}{w+d}. \quad (4.2)$$

Here, w is the width and d the depth of a microfluidic channel.

When it comes to scaling of such a system one must take into consideration possible changes of dominant effects governing the physics (FIGURE 4.1). Scaling up already leaves the world of microfluidics behind and it's beyond the scope of this manuscript. Scaling down, to the size suitable for single nanotube sorting experiment - about one order of magnitude smaller than in cellular biology applications has to be properly examined in order to understand the behavior of the designed system. The field of microfluidics in these dimensions is only emerging, especially because of the rising requirements for precision, cleanliness, materials, instrumentation, and consequent rise in price when scaling down. The following paragraphs will, in a simple way, explain the basic physics involved and consider the possible changes in scaled down systems.

Another challenge comes from the smaller side of the length scale. The whole fluid dynamics is based on an assumption of fluid particles with continuously varying properties. This *continuity assumption* breaks down when quantum properties of individual molecules overweight the bulk properties of a fluid. In nanoscience, 100 nm is considered as a borderline where quantum phenomena can be already observed as they are not 'drowned' in the bulk properties [122]. Since the smallest characteristic length of the systems discussed in this manuscript are $\geq 1 \mu\text{m}$ the continuity assumption is valid and nanofluidic effects can be excluded from the consideration.

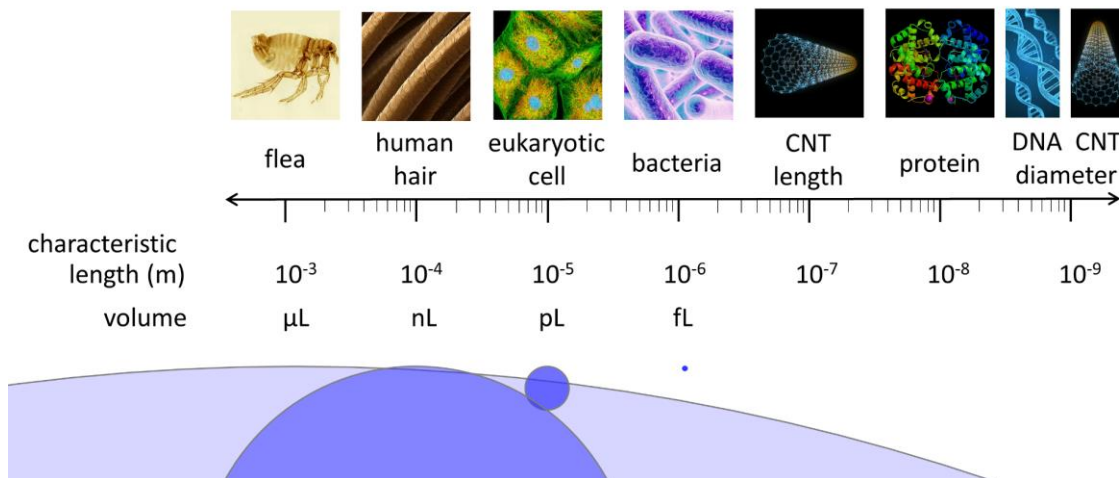


FIGURE 4.1: Definition of the scales used in this work. The characteristic length of most microfluidic systems is in nL and pL scales. Femtoliter microfluidic system reaches one order of magnitude lower, matching the size of bacteria.

4.3.2 Dimensionless numbers

In fluid mechanics, the dimensionless numbers express the relations between particular fluid parameters in a way that the resulting quantity is dimensionless. The resulting numerical value determines the behavior of a given system. Experimental experience usually gives two numbers (or orders of magnitude) where the system is in some way stable when outside of those two values, and a mixed regime exists in between them. There is a large number of these dimensionless numbers. Wikipedia alone lists more than sixty of them. Nevertheless, only few of them are usually considered when dealing with simple droplet-based microfluidic systems.

The Eötvös number

$$Eo = \frac{\Delta\rho g L^2}{\sigma}, \quad (4.3)$$

where $\Delta\rho$ is the difference in density between two fluids, g the gravitational acceleration, L the characteristic length, and σ the interfacial tension. The Eötvös number compares buoyant (gravitational) and capillary (surface/interface) forces. Due to small characteristic length in microfluidic applications (μm), generally $Eo \ll 1$, thus gravity effects can be neglected.

The Reynolds number

$$Re = \frac{\rho v L}{\eta} \quad (4.4)$$

Here ρ is the mass density, v the mean velocity of the fluid, and η the dynamic viscosity. The Reynolds number compares inertial and viscous forces and predicts the transition from laminar (low Re) to turbulent (high Re) flow patterns. In typical microfluidic devices $Re < 1$, decreasing linearly with the size of the system and with the speed of the mean velocity. Slow and small systems thus result to $Re \ll 1$ and the flow is laminar in vast majority of the cases.

The Weber number

$$We = \frac{\rho v^2 L}{\sigma} \quad (4.5)$$

compares inertial and capillary forces. This quantity is particularly useful in analyzing fluid flows where there is a strongly curved interface between two immiscible liquids. Typical situation is formation of bubbles or droplets. Similar to Re also We decreases linearly with size of the system and quadratically with the mean velocity. Slow and small systems thus again result to $We \ll 1$. From the typical magnitudes of Re and We , it follows that inertia generally becomes unimportant when the characteristic length of the system is downscaled to micron range. Therefore, the dominant forces at the microscale are capillary and viscous forces [123].

The capillary number

$$Ca = \frac{\eta v}{\sigma} \quad (4.6)$$

represents the relative effect of *viscous* forces versus *interfacial* tension and clarifies which force is (pre)dominant in a particular system. The η is usually the viscosity of the more viscous fluid in the system and v is the velocity of that fluid. For low capillary numbers ($Ca \leq 10^{-5}$) the flow is dominated by capillary forces whereas for high capillary numbers the capillary forces are negligible compared to viscous forces. The capillary number can then predict the regime of droplet formation or the effect of the continuous phase on the droplet shape [14].

The Bond electric number

$$Be = \frac{\varepsilon_0 \varepsilon_r L E^2}{\sigma} \quad (4.7)$$

describes the relative importance of electrostatic forces versus capillary forces when an electric field is present in the system. Here, ε_0 is the vacuum permittivity, ε_r the relative permittivity of the fluid, and E the applied electric field. The electrostatic forces dominate the system if $Be \gg 1$, while the capillary forces determine the system behavior if $Be \ll 1$ [124]. The system between these extremes is influenced by both electrostatic and capillary forces. Be will decrease with characteristic length, therefore the possibility to manipulate very small objects is not clear and probably has to be compensated by very high fields, bringing new challenges to field design and implementing the electrodes [14].

4.3.3 Navier-Stokes equations

The model of incompressible Newtonian liquid holds very well for the liquids used in microfluidic systems [125]. Then, the movement of fluid particles – elements of fluid big enough to avoid quantum phenomena but small compared to the dimensions of the system – is governed by Navier-Stokes equations, a case of Newton's second law:

$$\rho \left[\frac{\partial \vec{v}}{\partial t} + (\vec{v} \cdot \nabla) \vec{v} \right] = -\nabla p + \eta \nabla^2 \vec{v} + \vec{F}, \quad (4.8)$$

$$\nabla \cdot \vec{v} = 0, \quad (4.9)$$

where ρ is density, \vec{v} flow velocity, t time, p pressure, η dynamic viscosity, and \vec{F} stands for body forces acting on the fluid particle, like buoyant or electrical forces. Equation (4.9) is a direct consequence of the incompressibility assumption. In the case of microfluidics, the Navier-Stokes equation can be significantly simplified by comparing the relative importance of inertial term $\rho(\vec{v} \cdot \nabla)\vec{v}$ and viscous term $\eta \nabla^2 \vec{v}$. Their ratio is expressed by Reynolds number, eq. (4.4).

The characteristic length L for typical microfluidic device is in the order of 10^{-6} m, ρ is in the order of 10^3 kg·m⁻³ and η in the order of 10^{-3} Pa·s (decane, water). In such conditions, unless the fluid velocity would be ridiculously high ($\geq 10^2$ m·s⁻¹), the Reynolds number confirms that the flow is linear, inertial forces

are negligible in comparison to the viscous forces and Navier-Stokes equation becomes linear. For established flows ($\partial\vec{v}/\partial t = 0$), the hydrodynamics is described by the Stokes equation:

$$\eta\nabla^2\vec{v} - \nabla p + \vec{F} = 0. \quad (4.10)$$

4.3.4 Poiseuille flow

The Navier-Stokes equation (4.8) is notoriously known for difficulties in finding its analytical solution¹³. A class of solutions for pressure-driven, steady-state linear flows in channels is known as Poiseuille flow. This solution is valid for systems with $\text{Re} < \pi^2$ [126], well covering the realm of microfluidics. This class is of high importance for the elementary understanding of liquid behavior in a microfluidic system.

The closest simple channel shape to the channels used in this work is a channel with rectangular cross section. Despite the linearization and obvious symmetry in this case, no analytical solution is known to the Poiseuille flow problem with a rectangular cross section. The closest one can get analytically is a Fourier sum

$$v_x(y, z) = \frac{4h^2\Delta p}{\pi^3\eta L_{\text{CH}}} \sum_{n,\text{odd}} \frac{1}{n^3} \left[1 - \frac{\cosh\left(n\pi\frac{y}{h}\right)}{\cosh\left(n\pi\frac{w}{2h}\right)} \right] \sin\left(n\pi\frac{z}{h}\right) \quad (4.11)$$

representing the solution [125]. Here, Δp is the pressure drop along the channel, η the dynamic viscosity, and L_{CH} the length of the channel. Remaining geometrical quantities together with the velocity profile is depicted in FIGURE 4.2.

The flow rate Q and flow speed v can then be well approximated [125] as

$$Q \approx \frac{h^3 w \Delta p}{12\eta L} \left[1 - 0.63 \frac{h}{w} \right] \quad (4.12)$$

and

$$v \approx \frac{h^2 \Delta p}{12\eta L} \left[1 - 0.63 \frac{h}{w} \right]. \quad (4.13)$$

4.3.5 Hydraulic resistance

The steady-state flow of an incompressible fluid through a straight channel driven by pressure drop Δp results in a constant flow rate Q , eq. (4.12). This is expressed in Hagen-Poiseuille law

$$\Delta p = R_{\text{hyd}} Q = \frac{1}{G_{\text{hyd}}} Q, \quad (4.14)$$

where R_{hyd} and G_{hyd} are hydraulic resistance and hydraulic conductance, respectively. The hydraulic resistance itself arise from the viscous dissipation of

¹³ The analytical solution of Navier-Stokes equation is one of the seven Millennium Problems listed by the Clay Mathematics Institute of Cambridge, Massachusetts.

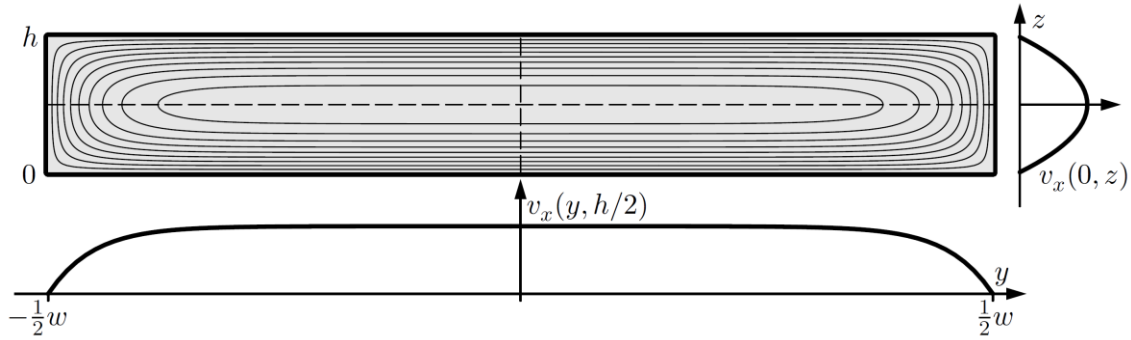


FIGURE 4.2: Contour lines plot and cross sections of the velocity field $v_x(y, z)$ for the Poiseuille flow in a rectangular channel. Figure courtesy of Henrik Bruus [124], used with permission.

mechanical energy into heat by internal friction in the fluid. The Hagen-Poiseuille law, eq. (4.14), for movement of fluids in microfluidic channels represents full analogy to Ohm's law for electrical potential drop driven electrical current in a wire with certain resistance. The hydraulic resistance for a straight channel with rectangular cross section can be easily derived from equations (4.12) and (4.14), and takes form

$$R_{\text{hyd}} = \frac{12\eta L}{1 - 0.63(h/w)} \frac{1}{h^3 w}. \quad (4.15)$$

Even if not so straightforward as in the case of electrical conductors, the resistance grows linearly with channel length and drops with growing cross section area. The rules for calculating the resistance of straight channels does not deviate from rules from electrical circuit theory: the resistance of channels connected in series simply sums up whereas the resistance of channels connected in parallel is equal to inverted value from sum of inverted resistances. The analogy goes even further, and Kirchhoff's laws can be applied for the microfluidic circuits [125].

1. The sum of flow rates entering/leaving any node in the circuit is zero.
2. The sum of all pressure drops in any closed loop of the circuit is zero.

4.3.6 Flow of confined droplets

For the sake of this manuscript, we will restrict the discussion only to the case of droplets confined in a channel with rectangular cross section. Since the Stokes equation describes a laminar flow in the microfluidic system, nothing like a droplet formation should be possible and only a laminar co-flow should be observed. However, special conditions exist on the moving interface of two immiscible liquids. With suitable chosen confining geometry, the growing shear stress and interfacial tension may favor the situation when one of the flows spontaneously breaks and a droplet is formed [121].

The basic assumption for droplet flow at equilibrium is the existence of a thin film of the continuous phase always wetting the walls and having somewhat larger 'triangular' sections of the continuous phase in the corners of the channel (FIGURE 4.3). The presence of moving droplets in confined channels leads to pressure fluctuations [127] as well as increases the overall pressure drop in the

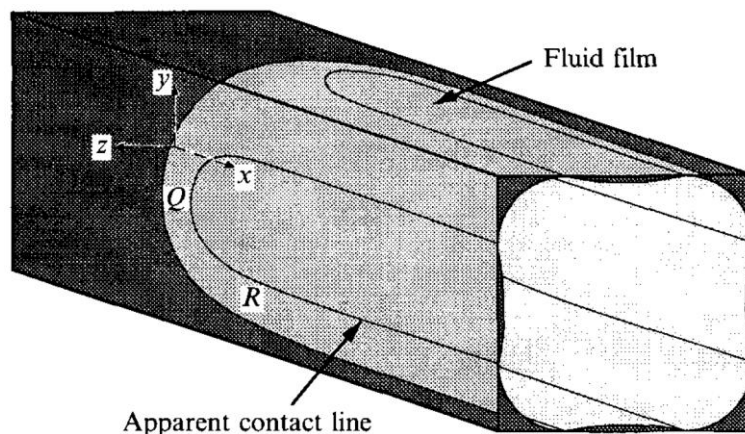


FIGURE 4.3: Cross section of a long droplet flowing in wetting liquid in a square channel. Figure reprinted by permission from [127]. Copyright Cambridge University Press 1995.

microfluidic channel [128]. The droplets alter the flow field of continuous phase, which leads to elevation of the viscous stress together with the presence of a uniform fluid film of the continuous phase on the solid boundary. This is even amplified by the presence of confined droplets, which try to minimize their surface energy and become spherical, resulting in friction impeding the movement of the droplets. In the case of rectangular channels, the situation is even more complex due to the nonuniform film thickness [129] leading to the variability in the flow strength between the corners and the thin lubrication films (FIGURE 4.3) and leaking of the droplet content into the channel edges [130]. All these factors cause general reluctance of the confined droplets towards movement forward and bring a set of challenges to deal with when designing the microfluidic system.

Experimental results show that for small confined droplets (droplet length/channel width ≤ 4), the pressure drop over an individual droplet is independent of the droplet size and the capillary number, and weakly depends on the ratio of the viscosities of the two immiscible phases. The pressure drop is dominated by the dissipation due to the end half-spheres. The net pressure drop is just a sum of the pressure drop increments from individual droplets [130].

To conclude these general findings, there seems to be *no fundamental discrepancy with the main assumptions of microfluidics when scaling down to femtoliter volumes*. The capillary and Reynolds numbers grow smaller with smaller dimensions approving the Stokes flow approximation with even smaller error. On the other hand, the system dimensions are large enough to avoid nanofluidic phenomena [14]. The expected behavior, not different from the well-described systems, supports the motivation towards planned miniaturization. However, the surface/interface related effects, often neglected while studying larger systems, are expected to grow as the surface vs. volume ratio grows in miniaturized systems. The techniques utilizing electric field are expected to be far less efficient in systems with reducing characteristic length and their implementability has to be experimentally verified.

4.4 Basic operations in droplet-based microfluidics

The droplet-based microfluidics offers a wide variety of actions with the immiscible phases present in the system. They include droplet formation with content encapsulation, droplet fission and fusion, mixing of reagents inside of a droplet, droplet content detection with sorting, droplet trapping, and on-chip storage [10,11,14,118,120,123,131]. In the following paragraphs, the overview of main operations of droplet-based microfluidic systems is presented with the focus on the operations developed for this project.

4.4.1 Droplet formation in open and confined systems

Emulsification is a synonym for droplet formation. An emulsion is a disperse system, consisting of two immiscible liquids, which in the vast majority of cases are *water* and *oil*. To disperse two immiscible liquids, a third component, emulsifier, is needed. While the two immiscible liquids separate quickly after agitation, the emulsifier self-placed on the liquid-liquid interface brings the necessary kinetical stability and prevents the phase separation. The emulsion science is deeply studied and widely applied in food industry, cosmetics, mechanical and civil engineering [132-135] and the choice of the emulsifier system¹⁴ for given oil-in-water (O/W) or water-in-oil (W/O) is summed up in a set of relatively simple rules, called hydrophilic-lipophilic balance (HLB) system [136-138]. The proper choice of the emulsifier system not only sustains the stability of the emulsion but also directly determines which phase will become continuous and which will become disperse. Hence, in the open system, the formation of water droplets in oil phase or oil droplet in water phase is determined by the emulsifier present.

The droplet formation in confined regime is governed by quite different rules. The type of produced emulsion is determined by the interfacial tension on the solid-liquid interface [10,139-142]. In other words, the contact angle of a given liquid on the channel surface will dictate whether the liquid will wet the channel walls and become continuous phase or will roll up and form a droplet [121]. The presence of an emulsifier plays only a secondary role in droplet formation, having partial influence on formation regime and flow type [10,141]. Nevertheless, the presence of the emulsifier in the emulsion is crucial for emulsion stability [132,143].

4.4.2 Droplet formation in confined regime

The production of emulsions in confined regime brings many advantages over other emulsion production methods. The unprecedented monodispersity, stability, repeatability and possibility to keep track on every single droplet and thus perform numerous amount of independent experiments are just some of them. In addition, low reagent consumption facilitates experiments with rare, expensive or dangerous substances. The limited amount of produced emulsion is partially possible to solve by increasing the frequency of droplet production and

¹⁴ The most efficient emulsifier is in most cases a blend of various basic pure emulsifiers.

parallelization. However, this is usually not a bottleneck as the droplet formation rate is nowadays well ahead of detection techniques [118,121]. The droplet formation methods can be both sequential and continuous. The sequential methods, known also as drop-on-demand, are relatively rare [10,14,144]. The continuous droplet production methods are widely used and there are many reviews covering this area [10,11,118,120,123]. Four different configurations are used for continuous droplet production.

Co-axial production

This method arises from fluid flows in capillaries and was the first one used [121]. A co-axial set of capillaries (FIGURE 4.4(a)) brings the liquids to the place of droplet formation, with the innermost capillary carrying the liquid to be dispersed first, and the outermost capillary carrying the continuous phase. This system is the most complex for manufacture in small scales but allows easy creation of complicated multiple emulsions [145].

Step-emulsification

A laminar co-flow of phase to be dispersed confined from both sides by continuous phase is brought through a step-like opening to a deep and wide reservoir. The abrupt change of the confining geometry induces droplet break-off (FIGURE 4.4(b)). The produced droplets are usually smaller than the reservoir and behave differently compared to the confined regime. The step-emulsification technique is able to produce highly monodispersed droplets at unprecedented rates (up to MHz) [12,14,146-149].

T-junction

The droplet formation is induced in the perpendicular intersection of the channels with continuous phase and phase to be dispersed (FIGURE 4.4(c)). The tip of the to-be-dispersed phase enters the straight channel with continuous phase. The induced pressure gradient and shear force push the tip down the channel, which causes thinning and consequent break of the dispersed phase into droplet. The production of droplets in T-junction does not reach the high formation rates or monodispersity of other systems, however, relatively stable droplet formation can be reached at small flow rates, where other configurations do not work [119,139,141,150-152].

Flow-focusing

The continuous phase symmetrically acts on the flow of the phase to be dispersed as they are forced through a narrow nozzle in the device (FIGURE 4.4(d)). The droplet formation occurs in the point of the highest shear stress, usually in the narrowest point of the nozzle. The symmetry of the situation leads to increased droplet production stability, rate, and monodispersity compared to the T-junction [140,150,153-156].

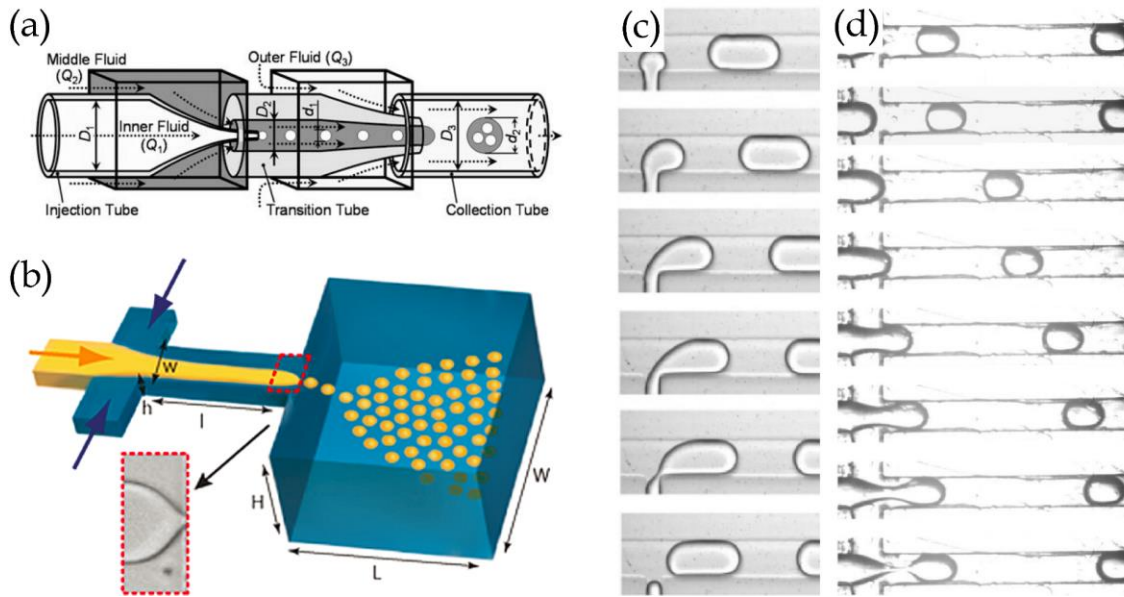


FIGURE 4.4: Different passive geometries used to produce droplets in microfluidic system: (a) co-axial, (b) step-emulsification, (c) T-junction, (d) flow-focusing. Figure (a) reprinted with the permission from [143]. Copyright John Wiley and Sons, 2007. Figure (b) reprinted with permission from [145]. Copyright 2010 American Chemical Society. Figure (c) reprinted with permission from [150]. Copyright 2012 by the American Physical Society. Figure (d) reprinted from [153], Copyright 2012, with permission from Elsevier.

4.4.3 Compartmentalization

Reliable compartmentalization of the experimental reagents is an essential step for quantitative experiments. The encapsulation of different elements like microbeads, cells, DNA, or other molecules is governed by the same rules in the randomly populated liquid phase. The number of encapsulated elements follows the binomial distribution. For rare events, like a single element encapsulation, the binomial distribution converges to Poisson distribution [118,144]

$$P(k, \lambda) = \frac{\lambda^k e^{-\lambda}}{k!}, \quad (4.16)$$

where P is the probability of encapsulation, λ average number of encapsulated elements per one droplet, and k the number of elements in the droplet. The λ is a variable, tunable with the concentration of the phase containing encapsulated elements. The highest number of droplets encapsulating exactly one element is found at $\lambda = 1$ (37 %) but for the price of specificity as the number of droplets containing more than one element is 26 %. Lowering the λ decreases the number of droplets with multiple elements, however, it increases the number of empty droplets leading to dropping number of executable experiments (FIGURE 4.5). The importance of exactly single element encapsulation is the parameter leading to the choice of λ , as it is a trade-off between too many empty droplets versus too many droplets occupied with multiple elements. To improve the probability of exactly single element encapsulation, several approaches were reported, using either exact geometrical positioning of the units prior to the encapsulation

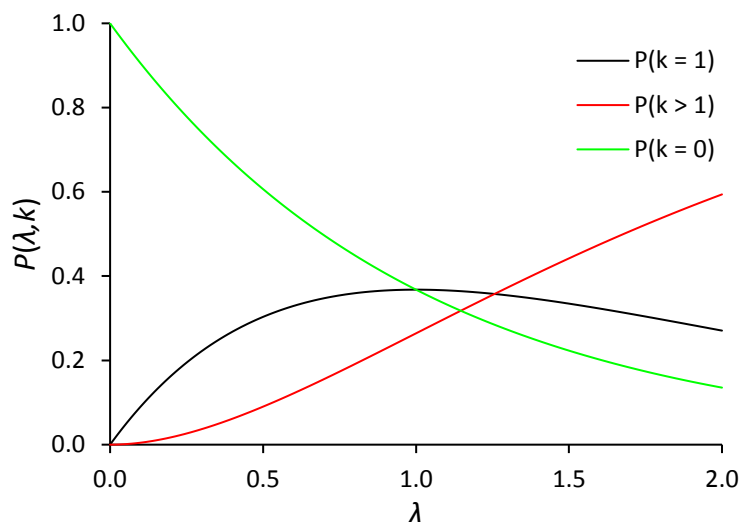


FIGURE 4.5: The probability of having zero, exactly one, and more than one units encapsulated in one droplet on the average number of encapsulated units per one droplet λ (concentration of the phase carrying units to be encapsulated).

beating the random appearance, or post-encapsulation sorting of the droplet with exactly one unit [120,144]. Their employment is, however, strongly limited for big elements and for systems, where contribution from every element is recognizable, respectively.

4.4.4 Droplet trapping

Several operations on the microfluidic chip require either the whole flow including droplets to be stopped or only the droplets to be stopped while the continuous phase keeps flowing. The reasons vary widely, from prolonged time for droplet (content) characterization to long on-chip synthesis or incubation. Numerous active protocols were reported, including optical tweezers, magnetic, electrostatic or dielectrophoretic traps, just to name a few [118]. Also, mechanical stopping of the flow can be used in rigid microfluidic systems [157]. Nevertheless, a vast majority of the trapping strategies use complex channel patterns utilizing the surface tension of confined droplets [158-163]. The existence of an additional pressure drop over every fully confined droplet [128,130] points at viscous forces acting at the channel surface as the droplet tries to minimize its surface energy and become spherical. If the geometry of the channel locally allows the droplet to minimize its surface energy and the continuous phase to bypass it, the droplet will stay trapped at that place. The droplet leaves the trap only when it receives energy large enough to increase the surface energy back to the confined regime.

4.4.5 Droplet content characterization

Various analytical techniques have been used to detect and/or characterize the encapsulated content of the droplets [118,164,165]. The used method must be tailored for the microfluidic system and analyzed reagents. The methods can be classified to several categories based on the physical principle. The imaging-based techniques utilize optical detection often linked to pattern recognition

automated software. Bright-field microscopy, conventional fluorescence microscopy and FTIR¹⁵ are examples from this category. The laser-based molecular spectroscopy is based on laser excitation and collection of signal originating from consequent physical process. These processes include laser-induced fluorescence, fluorescent resonant energy transfer, fluorescence correlation spectroscopy, Raman spectroscopy, and surface-enhanced Raman spectroscopy. The list of detection techniques continues with electrochemical analysis, capillary electrophoresis, mass spectrometry, nuclear magnetic resonance spectroscopy, absorption spectroscopy, and chemiluminescence. Every technique mentioned above has its pros and cons and its implementation is part of the design process of a microfluidic system.

4.4.6 Droplet sorting

A large fraction of microfluidic devices take their advantage over conventional systems by possibility of precision droplet manipulation at high frequencies. The main application of droplet manipulation is in the sorting, where mixture of different sized droplets, particles, or droplets occupied with different content can be reliably sorted. Both passive and active sorting systems have been developed and used in microfluidic devices. While passive approaches utilize the hydrodynamic forces and can be used to sort droplets only if they differ in size or density [166], the active sorting protocols allow to execute sorting based on any measurable characteristic of a droplet. Some of the active sorting methods can directly respond to the droplet characteristics such as magnetic [167] or electrostatic sorters [168] but their utilization is rather limited as they work only with droplets, which carry magnetic or electrically charged components, respectively.

The most versatile and thus most used is a group of sorting techniques, which are independent on the droplet content. They are usually linked to some of the characterization methods and the result of the characterization directly triggers the sorting mechanism for a specific droplet. The used methods are mechanical valves [169], thermal methods [170], electro-osmosis [171], optical [172,173] and acoustic [174,175] methods, and dielectrophoresis [12]. The developed sorting approaches covers a wide interval of droplet sizes (down to 4 μm) and sorting frequencies (up to 30 kHz) [144,176]. The deployment of a particular technique is dependent on the design of the experiment and this field is well covered by many review papers [10,11,118,144,177].

4.4.7 Droplet stability

The utilization of droplets as sealed microreactors is conditioned by their stability. The presence of small droplets of one phase in another is out of thermodynamic equilibrium and the preservation of the large area interface is energetically unfavorable and naturally results into coalescence. The creation of droplets in a microfluidic device is ruled by liquid-solid interfacial tension and droplets are stable as long as they are kept confined and separated. However, coalescence occurs

¹⁵ Fourier-transform infrared spectroscopy

immediately after the encounter between two droplets. An additional energy barrier bringing the emulsion into a metastable state can be created by the presence of an emulsifier, which decreases the interfacial tension between continuous and dispersed phase by forming an interlayer on their interface [10,178].

The choice of proper emulsifier depends on various factors such as the characteristics of both dispersed and continuous phase, material of the microfluidic device and the nature of the experiment itself. The choice of the emulsifier usually follows the rules of HLB system [136,137]. With the advent of microfluidic technology, new emulsifiers are developed especially for microfluidics [118,179], covering special needs of new applications, especially biocompatibility [178]. The concentration of emulsifiers used in microfluidic experiments varies across the literature. There is an agreement, however, that the concentration fully protecting from coalescence is way above CMC and that the creation of the emulsifier layer on the interface between the droplet and the continuous phase takes much longer time than in the non-confined regime [178,179]. This time must be taken into account when designing the microfluidic device and droplets must be protected from touching each other for the time of settling.

5 Manufacture of a microfluidic system

The goal of the first phase of the experimental section was to develop a procedure for the manufacturing of the microfluidic system, a novel platform for broad in-house use, aiming for the femtoliter droplet production and manipulation for single molecule (nanotube) spectroscopy and sorting. The experiments follow experimental findings from two consecutive Master theses by Rojas [16] and Pekala [17], where the fabrication of glass channels and their miniaturization and flow of liquids were investigated, respectively. Despite the knowledge from these groundworks, the miniaturization of the system and extreme requirements for precision and presence of defects led to the development of whole new set of procedures in the glass microfabrication.

5.1 The material

The manufacture of the microfluidic chip generally consists of two steps. The first is manufacture of open channels in a suitable *substrate*, followed by covering the open channels with a *coverslip*. A system of fully closed channels is created in this way and only very rare exceptions to this process can be found in the field of nanofluidics [180]. While the coverslip is usually made of glass, chosen for the obvious need of light microscopy to observe the phenomena at microfluidic scale, the choice of substrate materials is strongly dependent on the application and manufacturing possibilities.

Microfluidic devices can be manufactured from silicon [141,150,181] and glass [142,171,182,183], however the majority is made from polymers. The most used is polydimethylsiloxane (PDMS) [12,14,146,152,153,166,170,174,175], but acrylated urethane [119], poly(methyl methacrylate), polycarbonate and polyethylene terephthalate [121,184], and UV curable polymers and thermoplastic polymers [123] are also used. Especially the PDMS possess many advantages over other substrate materials, which makes it a popular choice. The chips made of PDMS are durable, flexible, inert, non-toxic, biocompatible, easy to handle, accessible and inexpensive [121,185], and allow rapid prototyping by molding techniques [123]. The elastomeric nature of PDMS offers itself for manufacture of on-chip active elements like micropumps and microvalves and the permeability to gases and water makes it the only material suitable for microfluidic treatment of living mammalian cells [9].

The microfluidic chips made from silicone quickly sank into oblivion, mainly due to their price and opacity. With more complex systems requiring

electrodes, their semiconducting properties also became a challenge [9]. Glass, however, is the most used material for equipment of chemical laboratories. It carries several properties, which makes it of high importance also for nowadays microfluidics. The manufacture shares many techniques with well-known silicon processing: it is cheap, accessible, and transparent. The glass, in contrast to PDMS, does not dissolve in acids and bases and does not swell in presence of organic solvents and mineral oils [121,185]. The non-permeability to water and gases allows experiments with W/O emulsions in glass chips, while the water droplets in PDMS usually diffuse to the chip material in short time [184] and basically prevent use of PDMS for this purpose. The well-defined surface of glass and its well established covalent surface modification procedures are crucial for stable droplet formation and manipulation, especially in miniaturized devices, while surface modification of PDMS is still rather tricky [123]. The glass, due to its rigidity, allows manufacture of channels with low depth to width aspect ratio and allows experiments with pressures, where elastomeric materials would collapse or rip. Glass is a perfect material for light spectroscopy due to its transparency in a wide interval of wavelengths. Its background fluorescence and autofluorescence is negligible compared to PDMS, which makes it an ideal material for chemiluminescence and fluorescence spectroscopy. Glass has also high resistance to mechanical stress and high temperatures, good thermal stability and low thermal expansion coefficient [121,185] allowing experiments with exotic parameters. Insulating properties and rigid structure predispose glass for easy implementation of electrodes by methods known from silicon processing, while alternative approaches has to be applied for elastomeric materials. Last, but not least, one common drawback of both glass and PDMS chips must be mentioned. The low heat conductivity leads in both to large temperature gradients for certain operations like application of high electric fields or focused laser beams [184].

The glass was envisioned as the substrate of choice [16,17] for the microfluidic system developed for this project. The suitability for optical spectroscopy and precise manufacture of micrometer-sized structures, well-defined surface and possibility of surface modifications, chemical stability, and possible applicability of high pressures were the main reasons why glass was prioritized over other substrate materials. The Menzel-Gläser 20x20 mm² #5 soda-lime glass coverslips were used for fabrication of microfluidic chips throughout the whole project. The soda-lime glass consists of roughly 73 % SiO₂, 14 % Na₂O, 9 % CaO, and 4 % MgO with trace amounts of Al₂O₃, Fe₂O₃, K₂O, and TiO₂ [17,186]. The main advantage of soda-lime glass, compared to quartz or borosilicate glass is the availability, low price and low transition temperature, advantageous for the bonding process.

5.2 Inlets and Outlets

The connection of microfluidic channels to the surface of the chip is often a highly challenging task, especially for miniaturized devices. In devices aiming for femtoliter droplet production, even a very small macroscopic hole will most

likely have volume larger than the whole network of channels, which can negatively influence the responsivity and stability of the system. Therefore, new approaches have to be applied for manufacturing the holes for fluidic ports. Several drilling strategies were developed, including diamond tip conventional drilling, sand blasting, wet and dry etching, and laser induced ablative drilling [184]. While the first three are not suitable for preparation of microscopic holes, dry etching and laser induced ablative drilling are able of manufacturing structures with depth to width aspect ratio $\gg 1$, hence producing deep holes with microscopic diameter.

Since the dry etching technique is tricky when it comes to masking and with available instrumentation it would be unreasonably time-consuming, the laser induced ablative drilling technique was used. A beam from Lambda Physik OPTex excimer laser (KrF, 248 nm) was tightly focused on the surface of the glass. The number of pulses necessary for drilling through the glass varies with time as the active medium ages. Nevertheless, the number was in the interval from 1000 to 2500 pulses per hole. The ablative drilling is a quite violent process causing high temperature gradients at the place of drilling. This causes swelling of the hole edges and deposition of ablated material around the edge from the side adjacent to the laser (FIGURE 5.1(a)). On the other side of the glass, a 2- to 3-times larger piece of glass than the hole diameter is cleaved away (FIGURE 5.1(b)) close to the end of the drilling process. The surface of the glass can be protected from deposition of the ablated material and cleaving can be minimized by regular duct tape on the glass surface, nevertheless, the swelling of the hole edges is always present. In this way, the position of the channels is effectively ruled on the other side of the glass slide as the elevated part negatively influences both the etching mask quality and proper closing of the channels.

5.3 Lithography technique

The transition of desired channel layout on the glass prior to the actual micromachining can be achieved in several ways. Depending on the size of

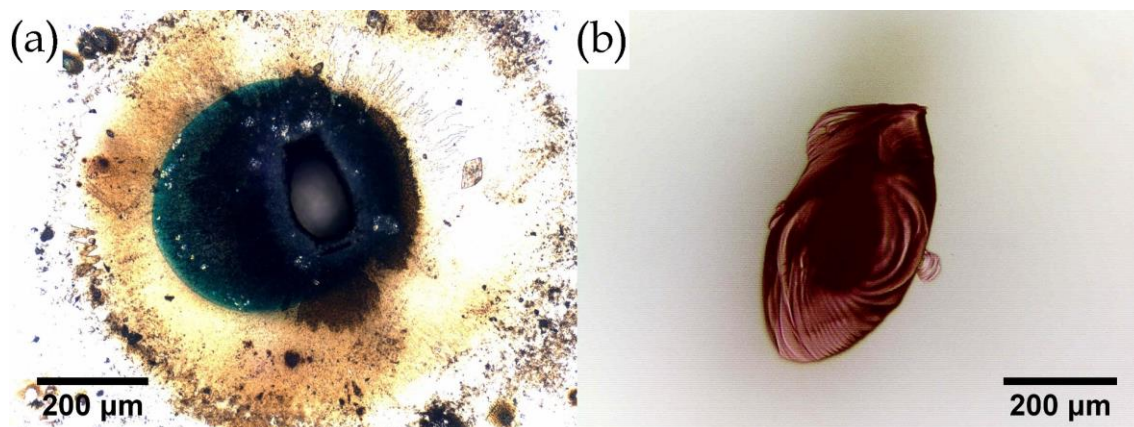


FIGURE 5.1: The inlet or outlet hole drilled by laser induced ablative drilling: (a) adjacent and (b) opposite side to the laser (unprotected drilling).

manufactured structures, sand blasting and laser ablation [187], direct MeV ion beam writing [16,188], and wet or dry etching [184] can be used in order to achieve desired resolution. For the purpose of femtoliter droplet microfluidic system, only etching techniques can achieve the required precision. Both wet and dry etching need etching mask to allow access of the etchant to the glass in places of planned channels while protecting it elsewhere.

The transfer of the channel layout to the glass is done via resist technology. A layer of resist is spread on the substrate and particular technique is used to change the chemistry of the resist in desired places. The chemically altered resist is then removed in developer and openings in the resist layer allows to reach the glass underneath. Photolithography is widely used for manufacturing microfluidic channels in glass [185,186,189-192] as it is much less demanding on the instrumentation and the photoresist exhibits very good masking properties – resistance against etching. In addition, photolithography is much faster compared to other lithographic techniques for manufacturing of repetitive patterns. In-house photolithographic equipment has, however, limited resolution ($>0.5\ \mu\text{m}$) and the time-consuming manufacture of the photolithographic mask is a significant disadvantage for projects, where the channel layout is constantly being developed. Since the development of experimental layouts with dimensions hitting maximum resolution of the photolithographic tool was one of the main parts of this research project, electron beam lithography (EBL) was chosen to transfer the layout from CAD software onto the glass substrate and PMMA A4 950¹⁶ was the used EBL resist throughout the whole project.

5.4 Instrumentation

The manufacture of precise micrometer-sized structures puts high requirements on clean environment and good control over surface cleanliness. Therefore, all the following steps were performed in ISO 5 clean room. Balzers Baltec BAE 250 e-beam evaporator was used for thin film deposition, Oxford Instruments Plasmalab 80 Plus for plasma cleaning and reactive ion etching (RIE), Raith eLine for EBL and imaging, and Carbolite CTF/12/65/550 tube furnace for thermal assisted direct bonding (TADB). In addition, common equipment of clean room was used including fume hoods, flowboxes, hot plates, bath sonicator, optical microscope, profilometer, and all the chemicals mentioned below. The values stated in the text below are readouts from the instruments as no special calibration was performed for the purpose of these experiments.

5.5 General description of the process

The process of glass microfluidic chips manufacture is known from the available literature [184-186,188,193]. These papers, however, describe manufacture of

¹⁶ Poly(methyl methacrylate), 4 % (w/w) in anisole, 950 refers to chain length.

microfluidic channels in dimensions at least 1 order of magnitude larger than those needed for droplet production on a femtoliter scale. In addition, glass is not the most frequently used clean room material and the processing steps are not so well established as *e.g.* silicon. Therefore, many manufacturing steps had to be learned or improved to reach the required precision. In addition, great care must be taken during the whole process to avoid any possible contamination of the substrate. The general procedure for creating structures in the glass usually goes as follows:

1. substrate cleaning
2. etching mask deposition
3. lithography
4. etching
5. etching mask removal
6. closing the channels

5.6 Substrate cleaning

The glass substrate must be perfectly clean in order to achieve good adhesion and quality of the etching mask leading to defect-free etching. Sonication in hot acetone and mechanical scrubbing with a cotton tip effectively removes leftovers from the tape protecting the glass during laser drilling, fingerprints and other residues. The glass surface is then rinsed with IPA¹⁷ and dried with N₂ flow. This is followed by chemical removal of organic residues either by RIE¹⁸ O₂ plasma cleaning (120 s, 200 W, 50 sccm¹⁹, 40 mTorr) or by etching in Piranha solution (H₂SO₄:H₂O₂ - 3:1) for 1 hour at 80 °C. While after the plasma cleaning the substrate is immediately ready for metal evaporation, the Piranha etch was always followed by 3 min sonication in deionized water (dH₂O) to remove the Piranha residues completely. Despite the similar oxidation mechanism, the Piranha etch was found to be much more effective in leaving the glass surface without any contamination, which can be also partially linked with the post-treatment sonication. This was confirmed both visually and by dark-field microscopy.

5.7 Etching

When it comes to precise manufacture of micrometer-sized structures on glass, both dry and wet etching techniques can be applied [194]. Either technique brings certain pros and cons, which impact on the result. Besides the technical parameters described in the following paragraphs, there are two main differences in the final manufactured structures. Wet etching in general provides very smooth

¹⁷ isopropyl alcohol

¹⁸ reactive ion etching

¹⁹ standard cubic centimeter per minute

etched surfaces, while RIE process often suffers from high surface roughness [187,195], which is unacceptable for smooth flows in microfluidic confined regime. More importantly, wet etching is in its nature isotropic, while the RIE process can be highly directional and hence anisotropic. This becomes of crucial importance for the manufacture of very small structures or structures with depth to width aspect ratio ≥ 1 , where the mask underetching [187,191,193,196] significantly alters the result (FIGURE 5.2, see also FIGURE 5.7(top left)). During the development of the manufacture protocol for channels in the glass, two independent processes were developed and tested. The protocol was developed for channel geometry able to confine droplets with volume of about 30 fL – the volume related to the excitation capabilities of the fluorescence microscope. Hence, the procedures are tailored for manufacture of channels with characteristic lengths, eq. (4.2), down to $\approx 1.3 \mu\text{m}$ and with the depth not exceeding $6 \mu\text{m}$.

5.7.1 Dry etching

RIE is a method of dry etching, especially popular in microfabrication. It utilizes chemically reactive plasma to react with the material. The plasma is usually generated under low pressure by radio frequency electromagnetic field. The vacuum pumping not only allows stabilization of the plasma but also removes the products of the etching. RIE etching of SiO_2 using fluoride-based precursor gas (SF_6 , CF_4 , CHF_3 , or C_4F_8) is a well-known process [184]. However, the use of the same chemistry is relatively limited for glass as it contains non-negligible amounts of oxides (Na_2O , CaO , and MgO), which creates non-volatile compounds during the etching [197,198]. They redeposit on the glass surface, which results in an effect

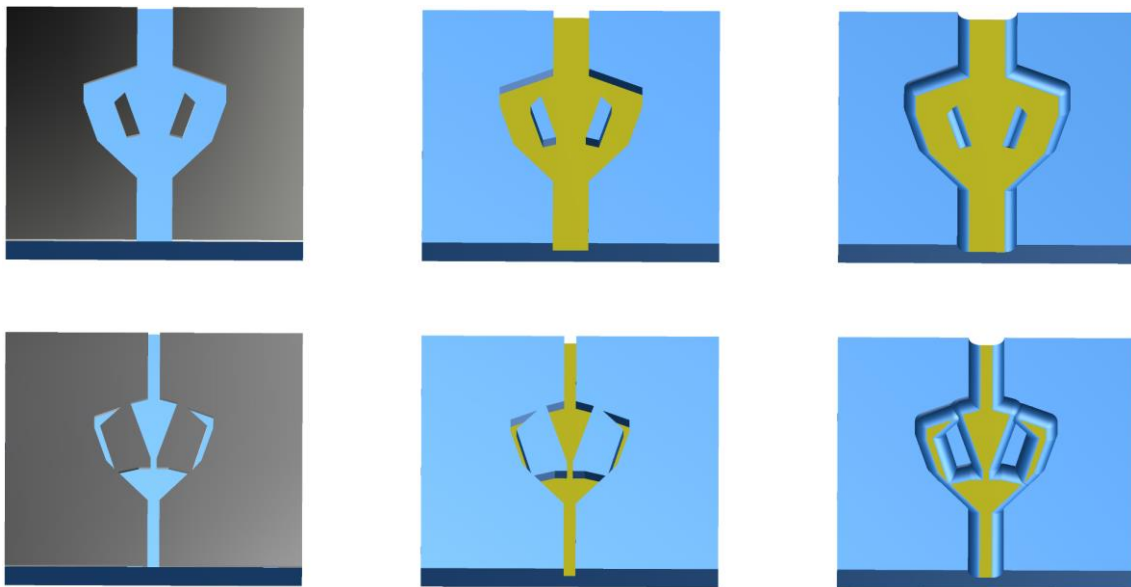


FIGURE 5.2: Different masking strategies (left) for anisotropic dry (middle) and isotropic wet (right) etching. The mask designed for dry etching (top left) results in well-shaped structures when dry etching is used (top middle), while the same mask would result in destroyed structures if it would be used for wet etching (top right). The mask designed for wet etching (bottom left) would result in incomplete structures if it would be used for dry etching (bottom middle), while the same mask result in well-shaped structures when wet etching is used (bottom right).

known as micromasking. This leads to significant reduction of the etch rate and high surface roughness as the non-volatile compounds redeposit on the glass surface and prevent further etching.

The way-around is to increase the ratio of physical etching (sputtering) compared to chemical etching [193,199,200]. The predominant physical etching, however, requires low chamber pressure conditions to work, which effectively reduces the density of the plasma. The magnetron RIE [187,201,202] or ICP-RIE²⁰ [197,198,201] offers significantly increased plasma density, but are generally less directional compared to basic RIE. All three techniques are, in addition, effectively limited by the amount of energy transferred to the etched substrate. Physical sputtering combined with poor heat conductivity of the glass creates large temperature gradients, decrease the control over the process and decrease mask selectivity [184]. Nevertheless, interesting etching rates of about $0.6 \mu\text{m min}^{-1}$ [201], $0.75 \mu\text{m min}^{-1}$ [197], and $1.2 \mu\text{m min}^{-1}$ [203] were reported for ICP-RIE process. The surface roughness, however, remains an issue as it is influenced by the instrument, chosen process, and glass composition itself [195] and its suppression requires careful fine-tuning of the process parameters.

The dominance of physical etching creates increased requirement on the masking material as the chemical selectivity plays negligible role. Hence, the mask must be very durable to resist the mechanical sputtering. Several masking materials are mentioned in the available literature with the clear preference for hard metals like Cr [195] or Ni [187,193,195,201], more rarely alumina, silica, or silicon [195,198]. The influence of resist is usually neglected as it gets quickly sputtered away. Even with hard metal mask, the selectivity is relatively poor for basic RIE etching as the physical sputtering is predominant, which results to the need for thick masks. ICP-RIE offers much better mask selectivity, reported to be close to 1:25 [203], 1:30 [187], or even infinity [197].

The mask

The prevalent physical sputtering require relatively thick etching masks. Various layered metal combinations were tested including Cr, Cr/Ni, Cr/Au, Cr/Au/Cr, and Cr/Ni/Cr. From those, the Ni mask showed the highest durability in agreement with the literature, while Au as a masking material was not found to be able to stand the dry etching process. Cr showed reasonable durability, however, the evaporated layer on the glass tend to possess a dense network of cracks as a result of internal stress (FIGURE 5.3(a)). After the removal of the resist layer, the RIE is able to etch glass through those microcracks and create a random pattern of undesired channels (FIGURE 5.3(b)). Since some issues with Ni adhesivity straight on the glass surface were observed, a thin Cr layer was always evaporated straight on the glass surface, followed by a thick Ni layer. For etching of $4 \mu\text{m}$ deep channels, a 10 nm Cr + 250 nm Ni mask was removed completely during the RIE process, but 10 nm Cr + 350 nm Ni lasted without problem. It means, that the Ni selectivity for the process with used parameters is better than 1:12, which is already a reasonable value for etching of shallow structures.

²⁰ inductively coupled plasma RIE

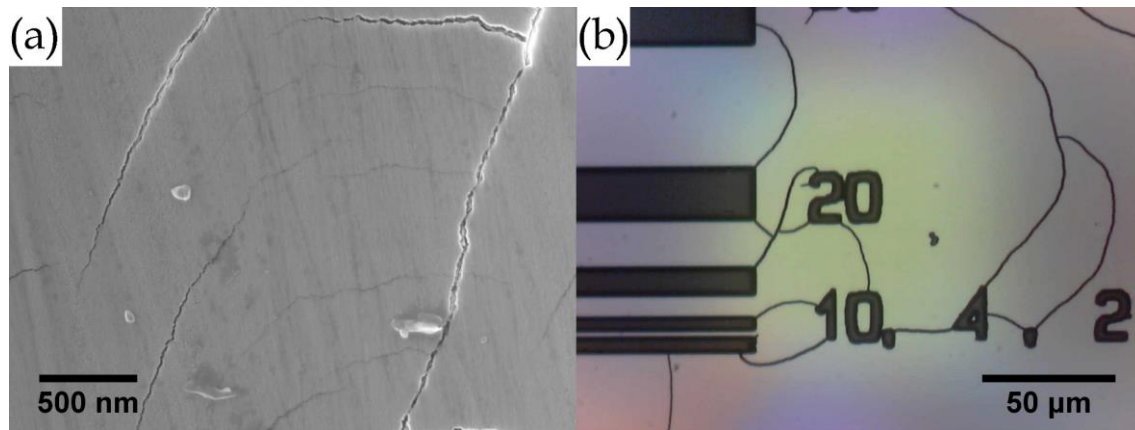


FIGURE 5.3: (a) SEM image of microcracks in 80 nm Cr layer evaporated on the glass. (b) RIE etching through the dominant microcracks in 200 nm Cr layer (sample Real_1_200Cr).

Transfer of channel layout

The EBL resist was spin coated on the evaporated metal layer at 3000 RPM for 60 s, resulting in a uniform layer with a thickness of about 200 nm. Spin coating at lower RPM resulting in thicker resist layer or hardbaking to increase the resist durability did not show any significant improvement of the resist lifetime during the RIE process. Since thicker resist layer generally decreases the resolution of EBL and post-EBL hardbaking often results in filling of the exposed structures by molten resist, the spin coating process was not altered. The exposed layout was developed in PMMA resist developer for 40 seconds.

The etching of the metal layers through the openings in the resist brought the need of experimental testing of suitable etchant. The Nichrome etchant (Sigma Aldrich) could not be used as it etches Cr at much higher rates than Ni and while the thick Ni layer is removed through the openings in the resist, the metal layer is significantly peeled off from the sides of the chip, where the etchant has access to the Cr interlayer. HNO_3 is known as an effective Ni etchant. It does not react with Cr, but it attacks PMMA at high concentrations. While the HNO_3 concentration was found to be a crucial parameter for the survival of the resist layer, elevated temperature was found to increase the Ni etch rate but not influence the survival of the resist layer. In addition, the increase of the water content increases the surface tension of the etchant, which struggles to wet structures via small openings in the hydrophobic resist. A trace amount of common cleanroom detergent was found to effectively decrease the surface tension. The optimal etchant composition was found to be 10 % (v/v)²¹ HNO_3 in dH_2O with a drop of the detergent. The etch rate was found to be $\sim 100 \text{ nm}\cdot\text{min}^{-1}$ at 70°C , leading to removal of the Ni layer through openings in resist in less than 4 minutes, while the first damage caused to the resist layer appeared well after $>10 \text{ min}$.

The Cr layer was then etched by standard Chromium etchant or Nichrome etchant (both Sigma Aldrich), which have great selectivity towards the resist and leave the etched surfaces very clean. When none of those were available, the home-made mixture of one part of NaOH (25 g in 100 mL dH_2O) and three parts

²¹ volume/volume

of $K_3[Fe(CN)_6]$ (30 g in 100 mL dH₂O) was used at room temperature. The etch rate was found to be $\sim 75 \text{ nm}\cdot\text{min}^{-1}$.

Glass RIE etching

The Oxford Instrument Plasmalab 80 Plus offers only the possibility of basic RIE process with Ar, O₂, SF₆ and CHF₃ process gases. The liquid nitrogen (LN₂) cooled stage is a big advantage for keeping the sample temperature under control. Both SF₆ and CHF₃ should be suitable for etching of the glass, while Ar or O₂ are used for better control of the chamber pressure or fine-tuning the quality of the etching process. Various combinations of chamber pressure, gas flow rate, ionization power²², and co-flowing gases were used for CHF₃. The maximum achieved etch rate was $\sim 12.8 \text{ nm min}^{-1}$ in relative agreement with values reported elsewhere [195,199]. This etch rate, however, was achieved at low chamber pressure, which causes unequal etch rate across the sample due to uneven pumping speed. Even on small 20x20 mm² sample, the etch rate on the edges of the sample ($\sim 12.8 \text{ m min}^{-1}$) is almost three times the etch rate in the middle of the sample ($\sim 4.5 \text{ nm min}^{-1}$). The settings resulting in even etching across the sample did not exceeded 3 nm min^{-1} , a practically useless value for the etching of structures with depth up to 6 μm .

Dry etching with SF₆ showed much higher etch rates. The optimal parameters of the process, the chamber pressure (FIGURE 5.4(top left)), the flow rate of the precursor gas (FIGURE 5.4(top right)), and the ionization power (FIGURE 5.4(bottom left)) were investigated. Low chamber pressure obviously increase the etch rate in agreement with [201], down to 15 mTorr. The amount of available gas is so low below this value that the plasma does not ignite, and no etching is observed. The SF₆ flow rate at constant pressure exhibits optimal value of 37 sccm with etch rate dropping for both higher and lower flow rate. This is related to proper ionization and proper utilization of ionized molecules before they are pumped away from the chamber. The etch rate was found to be different in the middle and close to the edges of the sample, similar to CHF₃ etch. The difference was, however, much smaller. The uneven etch rate was found to be dependent on ionization power with a value of 237 W, where it balances.

A challenge often reported together with RIE etching of narrow structures in glass is creation of so-called micro-trenches – deeper etched areas of the desired structure right beside the vertical walls (FIGURE 5.5(a)–(b)). The micro-trench depth compared to the depth in the middle of the channel was found to be dependent on so-called self-bias voltage. Self-bias voltage is a result of electron build-up on the powered electrode of the RIE instrument. It efficiently drives the physical etching as the electron build-up on the powered electrode attracts the ions towards the sample. Its value is influenced by chamber pressure, ionization power and type of process gas. The difference in depth of the channel and the micro-trench drops with increasing self-bias voltage (FIGURE 5.4(bottom right)). The self-bias voltage at optimal etching parameters is $\sim 500 \text{ V}$, thus reaching the minimal value. The minimization of micro-trenches at high self-bias voltages points at their origin in chemical etching.

²² Also known as RF forward power.

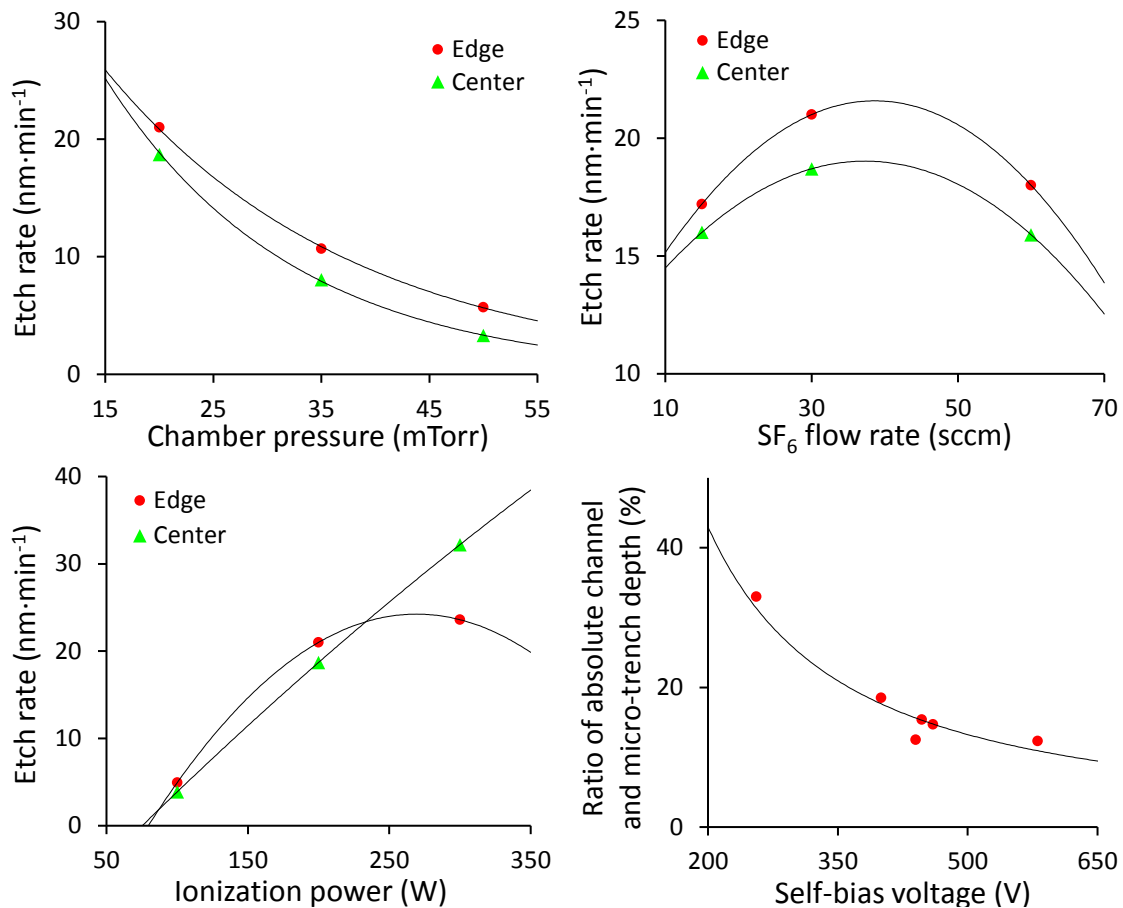


FIGURE 5.4: The dependence of SF₆ RIE etch rate on different parameters measured on the edge and in the middle of the sample. (top left) Dependence on chamber pressure at 30 sccm, solid lines are least squares fits of an exponential functions. (top right) Dependence on flow rate at 20 mTorr chamber pressure, solid lines are least squares fits of a quadratic functions. (bottom left) Dependence on ionization power 30 sccm at 20 mTorr chamber pressure, solid lines are least squares fits of a quadratic functions. (bottom right) The difference in depth of channels and micro-trenches as a function of self-bias voltage, solid line is least squares fit of a power function.

The optimized parameters (process gas SF₆, flow rate 37 sccm, chamber pressure 15 mTorr, ionization power 240 W) led to improved etch rate >26 nm min⁻¹ uniformly over the whole sample. This etch rate allows etching of 4 μm or even 6 μm deep channels in reasonable time of 150 min or 230 min, respectively. The surface roughness, however, remains an unresolved issue as it was shown later in microfluidic tests (FIGURE 5.5(c)–(e), see also FIGURE 5.8(a)). Also, a light lateral underetching takes place (about 10 % of the full depth), which can be of a critical importance for high precision geometries. An ICP-RIE update addresses all three issues – micro-trenching, surface roughness, and underetching. Nevertheless, even with basic RIE some optimization can be done.

As discussed earlier, the physical sputtering must outweigh the chemical etching to enhance the isotropy of the process and avoid micromasking [203]. However, the chemical etching cannot be totally restricted as pure physical etching works at low etch rate, significantly degrades the etching mask selectivity and due to poor heat conductivity of the glass leads to large temperature

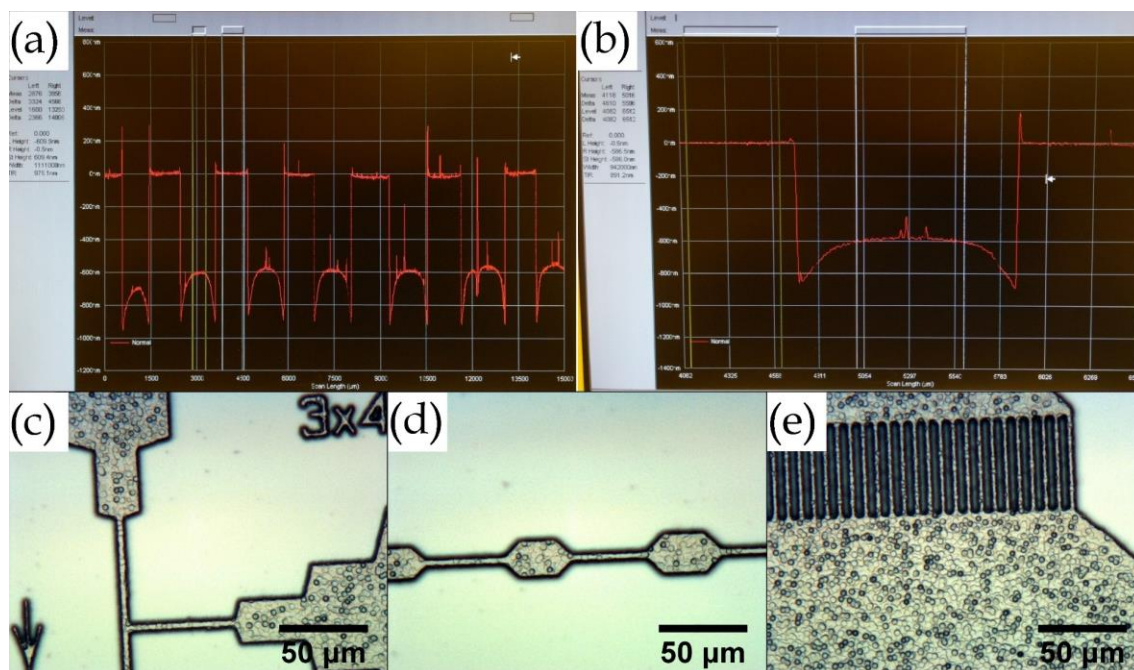
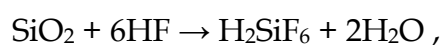


FIGURE 5.5: (a)-(b) Micro-trenches at the edges of the dry etched channel. A cross section view. (c)-(e) Surface roughness of 4 μm deep channel (sample RIE5).

gradients, possibly leading to fracture of the sample [184]. The ratio of physical etching can be enhanced by increase of self-bias voltage [201] or by change of the process gas chemistry. While the self-bias voltage is dependent on pressure in the chamber and the ionization power and both of them have given optimal values derived from other characteristics, the addition of co-flowing gas changes the ratio of molecules chemically and physically reacting with the glass. The addition of O_2 was shown to even aggravate the underetching and micro-trenching [199] by creation of etch catalyzing particles from the mask material, which is in accordance with our observations. On the other side, the addition of up to 50 % Ar was shown to decrease both the surface roughness [203], micro-trenching and underetching [197]. In addition, the physical etching can be further enhanced by applying external bias on the powered electrode [203]. Further investigation would be needed here, to find the optimal parameters for improved quality of the dry etching process.

5.7.2 Wet etching

The excellent chemical durability of glass makes it an ideal material for laboratory glassware. On the other hand, the same durability limits the possibilities when using glass as a substrate. From the liquid chemicals, only fluorine based substances, mainly hydrofluoric acid (HF), are known to etch glass at applicable rates. The overall reaction of HF with SiO_2 goes as follows [204]:



with the actual reaction path being relatively complex [205]. The etch rate is strongly dependent on HF concentration [204] and glass composition, and can be

controlled by simple dilution with H₂O. The etch rate is also influenced by factors like temperature, stirring, sonication and glass annealing prior to the etching [184].

In the applications with extreme requirements for precision a mixture of buffering agent, like NH₄F or HNO₃ [185], and HF is used, resulting in improved control over the etching process. Common glass contains besides SiO₂ also other oxides, which form products insoluble in HF/H₂O during the etching. The addition of HCl or H₃PO₄ to the HF/H₂O mixture removes the insoluble products and further improves quality of the etching [184,190].

The mask

The material for etching mask used for wet glass etching must fulfil only two basic requirements, stability in the etchant and good adhesion to the glass surface. Many mask materials have been reported, including photoresist, amorphous and crystalline Si, Ag, Mo, Ti, and multilayers Cr/Au and Cr/photoresist [196]. The thin layer of masking material must meet several quality criteria including low residual stress, stress gradient, and hydrophobicity [184]. While stress may lead to cracks, which allow etchant to reach the glass and generate pinholes, the hydrophobicity defines if the cracks (or any other imperfections in the resist and mask), if existing, will promote or restrict etchant propagation through them.

The photoresist alone was reported to be sufficient masking material for wet etching of relatively shallow structures in the glass, surviving from 2 minutes in highly concentrated HF [184,206] up to 40 minutes if specially treated and in diluted HF [186]. Thus, also PMMA, the used EBL resist, is expected to provide sufficient protection of the underlying glass as it exhibits good stability in diluted HF [207]. The EBL technique, however, requires a way, how to remove the electron beam induced charge from the sample. A thin metal layer is necessary to fulfill this condition.

The Cr and Cr/Au etching masks show superior stability in both highly concentrated and diluted HF [184,185,189,190] and in multilayer design Cr/Au/Cr/Au were reported to successfully protect glass surface during etching of 500 µm deep holes [191]. This was a reason, why Cr/Au multilayer was used in experiments prior to this work [16,17]. Since Cr exhibits excellent adhesivity to both glass and Au, while Au readily peels off from glass surface, the Cr was always used as an interlayer. It was found early on, that this protocol is overly complicated as only thin Cr layer with EBL resist is able to provide good protection of the glass surface. The adhesivity of the Cr also provides superior protection against notching effects [189]. Both the quality of Cr mask and PMMA layer are then crucial for flawless results of the etching.

Certain residual stress builds up in the evaporated Cr layer, which is obvious from the microcracks on the Cr surface (FIGURE 5.3(a)). It was found, that the size of the microcracks increases linearly with the thickness of the evaporated Cr layer. These cracks then allow HF to reach the surface of the glass in the places where the resist layer is damaged and cause the evolution of pinholes – the biggest issue connected to wet etching of glass. The common way how to obtain thin metal films of better quality is evaporation at 77 K, the temperature of liquid nitrogen. Indeed, both the visual and optical microscope check showed slightly

improved quality of the metal film, however for a price of excessive internal stress. The sharp corners and microstructures etched to the IN_2 Cr layer through the resist act as stress concentrators. In these places, cracks are initiated and propagate away from the desired structure. The HF consequently reaches the glass through the cracks and destroys the fine pattern of the microfluidic channels (FIGURE 5.6(a)). In addition, the Cr mask evaporated on the glass surface cleaned by RIE method showed poor adhesivity and caused wicking of the HF etchant under the mask, causing unpredictable underetching (FIGURE 5.6(b)). Therefore, only 80 nm thick Cr mask evaporated on Piranha cleaned glass at room temperature was used. The mask prepared in this way lasted without problems several consecutive etching cycles with total depth of 12 μm .

The resist quality was found to be the most crucial parameter for positive result of the whole etching process. Most of the failures of the etching could be contributed to improper application of the resist or to its insufficient quality. One of the most obvious problems is linked to old or improperly stored resist. If the resist comes into contact with water, most often from air humidity, the water dissolves in it and evaporates during the post-baking process, creating a number of openings in the resist layer. The openings behave the same way as exposed pattern and the following etching goes through the Cr mask to the glass, creating visually ugly and mostly nonfunctional devices (FIGURE 5.6(c)).

There are several ways how to improve the resist durability. A slower spin coating speed leads to thicker PMMA layer. For PMMA A4 950, 3000 RPM gives resist thickness ~ 200 nm, the 2000 RPM leads to ~ 300 nm, and 1000 RPM to ~ 400 nm. Spin coating at lower speeds does not bring any further improvements as the centrifugal field is not able to rip the excessive resist material from the edges of the sample and the layer becomes uneven. Further thickening of the layer could be done with more viscose resist, like PMMA A7 950 but for the price of decreasing the resolution of the finest structures.

Another improvement of resist durability can be reached by hardbaking. After the EBL process, the resist is heated above its melting point, in the case of PMMA to 190 – 200 $^\circ\text{C}$. This induces both chemical changes in the resist layer leading to its significant hardening [17] and ‘self-repair’ of the liquidized polymer by filling the microdefects and also the microcracks in the Cr mask [206]. Therefore, even if the resist layer is attacked, the Cr layer with filled cracks provides excellent protection from the etchant. The process of hardbaking also causes rounding of the sharp features exposed during the EBL as the round shapes are energetically more favorable for the molten resist (FIGURE 5.6(d)–(e)). This effect becomes even more significant with thicker resist layer. The fine structures can sometimes get filled with the molten resist and lead to failure of the etching (FIGURE 5.6(f)).

The particular set of parameters for resist deposition is dependent on the dimensions and the need for detailed preservation of the structure to-be-etched. In general, the best results are achieved with PMMA A4 950 spin coated at 1000 RPM without hardbaking for the finest structures (~ 1 μm), 3000 RPM with hardbaking for medium-sized structures (>5 μm), and 1000 RPM with hardbaking for the largest structures (>20 μm). These limits often require splitting of the

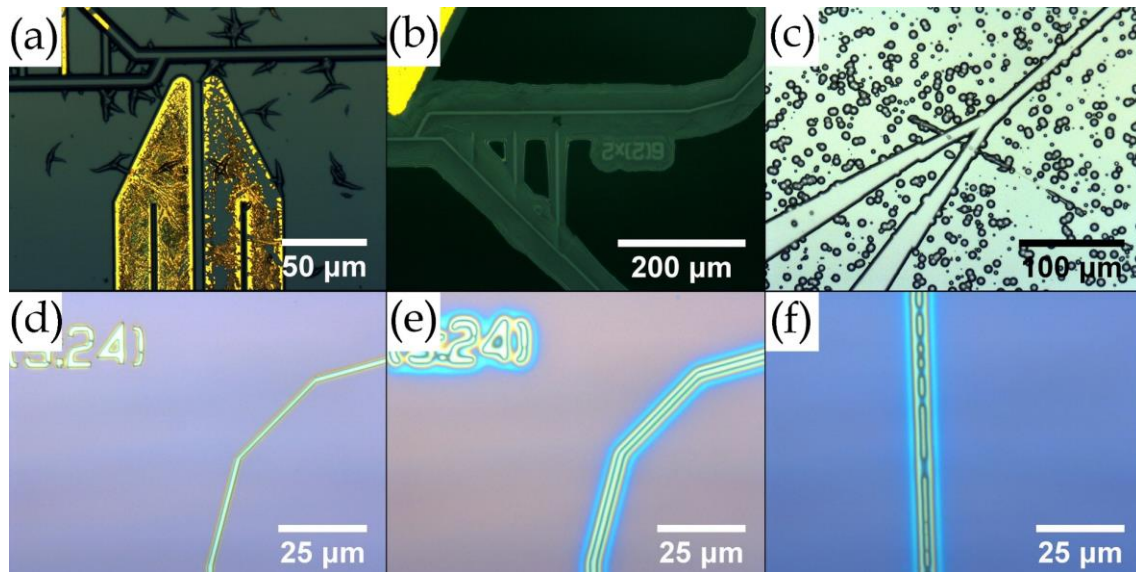


FIGURE 5.6: (a) IN_2 evaporated mask leading to corner induced cracks in the metal mask. (b) Peeling of the Cr mask evaporated on RIE cleaned glass. (c) Pinholes etched through the mask due to poor quality resist. (d)–(e) The effect of the hardbaking on the developed structures. (f) Hardbaking caused failure of the developed structure.

EBL+etching process to several consecutive steps. The areas of the sample, which does not contain any exposed patterns can be additionally protected with ordinary transparent duct tape prior to any etching. This process has been proven to be highly beneficial in order to keep the surface of the glass in perfect condition for the next etching step.

Transfer of channel layout

The transfer of the channel layout was carried out similarly to the process described in dry etching section. The EBL resist was spin coated by the rules listed above, according to the dimensions of the manufactured structures. The exposed layout was developed in PMMA resist developer for 40 seconds. If possible, the resist was hardbaked at $200\text{ }^\circ\text{C}$ for 120 minutes. The PMMA is naturally hydrophobic, which is beneficial as it does not promote water-based Cr etchant wicking through possible microdefects in the resist layer. The Cr mask was then etched by Chromium or Nichrome etchant (both Sigma Aldrich), or by home-made NaOH (25 g in 100 mL dH_2O) and $\text{K}_3[\text{Fe}(\text{CN})_6]$ (30 g in 100 mL dH_2O) mixture.

Glass wet etching

The two main challenges associated with wet glass etching is the hazardous nature of HF and the isotropic nature of wet etching. While the risks related to work with HF can be minimized by meticulous following of safety rules, the effects caused by isotropic etching must be simply taken into account during the layout design. The influence of underetching on the etched structure, compared to the layout exposed to the resist and transferred on the metal mask can be expressed as

$$W_E = W_M + 2D_E, \quad (5.1)$$

where W_E is the final width of the etched structure, W_M the width of the opening in the mask, and D_E the depth of etching (FIGURE 5.7(top left), see also FIGURE 5.2). The influence of the underetching grows with growing depth to width aspect ratio. While the influence is nearly negligible for wide and shallow channels, there is an intrinsic limit for the largest depth to width aspect ratio being 1:2 with infinitely small opening in the etch mask. Therefore, the smallest possible structure with depth $2\ \mu\text{m}$ will have width $>4\ \mu\text{m}$, with depth $4\ \mu\text{m}$ will have width $>8\ \mu\text{m}$, and with depth $6\ \mu\text{m}$ will have width $>12\ \mu\text{m}$. The lateral underetching width being exactly equal to the vertical etching depth was proven in every experiment (FIGURE 5.7(top right)).

The etch rate of HF is a function of concentration, glass composition, other reagents, and temperature. A diluted HF solution was used for etching of the sample, as the etched structures were relatively shallow and the slow etch rate gives good control over the etching process. The composition of the etchant was taken from preceding works [16,17]. The used etchant contained $\sim 6\%$ (v/v) HF, and $\sim 0.5\%$ (v/v) HCl in dH_2O . The etch rate was measured to be $0.64\ \mu\text{m}\ \text{min}^{-1}$, which is about $2/3$ of the value measured in [16,17]. This observation can be contributed to significantly smaller structures manufactured in this work, as the access of the fresh etchant to the glass is hampered. The etch rate was found to be constant even for the deepest $6\ \mu\text{m}$ structures if the etchant was stirred during the etching process. If no stirring was applied, the etch rate was constantly dropping for deeper structures together with decreased isotropicity (vertical etch rate is higher than lateral) due to impeded access of the fresh etchant to the glass and removal of the etching products [191]. It is, however, difficult to predict the anisotropy and real depth of etching and thus, the stirring was always used. The etched surface was very smooth with roughness similar to the original unetched surface of the glass (FIGURE 5.7(bottom(a)-(c))). This surface provides good environment for smooth flow of confined droplets.

The effect of hardbaking is notably beneficial during the glass etching, as the resist seems to be wet by the HF etchant despite the fact that PMMA is naturally hydrophobic. For non-hardbaked resist, the presence of possible microdefects allows the etchant to reach microcracks in the Cr mask and etch the glass creating pinholes. The amount of pinholes is, however, reduced nearly to zero for hardbaked resist, testifying for filling of the defects in PMMA and microcracks in the metal mask. The annealing of glass was reported to also increase etch rate [184,189] or remove residual stress in the glass [186]. These parameters become of crucial importance for deep etching. In our experiments, however, the annealing did not show any measurable improvement of the process and therefore was not used.

5.7.3 Combined etching

An attempt was made to decrease the surface roughness of the surfaces etched by RIE method by short wet etching. The glass chip protected with mask consisting of $200\ \text{nm}\ \text{Cr} + 200\ \text{nm}\ \text{Ni} + 40\ \text{nm}\ \text{Cr} + \text{PMMA}$ resist was etched by RIE to obtain $4\ \mu\text{m}$ deep channels. The mask was removed, and the chip was immersed in HF etchant for a time resulting to $0.5\ \mu\text{m}$ etching depth. The flat glass surface

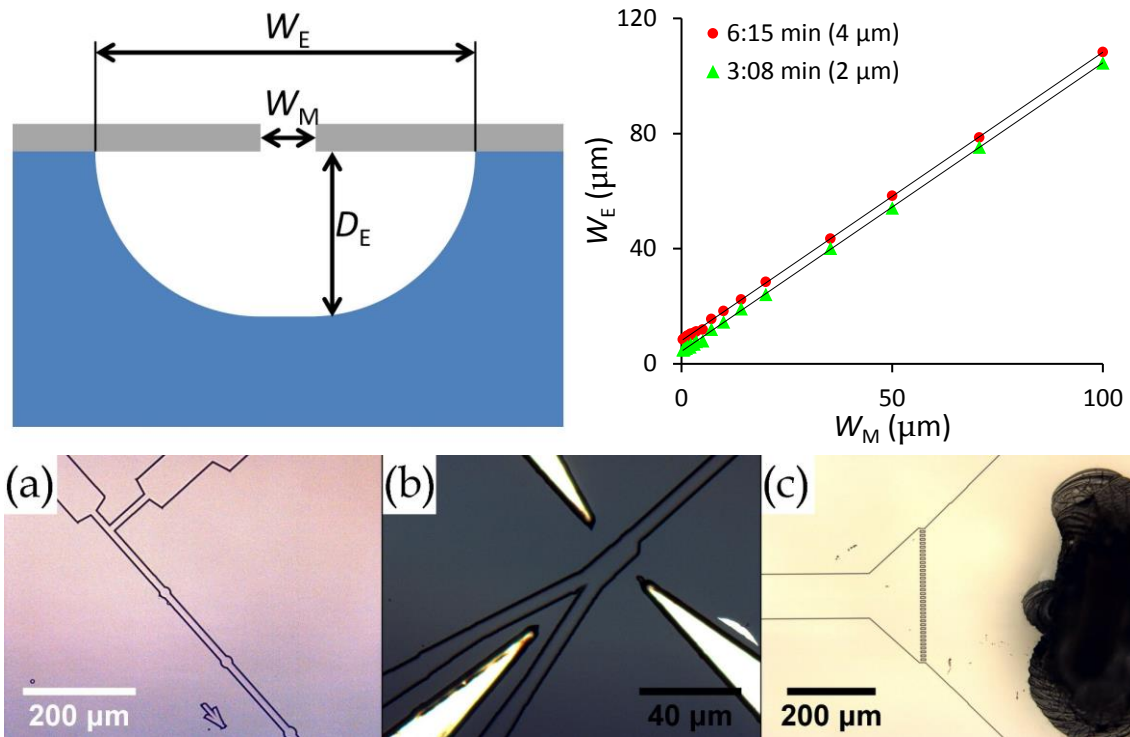


FIGURE 5.7: (top left) Isotropic wet etching of small structures (equation (5.1)). The blue glass is covered with grey Cr mask. Not in scale. (top right) The width of etched structures W_E as a function of the mask opening W_M . The y-axis intercept is equal to $2D_E$. (bottom(a)-(c)) Surface roughness of 4 μm deep wet etched channels.

was expected to etch equally with the bottom of the channels, thus not changing the depth of the channels. The width of the channels was expected to enlarge twice the etching depth, accordingly to eq. (5.1). There was no significant change in roughness measured by profilometer (FIGURE 5.8(a)-(b)), while small improvement could be observed visually (FIGURE 5.8(c)-(d)). The main issue, however, was the evolution of previously invisible cracks all over the sample surface (FIGURE 5.8(e)-(f)). They can be linked to RIE attacking the glass surface via the microcracks in thick Cr layer after the Ni layer was sputtered away. The HF etchant then accelerate the evolution of microcracks in the glass, similar to the process described in [204]. The thicker Ni based mask, developed in the last stages of RIE process development, should remove the issues with cracks. However, the real benefit of HF smoothening the glass surface remains questionable.

5.7.4 3D channels

Certain functionalities of microfluidic systems requires channels with different depths within a single microfluidic chip, like step-emulsification (FIGURE 5.9(a)) [12], trapping [160], or transition from confined to free regime (FIGURE 5.9(b)) [11]. These requirements create high demand on exact positioning and alignment of the layout transfer, where the precision of EBL was found highly beneficial. There are essentially two possible approaches for etching of such 3D

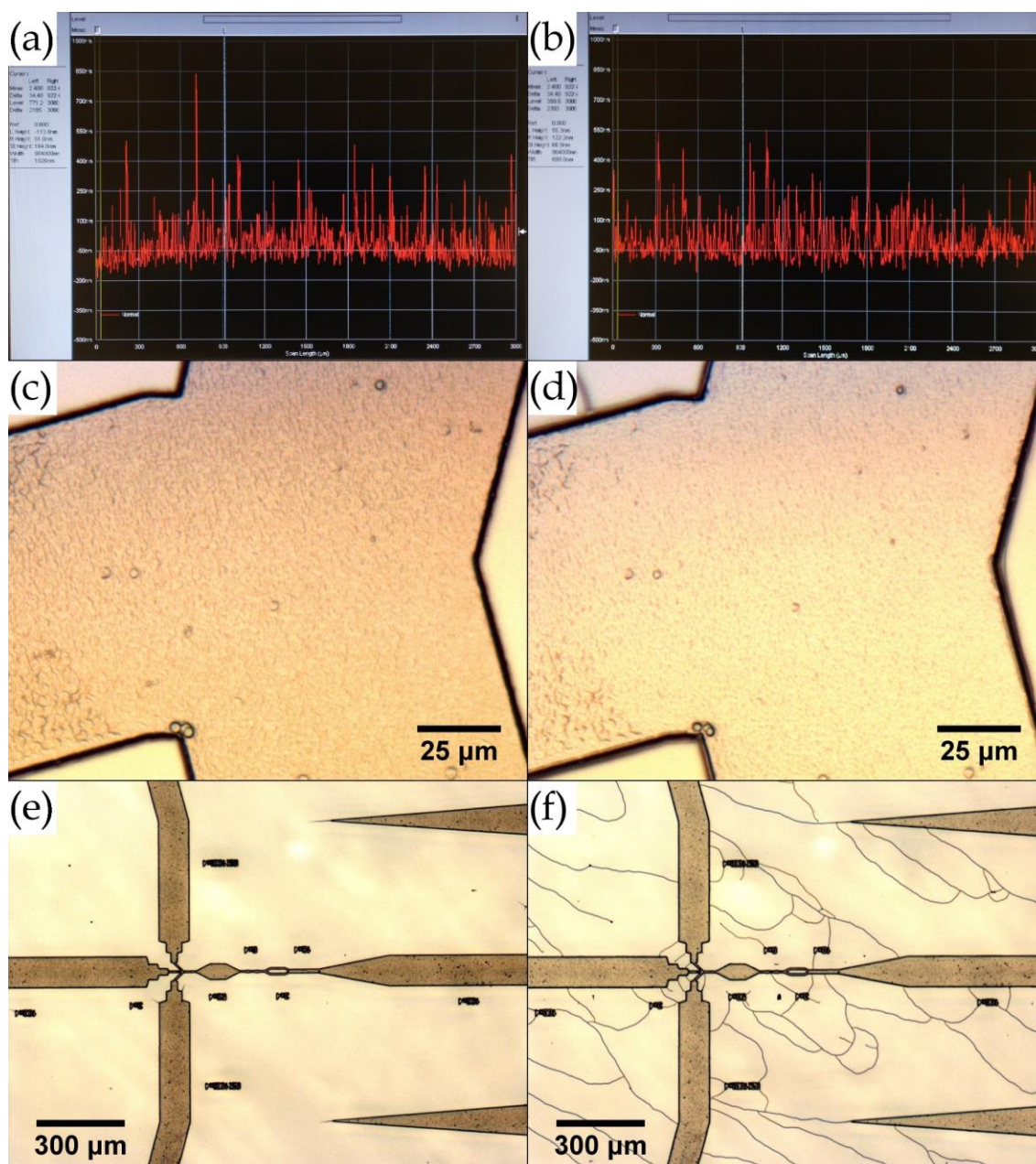


FIGURE 5.8: The surface profile of 4 μm deep RIE etched channel before (a) and after (b) HF solution treatment. The surface of the channel before (c) and after (d) HF solution treatment. The surface of the glass substrate before (e) and after (f) HF solution treatment (sample Real_6_Cr_Ni_Cr).

structures. The first one is *sequential* creation of openings in the Cr mask, first for the deepest structure followed by repeating the spin coating, exposure, and etching sequence for every depth up to the shallowest structure (FIGURE 5.9(c)). The depths of the structures sum up, resulting in the required depth for every structure. The main disadvantage of this process is that for second and following etching steps, the resist must be removed to allow the etching of previously pre-etched structures. This creates a situation, where the HF based etchant has direct access to the microcracks in the Cr mask and usually results in serious damage of the sample. The second, *consequential*, approach consist of full depth etching of desired structure, complete removal of the old mask and deposition of the new

one, followed by next exposure and etching sequence. This approach brings substantially better results, but it is very time consuming. In addition, the protection of already etched structures with Cr mask requires evaporation on tilted rotation stage and thick layers of evaporated metal.

A compromise between these two approaches is a strategy, where the structures are etched always *full depth*, but only the resist layer is renewed between individual exposure and etching sequences (FIGURE 5.9(d)). The depth of etching, size of the etched structures, hardbaking, thickness of the resist, and duct tape protection are variables, which in proper combination lead to good results. Nevertheless, the employment of the hardbaking must be carefully considered as the molten resist tends to flow down to the etched channels, revealing the most vulnerable elements of previously etched structures - the edges of the channels.

After the etching of the channels by either way, the metal mask must be removed prior to the enclosure of the channels. This is done by etching in appropriate etchant the same way as for the transfer of channel layout.

5.7.5 Conclusion on etching methods

Both dry and wet etching procedures for manufacture of microfluidic channels in glass were developed. The RIE procedure would be very beneficial for manufacture of microfluidic chips requiring depth to width aspect ratio ≥ 1 or very narrow structures but it suffers from high surface roughness and micro-trenching.

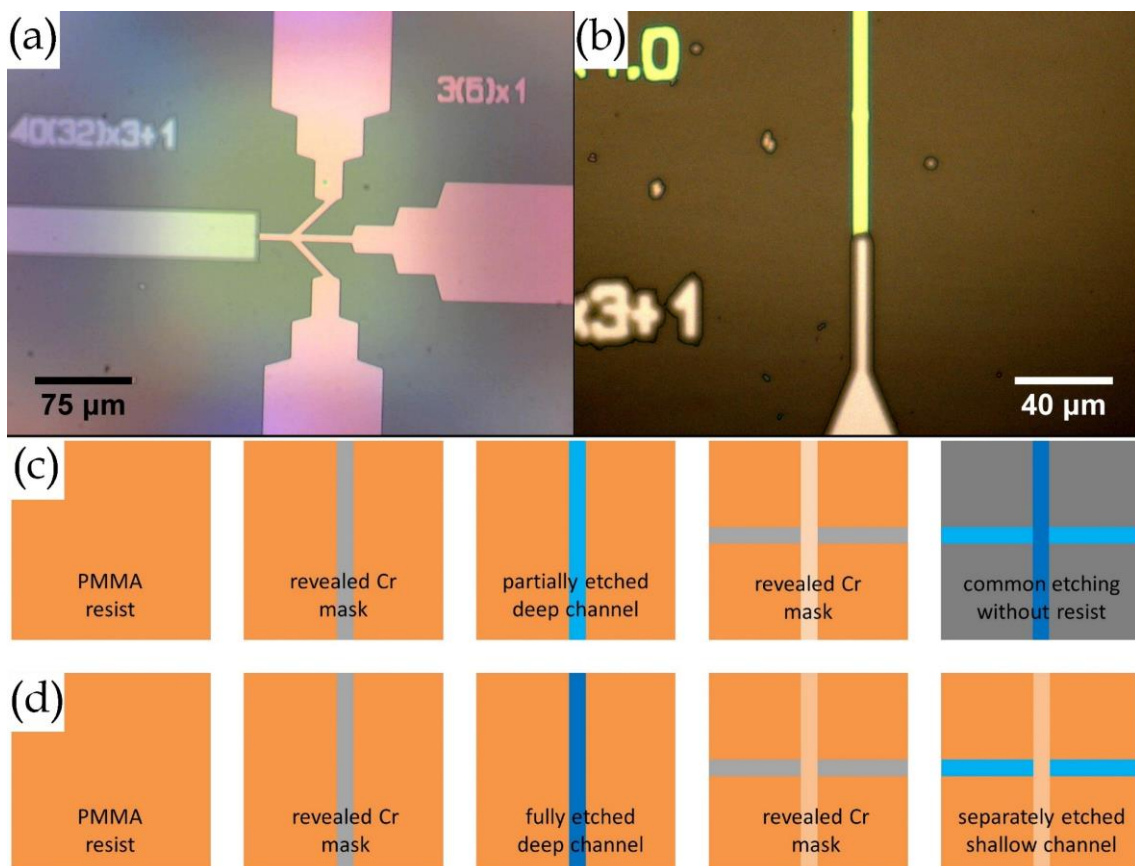


FIGURE 5.9: (a) Step-emulsification 3D structure. (b) Confined to free regime transition 3D structure. (c) Sequential etching of 3D channels. (d) Full depth etching of 3D channels.

The wet etching is, however, sufficient for designed microfluidic chip for fully confined femtoliter droplets and the channel profile is smooth and well defined. Therefore, wet etching of channels in the glass was used for the microfluidic experiments. Nevertheless, for applications where the properties of wet etching would limit the performance of the system, further fine-tuning of developed RIE protocol in proposed way should lead to channel geometry and surface of desired quality.

5.8 Bonding

The bonding is a process of closing the channels etched in the substrate by another glass slip, the cover glass. For microfluidic applications, three main protocols are described in the literature: adhesive bonding, anodic bonding, and direct bonding [184]. The *adhesive* bonding uses special polymer-based cements to ensure good adhesion between the patterned and cover glasses. The size of channels, risk of channel contamination, and mainly the presence of polymers in devices designed for fluorescence spectroscopy do not favor this technique. The *anodic* bonding is a useful technique for bonding of two different materials, mainly silicon and glass. A high voltage applied across the glass/silicon device at an applied pressure and elevated temperature causes migration of Na^+ from glass towards the negative electrode and creation of permanent chemical bond between the substrate and cover glass.

The *direct* bonding, however is an ideal solution for bonding of two chemically identical pieces of glass since it results in sealed channels surrounded by the original glass only. There are two different processes that may happen when two pieces of glass are brought together, or *assembled*.

1. If two planar pieces of glass with surface roughness <2 nm [184] are assembled, they adhere together by intermolecular forces including van der Waals forces, hydrogen bonds, and dipole-dipole interactions. This technological process is called *optical contact bonding* and is often used for bonding prisms and other optical components [185,208].
2. If two glass surfaces covered with hydroxyl groups are brought to close proximity an *activated covalent bonding* will take place and 2 -OH groups will create a covalently bonded oxygen bridge with one H_2O molecule diffused in the process (FIGURE 5.10(a)) [209]. This process, however, requires even smaller surface roughness, at the scale <2 Å.

Besides the low surface roughness, both processes require meticulous cleaning of the bonded surfaces, as the employed forces are of a very limited range and any impurity can block the assembly process. The reported cleaning protocols almost always include treatment in Piranha solution [186,188,192,210,211], similar to the process described in Substrate cleaning. This treatment is known to fully cover the glass surface with dangling hydroxyl groups. Therefore, it is believed that

both phenomena are employed in the assembly process, even though it is often described only as optical contact bonding.

The bonding can be further strengthened by an applied pressure and annealing [184,185], however, the bond strength is always relatively weak. For certain applications where higher bond strength is required the *fusion* bonding (referred as thermal assisted direct bonding (*TADB*) [210]) has to follow. The assembled glasses are under pressure heated up above their glass transition temperature, which allows the two pieces of glass to fuse together and virtually become a single piece of glass. The choice of temperature and pressure are crucial as too low values will not lead to fusion, while too high values will cause collapse of the channels and deformation of the chip. The fusion temperature should be in the interval of the glass transition temperature and the softening temperature [208], which are both composition dependent. The appropriate pressure is then a function of the glass composition (temperature), surface roughness, and dimensions of the etched structures. Successful TADB was reported on chip with deep channels under higher temperatures and pressures with glass surface roughness ~ 50 nm, where the use of softer glass compensates the surface roughness [210]. However, for very shallow channels, the surface roughness must be very small as the softer glass would not only compensate for the surface roughness but would also cause the collapse of the channels [192].

The values in the literature for temperature and pressures for soda-lime glasses are quite consistent, reporting the temperatures 575 °C [188] or 580 °C [16,17,186,210] and the pressures 6 kPa [188], 7.3 kPa [16], and 28 kPa [210], with the time while the sample was held at given temperatures varying from 6 hours [192] to only 20 minutes [186]. An important parameter, closely linked to the temperature, is the cooling rate. It must be kept low to avoid thermal gradient induced stress resulting in cracks. The reported cool down rates are from 1 °C min^{-1} to 5 °C min^{-1} [186,188,192].

Activation

The experimental bonding protocol is based on experiments done prior to this work [16,17], which combines the direct and fusion bonding. They were, however, significantly altered, mainly due to the findings reported in [186,211]. A Menzel-Gläser 18×18 mm² #5 soda-lime glass coverslip was cleaned in acetone and IPA following the protocol for the drilled glass. Both the glass chip with etched channels and the cleaned coverslip were activated in Piranha solution for 1 hour at 80 °C. The activation is followed by thorough sonication in dH₂O, where the water is replaced every 3 minutes. This serves for both removal of the Piranha residues and possible impurities. The RIE O₂ plasma treatment is also known to activate the glass surface, however, the wet activation process performs much better in leaving the surface clean for the assembly.

Assembly

Both glasses are carefully dried with N₂ flow and placed on a hot plate at 160 °C to remove any residual humidity. The glasses are then brought into contact. If the surfaces were properly prepared, the glasses are observably attracted to each other, requiring no pressure to promote the adhesion. If performed correctly, the

interface between the glasses disappear and the assembled chip looks like a single piece of glass. It requires excessive force, often leading to rupture of the glass, to separate the individual glasses after the assembly. This further supports the belief that both molecular forces and covalent bonds are involved in the assembly process. The assembly process is the most demanding part of the whole manufacture, when it comes to random appearance of impurities. While a randomly placed impurity usually does not cause troubles in other stages of the manufacture, unless directly in the place of the etched structures, an impurity even relatively far away from the channels prevents proper sealing of the channels and causes leaking of the microfluidic system. Some authors propose to perform the assembly under water [186,193], which should minimize the appearance of impurities, however, the success rate was found to be much lower than for the dry assembly in our experiments.

TADB

The presence of the impurities is easy to identify as they create interference patterns (Newton's rings) concentrically placed around the impurity (FIGURE 5.10(b)). The TADB process does not soften the glass enough to flow evenly around the small impurities before the channels collapse. Hence, if the impurities are detected between the glasses, they must be separated, and the cleaning process must be repeated. The TADB process is carried out in a furnace under slow

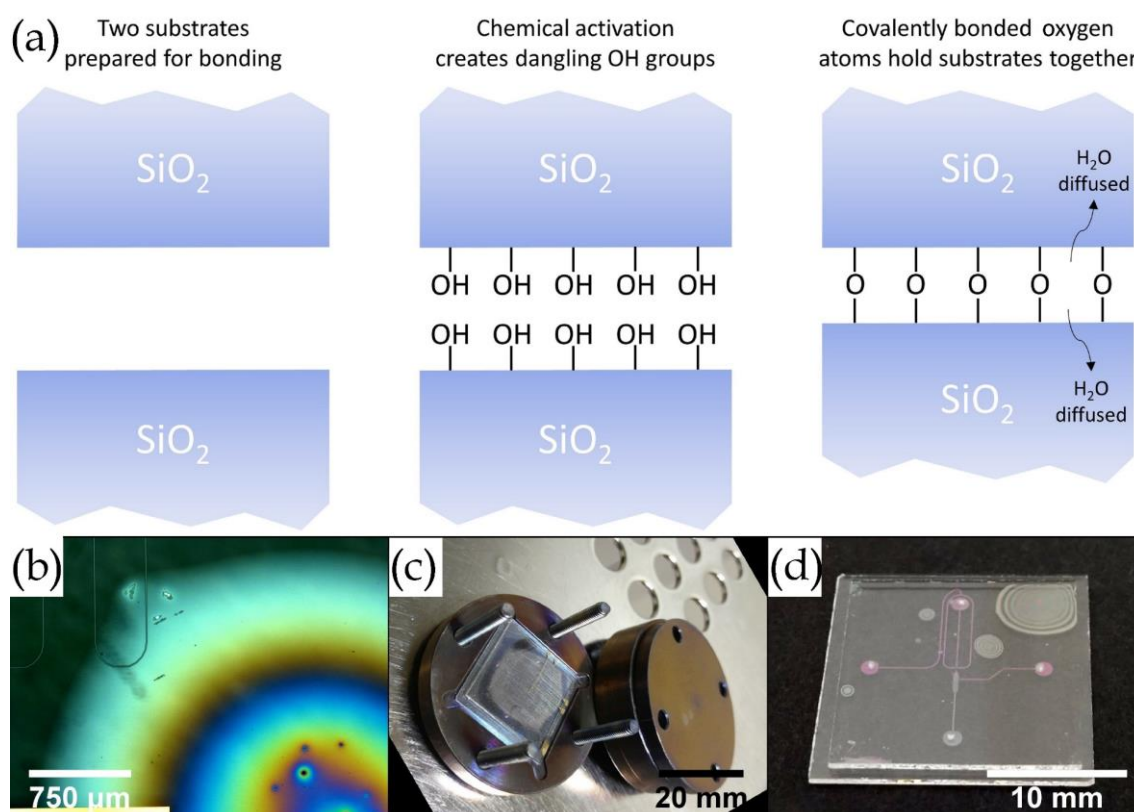


FIGURE 5.10: (a) Activated covalent bonding [207]. (b) Impurity between two glasses, creating characteristic Newton's rings. (c) TADB support and weights. (d) The ready bonded chip. Newton's rings outside of the channel areas do not interfere with proper function of the chip (Sample 26(2)).

N₂ flow to avoid oxidation. The support and the weights are manufactured from stainless steel (FIGURE 5.10(c)), since other tested materials do not perform optimally, *e.g.* brass contaminates the furnace and copper readily fuses together with the glass. The applied pressure was 2.5 kPa, relatively low compared to previous protocols [16,17], which significantly decreased the probability of collapsed channels while still obtaining high quality bond. The temperature was increased to 585 °C at the rate 5 °C min⁻¹ and kept constant for 2 hours. Then natural cooling was allowed, which due to the thermal insulation of the furnace was ~3 °C min⁻¹ at the beginning and exponentially decreasing in accordance with Newton's cooling law. With this cooling rate, well within the reported values, there was no need for active control of the cooling process. After cooling down to <100 °C, the fused chip (FIGURE 5.10(d)) was used for microfluidic experiments.

5.9 Electrodes

Some techniques integrated in lab-on-a-chip devices require incorporation of electrodes. While electrodes are rarely used for sample characterization (impedance spectroscopy [184]), they are widely implemented in all kinds of particle or droplet manipulation. The drop-on demand, mixing, sorting, fission, and fusion [10,14,131] can be all controlled by electric fields, which require electrodes to create these fields locally, affecting the droplets by the desired way. Many ways how to integrate electrodes to a microfluidic chip were reported including planar and 3D metal electrodes, extruded electrodes, channel sidewall electrodes, insulating structures changing locally the electric field, doped silicon and doped PDMS [184,206,212]. Some authors even use an independent system of microfluidic channels, which are filled with a low melting point alloy [213] or a saline buffer solution [12] after the chip with channels is sealed.

In this project, the electrodes were used for droplet sorting. Since contactless dielectrophoresis [214] fulfills all the requirements for the nature and scale of the designed system (see 6.5.4 Droplet sorting), the electrodes were needed to create a highly localized nonuniform electric field in the chip. Standard soft lithography procedures were used to create 2D metal electrodes, a straightforward solution that should work well with the available instrumentation.

The simplest way to incorporate planar metal electrodes is the evaporation directly on the surface of the glass slide with the channels [184]. The electrodes are then covered together with the channels by the cover glass. First, Cr was chosen as the material for electrodes due to its high melting point. The glass with already etched channels was spin coated with PMMA and 10 nm thick layer of aluminium was evaporated on the top to lead the EBL induced charge away from the sample. After Al removal and resist development ~100 nm Cr was evaporated on the sample. Standard lift-off was then used to clean the areas with resist, leaving only the metal electrodes on the sample. The assembly of the cover glass went as expected, and even the 100 nm high electrodes did not show any sign of separation between the patterned glass and the cover glass in the form of Newton

rings. The consecutive thermal bonding, however, lead to two interesting observations. The electrodes were 'leaking' or diffusing in the bonding plane, despite their melting point being well above the TADB temperature (FIGURE 5.11(a)). The electrodes also partially changed color and became absolutely nonconductive (FIGURE 5.11(b)). We speculate that the first issue is connected to melting point depression, which together with the pressure from the cover glass may lead to such a behavior. The second issue showed to be crucial for the whole concept of thermal treatment of metals evaporated on glass substrate and will be described in the following paragraphs.

The solution for the leaking electrodes was to immerse them deeper in the glass. Besides the release of the pressure causing the metal to diffuse, this solution brings two additional advantages. The contact with the cover glass is totally eliminated and, if the electrode immersion depth is half of the channel depth, the situation becomes symmetrical (FIGURE 5.11(c)), which makes the electric field effects easier to model and understand. The burial of the electrodes to half the depth of the channels brings the need for etching of one more 'channel', to which the electrode material is evaporated. That increases the possibility of defects interfering with the channels, meaning destruction of the functionality. The process puts several requirements for the material of the electrodes:

- good conductivity
- thermal stability (melting point well above TADB temperature)
- not attacked by Cr etchant (etching mask removal)
- not attacked by Piranha (activation process)
- good adhesion to the glass surface (to withstand the vigorous sonication during activation)
- acceptable solderability (connection to outer world)

These requirements virtually narrow down the choice to noble metals: Au, Pd, and Pt. Also other metals were tested, including Ag, Al, Ni, and Cr but all of them failed at some point, as expected. All noble metals are known for their poor adhesivity to the glass surface. To overcome this issue, usually a thin (several nm) layer of either Cr or Ti are evaporated between the glass and the electrode material. These two metals adhere readily to both glass and noble metals, serving as a good sticking layer. A thin layer of Cr is usually well protected by a thick layer of noble metal and can well survive the Cr etching mask removal.

Our experiments showed that even Pd is attacked by hot Piranha solution, leaving only Au and Pt as metals of choice. Au was chosen as the material for the electrodes for its availability in the cleanroom. Both the Cr+Au and Ti+Au combinations can well survive all the chemical treatment, however, the TADB discriminates the Cr+Au combination as the Cr is known to diffuse to Au layer already during low temperature annealing, affecting its adhesivity, conductivity and surface quality [215,216]. This was confirmed in our experiments (FIGURE 5.11(d)-(e)), where the quality of TADB samples with electrodes of 10 nm Ti + 50 nm Au highly surpasses the quality of 10 nm Cr + 50 nm Au. The combination of Ti+Au was then chosen as the electrode material.

Troubleshooting

Two more issues linked directly to glass used as the substrate material should be mentioned. The electrodes occasionally peeled off during the sonication in dH₂O after the Piranha activation, especially towards the tips of the electrodes (FIGURE 5.6(a)). It was first thought that it is somehow related to Piranha corrosivity. The random appearance of this effect and its link with sonication later helped to associate this problem to HF etching of the 'electrode channels'. An improper water rinse after glass etching may leave some etching products dissolved in water on the microfluidic chip. As the water dries up, the capillary force drags the etching products to the narrowest places, where the water soluble residues stay during evaporation, lift-off, and Piranha treatment. They dissolve again during the consecutive sonication in dH₂O, taking away the electrodes evaporated on them. A careful rinsing and preventive sonication in dH₂O prior to the metal evaporation completely eliminates this issue.

The other issue stretches over the whole process of microfluidic chip manufacture. During the TADB, wherever the metal is in contact with the glass, the troubles with lost conductivity, color change (FIGURE 5.11(b)&(g)), and occasional total disappearance of the metal were regularly present. These effects, significantly increasing the failure rate of the manufacturing process, were finally

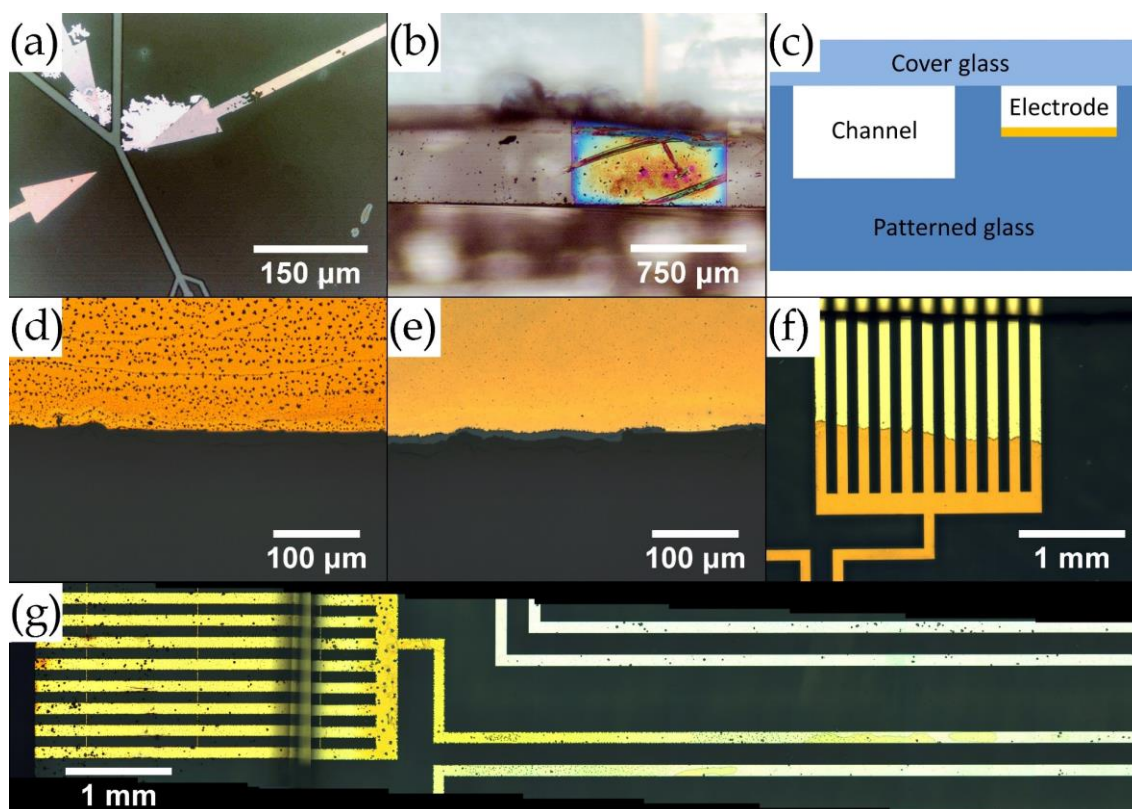


FIGURE 5.11: (a) 'Leaking' of the Cr confined between two glasses during TADB. (b) 30 nm thick Cr electrode connection pad after TADB. (c) Symmetrical position of the electrode relative to the channel (not in scale). The quality of (d) 10 nm Cr + 50 nm Au and (e) 10 nm Ti and 50 nm Au after TADB. (f) The electrodes protected by a layer of SiO₂ (orange) and end of the connection pad with exposed Au for soldering (yellow). (g) The color change along the electrode after TADB shows different stage of glass interaction with the metal.

linked to a process known from vacuum technology as glass-to-metal seal [217]. Especially Cr, and in limited amount also Ti, readily diffuse to softened glass, forming nonconductive oxides. The strength of this effect is dependent on many parameters, hence explaining the random nature of observed effects. Nevertheless, the deposition of a diffusion barrier between glass and the metal, namely SiO₂, successfully suppressed these effects.

Manufacture of the electrodes

The protocol for electrode integration then goes as follows: the 'channels' for electrodes are manufactured as described above. Extra sonication in dH₂O and RIE O₂ plasma cleaning are performed before the evaporation. Then 50 nm SiO₂, 4 nm Ti, and 50 nm Au is evaporated. The evaporation is interrupted to cover the contacting pads (FIGURE 5.11(f)) with duct tape and consequently 4 nm Ti and 50 nm SiO₂ is evaporated to further protect the metal. The lift-off process in acetone removes the electrode material from everywhere except the electrodes and consequently the Cr mask is etched away. Due to extreme corrosivity of the Piranha solution, the chips with electrodes were activated only for 5 - 10 minutes at room temperature. Nevertheless, the shorter time of activation showed no negative influence on assembly and/or TADB quality.

The electrodes were always designed as a loop with two separate contact pads, so the conductivity and proper connection to the outside world could be checked. The resistance of electrodes after assembly is approximately equal to the value which can be calculated from dimensions of the loop and the resistivity. After TADB, the resistance drops about 25 % below the value measured before.

Conclusion on electrode manufacture

The protocol for integration of electrodes to the microfluidic chip was successfully developed, despite the challenges related to manufacture protocol limited choice of metals and unexpected interaction of metals with the glass during the TADB process. Nevertheless, the process of manufacture remains challenging due to the high requirements on precision, precise alignment of the structures and quality of the surfaces. In addition, the electrode material sometimes accidentally adheres on the channel surface (FIGURE 5.6(a)), which affects both the electric field in the close proximity of the electrodes as well as it alters the surface properties of the channel. This is probably due to the hardbaking process, where the molten resist reveals certain parts of the already etched channels, where the metal is then evaporated. Therefore, the electrode integration process still requires some fine-tuning of the parameters to avoid this effect. Examples of ready-made chips are plotted in FIGURE 5.12.

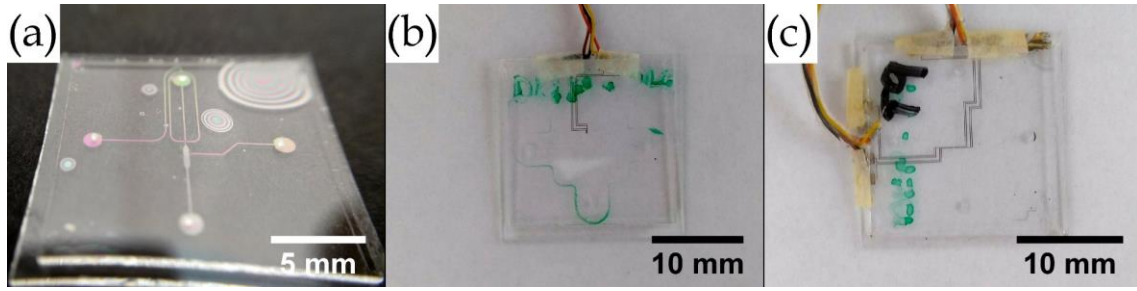


FIGURE 5.12: Examples of manufactured chips (a) 3D channels without electrodes, (b) simple channels with one pair of electrodes, and (c) 3D channels with two pairs of electrodes.

6 Operation of a microfluidic system

The manufacture of a microfluidic chip is all done in the cleanroom environment due to its great sensitivity to any contamination. After the bonding process, the channels are well protected, and the microfluidic chip becomes surprisingly resistant to outside environment. Therefore, all the following procedures and microfluidic experiments were executed in regular laboratory environment, without any special precautions taken when working with the chip.

6.1 World-to-chip interface

Similar to integrated circuits, the microfluidic devices cannot work independently. Despite the great integration of functionalities on the chip, they inevitably depend on connection with peripheral devices. With growing complexity, not only fluidic connections but also power supply and data interchange with the chip must be enabled. Despite the boom of the microfluidic technology, there is no systematic approach in the macro-to-micro interfaces, especially when it comes to the transportation of the fluids. The individual technical solutions usually come together with a particular microfluidic system. The existing solutions are summarized in several reviews [218,219].

The design of world-to-chip interface for a particular system is based on several requirements given by the nature of the microfluidic experiment, used reagents, pressures, and the material of the chip. The design must take into account whether the microfluidic chip is designed as disposable or for repeated use. While the connectors for disposable chips should be fast and easy to connect and disconnect, the connectors for repeatedly used chips can be permanent. While the first system usually requires complex custom-made holders, the permanent connectors are often simply glued or utilize commercially available fittings [184]. The time-consuming design of a socket-like [220] holder for microfluidic chips is in longer time balanced by no need for connecting of every single chip. The design for repeated use, however, must take into account a number of parameters, which, compared with permanent connectors cannot be altered from chip to chip. These include *geometrical parameters*: configuration of the outlets (connecting from the edges [221] or from the surface [220] of the chip), field of view, the area of the connectors, compatibility with the microscope, ease of assembly, and configurability of the holder; *processing parameters*: pressure and temperature tolerances, material compatibility, dead volume; and last but not least the cost.

The developed microfluidic chips are designed for repeatable use. However, the development of a functional channel network caused that every chip was used virtually only once, as observations were immediately used for improvements in a new chip. This prototype testing raised a need for a socket-like microfluidic holder for repeatable use. The holder (FIGURE 6.1(a)&(c)) was designed following the dimensional requirements given by the microfluidic chip and the focal length of the used microscope objectives (Nikon LU Plan 50x/0.55 NA, Olympus NeoSPlan 5 NIC 0.13, Olympus NeoSPlan 10 NIC 0.25). Due to the placement on the microscope stage, the tubes bringing the fluids were placed from the sides of the bulk brass machined holder, which also allowed easier manipulation. The expanded ends of PTFE²³ 1/16" OD - .020" ID tubes were sealed to the side of the holder body via 0.74x1.02 O-rings. The L-shaped 1 mm holes drilled into the body of the holder lead the fluids towards the microfluidic chip (FIGURE 6.1(a)& (b)). The interface between the holder and the microfluidic chip is again sealed with O-rings. The tight seal is in both cases secured by brass lids tighten to the holder body. The holder is equipped with a temperature probe port, which together with a Peltier heater/cooler allows experiments at chosen temperatures (see 6.2.2 Silinization in enclosed channels).

The holder has integrated one important functionality, which is - to the author's best knowledge - not discussed elsewhere. The flow rate at which the channel network is designed to work is in the range²⁴ 50 - 5 000 fL s⁻¹. Even using maximum available pressure and taking into account different dynamic viscosity of air and the liquids in question, the maximum flow rate for bringing the fluids to the chip is ~1.2 nL s⁻¹ (see eq. (4.12)). Since the inner volume of the 30 cm long supply tube together with the L-shaped channel inside the holder is close to 80 000 nL, the filling times become ridiculously long. The air vent valves integrated into the holder body (FIGURE 6.1(b)) decrease the filling volume more than 40-times, significantly reducing the filling time. Taking into account the compressibility of air, the experimental filling time drops to reasonable ~10 minutes.

Minimization of the dead volume is a critical part of the design of a microfluidic system. The dead volume is a portion of internal volume of the system, which is out of the flow path [222]. The fluids entering this volume may not be recovered or they can recover at random time, which makes the microfluidic system unpredictable. This is of crucial importance when different samples share the same path as they can contaminate each other [223]. The holder was not designed for experiments requiring change of samples within individual experiments, therefore the dead volume issue was not systematically solved in the holder design. On the other hand, the reagents used in this project are homogeneous so there was no expected risk of contamination.

The electrodes were connected by soldering of thin wires straight on the electrode pads on the edge of the chip. Since the flux from tin based soldering alloy was found to be aggressive towards the material of the pads, pure indium was used instead. Since molten indium wets glass, the design of the electrode

²³ polytetrafluoroethylene (Teflon)

²⁴ Droplet formation at ~600 mbar measured during the most recent experiments.

pads with strips of exposed glass (FIGURE 5.11(f)-(g)) further strengthens the connection. The connection was finally casted in superglue (FIGURE 6.1(d)) and covered with paper tape to rule out the possibility of conductive contact with the holder.

The developed holder is robust, allows fast change of the microfluidic chip, and is capable of virtually unlimited number of uses. It was tested to reliably work under pressure of more than 5 bars with no observed leaks and at temperatures ranging from 10 °C to 80 °C. The holder offers chemically resistant environment, where the reagents come in contact only with the PTFE supply tubes, brass, and O-rings. The next generation, however, could benefit from integrated electrical connectors and larger field of view. Also the dead volume miniaturization should be systematically addressed.

6.2 Surface properties of the channels

The type of emulsion - W/O or O/W - generated in a microfluidic system is determined by the different behavior of oil and water at the liquid - channel wall interface (see 4.4.1 Droplet formation in open and confined systems). The liquid, which wets the channel surface better will become a continuous phase, whereas the other liquid will form droplets. The stability of the system increases with increasing difference between the contact angles²⁵ of the two liquids in question. While many polymers are naturally hydrophobic and thus suitable for W/O droplet formation, glass surface is intrinsically hydrophilic. Hence, the glass channels are incapable of forming W/O emulsions without further surface

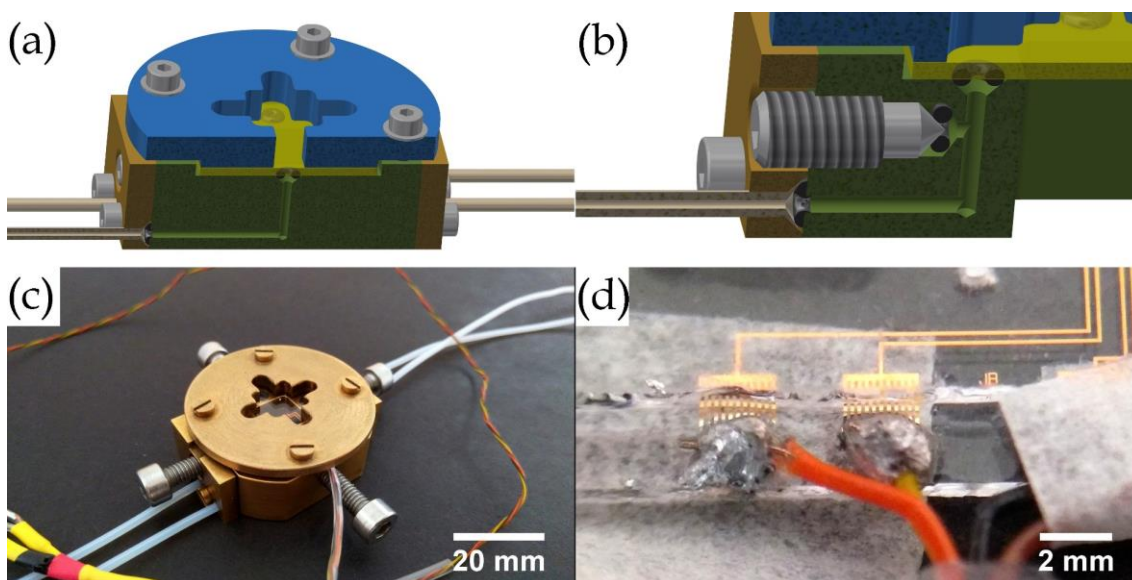


FIGURE 6.1: (a) The L-shaped holes in holder body bring liquids towards the microfluidic chip. (b) An air vent allows much faster filling of the inlet tubes. (c) A picture of holder with assembled microfluidic chip. (d) Detail of connected electrodes.

²⁵ A measure of wetting abilities of a given liquid on particular surface.

treatment. The most primitive way is to fill the channels with the continuous oil phase prior to droplet formation [134] or even store them filled with the oil phase [141]. After injection of the water phase, the channel is able to function for certain amount of time with the oil covered surface mimicking hydrophobic behavior. This approach, however, as also confirmed in our early experiments, suffers from poor repeatability and works only for short periods of time until the water phase reaches the glass walls and reverses the emulsification process.

6.2.1 Hydrophobic treatment of the glass surface

A permanent change of channel surface character to (super)hydrophobic is usually achieved either by creating artificial roughness repelling water [224], or by chemical modification, where amphiphilic molecules are bonded to the glass surface, creating a hydrophobic surface. This technique represents significant improvement of Langmuir-Blodgett monolayers, utilizing direct adsorption on solid surface without the need for specific instrumentation [225]. There is a wide variety of molecules, which can covalently bond to the surface and a plethora of approaches how to run the glass surface treatment [185,226,227]. Nevertheless, the most studied and established systems for glass surface treatment use silane chemistry [226,228], namely organosilanes [229]. Their silane end bonds to glass, while the functional group on the other side of the hydrocarbon chain determines the properties of the surface [230]. The assembly is a spontaneous molecular process [225], which at ideal conditions results in a tightly packed monolayer, often referred as self-assembled monolayer (SAM). The process of introducing silane based chemistry on the glass surface is called *silinization* [123,144,231-233].

The silinization of glass almost exclusively uses the trichlorosilane functional group for bonding of the organosilane on the surface [225,231]. This reactive group is physisorbed on the glass surface, hydrolyzed and subsequently covalently bonded to the glass surface via hydroxyl groups on its surface [231]. The densely packed molecules cross-link, thereby further strengthening the SAM, and reaching virtually infinite shelf-life [232,234]. The functional group on the other end is the hydrocarbon chain alone, strongly repulsing water from the treated surface. This surface is, however, perfectly suitable only for hydrocarbon based oils. The employment of oils based on different chemistry requires utilization of silinization molecules with different functional group [14,127,142,235].

The creation of a hydrophobic surface on glass is a process, which in general consist of 5 steps [228,231].

1. Choice of chemistry: There are several key factors, which determines the success of SAM creation and its quality. The choice of silinization chemistry is a tradeoff between molecules with short hydrocarbon chains, which still allows water molecules to reach the glass surface [232] but are more likely to self-assemble to flawless SAM; and molecules with long hydrocarbon chains, which protects the glass surface better but are more difficult to work with [225]. The most often used molecule for creating hydrophobic glass surface, compatible with hydrocarbon oils, is

octadecyltrichlorosilane (OTS) [230-233,236], but also other systems like vinyltriethoxysilane [224] or octyltriethoxysilane [237] are used.

2. Cleaning and hydroxylation: These two steps are often not distinguished in the literature, mostly due to the reason that many cleaning protocols inherently introduce hydroxyl groups on the glass surface. Nevertheless, the aim of cleaning is to remove impurities and contaminants, while the aim of hydroxylation is to hydroxylate the surface, an inevitable requirement for covalent bonding of the silane molecules (FIGURE 6.2(a)). The cleaning is done by usual cleanroom procedures such as cleaning with acetone, IPA, and sonication; while the hydroxylation is reached by oxidative treatment, *e.g.* Piranha etch [181,230,238], exposure to UV radiation [232] alternatively enhanced by O₂ atmosphere [234], H₂O₂ treatment [225], HNO₃ and NaOH treatment [239], or oxygen plasma RIE activation [231].
3. Treatment: the treatment itself is a very delicate operation, success of which critically depends on many parameters. First, the formation of a high quality monolayer is critically dependent on the presence of a trace amount of water (FIGURE 6.2(b)) [229,234,240]. While the total absence of water leads to incomplete monolayer, excess of water causes uncontrollable formation of multilayers and in the worst case leads to precipitation of the OTS in the form of flakes. The control of water content is especially challenging taking into account, that already regular air humidity means too much water and often causes formation of precipitations during silinization with OTS [231,239]. The presence of water is even more important than complete hydroxylation. Glass, due to its composition, cannot be fully covered by hydroxyl groups [227] but with the right amount of water complete monolayers can be formed, which means that cross-linking can hold surface active molecules in their places even if they are not bonded to the glass surface [233]. The deposition of OTS can be performed either from *vapour* or *liquid* phase. The vapour deposition is done usually in vacuum and the evaporating OTS molecules are the only component [12,127,231]. This system is less vulnerable to many external influences; however, it lacks the control of water presence. The wet deposition brings the OTS to the surface dissolved in a suitable solvent. The trace amount of water is introduced on the glass surface just prior to the silinization by rinsing in water and drying with cold air [230,231] or by moderate heating [232], flow of water vapour [230], or water saturated N₂ [234]. Strong organic solvents are used as an OTS carrier, *e.g.* toluene [182,235,238,239], hexane [238], benzene, acetone, ethanol [231,233], or bicyclohexyl [230]. The trace amount of water in solvent is also reported as crucial, with an ideal concentration of $\sim 1.5 \text{ mg} \cdot \text{L}^{-1}$ [233]. With this requirement, toluene and benzene were found to be the most effective solvents as the amount of water possible to dissolve in them converges to this value. In the case, where neither toluene nor benzene can be used, hydrocarbon oils with chain length matching the length of the hydrocarbon chain in the organosilane [232,233] are used, making hexadecane ideal for

silinization with OTS [181,225,230,234,240,241]. Due to poor water solubility in hexadecane, the carrier liquid often contains up to 30 % of carbon tetrachloride, chloroform or a mixture thereof [225,230,232,234] which helps both to dissolve the chlorinated functional group [232] and introduce the necessary amount of water into the system [234]. The length of the hydrocarbon chain in the active molecule directly determines the optimal silinization temperature [230], which must be, in the case of OTS below ~ 18 °C [232,234,239]. The concentration of OTS in the solvent does not vary greatly amongst the reported protocols, being in the interval $0.4 \text{ mL} \cdot \text{L}^{-1}$ [232,233,239] to $5 \text{ mL} \cdot \text{L}^{-1}$ [181,230,240]. The time of glass immersion in the OTS solution varies from 1 minute [225,234,240] to 1 hour [232,233] with an observation that the silinization over 15 minutes neither further improve nor decrease the quality of the surface [239].

4. Improvement: Immediately after the treatment the glass surface must be rinsed to remove unbonded OTS and prevent their polymerization due to the air humidity. All possible solvents are used for rinsing, usually following the carrier liquid chemistry in the case of organic solvents. For the hydrocarbon based carrier liquids, methanol [240], chloroform [225,230,239], acetone [239], and ethanol [181] are reported as suitable rinsing agents. The created layer is metastable, and the rearrangement and bonding of the functional groups is still ongoing after the rinsing [239]. This cross-linking process can be enhanced by post-treatment baking and it significantly improves the quality of the final layer [232,235,238,241], with the reported temperatures varying from 110 °C to 200 °C and times from 1 to 24 hours.
5. Removal (optional): the incomplete, damaged or worn-off hydrophobic layer can be removed by oxidation and repeatedly redeposited [231]. This, however, brings a limitation to the employment of OTS treated glass surfaces in the high pH environment, where the Si-O-Si bond is readily hydrolyzed, and the hydrophobicity is destroyed [226].

6.2.2 Silinization in enclosed channels

The surfaces silinized prior to bonding of the glass chips would restrict the assembly of the glasses as both the activation of the glass surface and the temperature used during TADB process would destroy the hydrophobic layer [236]. However, the majority of papers dealing with silinization describe treatment of open surfaces. There is only very limited amount of papers reporting silinization in glass channels [181,240]. In addition, the described systems are relatively large compared to the system developed in this work. Since vapour deposition was excluded already at the beginning due to the lack of control of water content and small dimensions of the channels, the liquid deposition protocol was developed. The challenges, mostly related to the size of the system and the chemical compatibility, are described in the following paragraphs. The final silinization procedure is based on protocols of hydroxylation [239], OTS solution [234], and baking [238]. The reagents used were regular laboratory solvents, only OTS (≥ 90 %) and hexadecane (99 %) were purchased from Sigma-Aldrich and used as received.

1. Choice of chemistry: Since the microfluidic channels are made of glass and a hydrocarbon oil is planned as continuous phase, OTS was chosen as the molecule for hydrophobic treatment of the channel surfaces. The polar head group $-\text{SiCl}_3$ bonds to glass, while the long-chain alkyl group $-(\text{CH}_2)_{17}\text{CH}_3$ creates a hydrophobic environment (FIGURE 6.2(a)).
2. Cleaning and hydroxylation: The etched microfluidic channels are thoroughly cleaned prior to their enclosure, with the last step being a long Piranha treatment, which besides the activation of the glass surface also removes possible contaminants. Due to the small channel dimensions, there is little risk of contamination after the TADB. Hydroxylation in the enclosed channels is possible only by injecting strong oxidizing agent in the channels. The attempts to flow Piranha solution through the microfluidic network showed that the brass holder supplying the solution for the microfluidic chip is strongly attacked, which leads to contamination and failure of the chip. The microfluidic chip can be treated with Piranha also by applying a drop of the solution on the inlet hole since the channels get filled by capillary force. The open manipulation with hazardous Piranha solution, the inherent inability to continuously supply fresh solution for more effective treatment, and the tricky consequent rinsing of the microfluidic network strongly disfavor this solution. The most practical hydroxylation method was the *surface treatment right after the TADB process*. The activation process prior to the TADB hydroxylates the glass surface (FIGURE 5.10(a)) and there is still enough surface $-\text{OH}$ groups preserved after the thermal bonding. Since complete coverage of the surface by hydroxyl groups is not required for successful silinization [233], it is possible to completely skip the cleaning and hydroxylation step for freshly bonded chips²⁶. In either case, the high surface energy after Piranha treatment [230] makes the channels sensitive to possible impurities, which come into contact with them, hence special attention must be paid to the purity of the reagents during silinization.
3. Treatment and rinsing: The chip can be removed from the TADB furnace, when it has cooled down to $<100\text{ }^\circ\text{C}$. Since the high temperature during TADB process leaves the channel surfaces totally dry, the chip is filled with dH_2O and dried by flow of N_2 until no visible signs of water presence are observed. This cold drying preserves necessary water molecules adsorbed on the glass surface [232]. The OTS solution is then injected into the channels either via one or two of the inlets in a way that uniform flow of the solution is established in every part of the chip. The toluene-based solution is not applicable as formation of gel blocking the small channels was observed, possibly by a gelation process reported in [242]. The hexadecane-based solution was found to be too viscose for the cross section of the smallest channels. In addition, the melting point of hexadecane is $\sim 18\text{ }^\circ\text{C}$, which restricts the silinization at ideal temperature. The addition

²⁶ This approach virtually prohibits utilization of RIE O_2 activation prior to TADB. As it was found during silinization experiments, the directionality of the treatment causes incomplete hydroxylation on vertical walls of the channels and thus a defective silane layer.

of chlorocarbons allows creation of a hydrophobic layer but the repeatability of the process is very low. In addition, the consequent rinsing in chloroform or carbon tetrachloride resulted in nearly 0 % yield of usable chips as they often got filled with a liquid solidifying inside of the channels during the drying process. Since the longer rinsing times resulted in higher failure probability, a material incompatibility was thought to be the issue [243]. Indeed, after change of O-ring material from NBR to Viton®, the majority of solvent related issues disappeared. The final OTS solution composition is 1 mL of hexadecane, 150 μ L of CCl_4 , 50 μ L of water saturated mixture of $3\text{CHCl}_3+2\text{CCl}_4$, and 10 μ L of OTS. This solution is pushed through the chip for 60 minutes, while the chip is kept at 16 - 17 °C by Peltier-based thermostat (FIGURE 6.2(c)). Attention must be paid to the direction of flow if the microfluidic network contains 3D structures. While the flow from shallow regions to deep ones does not cause any issues, it is virtually impossible to avoid blockage of the chip caused by small impurities at deep to shallow intersection. After 1 hour, the solution is pushed out by a N_2 flow and the chip is filled and rinsed with IPA at room temperature. Besides being miscible with both hexadecane [244] and chlorocarbons, IPA has an ideal cleaning properties leaving almost no residues after drying. The chip is then dismantled from the holder and both the holder and the chip are carefully washed with IPA. This step is necessary for cleaning of the large dead volumes on the chip-holder interface and in the holder itself. The chip is then returned back to the holder for more IPA rinsing, repeating IPA and N_2 cycles until the chip is perfectly dry. The dead volumes inside of the chip sometimes also resulted in improper cleaning, which led to changing the design to nearly zero dead volume, however, at the expense of higher requirements for the positioning of input and output holes (FIGURE 6.2(d)-(e)).

4. Improvement: The chip is cured on a hot plate at 200 °C for 2 hours [238]. This process sometimes even cures the surfaces, which right after the OTS look improperly silinized but still do not restrict the flow. If the chip contains electrodes, the soldering must take place not earlier than after this step as both indium and cyanoacrylate melts at temperatures below 200 °C.
5. Removal (optional): The oxidation, which would remove the hydrophobic layer inside of the microfluidic channels could be achieved *e.g.* by Piranha treatment. Despite the challenges linked to employment of Piranha in microfluidic chips described earlier, the size of the system designed in this work is a major problem. The precipitates formed when some parameter is wrong immediately pile up in the narrowest place of the chip causing permanent blockage. This blockage leads to halt of the flow. Since the flow is blocked, the Piranha solution cannot proceed through the microfluidic channels and such a chip is useless. The hydrophobic layer itself was not observed to wear off or get damaged even after 2 years of use and storage in ambient air. Therefore, there was no need to test the removal of hydrophobic layer from chips with working flow.

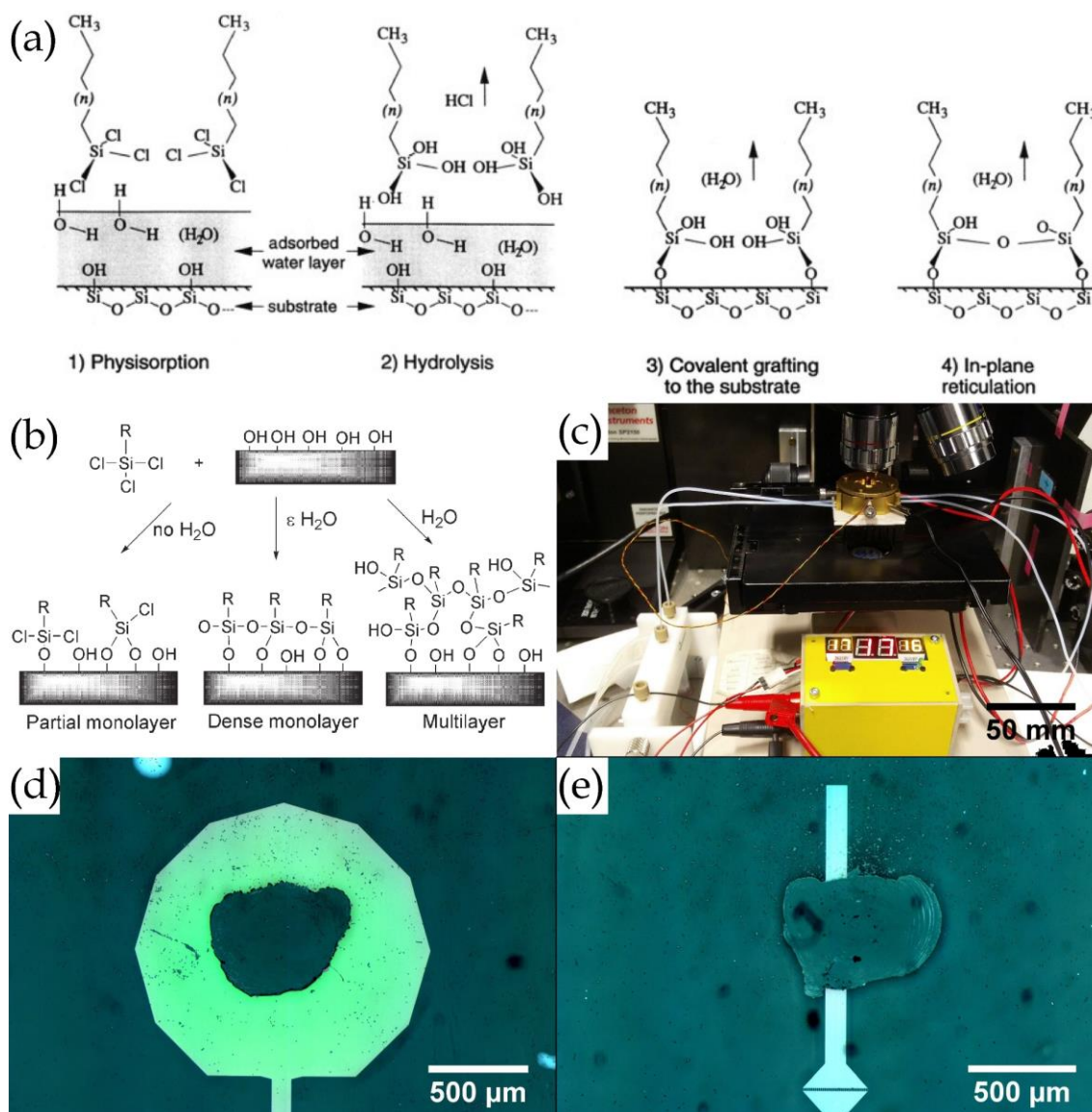


FIGURE 6.2: (a) A scheme proposed for the silinization reaction. (b) Influence of water content on the silinization reaction. (c) Cooling the holder during silinization. (d) Dead volume difficult to clean from OTS solution. (e) Improved dead volume design. An inline filter can be seen in the bottom part of the figure. Figure (a) reprinted with permission from [230]. Copyright 1994 American Chemical Society. Figure (b) reproduced from [227] with permission from the Royal Society of Chemistry.

The developed protocol for liquid silinization of micrometer-sized microfluidic channels is very sensitive to many factors, however, highly repeatable if performed properly. While the reagents do not require any special improvements prior to their use; the water content, temperature during silinization, proper rinsing and baking are crucial for a perfect result. The success rate of silinization process is well over 90 % and the created hydrophobic surfaces do not change their properties even after heavy use and during long periods of dry storage. The detailed protocol for manufacture and surface treatment of the microfluidic chip is attached at the end of this manuscript as Appendix B.

6.3 Instrumentation

All microfluidic experiments were pressure driven by Fluigent pressure controllers. The MFCS FLEX controller with 4 channels providing maximum pressures of 345 mbar (1x), 69 mbar (2x), and 25 mbar (1x) was used successfully at the beginning of the project [17,18], however, the shrinking dimensions of the system required higher pressures (see eq. (4.12)). The MFCS EZ controller with 2 channels providing a maximum pressure of 2000 mbar (2x) was used for most of the microfluidic experiments described below. Two in-house N₂ gas lines with pressure regulators up to 5 bar were used for the silinization process, rinsing, and drying of the chip. The Fluiwell system was used to feed the microfluidic chip with liquids. The functionalities of the microfluidic chip were observed using an Olympus BH2-UMA upright microscope equipped with Olympus NeoSPlan 5 NIC 0.13 and Olympus NeoSPlan 10 NIC 0.25 objectives. The Logitech C310 HD webcam was used to capture the field of view. The videos and photos were recorded in Logitech webcam software, while time-lapse videos were recorded in Yawcam software.

6.4 Reagents

The choice of reagents was built upon the properties of the disperse phase - the water solution of carbon nanotubes. Modern, commercially available microfluidic systems almost exclusively work with the system of fluorinated surfaces, fluorinated oils and fluorinated emulsifiers [12,14,120,245,246]. The advantages of fluorine based systems is mainly the stability of the water droplets and compatibility with polymer-based microfluidic devices. The search for a suitable oil for continuous phase in a glass microfluidic chip is part of former work [18]. Since the limitations prevailing for many polymer-based microfluidic chips do not apply for glass systems, linear hydrocarbon oils can be used. The linear hydrocarbon oils, liquid at room temperature - from pentane to heptadecane, offer wide selection in parameters like viscosity, density and solubility in water (TABLE 6.1). Due to the microfluidic application, *n-decane* was chosen for its viscosity being similar to that of water. The emulsions created from water and decane commonly utilize sorbitan emulsifiers (SPAN family) [118,119,132,143,247-249], polyethoxylated sorbitan emulsifiers (TWEEN family) [149,250], or their mixture [139,251,252]. The Sorbitan monooleate (SPAN 80) and Polyethylene glycol sorbitan monooleate (TWEEN 80) were used as emulsifiers in this study. The HLB values are 4.3 and 15.0, respectively, and their mixing allows preparation of an emulsifier with virtually any HLB value from the given interval [136,137,253]. The microfluidic experiments in this section were performed with Type II purified water from Millipore Elix UV 3 system with resistivity >10 MΩ·cm and TOC <30 ppb without any further treatment. The interface of the used liquids and natural versus OTS treated glass surface is plotted in FIGURE 6.3.

TABLE 6.1: Physical properties of alkanes and their solubilities when in contact with water [254,255].

	Density (g·mL ⁻¹)	Melting point (°C)	Boiling point (°C)	Solubility in water (μL·L ⁻¹) 25 °C	Water solubility (μL·L ⁻¹) 25 °C	Viscosity (mPa·s) 20 °C
Pentane	0.626	-130	36	63.978	66.427	0.24
Hexane	0.661	-95	69	20.264	63.067	0.30
Heptane	0.680	-91	98	3.681	59.409	0.39
Octane	0.703	-57	126	0.902	56.961	0.54
Nonane	0.718	-54	151	0.230	54.448	0.71
Decane	0.730	-30	174	0.055	52.172	0.92
Undecane	0.740	-26	195	0.013	50.117	1.19
Dodecane	0.750	-10	216	0.008	48.342	1.50
Tridecane	0.756	-5	234	0.006	46.542	1.88
Tetradecane	0.762	5	255	0.005	44.943	2.34
Pentadecane	0.769	13	270	0.004	43.560	2.86
Hexadecane	0.770	18	287	0.004	41.981	3.47
Heptadecane	0.777	22	302	0.004	40.852	N/A
H ₂ O	1.000	0	100	N/A	N/A	0.89

6.5 Operations on the microfluidic chip

The following paragraphs describe developed functionalities of the microfluidic system with particular focus on the solutions required for CNT sorting application. The droplet formation, droplet stability, storing, trapping, and sorting were iteratively designed and tested as they form an interlinked system, where every change tends to influence the behavior of the whole system. The experimental results are presented together with general considerations and possible solutions for systems with different requirements.

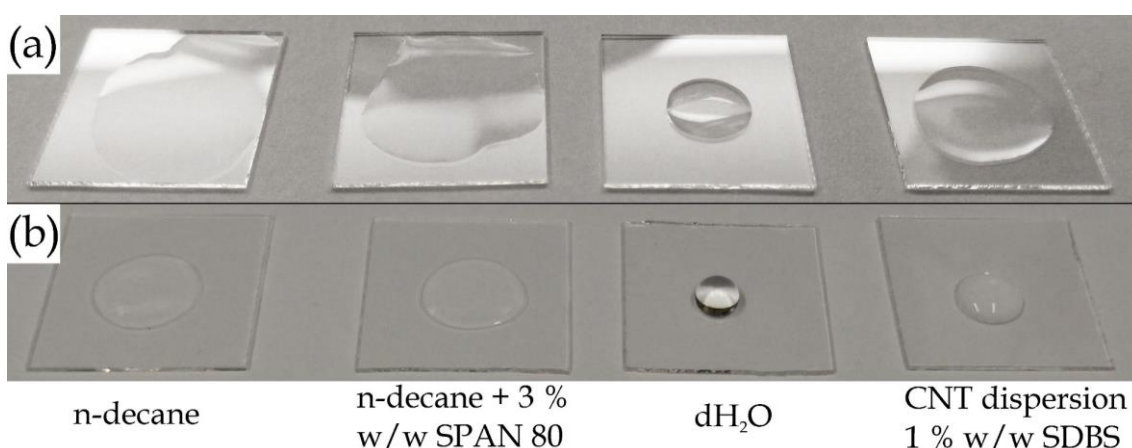


FIGURE 6.3: The reagents used in microfluidic experiments (20 μL) and their contact angle with (a) untreated glass, (b) silinized glass.

6.5.1 General description

The design aims at development of a microfluidic system with continuous droplet formation at very low frequencies. The simplicity of the manufacture and low requirements for peripheral instrumentation is a key requirement for eventual parallelization of the sorting. Therefore, the geometries for creation, transport and trapping of femtoliter droplets were all developed as passive with the sorting valve being the only actively controlled element of the chip. The general layout of the system is plotted in FIGURE 1.1.

The depth to width aspect ratio of manufactured channels is always $>1:2$ due to the isotropic nature of wet etching (see Glass wet etching, p. 98), which is the determining condition for the design of the microfluidic system. The droplets with diameter larger than the depth of the channel are then confined at least from the bottom and the top and in this configuration, resulting in general reluctance to move with the flow of the continuous phase (see 4.3.6 Flow of confined droplets), unless confined also from the sides or in high velocity flow of the continuous phase.

The movement of the liquids inside of the microfluidic channel with quasi-rectangular rather than square cross section (FIGURE 5.7(top left)) did not show any fundamental discrepancies from the expected behavior defined in equations (4.12)–(4.15). The non-linear flow patterns could be observed in places, where the width, depth, or direction of the channel abruptly changes. Together with minimizing the dead volumes on the chip, smooth transitions and straight channels are preferred in the design. The inlet holes are connected straight to the channels (FIGURE 6.2(e)). Several tested geometries of the channel width change are plotted in FIGURE 6.4(b) – (e). The subtle change of the channel width (FIGURE 6.4(e)) was found to minimize the pile up of possible impurities and creation of a plug. In addition, a particle trap was designed as inline filter with ‘pore’ size smaller than the narrowest place in the channel (FIGURE 6.4(a), see also FIGURE 6.2(e)).

6.5.2 Droplet formation

The production of femtoliter droplets in *fully confined regime* brings high requirements for the size of the manufactured structures, which need to match the droplet dimensions not only in the vertical but also in the horizontal dimension. The droplet production in *non-confined regime* allows easy production of droplets

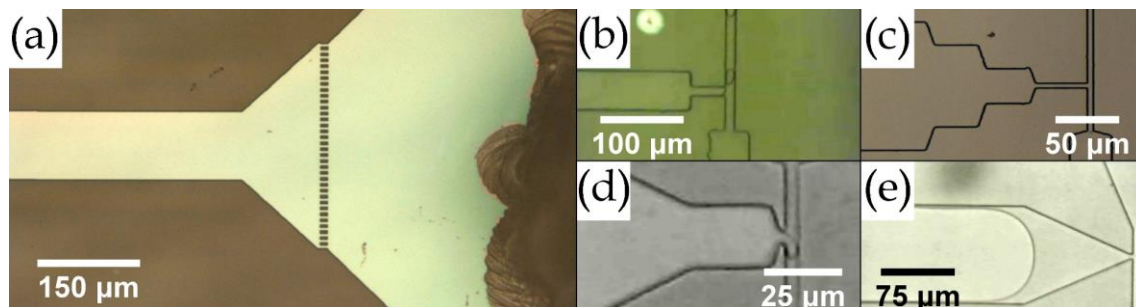


FIGURE 6.4: (a) In-line microfluidic filter. (b) – (e) Various geometries of the channel width change.

much smaller than the channel dimensions [12,123,140,148,153] and eases the manufacturing, however, it lacks the possibility of droplet formation at low frequencies and complicates further precise positioning and trapping. The essential need for regular supply of droplets for a trap, where a droplet would stay stationary for the time of measurement and then allow the next droplet to enter, led to the development of a fully confined microfluidic system, where the droplets behave as plugs, filling the full cross section of the channel (FIGURE 4.3).

The size of a droplet is the determining factor for the dimensions of the channel network in a microfluidic system working in the fully confined regime. The expected length of individualized SWCNTs, the cross section of the focused laser beam for excitation of fluorescence signal, and the possibilities of manufacture led to the requirement that the droplet's *spherical* diameter should stay below 5 μm (volume ≤ 65 fL). This size of droplets is unprecedented, since the vast majority of microfluidic devices described in the literature are in nanoliter to picoliter domain [12], with very few exceptions [12,14,148,159]. The formation and manipulation of droplets in such a miniaturized system brings a new set of challenges with precision of manufacture, control of pressure and flow rate, purity of liquids, and interactions of materials at highly curved interfaces.

All the functionalities of the microfluidic system described below were developed with the aim for manipulation of droplets with the diameter ≤ 5 μm . Due to the quasi-rectangular shape of the wet-etched channels, the droplets have a shape of 'noodles' or flat cylinders rather than spheres (FIGURE 6.5(a)). Therefore, the depth of the channels must be smaller than the planned droplet diameter. The basic depth used in the majority of manufactured channels was 2 μm . Together with the underetching (FIGURE 5.7(top left)), the smallest achievable channel width is ~ 5 μm . Three droplet formation geometries were developed and tested.

- The *step-emulsification* geometry (FIGURE 6.5(b)&(c), supplementary movie [M1](#)^{27,28}) produces highly monodispersed (<1 %), densely packed droplets. The size of the droplets is largely geometry dependent, while the frequency of formation is ruled by net pressure or net flow rate (FIGURE 6.6(left)). The droplet diameter was found to fluctuate around the value of 4-times the depth of the channel prior to the step, slightly depending on the pressure ratio of the continuous and disperse phase (FIGURE 6.6(right)). This finding is in partial disagreement with [14,146], where 3-times the depth dependence was observed. The system reaches up to 3 kHz droplet formation frequency at pressure of 3 bar applies on both continuous and disperse phase. The frequency can be further increased by increasing the applied pressure.
- The *flow-focusing* geometry (FIGURE 6.5(d)&(e), supplementary movie [M2](#)²⁹), produces monodisperse droplets, usually well separated by continuous phase. The droplet formation frequency and droplet sizes are given by similar rules as in the step-emulsification geometry. However, multiple

²⁷ M1 - <https://jyx.jyu.fi/handle/123456789/58966>

²⁸ Detailed information about the supplementary movies can be found in Appendix C.

²⁹ M2 - <https://jyx.jyu.fi/handle/123456789/58967>

capillary number dependent droplet formation regimes can take control over the droplet formation and abruptly change the droplet formation characteristics [120,156].

- The *T-junction* geometry is the only geometry allowing production of droplets in fully confined regime. The confined regime significantly influences the droplet formation frequency and droplet size, making the T-junction system highly dependent on geometry of a particular system.

T-junction

The spectroscopy of single CNT in a droplet requires integration time long enough to distinguish the signal from the noise. The time sufficient for reliable detection of a single nanotube was proposed³⁰ to be ~ 1 s, hence the goal for droplet formation frequency was about 1 Hz. Since one of the main advantages of microfluidics lies in the possibility of fast screening [256], the general effort is focused on the development of systems with high droplet formation frequency. A plethora of papers describe physics, manipulation techniques, and channel geometries for high frequency droplet formation. On the other hand, there is very little activity in the field of droplets produced at ultralow frequencies. This is easy to understand, as the slow formation of droplets, especially with the size needed in this experiment, is related to a large set of issues, especially to instability of droplet formation [162,251]. The pressure actuated drop-on-demand approach was tested but the response of the system was too slow [14], while the stability of the whole microfluidic system was disturbed in an unacceptable way. Other drop-on-demand techniques were not tested as they employ active elements and their employment was not preferred in order to keep the system as simple as possible.

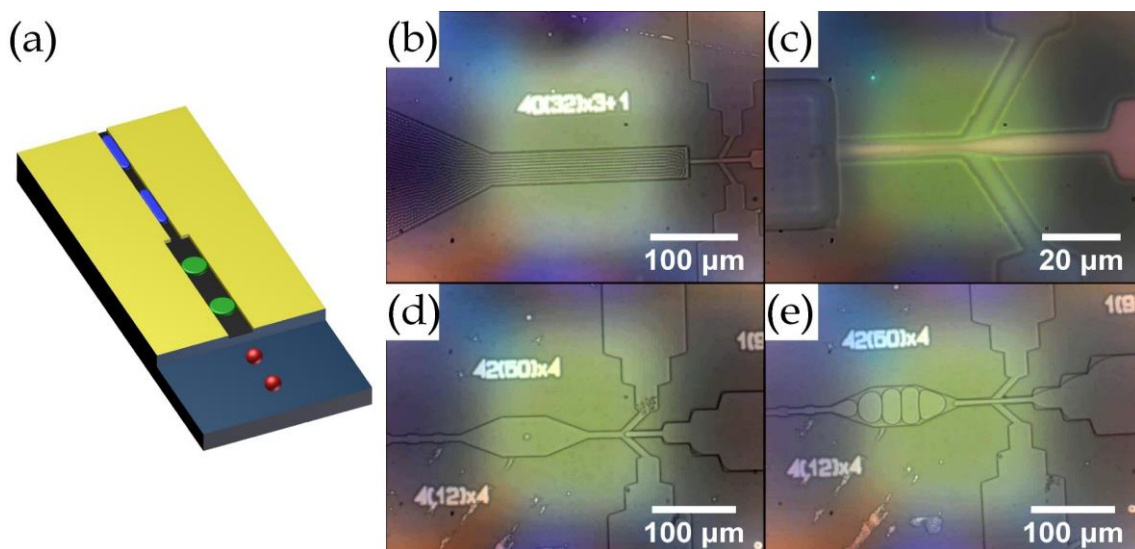


FIGURE 6.5: (a) Droplets with the same volume in confined and free regime. (b) Step-emulsification (chip 26, oil 3 bar, water 3 bar). (c) Step-emulsification detail. (d) Flow-focusing (chip 18, oil 0.5 bar, water 0.25 bar). (e) Flow-focusing (chip 18, oil 0.3 bar, water 0.28 bar).

³⁰ Based on measurements of highly diluted CNT dispersion in microfluidic channel.

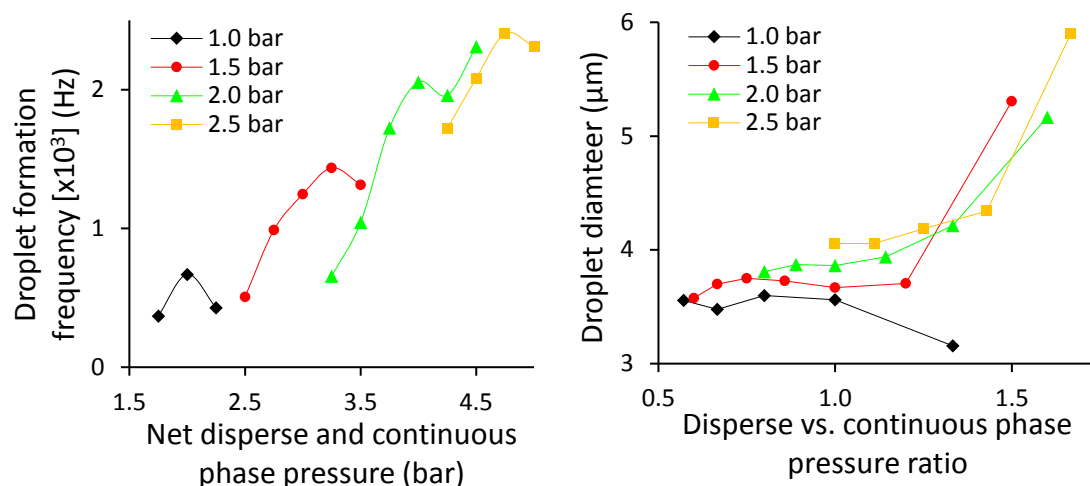


FIGURE 6.6: (left) Droplet formation frequency as a function of net pressure in step-emulsification geometry. Different colors mark experimental series with set water pressure. (right) Droplet diameter as a function of pressure ratio in step-emulsification geometry. Different colors mark experimental series with set water pressure.

Step-emulsification and flow-focusing are two examples of droplet formation geometries with excellent performance at relatively high flow rates and high droplet formation frequencies. However, they totally fail in spontaneous droplet formation in confined regime at low frequencies. The T-junction geometry, even though relatively rarely used, was found to be capable of regular spontaneous droplet formation even at frequencies below 1 Hz, with the monodispersity <5 %.

The droplet break off in T-junction geometry is determined only by capillary number $Ca = \eta v / \sigma$, eq. (4.6). When Ca reaches a certain value, the droplet formation occurs. This value is constant for a particular channel geometry [10]. Since the viscosity η and interfacial tension σ are constant for a given experiment, the increase of continuous phase velocity will trigger the change of the flow pattern from laminar co-flow to droplet formation [152]. The flow of two liquids at the T-junction gradually changes from a laminar co-flow via squeezing and dripping to a jetting regime [152,257,258] with growing capillary number (FIGURE 6.7). An exotic balloon regime is possible to achieve only with highly asymmetric geometries [150].

Since the droplet formation frequency inherently increases with increasing capillary number, the *squeezing* regime is the most suitable for low frequency droplet production. The cross section of channels used for the T-junction was $5 \times 2 \mu\text{m}^2$, on the edge of physical possibilities of wet etching with $2 \mu\text{m}$ channel depth. The regularity of droplet production is strongly affected by the shape of the water inlet. Since hydrophobic, the long narrow channel bringing water to the T-junction (FIGURE 6.4(b)&(c)) is filled with the continuous phase after droplet break off due to the capillary force. An increased pressure is needed to overcome this effect, which often leads to reverse flow of water in the channel bringing oil to the T-junction. Funnel shaped water inlets (FIGURE 6.4(d)&(e), supplementary movie [M3](#)³¹) minimize this effect and were exclusively used.

³¹ M3 - <https://jyx.jyu.fi/handle/123456789/58971>

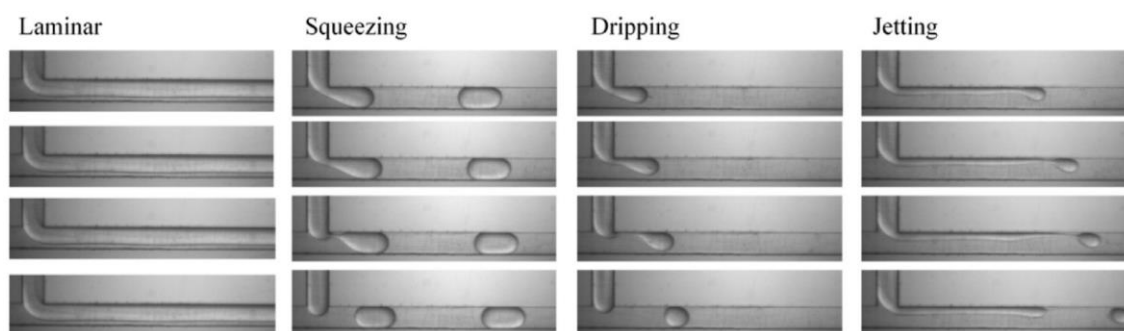


FIGURE 6.7: Droplet formation regimes in T-junction geometry. Figure reprinted from [150], Copyright 2016, with permission from Elsevier.

Droplet formation frequency

Droplet formation frequency in a T-junction is a function of *continuous phase flow rate* and *pressure ratio* of continuous and disperse phase. The flow rate is, however, enormously challenging to measure in femtoliter-sized microfluidic systems and it suffers from large measurement error. The pressure of continuous phase is easy to measure and maintain steady and it can be used as a parameter instead of the flow rate. Since the flow rate at the same pressure varies according to channel geometry (see eq. (4.12)), the droplet formation frequency varies from chip to chip (FIGURE 6.8(top left)). Therefore a geometrical factor describing the channel resistance (see eq. (4.15)) must be used when comparing results from different microfluidic chips. For instance, the chip DEP-T12 has outlet channels with cross section $13 \times 6 \mu\text{m}^2$, compared to chip DEP-T9 with outlet channels with cross section $6 \times 2 \mu\text{m}^2$. The factor describing the difference in resistance of this two chips is ~ 0.94 (FIGURE 6.8(top right)).

The partial dependence of the droplet formation frequency on pressure ratio of continuous and disperse phase can be seen in FIGURE 6.8(top left)&(top right). At constant oil pressure, the decreasing water pressure (from left to right) causes first increase and then decrease of the droplet formation frequency. It should be noted, that the whole interval of water pressures in which the frequency can be 'tuned' is only 15 mbar at the low oil pressure (400 mbar) and no more than 40 mbar at high oil pressure (1 000 mbar). Therefore, precise control of pressure and stability of pressure source are essential for maintaining stable droplet formation.

The relative standard deviation of the droplet formation frequency decreases with increasing oil pressure (from left to right in FIGURE 6.8(top right)). In another words, the higher droplet formation frequency is generally more regular. At constant oil pressure, the relative standard deviation decreases with higher water pressure (from right to left in FIGURE 6.8(top right)). Hence, larger droplets lead to more regular droplet formation. Nevertheless, the relative standard deviation is rather large, in interval 100 – 150 % for low continuous phase pressure (400 mbar) and dropping to 50 – 100 % for higher pressure (1 000 mbar). It should be noted that the droplet formation frequency was measured after the droplets were pushed several millimeters up the narrow channel in confined

regime (supplementary movie [M4](#)³²) Consequently, the irregularity of droplet production for smaller droplets can be caused by the smaller droplets snagging in the channel since it is easier for the continuous phase to leak around them.

Droplet size

The size of the droplets produced in a T-junction in confined regime is determined mainly by the area of the T-junction cross section. The droplet size can be tuned by altering the continuous and disperse phase flow rates or changing the relative viscosity between the liquids within a certain interval given by the geometry [10]. In practice, the size of droplets can be tuned by altering the pressure ratio of continuous and disperse phase (FIGURE 6.8(bottom left), supplementary movie [M4](#)), similarly to the frequency. Hence, the droplet size is directly linked to the droplet formation frequency. The geometrical factor comparing chips with different channel geometry does not play an essential role here, it only helps with the prediction of the droplet size related to particular pressure ratio (FIGURE 6.8(bottom right)). The droplet size at constant oil pressure is almost a linear function of the continuous versus disperse phase pressure ratio, with droplets growing in size with increasing ratio of the disperse phase (FIGURE 6.8(bottom right)).

The relative standard deviation in the droplet size is $\leq 5\%$, with the polydispersity decreasing with increasing oil pressure (from left to right in FIGURE 6.8(bottom right)). In another words, the droplet formation at higher frequency leads to more monodisperse droplets. At constant oil pressure, the relative standard deviation decreases together with water pressure (from left to right in FIGURE 6.8(bottom right)), hence the smaller droplets are more uniform in size.

Propagation of droplets in microfluidic channel

The requirements for the size and frequency of the droplets for single CNT spectroscopy demand excellent pressure control and stability. The Fluigent MFCS EZ pressure controller allows pressure control with resolution of ~ 0.6 mbar and the pressure stability is ~ 2 mbar, independent on the absolute pressure. It is therefore beneficial to work at higher pressures as the relative instability is smaller³³. In addition, certain flow speed of the continuous phase is needed for working droplet formation at given reagent composition and surface properties (see eq. (4.6)). The use of higher pressures seems to be inevitable for precise control of the droplet formation, size, and frequency. The droplet frequency, however, steeply increases with growing oil pressure (FIGURE 6.8(top right)). The solution for maintaining low droplet formation frequency at higher operating pressure is the increase of the channel hydraulic resistance. The hydraulic resistance is a linear function of channel length at constant channel width and depth (see eq. (4.15)). Therefore, a simple extension of the channel length causes that higher pressure is needed to reach the same flow rates.

³² M4 - <https://jyx.jyu.fi/handle/123456789/58972>

³³ Private correspondence with Fluigent.

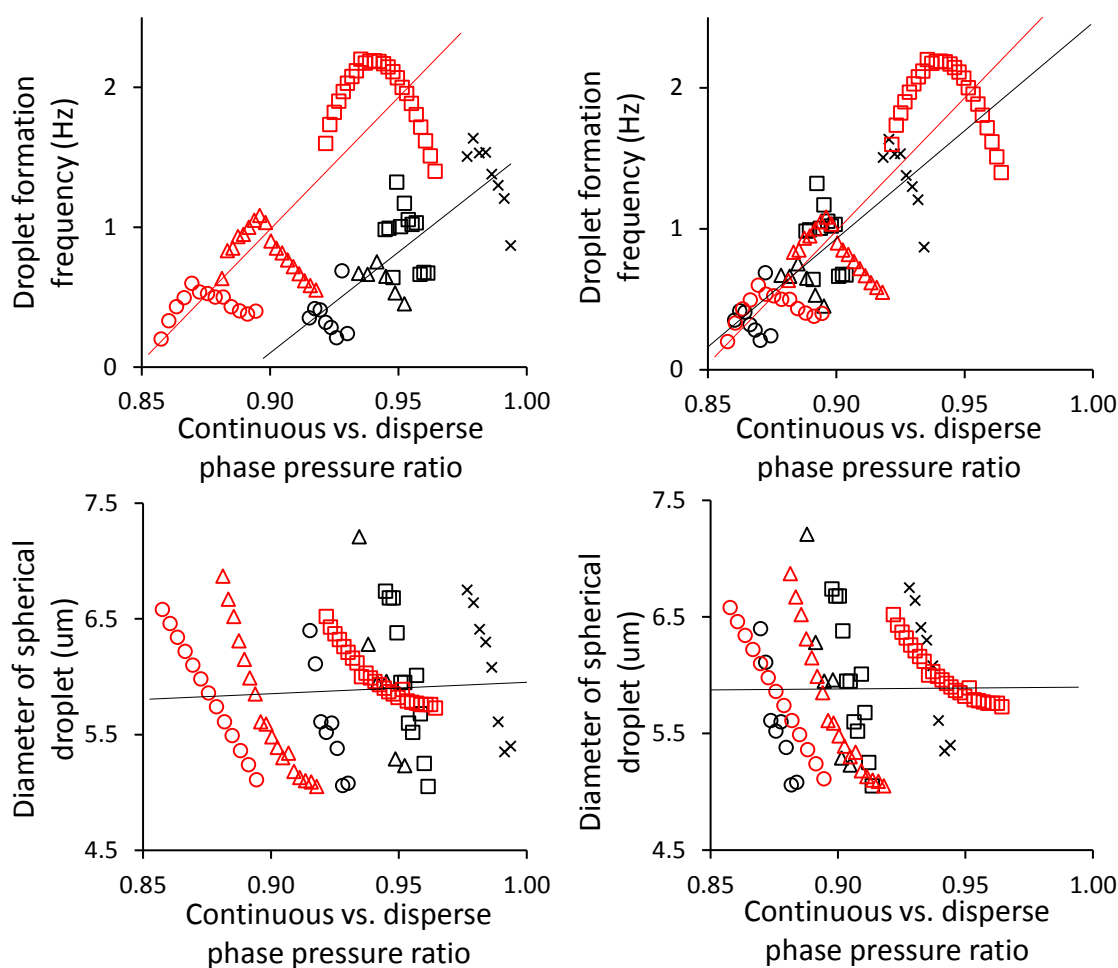


FIGURE 6.8: T-junction droplet formation frequency and droplet size as a function of pressure ratio. The red data points were measured in chip with lower hydraulic resistance (DEP-T12) compared to the black data points (DEP-T9). Data points marked with the same symbol belong to series with constant continuous phase pressure: \circ 400 mbar, Δ 500 mbar, \square 600 mbar, \times 800 mbar, \diamond 500 mbar, \triangle 750 mbar, \square 1 000 mbar. (top left) Droplet formation frequency - as measured. (top right) Droplet formation frequency - calibrated with hydraulic resistance difference factor. (bottom left) Diameter of spherical droplet - as measured. (bottom right) Diameter of spherical droplet - calibrated with hydraulic resistance difference factor.

Droplet flow unified in one channel

The channels prior to the droplet formation must be kept large for the good control of pre-filling stage, so the oil and water do not enter the wrong areas (FIGURE 6.9(a)) and their elongation would not be effective. The trap must be kept in close proximity to the sorting area because the spectroscopy and consequent sorting must fit the microscope field of view for automated measurements, and the output channels must allow free movements of the droplets. Hence, for the designed microfluidic system, the most suitable part for channel elongation is the channel right after the droplet formation. The location of the elongated channel to this part of the channel network has an added value in keeping the droplets at constant distances, a necessary requirement for the droplet sorting (FIGURE 6.11(right)) and droplet stability (see 6.5.5 Droplet stability).

The narrow channel was designed in the form of meandering ‘snake’, which allows to compress a long channel to a small area (FIGURE 6.9(b)). The length of the narrow channel was tested in the interval from 3 up to 20 mm. The length finally used in the majority of the advanced chips stabilized at ~ 13 mm, a truly large value compared to the $5 \times 2 \mu\text{m}^2$ cross section of the channel. A channel with these parameters allows ~ 1 Hz droplet formation at ~ 750 mbar for both continuous and disperse phase (FIGURE 6.8(top right)).

The droplet formed in the T-junction, if fully confined, propagates forward in the microfluidic channel at the speed given by the flow rate of the continuous phase and the cross section of the channel. The presence of a droplet in the channel, however, causes a pressure drop [127,128], which sums up with every droplet present in the channel. This brings difficulties when establishing and maintaining the droplet flow and its regularity [118]. This issue is negligible at high frequencies or in short channels, where the pressure fluctuations quickly stabilize, while the low frequency droplet production and their propagation in the long channel utilized in this project inherently magnify the instability. With up to 100 droplets present in the ‘snake’ channel at the same time, establishing the droplet flow is a highly sensitive operation as the hydraulic resistance of the droplet flow changes with every new droplet entering or leaving the confined regime. Partial improvement of the system was obtained by widening the channels to the maximal possible dimension still maintaining the confined flow (FIGURE 6.5(a)). Despite this improvement, it still takes relatively long period of time until the droplet flow stabilizes. After initiation of the droplet formation or after any change of parameters, droplets tend to pass the ‘snake’ channel in waves (groups) interrupted by a gap, where the pressure fluctuations in the channel network prevents formation of new droplets. When the group partially passes the ‘snake’ channel, the pressure balance is brought back to normal and droplet formation reoccurs. The instability in droplet production slowly disappears with time and a steady situation is established in the whole channel system. The microfluidic chips containing the ‘snake’ feature take about 15 – 20 minutes to stabilize the droplet formation and propagation. Therefore, every data point in FIGURE 6.8 was taken after change of parameters followed by >30 minutes stabilization time (also in supplementary movie [M4](#)). Nevertheless, once balanced, the flow is very stable, and the droplet frequency and size remain constant for virtually unlimited time³⁴.

Droplet flow after bifurcation

Splitting one channel into two or more is a frequently used microfluidic geometry. It finds utilization in droplet splitting [10,12,131,259], but more importantly in droplet sorting [118,144,168,174]. In general, the flow rate of the continuous phase splits according to the hydraulic resistance of the channels after bifurcation, following rules equivalent to Kirchhoff's laws for electronic circuits (see 4.3.5 Hydraulic resistance). Since the droplets are driven by the continuous flow, a droplet at the bifurcation preferably enters the channel with lower hydraulic resistance. This behavior is utilized in many microfluidic sorting techniques, where all the droplets enter the channel with lower resistance, except those, which are

³⁴ The longest uninterrupted droplet formation experiment lasted over 20 days.

actively directed to the channel with higher resistivity channel by an active sorting element [12,13,174,256,260]. This approach brings stable results but only at high flow speed and at high droplet frequency. In the case of slow droplet frequency, the situation must be considered more carefully.

- If a droplet enters a channel, which keeps the droplet in confined regime, the hydraulic resistance of the channel abruptly increases, changing the hydrodynamic situation in favor of the other channel [11]. In this way a system where the droplets regularly alter the output channel can be designed. A pressure shortcut can be added between the channels (FIGURE 6.9(c), supplementary movie [M5](#)³⁵) [174,246,256] to balance the pressure between the channels, however, the originally designed pressure ratio is not fully maintained and the characteristics of the output change with every entering droplet. Moreover, at the channel sizes on the edge of physical possibilities of wet etching, the pressure balancing shortcuts become similar in size to the regular channels. This often cause the droplets entering the balancers and restricting their functionality.
- If the output channels are much wider than the confining width, the droplets are directed to the channel with the least hydraulic resistance. However, the general reluctance of droplets to move when confined, even if only from the top and the bottom causes the droplets to stop as soon as the friction on the channel walls becomes dominant over the pushing force of the continuous flow. The flow speed in a rectangular channel is a complex function of the channel width (eq. (4.11)), nevertheless, in general it steeply drops with increased width of the channel and the push on the droplets fades. The droplets start to group in the channel, while the continuous phase just passes them by (FIGURE 6.9(d)). The droplet build-up decreases the effective width of the channel and thus the hydraulic resistance, which results in preferential droplet flow to the emptier channel. In addition, standing droplets influence the channel surface properties in the contact area, effectively decreasing the contact angle. This results to a situation where moving droplets prefer to take a path³⁶, which was previously in contact with standing droplets (FIGURE 6.9(e)).
- The third design consists of channels deeper than the spherical diameter of the droplets formed in the chip. In this geometry, the contact with any channel wall is effectively reduced (FIGURE 6.5(a)) and the droplets may move forward even with very small continuous flow speed. The drop in flow rate is so significant for the deep channels that altering their resistance does not lead to automatic flow of droplets to only one channel. However, if the bifurcation is placed in the confined regime, the length of outputs from the bifurcation can set the hydraulic resistivity ratio between channels. This solution was found to be working fine as long as the shallow outputs, prior to the deep section, are always emptied before the next

³⁵ M5 - <https://jyx.jyu.fi/handle/123456789/58973>

³⁶ This situation differs from high speed flow, where moving droplets in laminar flow are focused to the line with the highest flow speed.

droplet comes. Several geometries of the shallow-deep intersection were tested (FIGURE 6.9(f)-(h)). The narrow-shallow to wide-deep intersection (FIGURE 6.9(f)) was found to induce a droplet breakup, similar to the step-emulsification. The droplet transition, is smooth and droplet is well preserved if the pressure drop is minimized (FIGURE 6.9(g)&(h), supplementary movie [M5](#)).

6.5.3 Droplet trapping

The intensity of fluorescent signal emitted by a single molecule (nanotube) is obviously very low. This intensity is additionally diminished by losses in the optical components, and finally, hidden in the background noise originating from the sample, environment, and the detector. The single molecule detection or spectroscopy experiments utilize several approaches to increase the signal to noise ratio. A single molecule compartmentalized in the droplet can be cloned to obtain an ensemble of molecules with identical properties [12,159]. For spectroscopy of truly single molecule, even after optimizing all the parameters, long integration time is usually needed. With longer integration time, the molecule undergoes many excitation - relaxation - emission cycles and since some components of the

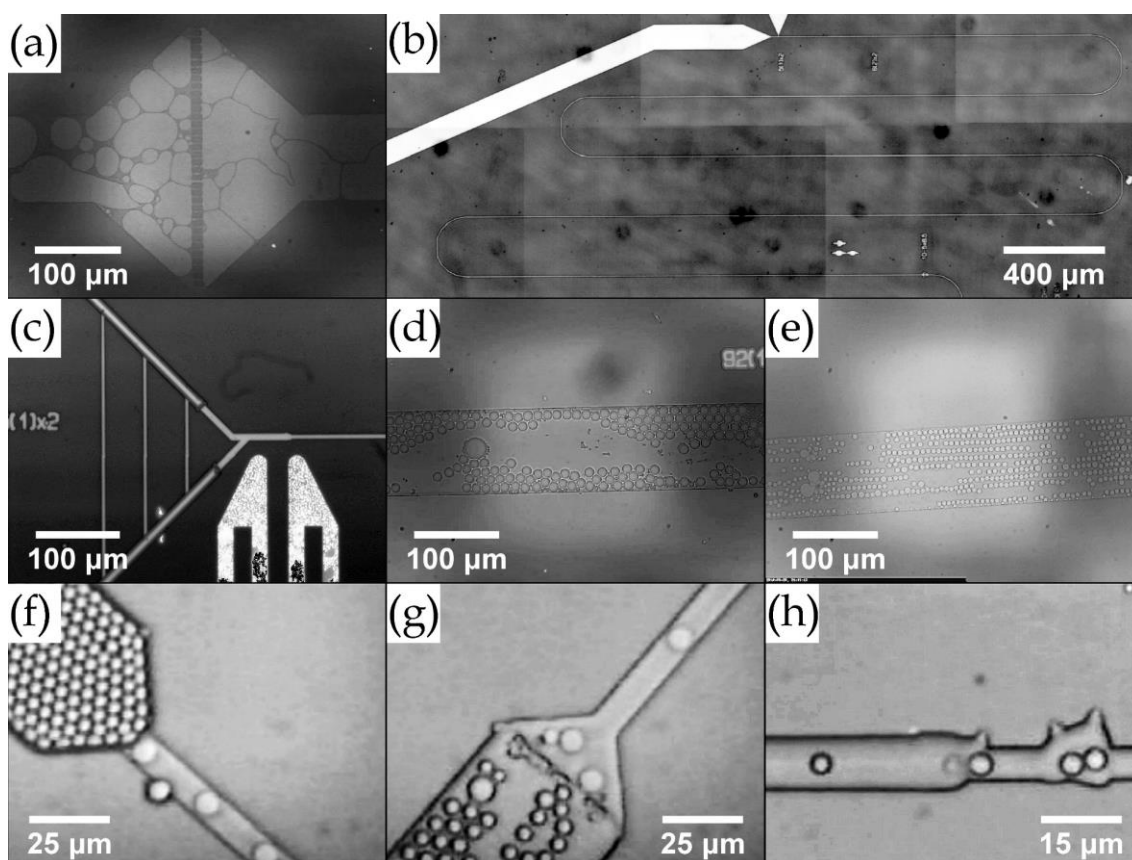


FIGURE 6.9: (a) 1 % aqueous SDBS solution accidentally entering the in-line filter. (b) The 'snake' channel increasing the net hydraulic resistance of the microfluidic system. (c) Pressure balancers placed after bifurcation. (d) Droplets confined in the wide channel, while the continuous phase just passes by. (e) Droplets following the path being in contact with previous droplet. (f) - (h) Various geometries of shallow-deep intersection.

noise are constant in time, the signal can raise above the noise. This is achieved either by stopping the flow and performing the measurement in static droplets [148,159], by temporal interruption of the flow [157,261], by active trapping [212,262], or by passive trapping [158,161,163].

Cloning as an option for magnification of the fluorescent signal from single CNT in a droplet is not viable, since there is no known method how to achieve it. Measurement in static droplets is indeed an option but static droplets have stability issues (see 6.5.5 Droplet stability) and their consequent sorting becomes tricky. In addition, the capacitance³⁷ of the system with minimized volumes effectively restrict the possibility of instantaneous stop of the flow, and last but not least, such a system does not possess the characteristics of an online system. The temporal interruption of the flow is also not applicable due to similar reasons plus the slow system response already discussed (see T-junction, p. 124). The active droplet trapping methods were not tested due to required simplicity of the system.

The passive droplet trapping methods utilize the forces on the droplet surface, which act towards the smallest surface-to-volume ratio. Therefore, the droplet always 'prefers' being spherical over cylindrical and cylindrical over elongated (FIGURE 6.5(a)). This effect, together with the droplet reluctance to movement in partially confined regime is used for construction of the droplet traps. In addition, a free path for the still-flowing continuous phase must be available. These structures are in general tricky to manufacture, as the side-channels, allowing the continuous phase to keep flowing while the droplet is trapped, must be smaller than the main channel guiding the droplet. With the main channel on the edge of wet etching possibilities, an unconventional design must be used. One of the ways is to utilize the perfect isotropicity of the wet etching of glass (FIGURE 5.7(top left)). This also results in the possibility to manufacture droplet traps only in the shallow (2 μm) part of the channel since the deep etched (4 or 6 μm) channels inherently exclude the manufacture of channels narrower than the aimed droplet diameter.

The simplest solution is a simple widening of the fully confining channel, where the droplet naturally slows down and stops, while the continuous phase can pass forward by the sides (FIGURE 6.10(a)). The advantage of this design is its simplicity; however, this geometry does not contain any obstacle for the forward droplet movement. The size of the trap can be only slightly larger than the diameter of the droplet to avoid more than one droplet in the trap. Therefore, the pushing force of the continuous flow is still rather significant, and the droplet leaves the trap at random time. The effort towards maximizing the measurement time discriminates this geometry as its potential is decreased both by unknown time for which the droplet will occupy the trap as well as wasted time when the trap is empty.

³⁷ Similarly to other parallels with electric circuits, the compressibility of the system elements can 'store' energy and release it after the pressure drops. The rigid glass system is here an obvious advantage [127] but any trapped air or even the flexibility of inlet PTFE tubes can effectively push the whole chip content out of the chip after the pressure supply is discontinued.

A variety of new geometries aimed at decreasing the empty time were designed and tested (FIGURE 6.10(b)-(g)). This iterative process resulted in a final design providing an environment, where the droplet is permanently trapped, until pushed out by new incoming droplet. It is achieved by an open triangular area with opening at the bottom, which is slightly smaller than the droplet diameter in confined regime. The droplet is pushed to the triangular section by the continuous phase flow, which is allowed to flow around the obstacle. The next incoming droplet closes the side-channels and forces the trapped droplet through the opening. The whole process of droplet exchange is very fast, resulting in nearly 100 % time occupancy of the trap (supplementary movie [M6](#)³⁸). Two slightly different versions of this trap were designed. The first is symmetric (FIGURE 6.10(h)) and the incoming droplet directly pushes the trapped droplet out. The speed of exchange and direct contact of the droplets, however, brings occasional issues with software image processing (see 8.2 Instrumentation and Automation) and coalescence (see 6.5.5 Droplet stability), respectively. The second design (FIGURE 6.10(i)) omits one of the side-channels, which leads to a small volume of continuous phase being always present between incoming and trapped droplet. The small layer of oil between two aqueous droplets effectively prevents the coalescence and allows reliable software distinction of the two droplets, and at the same time, causing only negligible decrease of the occupancy time (supplementary movie [M7](#)³⁹).

The chip manufacture process brings several issues to the reliable trapping of the droplets. Since only a small widening of the channel can partially act as a

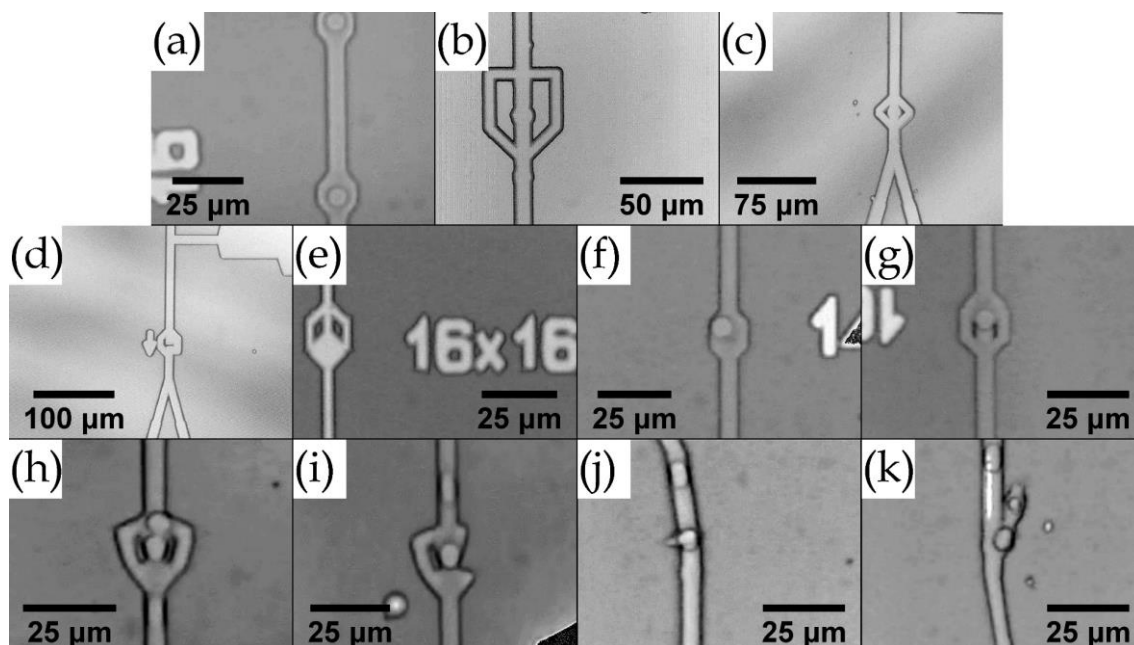


FIGURE 6.10: (a)-(i) Various passive droplet trap geometries. All structures are 2 μm deep and the droplets come from the top. (j)-(k) Etching defects disturbing the flow by acting as a droplet trap.

³⁸ M6 - <https://jyx.jyu.fi/handle/123456789/58974>

³⁹ M7 - <https://jyx.jyu.fi/handle/123456789/59018>

trap any possible defects interfering with the 'snake' channel introduce irregularity and increased possibility of coalescence in the droplet flow (FIGURE 6.10(j)&(k)). Therefore, only a flawless channel is suitable for droplet trapping. Last but not least, the trap exhibits optimal performance only within a narrow interval of droplet diameters. Due to the manufacture tolerances caused by wet etching, the traps etched through the same mask slightly differ from each other. Hence, the droplet size, which perfectly fits the trap varies from chip to chip. The final choice of continuous phase pressure and continuous versus disperse phase pressure ratio is based on the performance of the trap in the particular chip. By suitable choice of those parameters, accurate droplet frequency and droplet size can be tuned, resulting in optimal performance of the device.

6.5.4 Droplet sorting

The miniaturization of the microfluidic system brings new challenges also when it comes to the sorting. The manipulation of droplets in micrometer scale requires careful consideration of the physical principles of sorting methods and their evolution in scaled-down systems. The specific properties of the system developed in this project, namely, glass environment, W/O droplets (non-conductive, non-labeled), droplet size, and droplet frequency were the main criteria for selection of appropriate sorting technique. Based on numerous reviews covering the field of sorting [11,118,120,131,144,145,177], three applicable sorting techniques were identified.

- Hydrodynamics: Hydrodynamic sorting methods easily fulfill the requirements when it comes to fluid system, droplet size or frequency. For uniformly sized droplets, however, the only selection criteria is the hydraulic resistance of the channels after the split, since the rigid glass chip basically restricts any localized active agitation. The hydrodynamics is therefore used only to preferentially direct the droplets to one channel (see Droplet flow after bifurcation, p. 130), while another active sorting technique must be applied to deflect the droplets from the hydrodynamically driven path.
- Surface acoustic waves (SAW): An acoustic wave travelling on the material surface is known to effectively deflect droplets or particles in the flow [174,175]. The efficiency of SAW strongly decreases with the size of the droplets and the real impact on slowly moving femtoliter droplets would have to be investigated. However, the need for special design of electrodes and materials, and unavailable instrumentation restricted the utilization of this technique.
- Dielectrophoresis (DEP): DEP sorting is known to reliably sort droplets under 4 μm in diameter [12] and at frequencies over 30 kHz [176]. The low frequency of sorting in this project only demands precise aiming of the sorting impulse for the moment when the droplet is passing by the bifurcation. The speed of the droplets must not exceed a certain limit as the acting force must have enough time to deflect the droplet to the collection channel. DEP sorting was therefore chosen as the active sorting technique.

DEP - theory

Dielectrophoresis is a phenomenon in which a nonzero net force acts on a dielectric⁴⁰ particle in a non-uniform electric field. While the dielectric particle in uniform electric field experiences zero net force, the charge redistribution in non-uniform electric field results in a force directed parallel with the electric field gradient (FIGURE 6.11(left)). The theory of dielectrophoresis in microfluidics is well described in many papers [177,206,214,263]. Shortly, the dielectrophoretic force is given by

$$\vec{F}_{\text{DEP}} = \vec{p} \cdot \nabla \vec{E}(\vec{x}), \quad (6.1)$$

where \vec{p} is an effective dipole moment and \vec{E} is an applied electric field. For a spherical particle, the effective dipole moment can be expressed as

$$\vec{p} = 4\pi\epsilon_M R^3 f_{\text{CM}} \vec{E}, \quad (6.2)$$

where ϵ_M is the permittivity of the medium, R is the radius of the particle and f_{CM} is the Clausius-Mossotti factor. f_{CM} for a spherical particle is

$$f_{\text{CM}} = \frac{(\epsilon_P - \epsilon_M) + \frac{i}{\omega}(\sigma_P - \sigma_M)}{(\epsilon_P + 2\epsilon_M) + \frac{i}{\omega}(\sigma_P + 2\sigma_M)}, \quad (6.3)$$

where ϵ_P , ϵ_M and σ_P , σ_M are permittivity and conductivity of the particle and the medium, respectively, ω is angular frequency, and $i = \sqrt{-1}$. Combining equations (6.1) and (6.2), the DEP force acting on a spherical particle can be written as follows:

$$\vec{F}_{\text{DEP}} = 2\pi\epsilon_M R^3 f_{\text{CM}} \nabla(\vec{E} \cdot \vec{E}). \quad (6.4)$$

There are several general consequences arising from this equation.

- The DEP force is present only in non-uniform electric field, eq. (6.4).
- The magnitude of DEP force scales with $\sim R^3$ and $\sim E^2$, eq. (6.4).
- The magnitude of DEP force depends on difference in both the permittivity and the conductivity of the particle and the medium, eq. (6.3).
- The direction of the DEP force depends on the sign of the f_{CM} . If $f_{\text{CM}} > 0$, the particle will be attracted towards the electric field maxima and *vice-versa*, eq. (6.4).
- The DEP force attracting the particle towards the electric field maxima ($f_{\text{CM}} > 0$) can be in ideal case twice as strong as the DEP force repulsing the particle from electric field maxima ($f_{\text{CM}} < 0$), eq. (6.3).
- The magnitude of the DEP force is determined by relative conductivities of the particle and the medium in DC field, while by relative permittivity of the particle and the medium in AC field, eq. (6.3).

⁴⁰ Dielectric = non-conductive but polarizable.

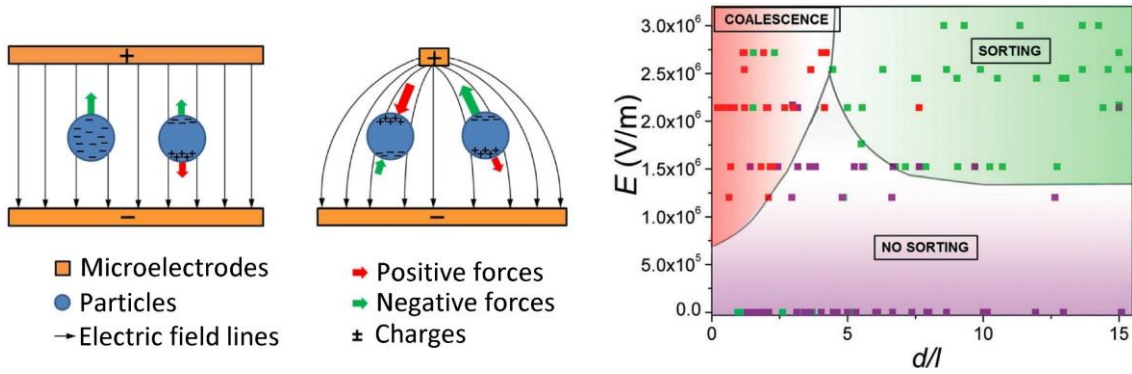


FIGURE 6.11: (left) The forces acting on a dielectric particle in uniform and non-uniform electric field. Reprinted with permission from [204]. Copyright 2014, IOP Publishing. (right) Phase diagram of the femtoliter DEP sorter. L is the length of the droplet in confined regime, while the d is the distance between two consequent droplets. Figure courtesy of Marie Leman [14], used with permission.

The frequency dependence in equation (6.3) makes AC-DEP an exceptionally versatile tool. Within one device and one electrode geometry, particles with relatively wide interval of properties can be successfully manipulated by tuning the frequency of the electric field [264]. The AC field also prevents electrode polarization and ion build-up [263] and is generally easier for implementation as the electroosmotic and electrophoretic forces do not appear in AC fields [177]. However, the frequency threshold where the DC-DEP related effects become negligible lies relatively high and the DEP can be considered ‘AC-only’ at frequencies ≥ 1 MHz [263,265]. Below this threshold, the dielectrophoresis works in a somewhat mixed regime. Nevertheless, in systems with similar conductivity of the particle and the medium and largely different permittivity, the frequency-dependent part of f_{CM} is way more significant and determines the behavior of the system. The time-averaged AC-DEP force acting on a spherical particle is given by

$$\langle F_{DEP}(t) \rangle = 2\pi\epsilon_M \text{Re}[f_{CM}] R^3 \nabla E_{RMS}^2, \quad (6.5)$$

where E_{RMS} is the root-mean-square of the applied electric AC field [263].

The particular popularity of DEP in microfluidics arises from its label-free nature, simplicity of the instrumentation, possibility to induce both positive and negative forces, and mainly from the favorable scalability [263]. The higher degree of integration in scaled-down devices allows to bring the electrodes much closer to the point of action. Hence, much smaller voltage is needed to create the same field (gradient). There is a wide variety of applications utilizing DEP force in microfluidics, *e.g.* separation based on various properties, concentration, focusing, trapping, filtering, patterning, and sorting [206,263,265].

The scalability is favorable only for manipulation of the same particle-medium system in scaled-down device. On the other hand, the DEP force drops with the cube root of the particle radius (see eq. (6.5)) and manipulation of the droplets in femtoliter scale requires significant increase in the voltage even for miniaturized microfluidic system.

Traditionally, the DEP electrodes are in contact with the liquid medium [206], which is a possible source of serious issues, especially when a strong field needs to be applied. It includes contact of the electrodes with the reagents and possible contamination, bubble formation, and fouling of the electrodes. Even more importantly, in the case of conductive fluids, intense joule heating and a consequent temperature rise may significantly affect the functionality of the system up to its total destruction in the case of biological samples [214]. However, a new technique of contactless dielectrophoresis (cDEP) was reported in 2009 [214]. This technique allows design of systems, where the electrodes are insulated from the reagents and gives possibility to create highly localized electric fields in close proximity to the point of interest. The applicability of this technique on sorting of femtoliter droplets was reported in 2015 [12,14].

In the microfluidic system developed within this project, the medium was n-decane continuous phase, while the aqueous droplets were considered particles. The relative permittivity of water and decane is ~ 80 and ~ 2 , respectively [266], a difference which calls for employment of the AC-DEP sorting technique. The task for electrodes implemented in the microfluidic chip is to create a localized non-uniform electric field in the place of droplet manipulation. Since the non-uniformity of the electric field must be in the scale of the droplet dimension, the electrodes have to be carefully designed to create an electric field of the right *shape*. The *position* of the electric field is also crucial for the proper performance of the DEP device.

- Electrode position: The electrodes must be generally positioned relatively close to the channel. In a system similar to ours [14], a distance of 40 μm is found to be borderline for the functionality of a DEP trap operating at 1000 V, while other similar systems have the channel and electrodes separated by a wall ranging from 15 μm [13] to 30 μm [260]. Understandably, the closer distance allows to decrease the voltage and thus lowers the requirement for the instrumentation. Our experiments confirmed that a properly assembled and thermally bonded microfluidic chip does not show any signs of leaking from the channel to the electrode area already at the distance of $\geq 5 \mu\text{m}$. The sorting chips were routinely prepared with $\sim 10 \mu\text{m}$ wall between the channel and the electrodes.
- Electrode shape: Many different shapes of the electrodes were designed (FIGURE 6.12(a)-(g)) and simulated in COMSOL (FIGURE 6.12(h)). Their geometry was based either on our own design (FIGURE 6.12(a)&(b)&(g)) or inspired (FIGURE 6.12(c)-(f)) by papers dealing with similar microfluidic systems [13,214,256,260]. The best sorting performance was observed with geometry of electrodes (FIGURE 6.12(e)) previously reported to reliably sort femtoliter droplets [12,14].
- Electric field: While the gradient of an electric field is set by the position and shape of the electrodes, its magnitude is effectively driven by the voltage applied across the electrodes. These parameters create the DEP force, which is, at some point, able to deflect the droplet to the proper channel. The literature rarely describes the estimation of the DEP force, e.g. [260].

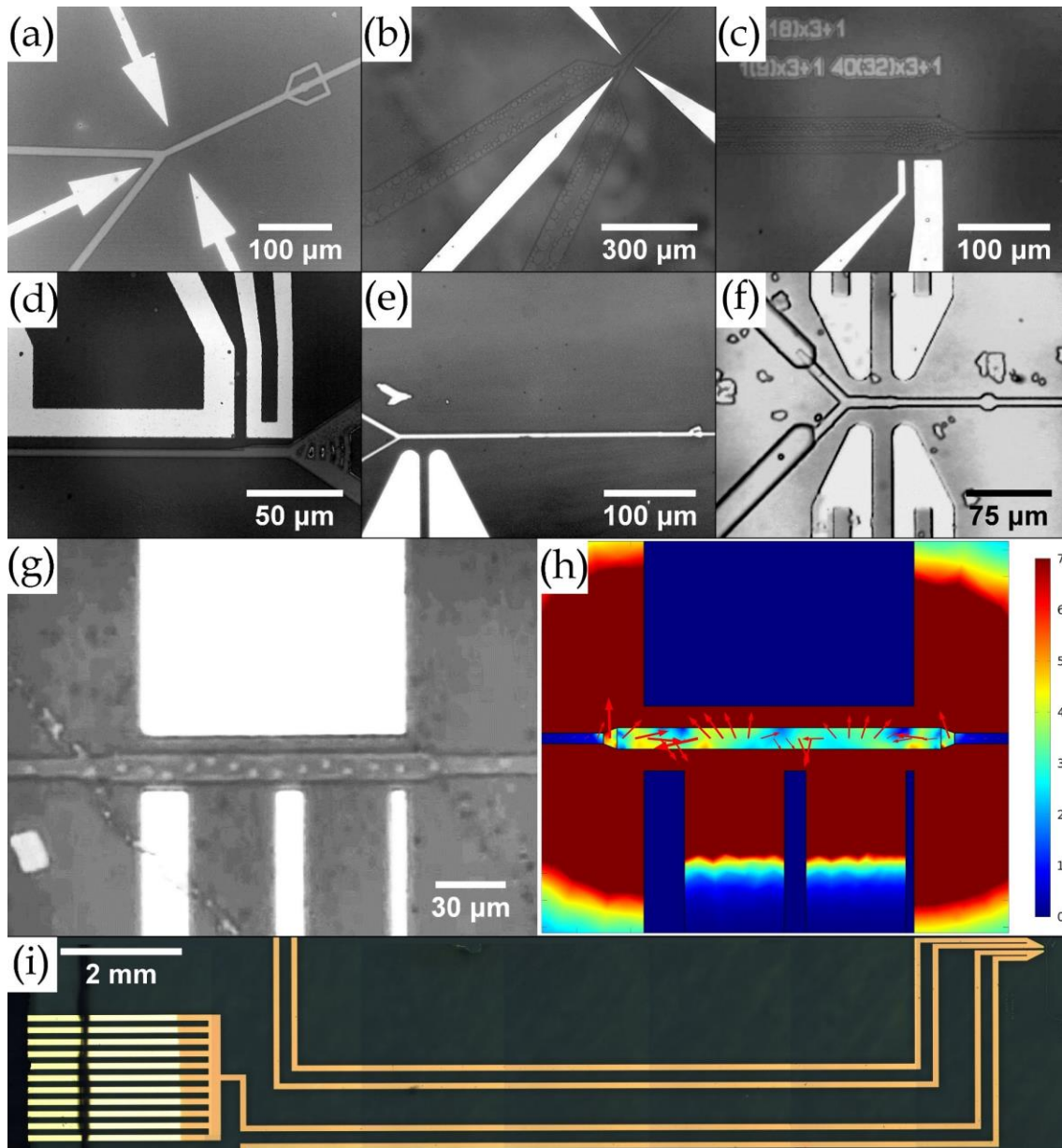


FIGURE 6.12: (a)-(g) Various geometries of DEP electrodes. Experimental testing (g) and numerical simulation of the DEP force (h) in the microfluidic channel. (i) Layout of the whole electrode. There is a connection pad on the left and an active tip on the right. The loop design allows verification of functionality.

More common description consists of the electrode geometry and characteristics of the applied voltage. The microfluidic DEP-based sorting systems comparable with the system designed in this work use AC voltage in the range of 100 - 1 600 V with frequencies between 1.5 - 125 kHz [12,13,183,214,256,260]. The driving voltage is generated either by a combination of a signal generator (NI DAQ card, R&S AM300) and a high voltage high frequency amplifier (Trek, Kepco) or by a custom-made high frequency high voltage signal generator [214]. The referenced sorting systems, except [12], work with larger droplets (20 - 25 μm) but also with more distant electrodes. The experiment reported in [12] confirms, that properly chosen geometry of electrodes and reduced distance from the

sorting point can successfully compensate the unfavorable size of the droplets (see eq. (6.5)).

DEP - instrumentation

Since no high voltage signal generator [214] nor high voltage high frequency amplifier [12,13,256,260] were available in-house, a need of source for DEP signal arose. The initial requirements were set as a generation of a 30 kHz square wave with an amplitude of up to 1 000 V, based on values from the literature of successful sorting experiments. The initial design based on a laboratory signal generator and high frequency 8:1 300 Ω AC impedance transformer failed due to too low output power of the signal generator. Next generations of the DEP signal generator were based on fast switching of high DC voltage from a KEITHLEY 2410-C 1 100 V SourceMeter®. The basic requirement for the switching element was the ability to switch high voltages. The switched power does not play a role here since there is no closed circuit loop following the switch. A DEP-driving circuit based on MOC 3083M optocoupler was successfully build and tested, however, the LED turn-off time theoretically limits the switching frequency to 5 kHz, and in practice to about 2.5 kHz.

The final solution is based on a high voltage FQP2N90 N-Channel QFET® MOSFET. The FQP2N90 connected to the DEP driving circuit allows switching of the high voltage at 30 kHz frequency with reasonably preserved wave shape. With further miniaturization, the signal generator was replaced by a 555 timer integrated circuit. Two versions of the DEP driver were designed, built, and tested. The first one uses an RC circuit to trigger the 555 timer at a fixed frequency of ~ 28 kHz (FIGURE 6.13(top)). The circuit is equipped with a manual switch, connecting or disconnecting the DEP signal from the microfluidic chip. Most of the sorting experiments presented in this section were performed using this circuit. The 555 timer in the second design (FIGURE 6.13(bottom)) is triggered externally from an Arduino Uno unit. The Arduino unit is controlled by automation software (see 8.2 Instrumentation and Automation) and allows comfortable selection of frequency and duty cycle, while the driven voltage amplitude is set on the high voltage generator. Nevertheless, the generation of signal with predictable wave shape is limited to ~ 30 kHz or by the pulse width of about 30 μ s.

DEP - sorting

The behavior of a droplet exposed to the electric field will vary significantly according to the environment the droplet is exposed to. The contact with channel walls, flow rate and speed of the continuous phase, and presence of (an)other droplet(s) may result in different outcome when exposed to the same electric field. The most obvious difference relies on the presence of another droplet in close proximity to the sorted droplet. If another droplet is within a certain distance from the droplet at which the DEP field is applied, electrocoalescence will take place rather than sorting [14,118,121,123,131] (FIGURE 6.11(right)). Hence, based on the design of the droplet flow, one can use the DEP technique for either active coalescence or active sorting. This possibility is limited to droplet microfluidics, as *e.g.* cells are not subject to coalescence.

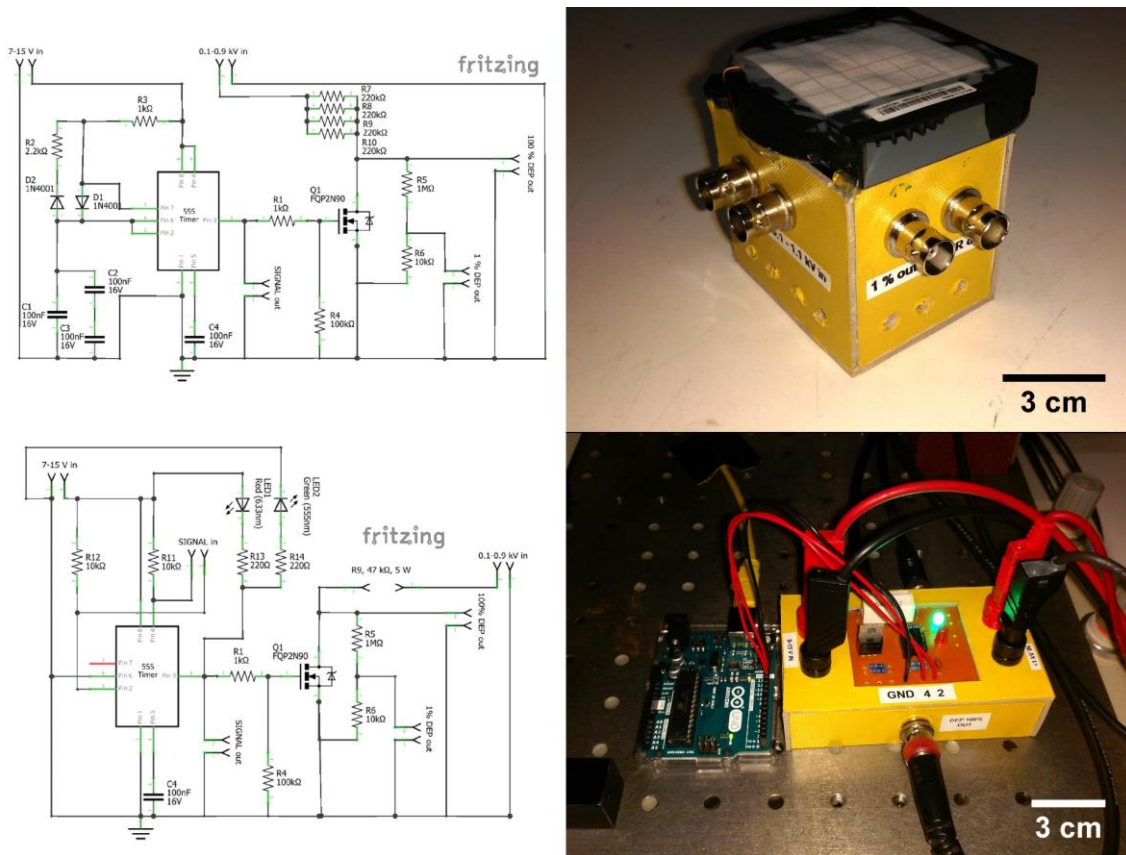


FIGURE 6.13: 28 kHz fixed frequency DEP driver: (top left) circuit diagram, (top right) assembled unit. Arduino controlled DEP driver: (bottom left) circuit diagram, (bottom right) assembled unit.

If sorting is the goal, the necessity to keep the droplets separated is generally applied throughout the relevant literature [13,183,256,260]. However, the explanation and experimental confirmation are rarely present [12]. There are two possible approaches how to prepare the droplets for sorting. They can be either kept separated from the moment of droplet formation [260] or reinjected from a densely packed reservoir by supplying more continuous phase from a new side channel [13,176,246,256]. Reinjection is usually preferred, especially for applications, where droplets undergo some sort of collective treatment before the sorting itself [12]. The main disadvantage of reinjection, however, is its low reliability at low frequency/speed flow, similarly to droplet formation. The experimental attempts to achieve droplet separation for this project showed acceptable regularity at droplet throughput of >100 Hz (FIGURE 6.14(a)). This value is in contradiction with ~ 1 Hz throughput needed for single CNT spectroscopy. In addition, coalescence of droplets close to each other is relatively far-reaching and often destroys all the droplets in the system (FIGURE 6.14(b)).

The system with low droplet frequency must therefore use an approach, where the droplets are kept separated from each other for the whole time from their generation until the sorting. The droplets are naturally separated by distances originating from the droplet formation frequency and the flow rate of the continuous phase. In non-confined regime, they freely flow at the flow speed of

the continuous phase (supplementary movie [M8](#)⁴¹). However, the undercut created during the wet etching process effectively prevents manufacture of traps with depth necessary for non-confined droplet flow. Therefore, the only geometry providing reliable separation of droplets and their regular supply for measurement and sorting is the fully confined regime. Actually, the utilization of the 'snake' pattern between the droplet formation and the trap was partially inspired by the need of keeping the droplets separated.

Since the sorting geometry is virtually identical with [12,14], the sorting phase diagram (FIGURE 6.11(right)) should reasonably represent the behavior of droplets influenced by the electric field. The different separation distance of the electrode - channel geometry used in our system ($\sim 60 \mu\text{m}$) manifests itself by a vertical shift of the phase diagram. Indeed, at fields below $3 \cdot 10^6 \text{ V}\cdot\text{m}^{-1}$ (amplitude of $\sim 200 \text{ V}$), the response of the system is negligible. With increasing voltage, the response of the system depends on the separation of the *confined* droplets.

- Droplets in contact immediately coalesce (FIGURE 6.14(b)&(c), supplementary movie [M9](#)⁴²), often disturbing the flow pattern as the doubled (tripled, ...) droplet is experiencing increased hydraulic resistance in the channel with limited cross section.
- Separated droplets are effectively directed to the desired channel (FIGURE 6.14(d)&(f), supplementary movie [M10](#)⁴³), with the optimal field of $6 \cdot 10^6 \text{ V}\cdot\text{m}^{-1}$ (amplitude of $\sim 400 \text{ V}$). The direction of the droplets without the applied field depends on the hydraulic resistance of the output channels and flow regime. The equivalent channels separate the droplets in $\sim 1:1$ ratio (supplementary movies [M5](#)&[M9](#)), while for the non-equivalent output channels are redistributed according to hydraulic resistance of the outputs (supplementary movies [M8](#)&[M10](#)).

The droplet in *free regime* is also subject to sorting when separated, however, it does not suffer from coalescence when in contact with another droplet. The doubled (tripled, ...) droplets seem to create dipoles, which orient in the direction of the electric field (FIGURE 6.14(e)). If the droplets are exposed to excessive fields above $10^7 \text{ V}\cdot\text{m}^{-1}$ (voltage above $\sim 700 \text{ V}$), they undergo violent process of deformation, breakup, coalescence and formation of satellite microdroplets (FIGURE 6.14(c)).

DEP - troubleshooting

There is no clearly better strategy for the sorting since both the shallow and deep sorting (supplementary movie [M8](#)) have their advantages and disadvantages. The output channels are very close to the electrodes and certainly affected by the DEP field, which, together with the slow speed of the droplets, amplifies the probability of post-sorting coalescence (supplementary movie [M10](#)). Since the coalesced droplets introduce significant irregularity to the output flow, the

⁴¹ M8 - <https://jyx.jyu.fi/handle/123456789/59019>

⁴² M9 - <https://jyx.jyu.fi/handle/123456789/59020>

⁴³ M10 - <https://jyx.jyu.fi/handle/123456789/59021>

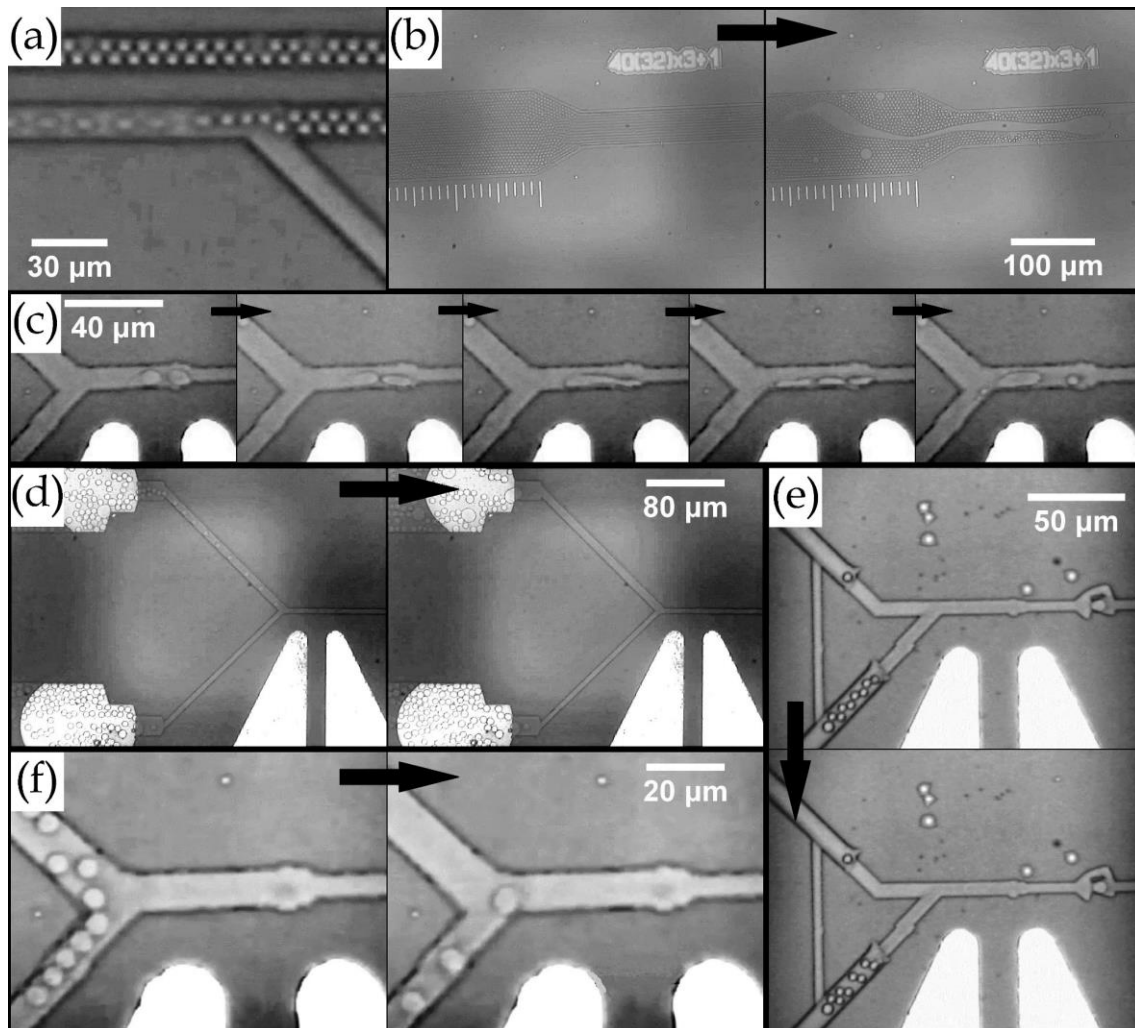


FIGURE 6.14: (a) Separation of densely-packed droplets. (b) DEP coalescence of densely-packed droplets. (c) Deformation and coalescence of droplets exposed to high DEP field. (d) Wider channel exhibits lower hydraulic resistance and droplets naturally flow through. When the droplets are exposed to DEP field, they are force flow to the channel with higher hydraulic resistance. (e) Droplets in free regime tend to create pairs. When exposed to electric field, such a pair orients according to the field orientation. (f) Droplets flowing randomly to either channel are under DEP field directed to only one channel.

presence of coalescence is highly undesirable. The DEP induced coalescence was never observed in the free regime, however, the grouping of the droplets at slow flow rates influences the throughput of the output channel.

The often reported observation of droplets reliably choosing the channel designed with lower hydraulic resistance [12,13,118,125,256,260] was not found to hold at the low droplet speed. Even with the clear preference for one output channel, the droplets sometimes enter the wrong channel and the idea of passive directing of droplets to only one output channel with 100 % reliability is naïve [11]. The main strength of sorting in the deep channel seems to be in the easier definition of the preferential flow (supplementary movie [M8](#)) together with the decreased risk of DEP induced coalescence. However, the exact geometry of the sorting area must still be fine-tuned as this geometry was implemented to the microfluidic system in very late stages of the project.

An attempt has been made to actively control the droplet flow to both the output channels (FIGURE 6.12(f)). However, two major issues arose with this geometry. The presence of the second pair of metal electrodes strongly influence the shape of the DEP field. No matter if the inactive pair of electrodes is kept grounded, floating, or on the high potential, the gradient of the electric field does not act on the droplets in the desired way. A new design of electrodes based on simulation would perhaps result in a better working geometry, however, one more significant issue has arose with the attempts to actively control both the output channels. Since every droplet has to be navigated to corresponding channel, the electric field would have to be applied virtually nonstop. The long-time active DEP field has, however, negative influence on the functionality of the whole microfluidic chip, even in surprisingly distant places. Distant coalescence alters functionality of the traps, changes the droplet size and droplet formation frequency, and even changes in the regularity of droplet formation are observed with the constantly applied electric field. This observation brings up the need of restricting the application of the DEP sorting only for the time necessary to deflect the droplet to the desired channel. The timing functionality is commonly applied for high-throughput sorting, where the DEP force must be addressed with high temporal precision [12,176,256,260]. Nevertheless, the low speed system apparently also requires precise timing of the DEP sorting impulse not so much due to the precision of the sorting but because of the negative effects on the whole system. The need for precise switching led to the development of the Arduino controlled DEP driver (FIGURE 6.13(bottom)) and the implementation of the timing and delay settings to the automation software (see 8.2 Instrumentation and Automation).

6.5.5 Droplet stability

The droplet stability issue must be addressed as it is crucial to keep the droplets stable from the moment of formation via trapping, spectroscopy, and sorting up to the relatively long periods (hours, or even days) prior to their future use. Aqueous droplets must be stable both in the environment of oil as well as in the presence of other droplets. In addition, content exchange between droplets must be avoided [14]. Since the pure existence of droplets in immiscible phase is energetically unfavorable, the presence of emulsifiers is needed to create a metastable configuration preventing the two phases from separation. The emulsifier also creates a barrier between the content of the droplet and the continuous phase environment. The SPAN 80 and TWEEN 80 emulsifiers were used to stabilize the droplets in this experiment (see 6.4 Reagents). The concentration of the emulsifiers needed to stabilize the femtoliter emulsion and related stability issues are addressed in the following paragraphs.

The CMC of SPAN 80 in decane was reported to be 0.001057 % w/w⁴⁴ [249] or 0.033 % [143] for a planar oil-water interface. These values are, however, much lower than the emulsifier concentrations regularly used in microfluidic experiments, where the values vary from 0.1 % [139] to 20 % [138] or even 30 % [247], but usually lie between 1 – 3 % [248,251,267]. This difference originates from the

⁴⁴ All emulsifier concentrations in this section are expressed in % w/w.

interfacial area being much larger in emulsions than for the planar interface. The surfactant molecules are localized on the continuous phase - droplet interface and micelle formation is initiated only at much higher concentrations. This effect is strengthened towards smaller droplets as their surface-to-volume ratio is a linear function of the droplet diameter. Therefore, the apparent CMC for microemulsions is much higher than for a planar interface [248].

One way how to approach the amount of required emulsifier is to calculate the concentration from the oil-water interfacial area and molecular area of the emulsifier at the interface. For a single layer of densely packed spherical droplets (FIGURE 6.9(f), FIGURE 6.14(b)), an elementary cell can be defined as a water sphere within a hexagonal prism. The volume not occupied by water is filled with oil phase. For a droplet with 4 μm diameter, the elementary cell consists of 33.5 fL of water and 49.6 fL of oil with the interfacial area of 50.3 μm^2 . The molecular area of SPAN 80 at the decane-water interface was reported to be $\sim 35 \text{ \AA}^2$ [143,249], which results in $1.103 \cdot 10^{-16} \text{ kg}$ of SPAN 80 necessary to create a complete monolayer. The CMC in this emulsion is then $\sim 0.3 \%$.

The concentration of emulsifier at CMC is, however, not a guarantee of stable droplets. The concentration providing stable environment is several times higher than CMC as interactions with microfluidic chip surfaces and spatial and temporal availability of the emulsifier play a significant role in the formation of the protective monolayer on the interface [14]. There is also evidence of molecular reorganization, and multiple layer formation, further increasing the 'consumption' of the emulsifier [143]. Therefore, the final concentration of the emulsifier must be experimentally tailored for a particular system.

There are plenty of possible droplet failure pathways in the microfluidic channel [132,179]. Five particular failure mechanisms were observed in the developed microfluidic system.

Coalescence

Insufficient amount of surfactant usually manifests itself by coalescence [14,123,251]. The droplets stay stable when separated but merge together immediately upon contact with each other (FIGURE 6.15(a)) or the droplet formation cannot even be initiated (FIGURE 6.15(b)). These effects can be observed at concentrations below 1 % of SPAN 80 in decane. The droplets are more susceptible to coalescence when confined, while the SPAN 80 concentration threshold for stable droplets is much lower for spherical droplets. This creates an additional reason why it is better to keep the droplets separated while confined (see DEP - sorting, p. 140). Nevertheless, the droplets are not vulnerable to coalescence at $\geq 1 \%$ SPAN 80 concentration in decane. In certain cases, the coalescence at higher SPAN concentration can be initiated by impact of one droplet to another one (end of supplementary movie [M4](#)) [158]. This effect cannot be simply solved by increasing the emulsifier concentration and must be addressed by proper channel geometry.

Droplet splitting

Independent of emulsifier concentration, the droplet may split upon impact (FIGURE 6.15(c)). Again, proper design of microfluidic channels is crucial in order to avoid unplanned droplet splitting.

Droplet deformation

The interfacial tension between water and decane [268] rapidly decreases with increasing emulsifier concentration up to the CMC. Above the CMC, the interfacial tension decreases at much slower rate [143]. Nevertheless, the introduction of additional surfactant, *e.g.* TWEEN 80 for the studied system, can decrease the interfacial tension almost to zero [251]. The forces determining the spherical shape of the droplets are minimized and even a subtle disturbance can cause deformation of the droplets (FIGURE 6.15(d)). The hydrodynamic properties of deformed droplets are quite different from cylindrical/spherical droplets and their behavior in the microfluidic system is difficult to predict. In addition, the presence of TWEEN 80 in the water phase drastically decrease its surface tension relatively to the channel walls. As the whole droplet formation process is driven by contact angles of the oil and water phases on the channel surfaces (see 4.4.1 Droplet formation in open and confined system), the droplet formation is negatively affected, often even disabled.

Micelle formation

At emulsifier concentration above CMC, the emulsifier not located at the interfaces starts to create micelles or nanodroplets with negligible amount of water [182]. This effect becomes prominent at relatively high emulsifier concentrations [251]. The micelles appear like 'fluffy' objects surrounding the droplets and their appearance is more obvious at slow flow rates (FIGURE 6.15(e)&(f)). The presence of micelles/nanodroplets was observed at SPAN 80 concentration ≥ 4 % and in combined systems of ≥ 3 % SPAN 80 in decane and ≥ 3 % TWEEN 80 in water. Since the micelles interact with the channel walls and tend to aggregate, their presence negatively influences flow in the microfluidic systems.

Droplet shrinking/leaking

The nearly negligible but existing water solubility in hydrocarbon oils [269] (see TABLE 6.1) causes leaking of the droplet content to the continuous phase due to the concentration gradient [12,132,161,270]. The water molecules from an unprotected droplet surface can easily penetrate in between oil molecules while the droplet volume decreases⁴⁵. The importance of this effect increases for droplets with high surface-to-volume ratio [14]. A simple estimation based on the parameters of the developed system can show the rate of water diffusion into the oil phase. A 35 fL water droplet will dissolve in ~ 650 pL of anhydrous decane (TABLE 6.1). At a continuous phase flow rate of 5000 fL s^{-1} , a single static droplet totally disappears in ~ 2 minutes.

⁴⁵ This effect is not the Ostwald ripening [12,14,132,133,178,179,247,252,271] where the smaller droplets shrink due to the content transfer to larger droplets via continuous phase. Since the droplets produced in developed microfluidic system are highly monodisperse, the driving force for possible Ostwald ripening is negligible.

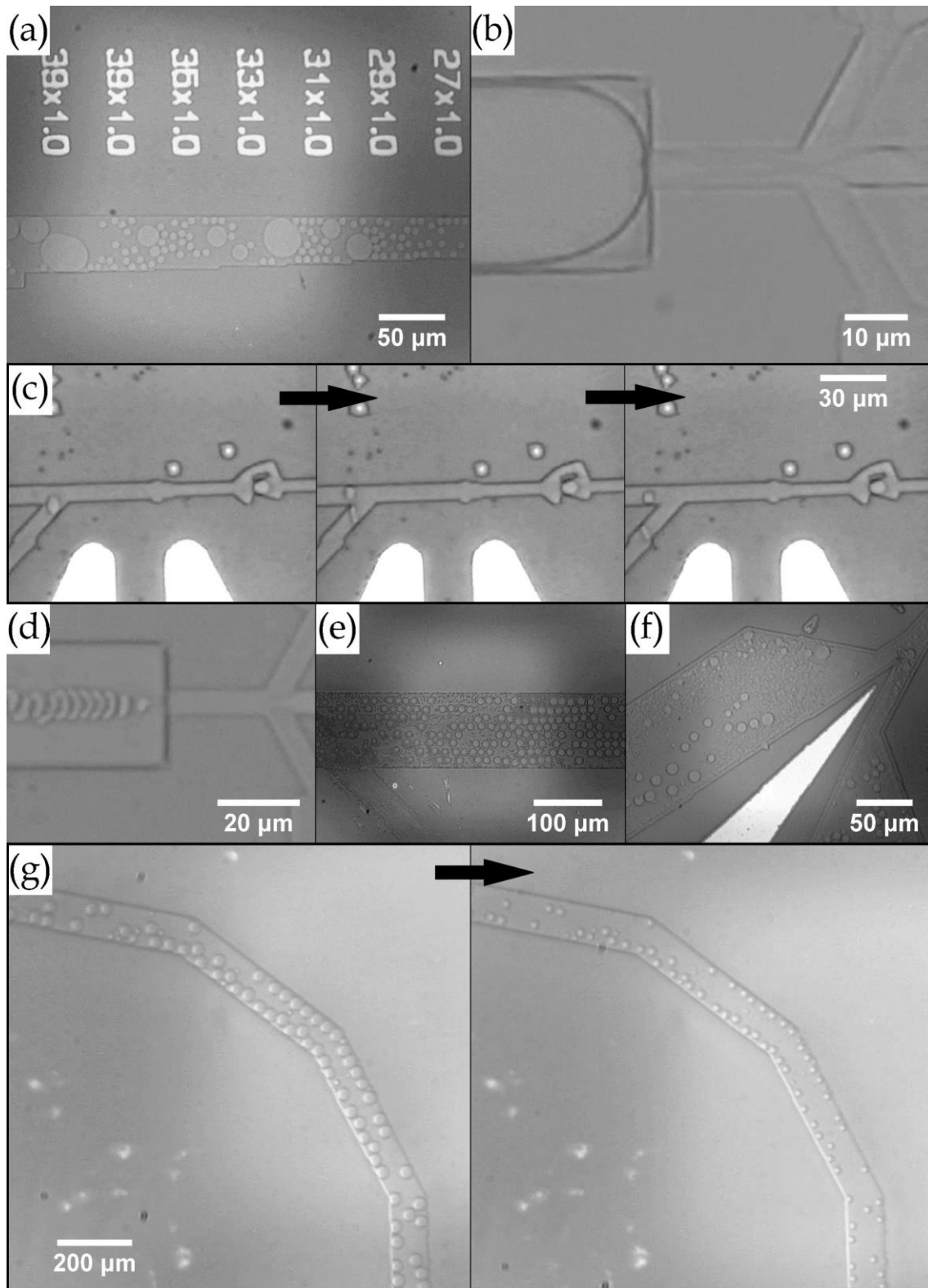


FIGURE 6.15: (a) Coalescence of droplets at low emulsifier concentration. (b) Droplet formation not initiated at low emulsifier concentration. (c) Droplet splitting upon impact on an obstacle. (d) Low interfacial tension initiated droplet deformation. (e)-(f) Formation of micelles at high emulsifier concentration. (g) Shrinking or leakage of confined droplets caused by slow flow of the continuous phase. The time difference between plotted frames is 16 hours.

The leaking of the droplet content can be impeded by the choice of oil with lower water solubility [247,270], the presence of emulsifier or by other reagents insoluble in oil [14,143,237,251,267,270,272]. The layer of emulsifier on the droplet surface significantly lowers the leaking rate, however, the droplet is never a fully sealed container as small molecules can always diffuse through the emulsifier layer [118,272]. The diffusion rate increases with decreasing droplet diameter as the lipophilic tails at the interface are less densely packed. The leaking rate is even faster for confined droplets, where the radius of curvature has its local extrema at the interface of confined and free regime (FIGURE 4.3) [130,253].

The addition of 1 – 3 % SPAN 80 significantly lowers the droplet leaking in the developed system. The nature of shrinking caused by leaking of droplet content to the continuous phase was confirmed in this study. Little to no droplet shrinking was observed for densely packed droplets (FIGURE 6.9(f), FIGURE 6.14(b), no change in size for 7 days) [252]. The shrinking was not observed for droplets confined in ‘snake’ channel with no access to ‘fresh’ decane, neither for droplets freely moving together with the decane flow, or for static droplets in static decane. This observation suggests an existence of a decane area saturated with water surrounding the droplet with a gradient of water concentration away from the droplet. The major unresolved droplet shrinking issue is the stability of static droplets in the flow of decane (FIGURE 6.15(g)). This situation takes place when the flow is stopped, *e.g.* for prolonged measurement of the droplet content. If the droplet is at least partially confined it remains static which makes the measurement easier. However, any flexible part of the microfluidic system or air bubbles trapped in the system tend to cause non-negligible flow of the continuous phase when the driving pressure is disconnected. This flow is a source of ‘fresh’ decane and the droplet content freely leaks to it (supplementary movie [M11](#)⁴⁶). In addition, the emptied droplets end up as emulsifier micelles which restrict further functionality of the microfluidic system.

Many possible ways were reported for how to improve the stability of the leaking droplets. Decane can be changed to another hydrocarbon oil without affecting the system properties too much. Hexadecane was reported to increase the stability of the system due to lower water solubility [247]. The difference in water solubility is, however, very small (TABLE 6.1) and our experiments did not show statistically significant improvement of droplet stability. In addition, hexadecane was found to be too viscose for efficient functionality of micrometer-sized channels. Another possibility is to saturate the decane with water before it is used in a microfluidic system [267]. The employment of water saturated decane in our experiments showed only subtle decrease of droplet leaking rate⁴⁷, however, the manipulation with saturated decane, namely the introduction of SPAN 80 became virtually impossible. Even a minimal excess of water leads to immediate formation of nanodroplets and depreciation of the continuous phase. Also, other reagents/solutes can be added to the system to improve its stability⁴⁸ [12]. The

⁴⁶ M11 – <https://jyx.jyu.fi/handle/123456789/59022>

⁴⁷ Partially probably due to improperly designed saturation protocol.

⁴⁸ For possible biological applications: the effect of NaCl dissolved in water phase and the effect of system temperature on the stability of the emulsifier layer is often discussed with inconclusive results [143,237].

only extra reagent tested with the aim of increased stability was TWEEN 80. Its presence, however, did not show any added value to the stability of the droplets and since it contributes to various instabilities in the system, the use of TWEEN 80 emulsifier was discontinued.

The final solution addressing the droplet shrinking lies in the geometrical design of the channels. The geometry of the system must be designed by applying following rules.

- Droplets must have possibility to move freely with the continuous phase (deep outputs).
- If the particular functionality of the chip allows it, grouping of the droplets is preferred over keeping droplets separated.
- If the droplets must be confined, they must be confined fully ('snake' channel).
- If the bypass flow of continuous phase is necessary (trap), the access to the droplet must be restricted by suitable geometrical structures (FIGURE 6.10(i)).
- If the droplets are requested to remain static (prolonged measurements), the rigidity of the system [157] and restricting the presence of air in the system [127] are crucial for minimizing uncontrolled continuous phase flow (see 6.1 World-to-chip interface).

7 Conclusion on microfluidics manufacture and operation

The manufacturing process and functionalities of the microfluidic system with the aim for single CNT spectroscopy and sorting were successfully developed and tested. The manufacturing process is robust and highly repeatable. The microfluidic system works at extremely low Reynolds number, eq. (4.4), and thus it is strictly laminar. The capillary number, eq. (4.6), suggests that both the viscous and capillary forces play a significant role in the system behavior. It results in lower droplet monodispersity and stability of droplet formation frequency, however, properly designed channel geometry makes the system sustainable. The tailoring of the microfluidic system for CNT sorting could still benefit from certain improvements. Shallower channels ($\sim 1 \mu\text{m}$) would bring the possibility to work with even smaller droplets and their reliable manipulation. Improvements in the geometry of the channels could bring increased manufacture fault tolerance and decreased risk of clogging. The specific droplet aimed sorting needs fine-tuning of the sorting parameters and some effort is needed to resolve the droplet leaking issue.

Several remarks should be highlighted before any broader employment of the developed microfluidic technology. The manufacture processes, especially wet etching, is tested only for very shallow structures. Any possible scale-up of the dimensions should be thought carefully. The sorting system based on cDEP is widely applicable as the electrodes are not in any contact with the samples. As the cDEP efficiency increases with growing dimensions of the system, it should be possible to achieve sorting with not such high requirements for the instrumentation (see eq. (6.5)).

The system was tested up to 6 bars of net pressure difference. Since the glass microfluidic chips are known to withstand pressures exceeding 100 bars without any problems [184], the possible applications requiring higher pressures would be probably limited by the durability of the world-to-chip interface and other parts of the microfluidic system.

BOOK III - CNTs IN MICROFLUIDIC SYSTEM

8 Microfluidics for carbon nanotubes spectroscopy and sorting

The success in preparation of a stable and high density dispersion of individualized SWCNTs together with development of femtoliter droplet-based microfluidic system became rudimentary cornerstones for the ambitious goal of 100 % pure CNT sorting. The basic idea was to simply replace the disperse aqueous phase in the successful microfluidic experiments by the prepared CNT dispersion. This process would lead to a combined technique consisting of single 'molecule' detection/spectroscopy (SMD/SMS) and fluorescence activated droplet sorting (FADS). While both of these techniques are relatively well established, their combination have not been reported to this day to the author's best knowledge. The following chapters describe the process of introducing the CNT dispersion to the microfluidic system and resolving of the related challenges.

8.1 Introduction to SMS and FADS

8.1.1 Brief history of SMS and FADS

SMS reaches way back in history to the case of gas spectroscopy at ultralow pressures. The single molecule sensitivity in condensed phase was attained nearly 30 years back [273]. Since then, a whole set of new knowledge has arisen from exciting experiments, particularly profiting from the data obtained from single molecules rather than from averaged information of ensembles. The abrupt development in the field already resulted in successful commercial applications like superresolution microscopy.

The rise and further development of SMS were made possible by both the increasing sensitivity of the detectors as well as by the discovery of new physical principles and detection techniques. The development in the field of confocal microscopy coupled with photomultipliers (PMT), avalanche photodiodes (APD), or state-of-the-art CCDs [274] brought unprecedented sensitivity, making laser-induced fluorescence (LIF) the most effective detection technique [118,164,165,274].

The advent of microfluidics opened a vast field of possibilities at very small scales. The utilization of fluorescence spectroscopy in microfluidic systems is particularly tempting since the background noise scales down with the detection volume while the signal remains constant [15,162,275]. Hence, the signal to noise ratio, the crucial factor for successful detection, increases by decreasing the detection volume. Confocal LIF microscopy inherently works with small detection volumes. This is, however, an obvious disadvantage for highly diluted samples

of large volumes. The low concentration of an analyte, its unknown position, and often also its random movement together with minimal detection volume makes the localization and detection of the analyte virtually impossible [165]. The replacement of various cells, cuvettes and capillaries by microfluidic channels allows much more effective exposure of the analyte to the detection system as the sample is focused to a small area of the microfluidic channel with better overlap with the detection volume. The conventional microfluidic systems (characteristic length in tens of μm) do not fully overlap with the confocal detection volume and special adjustments of the optical setup [13] or channel geometry [276] must be used to effectively detect signal from the complete sample. For the femtoliter scale microfluidics (characteristic length in units of μm), this is not an issue anymore as the detection volume fully overlaps with the microfluidic volume [165,275].

8.1.2 Current situation in SMS and FADS

The ultimate connection of microfluidic systems and fluorescence microscopy allowed new discoveries in research of single cells and even single molecules. The new systems allowed progress in cancer research [277], cellular biology [262], molecular biology [12,159], genetics [276,278], *etc.* Further development of microfluidic technology for single cell screening extended the functionality of the system to a concept known as fluorescence activated cell sorting (FACS) [261,279]. In FACS, the signal from the fluorescence detection is used to trigger an implemented sorting mechanism. The random appearance, difficult manipulation and cross-contamination of cells or bacteria dispersed in single phase was overcome by their encapsulation in droplet-based microfluidic devices [274]. The properties of compartmentalized cells are investigated in both static [159,280] and flowing [13,246,256] droplets, which can be further subjected to sorting. Since the cells are enclosed within the *droplets*, the latter systems are already referred to as FADS.

SMD in the flow of a single phase, and much more SMS, is highly challenging for the reasons described above. Even though the detection of a single fluorophore in flow was reported, there is a series of drawbacks discriminating this approach, mainly the cross-contamination, contamination of the walls, molecular clustering, clogging of the small cross section channels, and last but not least the signal intensity being proportional to the flow rate [275]. These factors limit the SMS only to the molecules immobilized on the walls of the microfluidic channel [15,278,281]. The more versatile solution is represented by encapsulated single molecules, mostly in static droplets [15,278,281,282] but also in droplets moving in the flow [12,159,276]. The sensitive detection techniques widened the possibility of FADS also to single molecules [12,176]. Nevertheless, SMD and SMS remain highly challenging techniques and single molecule detection or spectroscopy is not an easy task, especially in flowing microfluidic systems. Several issues must be carefully considered for proper understanding of single-molecular FADS.

1. In contrast with cells or microbeads which can be manipulated in the disperse phase prior to the droplet formation [120,144], there is no known way how to beat the Poisson distribution for the single molecules [276]. The system for single molecule sorting will always have a certain distribution of droplets occupied with 0, 1, 2, ... molecules and the particular distribution is dependent on the concentration of the molecules of interest in the dispersed phase (see FIGURE 4.5).
2. The reported SMD or SMS is rarely a true detection of a single molecule [148,282]. Either labelling of the detected single molecule with many fluorophore molecules [15,162,176,275,276,278,281] or, especially in biology, self-replicating properties (PCR, enzyme reaction, in vitro translation, rolling circle amplification, *etc.*) [12,183,277,281,283] are advantageously used. The labeling is, however, often a necessity due to the low or no fluorescent activity of the molecule of interest. Hence, the single-molecule detection is rarely truly single-molecule.
3. If the self-replicating processes are employed, an incubation period is needed. The encapsulated molecules are removed from the droplet formation chip, undergo incubation process and consequently are reinjected to the detection/sorting chip [12,13,183,256]. The time and special conditions needed for incubation obstruct the full integration of all functionalities and prevents realization of the fully automated and independent sorting system [148].
4. Unless the droplet content is strongly amplified or labelled with a high number of fluorophores [12,154,246,276], an extended period of time is required to collect enough photons for reliable detection. Therefore, the detection of single molecules is usually provided in static droplets [15] or in droplet traps, where the droplet is released back to flow after the data collection [157,162].
5. Due to the known properties of fluorophores, single-molecule FADS is usually based on detection rather than spectroscopy [15,162,274,276]. A single wavelength (or their combination [15,276]) can be detected by using emission filters and PMT or APD with much higher sensitivity compared to CCD detectors. The CCD detectors used in spectroscopy are much less sensitive and their utilization is limited in high speed or low signal detection systems [274].
6. The low signal to noise ratio resulting from generally weak signals requires a sensitive tuning of the detection threshold [273,276,278]. When the purity of the sorted ensemble is crucial, the molecular detection efficiency is necessarily less than 100 % in order to avoid false positive detection [275].

8.1.3 SMS and FADS for SWCNT sorting

The CNTs dispersed in water form a system similar to any other molecular dispersion. Nevertheless, there are some special properties compared to the general considerations listed above.

1. The Poisson distribution of molecules compartmentalized in the droplet is valid.
2. The nanotubes are inherently fluorescent, thus no labelling is required. The requirements for a successful detection of a fluorescent molecule are large absorption coefficient and quantum yield of emission, and photobleaching resistance. CNTs are relatively well fulfilling these parameters (see Fluorescence spectroscopy, p. 27). This allows their label-free fluorescence detection and sorting - a true advantage over other sorting protocols.
3. Due to the extreme conditions needed for cloning of carbon nanotubes [77], the 'self-replicating' scheme is not a viable strategy of amplification.
4. The droplets are trapped for an extended time but not violating the flowing nature of the microfluidic system (see 6.5.3 Droplet trapping).
5. Since the goal of this project is to recognize and consequently sort SWCNTs with different chiralities, the single wavelength detection is not a suitable approach. Characterization of a certain chirality must be based on a measurement of the full fluorescence spectrum. The InGaAs CCD arrays, conveniently used for NIR spectroscopy, are characterized by high quantum efficiency [284], however, they miss the possibility of electronic gain, a technique substantially increasing the sensitivity of PMT, APD, but also EMCCD and ICCD in the visible range. The sensitivity of the detector seems to be one of the true challenges for this project.
6. With the goal of high purity single chirality ensembles, false positive detections are unacceptable. The threshold for CNTs detection and chirality recognition must be set so that only a single nanotube with a clear bandgap will be sorted.

These conditions, together with the size of the microfluidic system, brings requirements on the edge of nowadays top-end instrumentation, which includes significant down-scaling of the sorting system, exceptional quality of the optical system and unprecedented sensitivity of the detection system, very precise control of the flows and a well-tuned sorting system.

8.2 Instrumentation and automation

Coupling of the developed microfluidic system with the optical system can be done in multiple ways [165]. However, the systems for direct observation of the behavior in the microfluidic chip and concurrent fluorescent measurements are usually similar [59,165,274]. The optical system, already described in Characterization, was primarily designed for CNT spectroscopy in microfluidic channels and the characterization of the bulk CNT dispersion was only a side task. Therefore, the optical system was used in unaltered configuration (FIGURE 8.1(a)&(b), see also FIGURE 3.2). Even though the full characterization of CNTs dispersed in a solution can be done only by full range excitation - emission 2D mapping [43], or by broadband excitation [285], several properly chosen excitation lasers can successfully replace the time-consuming 2D scanning with less than 1 %

error [59]. In addition, the system with laser excitation gains sensitivity by significantly higher excitation power (see 3.2.3 Remark on spectra acquisition). The utilization of one single laser line is only a first step towards a more complex excitation system after the sorting concept is demonstrated. The microfluidic chip, microfluidic pump, DEP generator and reagents were used as described earlier.

The possibility of long-term and reliable measurements required to build a control software, covering the whole operation of spectroscopy, decision making, and DEP sorting in a fully automated manner. Originally, the author's own software for the control of microfluidic pump and droplet recognition was compiled in LabView environment. The droplet recognition algorithm was based on ROI comparison (FIGURE 8.2(a)). Later on, the LabView program was replaced by a more complex software, developed by Pasi Myllyperkiö. The program development was done in Visual Studio 2015 environment. Several external libraries were used to interface the external devices. The imaging camera was interfaced with Microsoft DirectDraw tools. OpenCV software package via Emgu.CV (version 3.2.0.2682) C# - wrapper was used for the image recognition, based on the edge detection (FIGURE 8.2(b)). Spectrometer (Andor iDus camera) was interfaced by using Andor SDK - package (version 2.86). Spectral analysis and peak fitting were done using nonlinear fitting tools in GSL library version 2.4. The DEP driver firmware software was written on Arduino 1.8.3. This software fully automates droplet recognition (see also [183]), triggers spectroscopy measurement, spectra processing, decision-making algorithm, and the sorting process (FIGURE 8.2(c)&(d)).

The cycle starts at the moment when the software recognizes that there is a new droplet in the trap. This process is somewhat tricky as the droplet exchange in the trap is so fast that the software cannot reliably determine, whether a new droplet entered the trap, or the trap is still occupied by the same droplet (supplementary movie [M6](#)). This issue was partially solved by a new trap design (supplementary movie [M7](#)), however, the results are still not fully conclusive. Potentially, a different mechanism of droplet exchange detection could be applied, utilizing scattering of light on the exchanging droplets (supplementary movie [M12](#)⁴⁹). This idea is, however, not yet applied in the design.

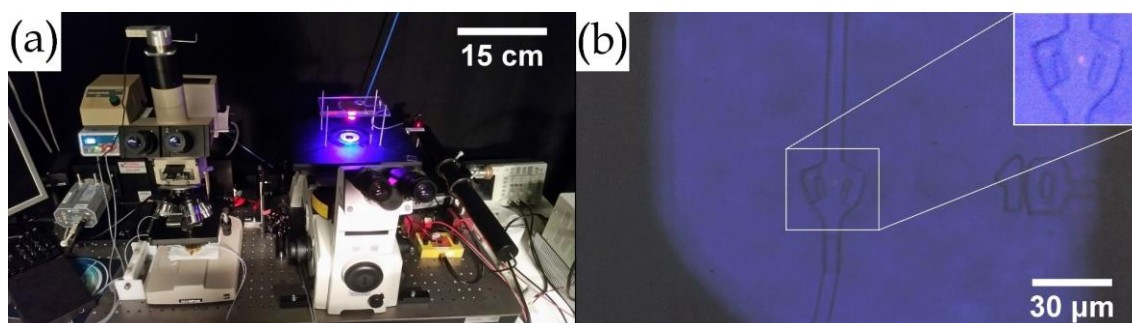


FIGURE 8.1: (a) The full setup for fluorescence spectroscopy in the microfluidic system. (b) A typical image from the camera, used for droplet recognition. The magnified area shows the laser beam focused on the trap.

⁴⁹ M12 - <https://jyx.jyu.fi/handle/123456789/59023>

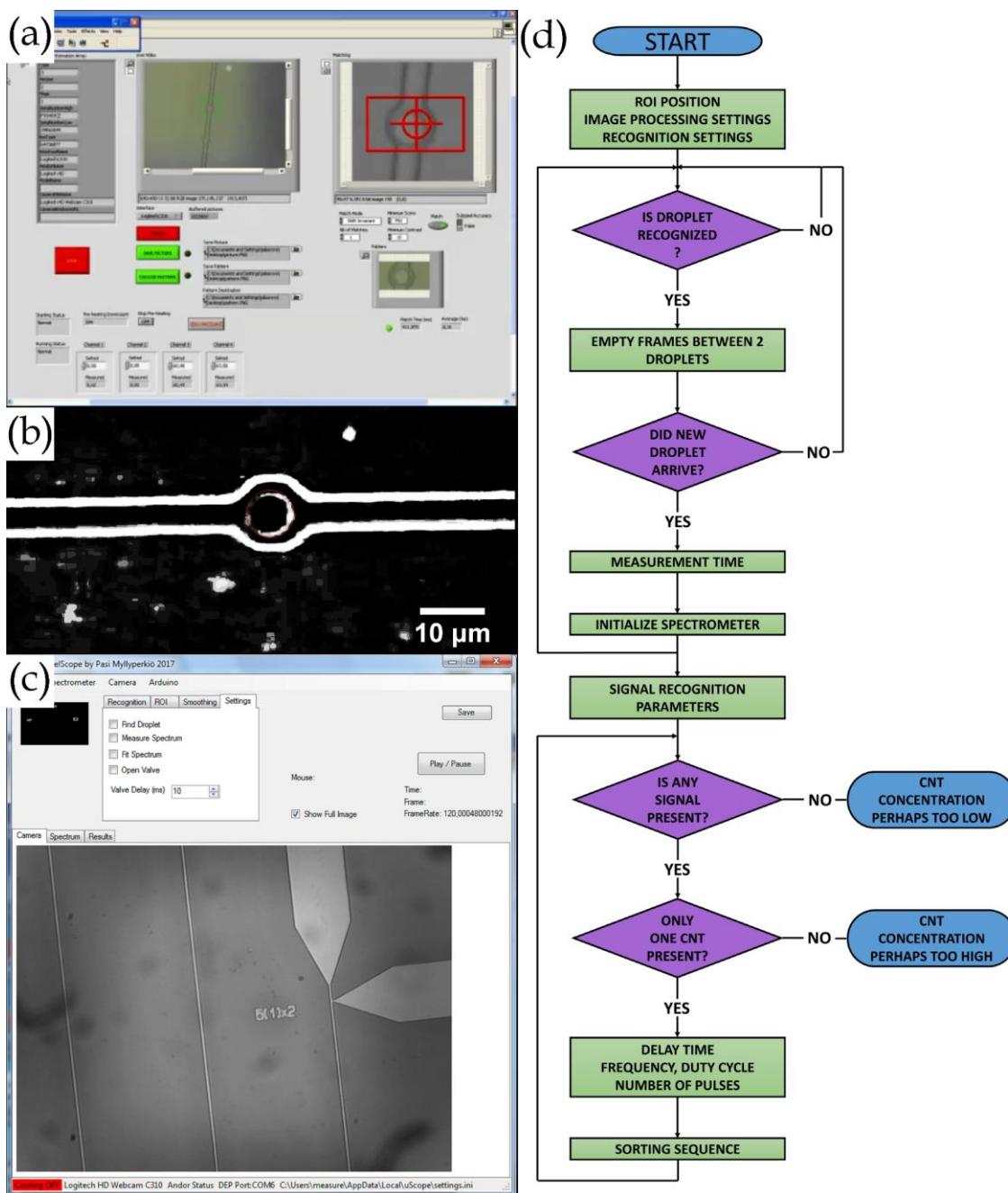


FIGURE 8.2: (a) Older LabView droplet recognition software. (b) Edge recognition function and search for round object in the new software. (c) User interface of the new software. (d) Flowchart of the new software.

The detection of a new droplet triggers the data acquisition by iDus camera. Since the excitation laser is always on, the measurement starts by just opening the electronic shutter of the camera. The acquisition time is fixed beforehand, and its exact value is based on the average time of trap occupation measured before the data collection. This solution originates from the very long time required by the camera to abort the data acquisition process. The possible waste of measurement time if the droplet occupies the trap longer or the possible short contribution from the next droplet coming too soon influences the overall measurement error much less than the delay caused by abortion of the acquisition process.

The spectra processing algorithm then evaluates, whether there is any signal measured from the droplet, how many peaks were detected, and what is their position. If the data match the selected criteria for a chirality to be sorted, the software triggers the DEP sorting sequence with a delay dependent on the flow speed and the distance between the trap and the sorting junction. Besides the delay, the software allows to set the frequency of the AC field and is limited only by the high voltage switching hardware (see DEP – instrumentation, p. 140), duty cycle and the length of the sorting sequence. The two concentration related terminators (FIGURE 8.2(d)) are applied if there is either too many or no peak detected for several measurements in a row. They serve the purpose of properly setting the dilution ratio of the CNT dispersion.

8.3 Ambient considerations

Injection of the SWCNT dispersion into the femtoliter scale microfluidic system brings a necessity to consider possible influences of the prevailing ambient conditions on the optical spectroscopy. The enhanced influence of the environment comes as another consequence of miniaturized microfluidic system. Due to the size of the microfluidic system together with the size of the focused laser spot and Rayleigh length of a Gaussian laser beam, the spectroscopy results will be inevitably influenced by both the glass and the continuous phase.

8.3.1 Glass contribution

Even though glass shows low autofluorescence compared to other microfluidic materials (see 5.1 The material), various admixtures from the glass composition can exhibit fluorescence behavior. Since the signal originating from a single CNT is expected to be very weak and certain volume of the glass is inevitably exposed to the focused laser light, the fluorescent behavior of the glass must be taken into account. Indeed, the glass fluorescence intensity can be up to 10-times larger than the signal from CNTs, when the laser is focused inside the channel. Further experiments seeking for the optimal position of the focal plane confirmed that the fluorescence of the glass virtually restricts the placement of the focal plane anywhere else but to the middle of the channel as the glass autofluorescence reliably covers any possible signal originating from CNTs.

The experimental data were obtained with the optical setup for CNT spectroscopy (see 3.2.2 Characterization) from ready-made microfluidic chips. The measured signal is unstable during the first several seconds, which can be related to the temperature changes caused by an intensely focused laser beam, or to autofluorescence bleaching [286]. A deconvolution to five Gaussian profiles sufficiently describes the fluorescence signal to be from the glass (FIGURE 8.3(left)), and the parameters of the deconvoluted functions are perfectly predictable and linear as a function of time (FIGURE 8.3(left inset)). Due to the initial instability of the signal, the reference measurement, as well as the data acquisition from the droplets, must always be taken with certain delay after the position of the laser

beam is set. The predictable nature of the glass autofluorescence allows its automatic subtraction in the control software. The influence of the glass was subtracted from all the data presented below.

8.3.2 Decane contribution

Since the decane wets the channel walls, it creates a thin layer between the droplet and the glass. Both the excitation laser light and the fluorescence signal must pass this layer. The decane is optically inactive in the VIS region, however a very weak absorption can be found in the NIR region [287] (FIGURE 8.3(right)). This band most likely originates from the 3rd overtone of the C-H stretch. Hence not the excitation, but the fluorescence signal can get partially absorbed on the decane layer separating the droplet from the channel wall. The silane monolayer on the glass surface can possibly add to this absorption as the hydrocarbon tails have similar molecular structure as decane. No measurable contribution of SPAN 80 emulsifier dissolved in the decane was observed. The overlap with the fluorescence signal is not significant and, in addition, the absorbance is negligible. For example, water itself absorbs stronger in this region [287]. Thus, no negative influence from decane on the spectroscopic result should be expected.

8.4 CNT dispersion in microfluidic system

8.4.1 CNT dispersion in microfluidic channel

Firstly, only the diluted SWCNT dispersion was driven through the microfluidic channel as a continuous phase. The dispersion was diluted with dH₂O with

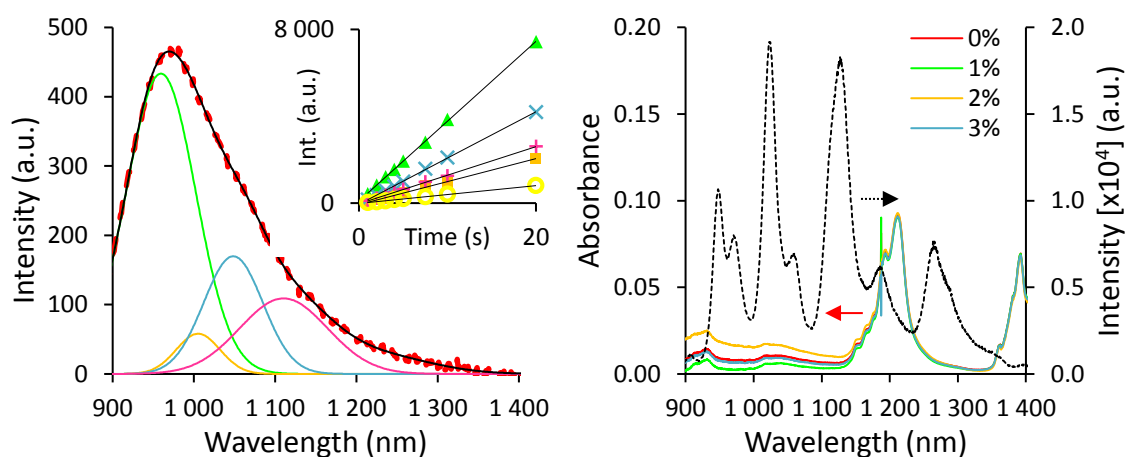


FIGURE 8.3: (left) The microfluidic chip glass autofluorescence in NIR region. The red dashed line shows the experimental data from 1 s exposure, the thin curves are deconvolution to Gaussian functions. The inset shows the time evolution of intensity of the deconvoluted Gaussian functions. (right) Decane absorption in the NIR region. Data were collected on FTIR Nicolet Magna-IR 760 ESP with 10 mm path length. The disproportion of the data in the <100 nm region comes from the decreasing sensitivity of the instrument. The dashed line marks the position of fluorescence emission from the CNTs. The magnitudes of the absorbance and the intensity are not in scale.

1 % w/w SDBS up to the point where only a very few (down to one) nanotubes pass through the detection volume. This can be observed as clear differences between consequently acquired spectra. At the given dilution, distinct peaks from individual CNTs with specific chirality start to appear at the acquisition time of ~ 1 s. This acquisition time became a key parameter for further development of the microfluidic device (see T-junction, p. 124). Differences are still observable at acquisition times as long as 3 s (FIGURE 8.4(left)) but they disappear with longer acquisition times as a result of many nanotubes passing the detection volume. The sum of all the individual spectra results in the regular spectrum usually obtained from bulk SWCNT dispersion (FIGURE 8.4(right)). This experiment proves the possibility of continuous phase flow of SWCNT dispersion in femto-liter scale microfluidics. It also demonstrates the viability of detecting individual CNTs in the flowing dispersion by a NIR fluorescence measurement.

8.4.2 CNT dispersion in droplets

Since the previous experiment showed that the flow of SWCNT dispersion in microfluidic channel is a viable process, the next step was measurement of the NIR fluorescence of the dispersion from stationary droplets formed in the microfluidic system. The results from the experiment are plotted in FIGURE 8.5. There is a clear difference between the spectra from individual droplets. Even at long integration times of 10 s in FIGURE 8.5, the fluorescence signal does not exhibit all the spectral features of bulk dispersion measured in a cuvette or in the open flow. This suggests, that the SWCNTs are really encapsulated within the droplets and there is no content exchange between the droplets nor leaking to the continuous phase (the decane spectrum is null). The sum of all the spectra FIGURE 8.6(left) again give a spectrum in agreement with the bulk CNT dispersion measurement (FIGURE 8.6(right)).

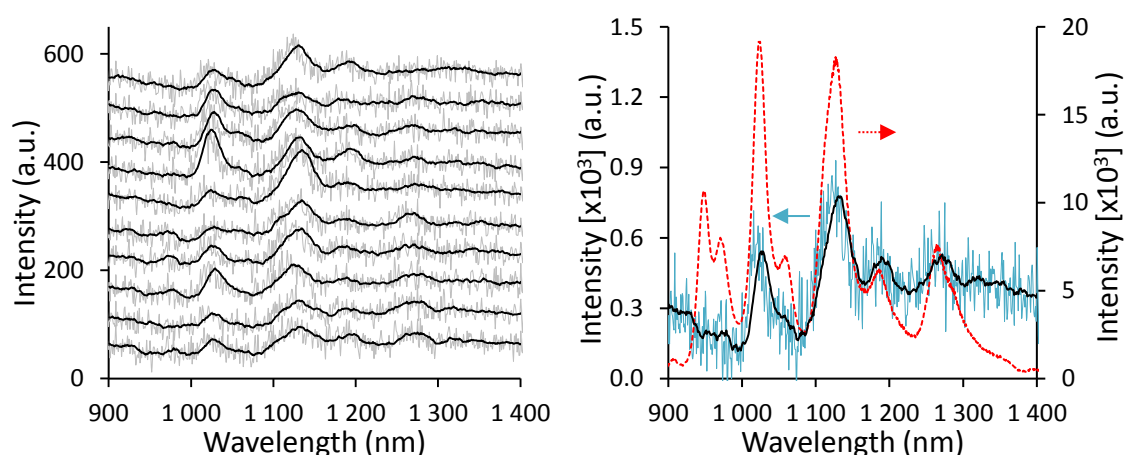


FIGURE 8.4: (left) Consecutively measured spectra of CNT dispersion (sample J3) flowing in microfluidic channel (chip 18). The acquisition time was 3 s per spectrum and the black line is a moving average trend line. The spectra are vertically shifted for clarity. (right) The sum of all the spectra from the left (blue line), its moving average (black line), and their comparison to non-diluted SWCNT dispersion measured from a cuvette (red dashed line).

The signal obtained from the droplets appears more noisy compared to the spectra from free flow of the CNT dispersion. This is most likely due to the presence of glass-decane-droplet interfaces together with relatively large size of the droplets. As the detection volume cannot cover the whole droplet, the signal to noise ratio decreases (see 8.1.1 Brief history of SMS and FADS). In addition, more than one chirality is present in almost every droplet. Further dilution of the CNT dispersion is necessary to achieve the single SWCNT in one droplet limit.

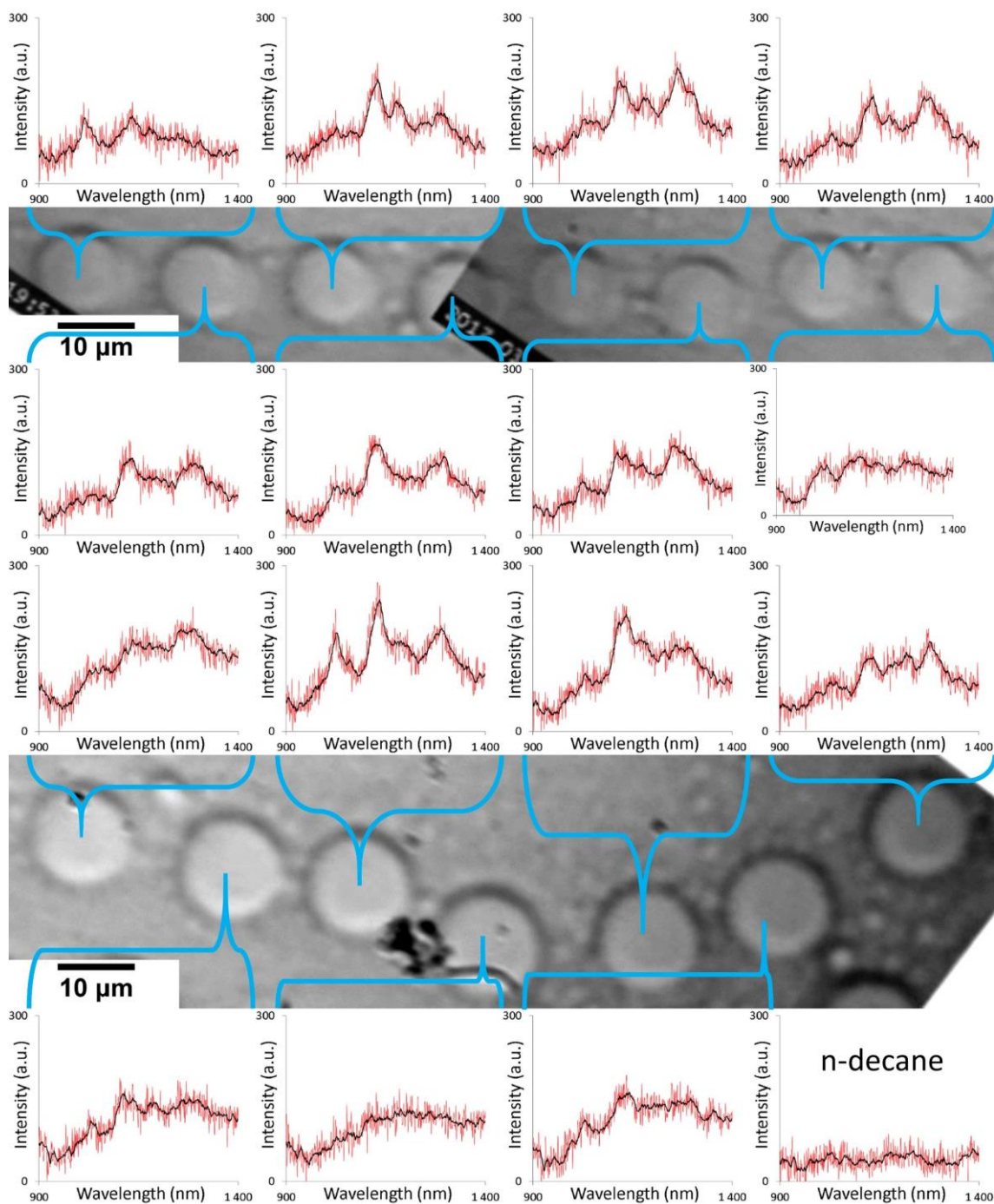


FIGURE 8.5: Spectra measured from individual static droplets in continuous phase of decane (sample D, chip 18). The acquisition time was 10 s per spectrum and the black line is a moving average trend line.

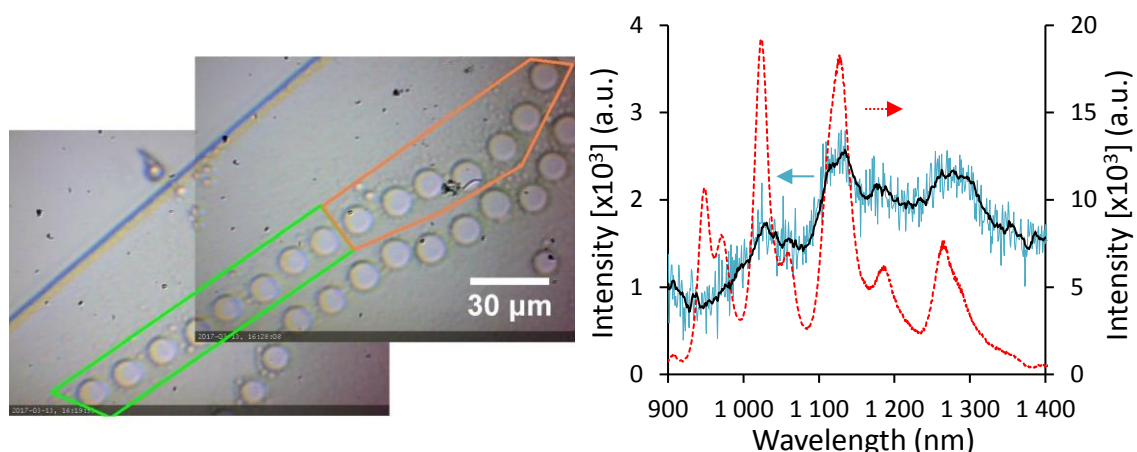


FIGURE 8.6: (left) Position of the measured droplets in the microfluidic channel. (right) The sum of all the spectra from droplets from FIGURE 8.5 (blue line), its moving average (black line), and their comparison with non-diluted SWCNT dispersion (sample J3) measured from a cuvette (red dashed line).

8.4.3 Continuous droplet formation with CNT dispersion

The success in detection of the fluorescence signal from individual droplets became a trigger for experiments with simultaneous use of all the subsystems of the microfluidic chip. Even with the limits arising from the system sensitivity, the Poisson distribution of nanotubes compartmentalized in individual droplets, the unknown concentration of nanotubes in the dispersion, and the limited number of emitting nanotubes upon 633 nm excitation, significant enrichment of a selected chirality can be achieved by sorting. These measurements would also serve as a library of spectra measured from droplets and help to determine the proper concentration of the CNT dispersion. At the very end of this iterative search for optimal concentration, sorting threshold, and excitation coverage, the aim of working with individual nanotubes can be achieved.

However, compared to dH₂O, the CNT dispersion behaves very differently in the microfluidic system. Even for the same microfluidic chip and at the same experimental conditions (supplementary movie [M13](#)⁵⁰), the droplet formation is unstable, irregular, and the droplets tend to have non-spherical shapes (FIGURE 8.7(a)&(b)). The droplets group to 'trains' and the traps are nearly ineffective (FIGURE 8.7(c)&(d)). The attempts to resolve this issue by altering the experimental conditions, namely the pressure ratio of the continuous and disperse phase, led to even more unpredictable behavior of the droplets (FIGURE 8.7(e)-(g)).

No pressure settings were found that would bring the abnormal behavior of the droplets back to the stable regime. Since the whole idea of the automatic droplet/CNT sorter is based on slow, regular, and stable droplet formation, this issue had to be reliably resolved. The similarity of the patterns from FIGURE 8.7(e)-(g) with FIGURE 6.15(d) suggests that the interfacial tension plays a key role in this issue. Indeed, the presence of SDBS surfactant does not only cover the

⁵⁰ M13 - <https://jyx.jyu.fi/handle/123456789/59024>

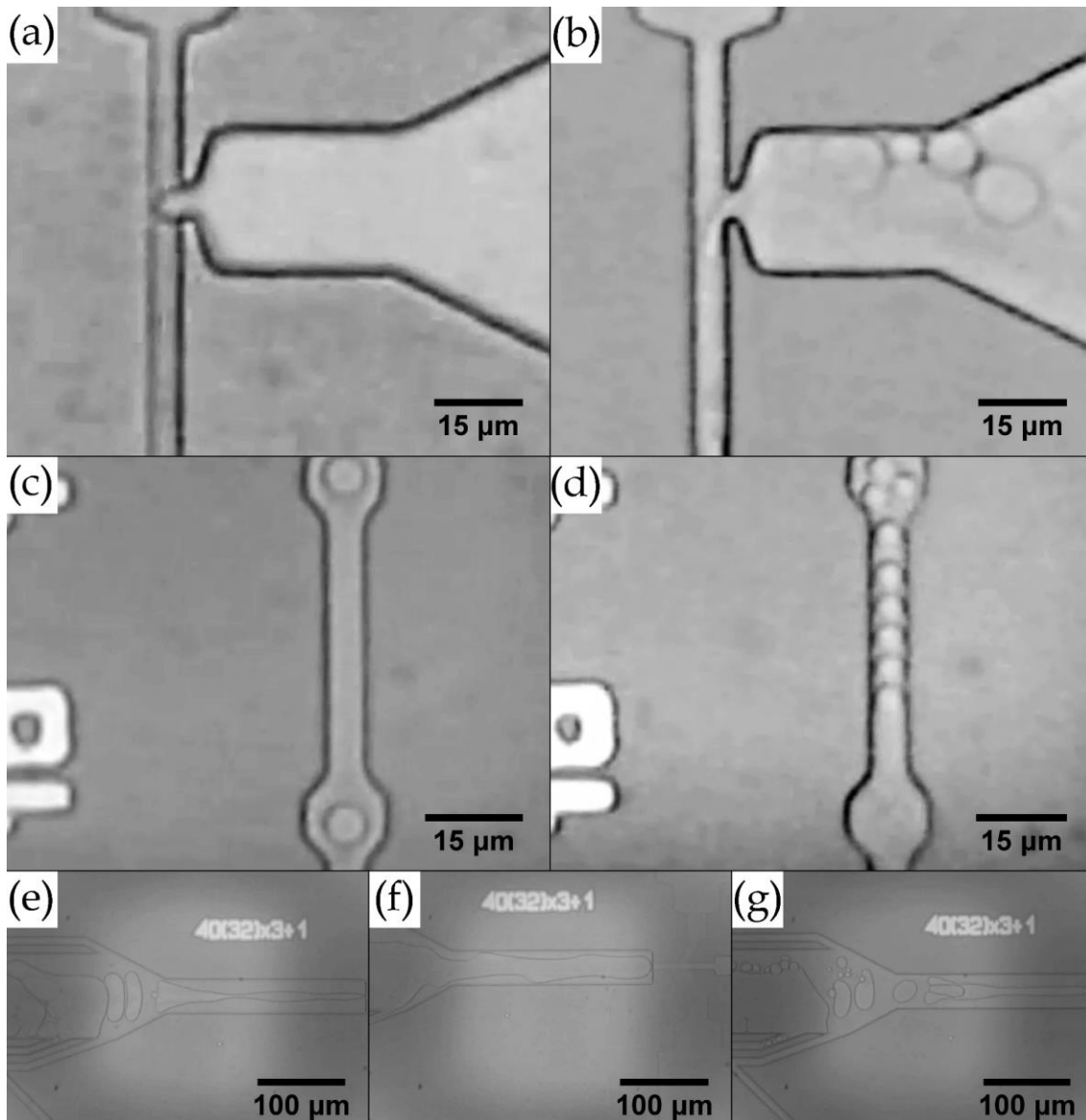


FIGURE 8.7: Comparison of droplet formation with (a) dH₂O and (b) CNT dispersion. Comparison of droplet propagation with (c) dH₂O and (d) CNT dispersion. (e)-(f) Unpredictable behavior of the fluids at trial pressure settings.

CNTs but also significantly alters the interfacial tension between the CNT dispersion and both the continuous phase and the channel walls.

The surface tension of water as a function of SDBS concentration is plotted in FIGURE 8.8. The data were obtained using Sigma 703 tensiometer by Du Noüy ring method [288]. The surface tension of pure dH₂O was measured to be $\sim 71.4 \text{ mN m}^{-1}$, in agreement with the literature [288,289]. The surface tension steeply drops upon the addition of SDBS surfactant down to the point of CMC [290]. The dH₂O - SDBS mixture reaches CMC at SDBS concentration $\sim 0.08 \%$ w/w and the surface tension reaches the value of $\sim 36.6 \text{ mN m}^{-1}$. At higher concentrations, the decrease of the surface tension slows down and eventually reaches a plateau at the value of $\sim 33.0 \text{ mN m}^{-1}$. The presented data were later used for determination of the SDBS concentration from the measured surface tension.

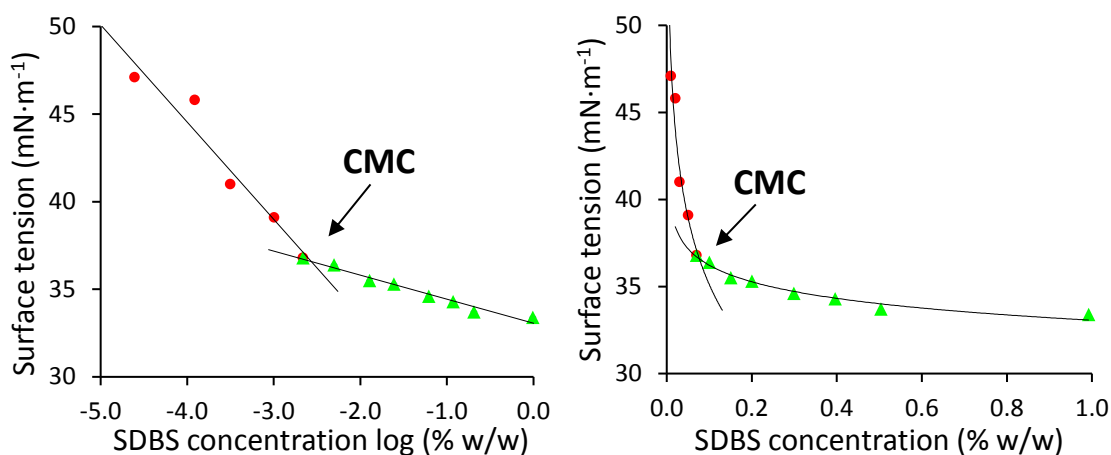


FIGURE 8.8: Surface tension of water as a function of SDBS concentration [288]. The black lines are linear and logarithmic fits, respectively.

The surface tension is directly related to interfacial tension as the presence of surfactant helps to ‘wet’ the surface in contact [139]. While the interfacial tension between the fluids does not play a critical role in the droplet behavior, at least in the confined regime, the interfacial tension between the disperse phase and the channel walls is crucial for the droplet formation and behavior in the microfluidic system (see 4.4.1 Droplet formation in open and confined systems). Further microfluidic experiments based on varying SDBS concentration in the disperse phase showed that a surface tension of $\geq 50 \text{ mN} \cdot \text{m}^{-1}$ is necessary to maintain the behavior of the system as it was designed. In other words, the SDBS concentration in CNT dispersion should not exceed 0.01 % w/w, about 100-times less than the optimal amount (see 3.3.1 Amount of surfactant).

8.4.4 CNT dispersion post-processing

When the SWCNT concentration in the dispersion needs to be decreased, the dispersion is usually diluted with an aqueous solution having the same concentration of SDBS as the original CNT dispersion [59]⁵¹. A decrease in the SDBS concentration could be easily achieved by diluting the CNT dispersion with dH₂O only. However, the concentration of the individualized SWCNTs decreases together with the SDBS and so does the fluorescence intensity following the Beer-Lambert law. With a dilution ratio as high as 100 : 1, the drop in fluorescence intensity makes the detection of SWCNTs both in channel and in droplets highly ineffective. Therefore, a protocol, in which the decrease of SDBS concentration would be much more effective than the related decrease of SWCNT concentration, had to be developed.

First, the preparation process of CNT dispersion (Appendix A) was altered by using SDBS at a concentration as low as 0.03 % w/w (sample C). The quality of the dispersion, evaluated by integrated fluorescence activity, was very poor. At the surfactant concentration below CMC, the surfactant molecules are located mainly at the water-air and water-vial interfaces and their availability in the bulk

⁵¹ The efforts to increase the SWCNT concentration are altogether focused on improving the preparation process [93], and post-processing techniques are not used.

volume is not sufficient to support the debundling process and keep the nanotubes separate (see also 3.3.1 Amount of surfactant, FIGURE 3.9(right)). In addition, the long-term stability was basically non-existing as the fluorescence intensity quickly dropped with time.

An alternative approach was based on observation of the subtle difference between the density of water and that of individualized nanotubes. A closer examination of the data measured during optimization of the centrifugal field and time (see 3.3.4 Centrifugation) not only proves that the individualized nanotubes possess a lower density than bundles or other unintentional particles but, more importantly, it shows that the individual nanotubes are slightly denser than the aqueous environment they are dispersed in. Centrifugal fields over 150 000g are clearly able to remove all the nanotubes from the dispersion and drive them into the precipitate (FIGURE 3.13(left)). The precipitate formed from a CNT dispersion is also known to contain only a small fraction of the overall amount of surfactant from the dispersion [105,113]. The possibility to concentrate the majority of the well individualized nanotubes to a very small volume was found to be a solution to the challenge of preserving the concentration of individualized SWCNTs while dramatically decreasing the concentration of SDBS.

Naturally, a series of questions about the feasibility of this approach arise. The presence of SDBS seems to be crucial for the (long-term) stability of the dispersions, and since a dynamic equilibrium is expected between the adsorbed and non-adsorbed surfactant [97], its removal could lead to a decrease and eventually to the loss of the protective coverage of the SWCNTs. In addition, the nanotubes are pressed closely to each other during the centrifugation process, which together with lowered surfactant coverage invokes the risk of serious rebundling.

The experimental protocol was designed and executed in two competitive pathways (FIGURE 8.9). In both cases, the goal was to obtain CNT dispersions with SDBS concentration *required* for proper functionality of the microfluidic system. That means in absolute numbers ≤ 0.03 % w/w of SDBS in the CNT dispersion.

- First approach: The ready-made CNT dispersion is first diluted with dH₂O to the required surface tension. The diluted dispersion is exposed to a high centrifugal field and consequently, the precipitate is collected and properly homogenized.
- Second approach: The ready-made CNT dispersion is first exposed to a high centrifugal field and the precipitate is collected. Consequently, the precipitate is diluted to the required surface tension and properly homogenized.

Observation of fluorescence from the supernatant shows obvious decrease of the integrated fluorescence intensity without any observable change in the shape of the spectrum. It means that individual SWCNTs are truly transported to the precipitate. The rate of transport is a function of both the centrifugal field and time of centrifugation. Depletion of nanotubes from the supernatant was not found to be dependent on the experimental pathway. The recovery of the precipitate,

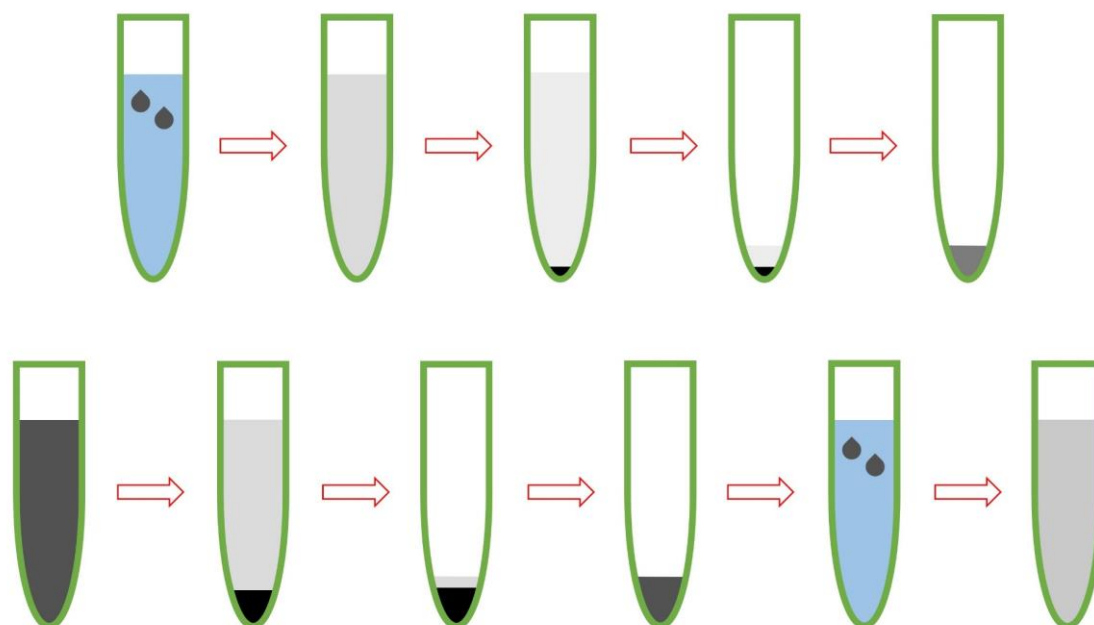


FIGURE 8.9: Two approaches for decreasing of the SDBS concentration in CNT dispersion. (top) Dilution precedes centrifugation. The ready-made CNT dispersion is firstly diluted with dH₂O, centrifuged, and then the precipitate is collected and homogenized. (bottom) Centrifugation precedes dilution. The ready-made CNT dispersion is firstly centrifuged, and the precipitate is collected and homogenized. The homogenized precipitate is consequently diluted with dH₂O.

however, strongly favors the first approach as its relative fluorescence intensity was found to be constantly higher. We speculate that the high centrifugal field compressing a large amount of nanotubes in the precipitate (second approach, FIGURE 8.10(b)) induces the rebundling in much larger scale than the limited SDBS coverage together with limited interaction of nanotubes (first approach, FIGURE 8.10(a)).

The first method was therefore further optimized and lead to the protocol described in Appendix A. A regular CNT dispersion is diluted to the required SDBS concentration with dH₂O. The SDBS concentration can be indirectly verified by surface tension measurement (FIGURE 8.8), however, the measurement error is relatively large at low SDBS concentrations. Hence, the dilution ratio is considered a more exact parameter of determining the final SDBS concentration. For this highly diluted SWCNT dispersion, the search for optimal centrifugation parameters resulted in centrifugation at the highest centrifugal field allowed by the Type 70.1 Ti Rotor [110] used in the Beckman-Coulter Optima L-90K Ultracentrifuge (450 000g). The 4 hour period of centrifugation was found to be sufficient to effectively drive the majority of the individual SWCNTs to the precipitate. The slightly darker precipitate (FIGURE 8.10(a)) is then carefully pipetted out of the vial. An amount as low as 200 μ L from 5 mL of centrifuged dispersion ensures high enough concentration of nanotubes in the resulting product. The homogenization of the pipetted volume is conducted by 30 min sonication of the sample placed in a glass flask in a bath-type sonicator and consequent filtering by 1.2 μ m and 0.45 μ m membrane filters (see 3.3.5 Filtration). In this way, a CNT dispersion with 30-fold decrease of the SDBS concentration but only 3.2-fold decrease of the

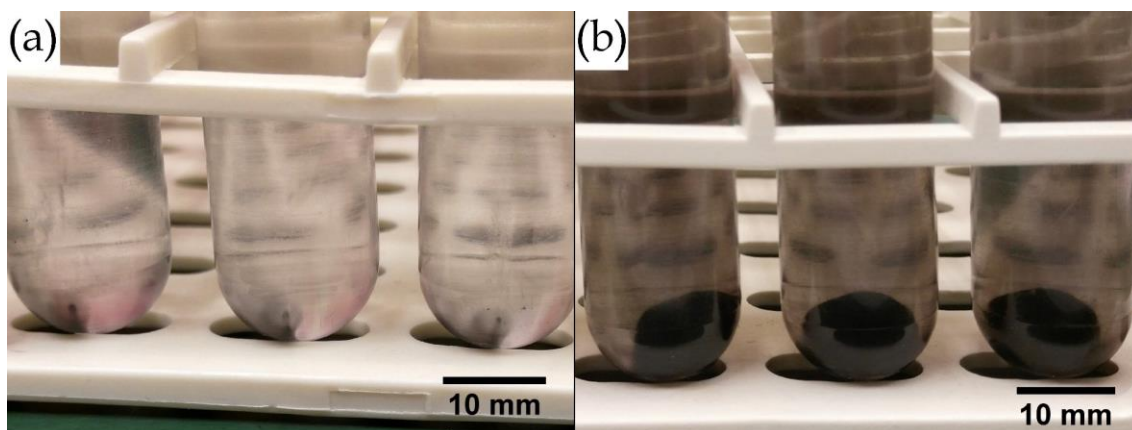


FIGURE 8.10: Post-processing precipitates from (a) diluted CNT dispersion (sample P), (b) not diluted CNT dispersion (sample D).

integrated fluorescence activity (FIGURE 8.11(top left)) was achieved. In addition, the shape of the normalized fluorescence spectrum is identical to the spectrum measured from samples prepared by the standard procedure, proving the quality of the dispersion.

Long-term stability of the low SDBS CNT dispersion

Since the stability of the CNT dispersion is thought to be enabled by the coverage of the nanotubes by surfactant molecules, the long-term stability of dispersion with low SDBS concentration was an issue to address. Long-term aging tests (FIGURE 8.11(top right)), however, show improved stability compared to the 1 % SDBS CNT dispersions (FIGURE 3.15(right)). In comparison of two dispersions with low SDBS concentration, the one with lower concentration of individualized SWCNTs show superior stability over the more concentrated one. This observation means that the dynamic equilibrium of the SDBS molecules in the aqueous environment and on the SWCNTs is not as straightforward process as reported [97].

Besides the improved stability, an unexpected feature of the aged dispersions with low SDBS concentration was observed (FIGURE 8.11(bottom left)). The position of the emission peaks shifts with time, firstly towards lower wavelengths (FIGURE 8.11(bottom right)). The sample with higher SWCNT concentration exhibits large redshift after more than 2 months of storage. Since both samples were measured always together, an instrumental or calibration error is out of question. Nevertheless, filtration with the 0.45 μm membrane filter returns the position of the peaks back to original. The filtration, compared to dispersions with 1 % SDBS concentration, does not improve the intensity of the fluorescence (FIGURE 3.15(left)). These results point towards some interaction of individual SWCNTs with non-fluorescent bundles or yet unknown dynamics of the SDBS surfactant in SWCNT dispersions.

Remarks on the CNT dispersion post-processing

The experimental effort in preparation of SWCNT dispersion with a low SDBS concentration results in a series of observations, which should be taken into account when preparing for the microfluidic experiment.

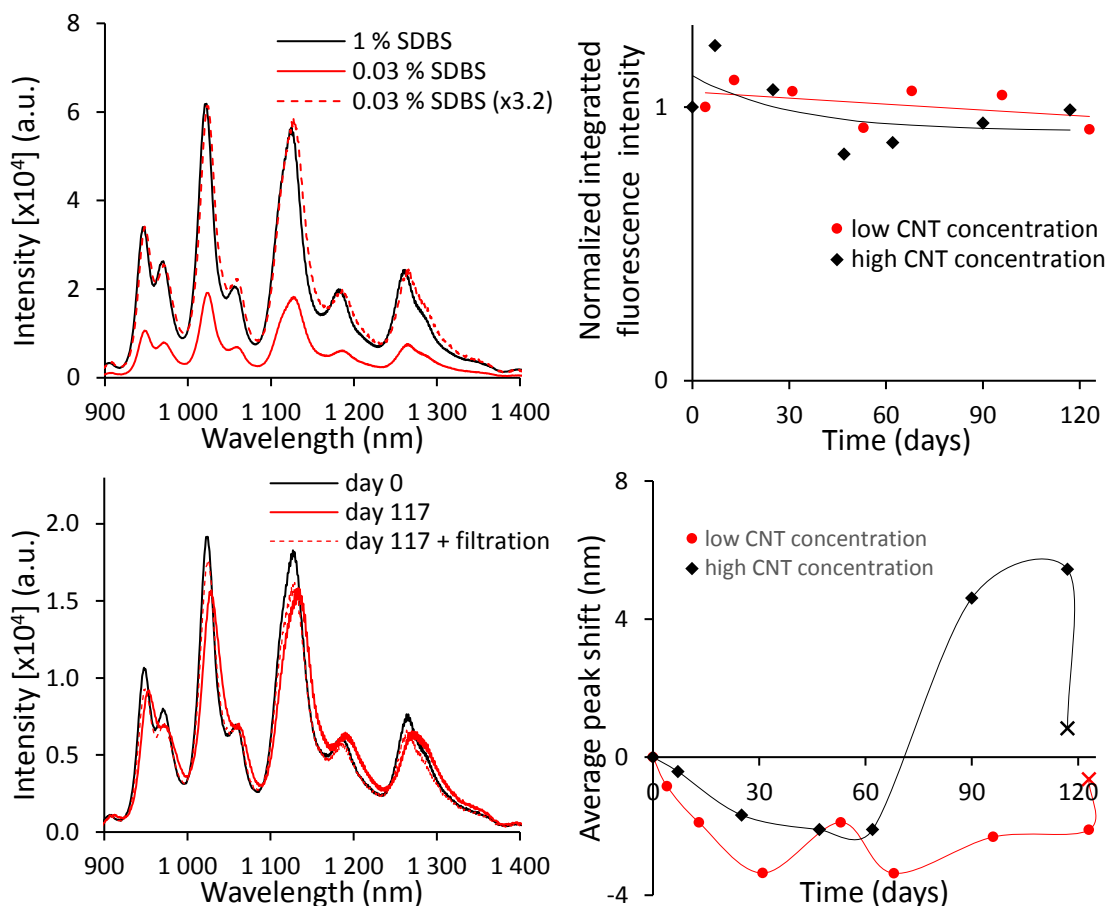


FIGURE 8.11: (top left) The 30-fold decrease of the SDBS concentration accompanied by only 3.2-fold decrease of the fluorescence intensity. (top right) Integrated fluorescence intensity as a function of time. The solid lines are least squares fits of an exponential function. (bottom left) An obvious redshift in the spectrum from the aged dispersion with low SDBS and high SWCNT concentration. The filtration reverses the redshift back to normal. (bottom right) An average shift of 5 major peaks (950 nm, 1024 nm, 1130 nm, 1187 nm, 1266 nm) as a function of time. The cross data points are measured after filtration. The solid line is just to guide the eye.

- The dilution ratio $\text{dH}_2\text{O} : \text{SDBS}$, prior to the post-processing centrifugation, should be as large as possible as the highly diluted samples result in better recovery after homogenization.
- The dispersions with low SDBS concentration should be always prepared from fresh 1 % SDBS SWCNT dispersion, since the latter ages faster (FIGURE 3.15(right) vs. FIGURE 8.11(top right)).
- The samples with lower CNT concentration are the most stable from the long-term point of view (FIGURE 8.11(top right), FIGURE 8.11(bottom right)). Hence, the samples should be diluted to the (final) experimental concentrations right after the preparation and they should not be stored in concentrated form.
- The resulting fluorescence intensity of the dispersion with low SDBS concentration is a function of many parameters and the results vary from batch to batch. Therefore the exact dilution ratios for experimental

fluorescence intensity cannot be simply stated and must be re-evaluated for every batch separately.

- The disadvantage of this process is the limited volume of CNT dispersion with low SDBS concentration after the post-processing (usually under 1 mL). This amount, even though small for bulk measurements, is more than enough for several microfluidic experiments.

8.4.5 Low SDBS disperse phase for droplet formation

As expected, the droplet formation was well re-established with the decreased SDBS concentration. Surprisingly enough, it was nearly impossible to detect any signal from the microfluidic channel. There was no signal observed in any channel, neither in the static nor moving droplets. The only exception was the disperse phase inlet channel. Since there was no problem in observing the CNTs in the inlet channel and no diffusion of CNTs to the continuous phase was observed, the reason for this behavior was unclear.

The attempts to achieve continuous droplet production led to a clearly visible build-up of SWCNTs (a *plug*) in the place of droplet formation (FIGURE 8.12(a)-(c)). This happens in the time period of 5 – 10 minutes from introduction of the CNT dispersion to the microfluidic channel and the plug creation process is cumulative. If the CNT dispersion was introduced to the chip only for a short time and no visible plug was created, a faster build-up was observed in the consequent run. The creation of the plug explains the missing nanotubes further in the microfluidic chip. Interestingly, the plug itself does not influence the droplet formation for a surprisingly long time after the plug is created (FIGURE 8.12(d)), even though the plug keeps collecting more and more nanotubes. The plug apparently does not influence the water flow, however, it creates an impermeable barrier for the trapped air (FIGURE 8.12(c)). The structure of the plug is also noteworthy, as the CNT density gradient grows in the direction of the flow (FIGURE 8.12(b)&(e)&(f)). The plug is not removable by any tested approach, including strong solvents, elevated temperature, sonication, high pressure, and reverse flow. The reverse flow can also trigger a formation of new plugs at places with limited cross section (FIGURE 8.12(e)). A measurement of the fluorescence response of the plug (FIGURE 8.12(h)) does not show the characteristic CNT spectrum, possibly due to massive rebundling. Anyhow, the build-up of a plug necessarily means a destroyed chip, an obviously unacceptable property of the developed system. As a result, the CNT dispersion with decreased concentration of surfactant ($\ll 1$ %) cannot be used in developed microfluidic chips if the design allows contact of the dispersion and the silinized channel walls.

Since no plug formation was observed when the 1 % SDBS CNT dispersion was manipulated within the microfluidic chip and no plugs were observed in the places, where the decane wets the hydrophobic channel surfaces, the interaction of CNT dispersion with low SDBS concentration and the hydrophobic walls in the place of limited cross section was thought to be the trigger mechanism for the plug formation. We speculate that the SWCNTs poorly covered by SDBS molecules may be rather strongly attracted to the hydrophobic OTS SAM (see 6.2.2 Silinization in enclosed channels). The plug formation probability is further

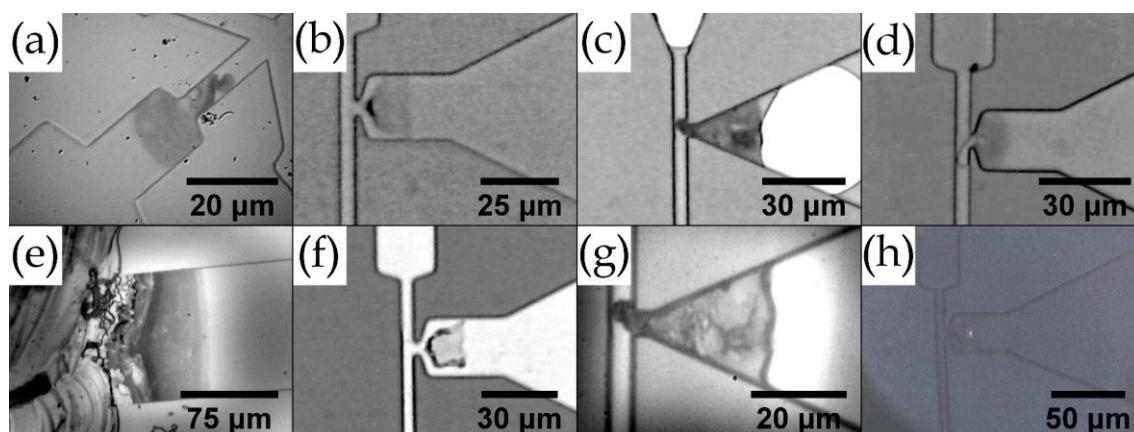


FIGURE 8.12: Plugs formed from the CNT dispersion with low SDBS concentration. The plugs are usually formed in the place with limited channel cross section and presence of OTS monolayer is a necessary condition for the formation of the plug.

amplified both by the close proximity of the walls and high chance of establishing an impenetrable network of nanotubes in the areas with limited cross section.

Selective surface treatment

A new approach of the OTS SAM treatment in the microfluidic system, selectively leaving the disperse phase inlet channel untouched, was developed. The system is not totally filled by the OTS solution, but dry nitrogen gas is pumped through the not-to-be-treated channel. The N_2 gas is forming bubbles in the flow of the OTS solution, being carried away to the outlets. The first experiments confirmed the viability of this approach, as the chip functionalities are not affected, and the chip was able to operate for a period of ~ 19 hours before the flow of the CNT dispersion got restricted (supplementary movie [M14](#)⁵²). Additionally, the plug formed in the area without the hydrophobic treatment was easily removed by setting a reverse flow at low pressure. This further supports our speculations about the interaction between poorly covered nanotubes and the hydrophobic channel surface. The details of the selective silinization are described in Appendix B.

⁵² M14 - <https://jyx.jyu.fi/handle/123456789/59025>

9 Summary and perspectives

9.1 Summary

The development of a microfluidic platform primarily designed for sorting of single SWCNTs encapsulated to femtoliter droplets is reported in this thesis. The development of an experimental system in the femtoliter scale requested an investigation of both theoretical aspects and experimental methods of microfluidics. The wide variety of fields, including microfabrication, hydrodynamics in microscale, surface and interfacial chemistry, electric fields in microfluidics, *etc.*, were thoroughly addressed in order to reach the goal.

BOOK I (partially also BOOK III) describes the evolution of the experimental protocol for stable dispersions of individualized and surfactant-protected SWCNTs. Low sonication power was identified as key parameter for achieving dispersions with low non-resonant background and high fluorescence activity. The parameters of consequent centrifugation were optimized for high yield of fluorescent nanotubes at minimal level of impurities. The surface tension of the dispersion was successfully altered in a large range by a novel protocol based on extensive centrifugation. The ability to tailor the surface tension was found to be crucial for the proper functionality of the microfluidic system. The resulting experimental protocol can be found in Appendix A.

BOOK II focuses on both manufacture and operation of a full-glass, spectroscopy-friendly chip for W/O droplet-based microfluidics in femtoliter scale. Both the dry and wet etching protocols for manufacture of the channels were successfully developed, however, the wet etching technology showed itself to be more suitable for the femtoliter systems. Closing of the channels was achieved by establishing an optimized adhesive-free thermal bonding process. A novel sandwich structure of electrodes, well surviving the harsh conditions during manufacture, was designed and implemented. The necessity of hydrophobic surface for W/O droplet-based systems was addressed by a silinization procedure, not previously reported in channels miniaturized to such extent. The tuning of the manufacture process resulted in step-by-step manufacture instructions attached as Appendix B.

The channel geometries for droplet formation, transport, trapping, DEP sorting and droplet on-chip stability were iteratively improved towards the outlined functionality. The final complex geometry allows generation of monodispersed droplets at a frequency below 1 Hz – an untrivial parameter, which allows long measurement of the droplet content at measurement traps. High efficiency of the passive trap for spectroscopy and the DEP sorting were demonstrated and

fine-tuned to high repeatability. It was shown, that the geometry of the channels is a crucial parameter for establishing the desired droplet behavior. A set of empirical rules for long-term on-chip droplet stability was compiled based on experimental observation. Even though the development was aimed at a chip with relatively specific properties, the vast majority of the gained knowledge can be directly used or easily extrapolated for microfluidic systems with different properties.

In BOOK III, the merger of the developed microfluidic technology and the high-quality SWCNT dispersion, with the aim for single nanotube spectroscopy and sorting, is presented. The droplet content recognition was demonstrated by detecting the signal from individual droplets, and the premise of droplets as sealed containers was proven by constant spectroscopy readings from particular droplets for an extended periods of time. Various challenges related to a continuous stream of droplets containing SWCNTs were observed, addressed and successfully resolved. The DEP sorting abilities together with the results presented in BOOK III proves the viability of the concept of Microfluidics for carbon nanotubes spectroscopy and sorting.

The demonstrated functionalities make the developed microfluidic platform a highly versatile tool for broad use across the fields of natural sciences. Both cellular and molecular biology, chemistry, and environmental sciences can profit from the developed functionalities. Hence, this work reaches beyond the narrow scope of SWCNT sorting and is truly a new experimental tool available for anyone who could benefit from it.

9.2 Perspectives

Despite the indisputable progress in the development of the microfluidic system, there are some loose ends to be tied up. Namely, the automated sorting of single droplets and the triggered spectroscopy of SWCNTs encapsulated within droplets. An automated computer controlled system will bring not only a large set of data for further optimization but mainly, it will allow an enrichment of the selected nanotube chirality in the sorted ensemble. The enrichment itself will be a sufficient proof of the system functionality.

Besides the obvious, there is a list of ideas, which were envisioned during the last stages of the work, but they were not put into practice yet.

- The CNT dispersion would benefit from a more established and repeatable quality assessment. A system of comparing the integrated fluorescence intensity to absorbance at excitation wavelength [59] gives a good comparison of the individualization and non-resonant elements in individual batches.
- The major issue during the manufacture of the microfluidic chip is occasional diffusion of electrode material into the channels, which alters the surface characteristics of the channels and strongly interacts with applied

electric field. Therefore, the order of manufacture of shallow channels, deep channels, and electrodes should be reevaluated.

- Access to ICP-RIE technology would allow to manufacture microfluidic structures with much higher precision and it would not be dependent on the estimation of wet etching isotropicity. For manufacture of structures requiring higher precision, this technique should be considered
- An experimental analysis of sorting strategy must be conducted. It should result in a study of whether the sorting in confined or in free regime is more reliable.
- The destructive influence of the applied electric field on the overall operation of the microfluidic chip should be addressed with properly designed grounding electrode surrounding the area where the electric field is applied [176].
- If the droplet recognition software will not bring sufficient accuracy to trigger the spectroscopy and sorting, a simpler solution consisting *e.g.* of a photodetector sensing the scattered light intensity from exchanging droplets should be designed (supplementary movie [M12](#)).
- If the low sensitivity of the iDus camera will become an issue, the employment of PMT or APD with proper filters should be reevaluated.
- For the excitation of a broader set of nanotubes from the ensemble, a set of excitation lasers or a coherent white light source should be considered.

Bibliography

- [1] Brock, D. C., *Understanding Moore's Law – Four Decades of Innovation* (Chemical Heritage Foundation, Philadelphia, PA, USA, 2006).
- [2] Iijima, S., and Ichihashi, T., *Single-shell Carbon Nanotubes of 1-nm Diameter*. *Nature* **363** (1993) 603-605.
- [3] De Volder, M. F. L., Tawfick, S. H., Baughman, R. H., and Hart, J. A., *Carbon Nanotubes: Present and Future Commercial Applications*. *Science* **339** (2013) 535-539.
- [4] Weisman, R. B., and Bachilo, S. M., *Dependence of Optical Transition Energies on Structure for Single-Walled Carbon Nanotubes in Aqueous Suspension: An Empirical Kataura Plot*. *Nano Lett.* **3** (2003) 1235-1238.
- [5] Paradise, M., and Goswami, T., *Carbon Nanotubes – Production and Industrial Applications*. *Mater. Des.* **28** (2007) 1477-1489.
- [6] Chaturvedi, P., Shah, P., Singh, A., Chaudhury, P. K., Harsh, D., and Basu, P. K., *Carbon Nanotube – Purification and Sorting Protocols*. *Def. Sci. J.* **58** (2008) 591-599.
- [7] Liu, B., Wu, F., Gui, H., Zheng, M., and Zhou, C., *Chirality-Controlled Synthesis and Applications of Single-Wall Carbon Nanotubes*. *ASC Nano* **11** (2017) 31-53.
- [8] Janas, D., *Towards Monochiral Carbon Nanotubes: A Review of Progress in the Sorting of Single-Walled Carbon Nanotubes*. *Mater. Chem. Front.* **2** (2018) 36-63.
- [9] Whitesides, G. M., *The Origins and the Future of Microfluidics*. *Nature* **442** (2006) 368-373.
- [10] Teh, S., Lin, R., Hung, L., and Lee, A. P., *Droplet Microfluidics*. *Lab Chip* **8** (2008) 198-220.
- [11] Yang, C., Xu, Z., and Wang, J., *Manipulation of Droplets in Microfluidic Systems*. *TRAC - Trend. Anal. Chem.* **29** (2010) 141-157.
- [12] Leman, M., Abouakil, F., Griffiths, A. D., and Tabeling, P., *Droplet-Based Microfluidics at the Femtolitre Scale*. *Lab Chip* **15** (2015) 753-765.

- [13] Baret, J., Miller, O. J., Taly, V., Ryckelynck, M., El-Harrak, A., Frenz, L., Rick, C., Samuels, M. L., Hutchison, J. B., Agresti, J. J., Link, D. R., Weitz, D. A., and Griffiths, A. D., *Fluorescence-Activated Droplet Sorting (FADS): Efficient Microfluidic Cell Sorting Based on Enzymatic Activity*. *Lab Chip* **9** (2009) 1850-1858.
- [14] Leman, M., *Droplet-Based Microfluidics at the Femtoliter Scale*. Ph.D. thesis, SMAER, Pierre and Marie Curie University, France (2015).
- [15] Chang, L., Yueyang, Q., Yong, L., and Ning, F., *Recent Advances in Single-Molecule Detection on Micro- and Nano-Fluidic Devices*. *Electrophoresis* **32** (2011) 3308-3318.
- [16] Rojas, L. R., *Fabrication Techniques for Developing a Functional Microfluidic Glass Device Suitable for Detection in Optical Spectroscopy System*. M.Sc. thesis, Department of Physics, University of Jyväskylä, Finland (2012).
- [17] Pekkala, I., *Microfluidics for the Spectroscopy of Carbon Nanotubes*. M.Sc. thesis, Department of Physics, University of Jyväskylä, Finland (2013).
- [18] Lehmuskoski, J., *Exploitation of Microfluidics and Raman Spectroscopy in Carbon Nanotube Separation*. B.Sc. thesis, Department of Chemistry, University of Jyväskylä, Finland (2013).
- [19] Iijima, S., *Helical Microtubules of Graphitic Carbon*. *Nature* **354** (1991) 56-58.
- [20] Radushkevich, L. V., and Lukyanovich, V. M., *О Структуре Углерода, Образующегося При Термическом Разложении Окиси Углерода На Железном Контакте*. *ЖФХ* (in Russian) **26** (1952) 88-95.
- [21] Oberlin, A., Endo, M., and Koyama, T., *Filamentous Growth of Carbon Through Benzene Decomposition*. *J. Cryst. Growth* **32** (1976) 335-349.
- [22] Charlier, J., Blase, X., and Roche, S., *Electronic and Transport Properties of Nanotubes*. *Rev. Mod. Phys.* **79** (2007) 677-732.
- [23] Shulaker, M. M., Hills, G., Patil, N., Wei, H., Chen, H., Wong, H. P., and Mitra, S., *Carbon Nanotube Computer*. *Nature* **501** (2013) 526-530.
- [24] Wu, Y., Lin, X., and Zhang, M., *Carbon Nanotubes for Thin Film Transistor: Fabrication, Properties, and Applications*. *J. Nanomater.* **2013** (2013) 627215.
- [25] Chen, Z., Farmer, D., Xu, S., Gordon, R., Avouris, P., and Appenzeller, J., *Externally Assembled Gate-All-Around Carbon Nanotube Field-Effect Transistor*. *IEEE Electron Device Lett.* **29** (2008) 183-185.

- [26] Hong, G., Diao, S., Chang, J., Antaris, A. L., Chen, C., Zhang, B., Zhao, S., Atochin, D. N., Huang, P. L., Andreasson, K. I., Kuo, C. J., and Dai, H., *Through-skull Fluorescence Imaging of the Brain in a New Near-Infrared Window*. *Nat. Photonics* **8** (2014) 723-730.
- [27] Odom, T. W., Huang, J., Kim, P., and Lieber, C. M., *Structure and Electronic Properties of Carbon Nanotubes*. *J. Phys. Chem. B* **104** (2000) 2794-2809.
- [28] Odom, T. W., Huang, J., Kim, P., and Lieber, C. M., *Atomic Structure and Electronic Properties of Single-Walled Carbon Nanotubes*. *Nature* **391** (1998) 62-64.
- [29] Saito, R., Dresselhaus, G., and Dresselhaus, M. S., *Trigonal Warping Effect of Carbon Nanotubes*. *Phys. Rev. B* **61** (2000) 2981-2990.
- [30] Matsuda, Y., Tahir-Kheli, J., and Goddard, W. A., *Definitive Band Gaps for Single-Wall Carbon Nanotubes*. *J. Phys. Chem. Lett.* **1** (2010) 2946-2950.
- [31] Nizam, R., Rizvi, S. M. A., and Azam, A., *Calculating Electronic Structure of Different Carbon Nanotubes and its Affect on Bandgap*. *Int. J. Sci. Technol.* **1** (2011) 153-162.
- [32] Ouyang, M., Huang, J., Cheung, C. L., and Lieber, C. M., *Energy Gaps in "Metallic" Single-Walled Carbon Nanotubes*. *Science* **292** (2001) 702-705.
- [33] Höper, R., Workman, R. K., Chen, D., Sarid, D., Yadav, T., Withers, J. C., and Loutfy, R. O., *Single-shell Carbon Nanotubes Imaged by Atomic Force Microscopy*. *Surf. Sci.* **311** (1994) 731-736.
- [34] Snowden, M. E., Edwards, M. A., Rudd, N. C., Macpherson, J. V., and Unwin, P. R., *Intrinsic Electrochemical Activity of Single Walled Carbon Nanotube-Nafion Assemblies*. *Phys. Chem. Chem. Phys.* **15** (2013) 5030-5038.
- [35] Colomer, J. F., Henrard, L., Lambin, P., and Van Tendeloo, G., *Electron Diffraction and Microscopy of Single-Wall Carbon Nanotube Bundles Produced by Different Methods*. *Eur. Phys. J. B.* **27** (2002) 111-118.
- [36] Warner, J. H., Young, N. P., Kirkland, A. I., and Briggs, G. A., *Resolving Strain in Carbon Nanotubes at the Atomic Level*. *Nat. Mater.* **10** (2011) 958-962.
- [37] Araujo, P. T., Maciel, I. O., Pesce, P. B. C., Pimenta, M. A., Doorn, S. K., Qian, H., Hartschuh, A., Steiner, M., Grigorian, L., Hata, K., and Jorio, A., *Nature of the Constant Factor in the Relation Between Radial Breathing Mode Frequency and Tube Diameter for Single-Wall Carbon Nanotubes*. *Phys. Rev. B* **77** (2008) 241403.
- [38] Fantini, C., Jorio, A., Souza, M., Strano, M. S., Dresselhaus, M. S., and Pimenta, M. A., *Optical Transition Energies for Carbon Nanotubes from Resonant Raman Spectroscopy: Environment and Temperature Effects*. *Phys. Rev. Lett.* **93** (2004) 147406.

- [39] Dresselhaus, M. S., Dresselhaus, G., Jorio, A., Souza Filho, A. G., and Saito, R., *Raman Spectroscopy on Isolated Single Wall Carbon Nanotubes*. *Carbon* **40** (2002) 2043-2061.
- [40] Kataura, H., Kumazawa, Y., Maniwa, Y., Umez, I., Suzuki, S., Ohtsuka, Y., and Achiba, Y., *Optical Properties of Single-Wall Carbon Nanotubes*. *Synth. Met.* **103** (1999) 2555-2558.
- [41] Iizumi, Y., Suzuki, H., Tange, M., and Okazaki, T., *Diameter Selective Electron Transfer from Encapsulated Ferrocenes to Single-Walled Carbon Nanotubes*. *Nanoscale* **6** (2014) 13910-13914.
- [42] O'Connell, M. J., Bachilo, S. M., Huffman, C. B., Moore, V. C., Strano, M. S., Haroz, E. H., Rialon, K. L., Boul, P. J., Noon, W. H., Kittrell, C., Ma, J., Hauge, R. H., Weisman, R. B., and Smalley, R. E., *Band Gap Fluorescence from Individual Single-Walled Carbon Nanotubes*. *Science* **297** (2002) 593-596.
- [43] Bachilo, S. M., Strano, M. S., Kittrell, C., Hauge, R. H., Smalley, R. E., and Weisman, R. B., *Structure-Assigned Optical Spectra of Single-Walled Carbon Nanotubes*. *Science* **298** (2002) 2361-2366.
- [44] Wang, F., Dukovic, G., Brus, L. E., and Heinz, T. F., *Time-Resolved Fluorescence of Carbon Nanotubes and Its Implication for Radiative Lifetimes*. *Phys. Rev. Lett.* **92** (2004) 177401.
- [45] Crochet, J. J., Sau, J. D., Duque, J. G., Doorn, S. K., and Cohen, M. L., *Electrodynamic and Excitonic Intertube Interactions in Semiconducting Carbon Nanotube Aggregates*. *ASC Nano* **5** (2011) 2611-2618.
- [46] Ishigami, N., Ago, H., Imamoto, K., Tsuji, M., Iakoubovskii, K., and Minami, N., *Crystal Plane Dependent Growth of Aligned Single-Walled Carbon Nanotubes on Sapphire*. *J. Am. Chem. Soc.* **130** (2008) 9918-9924.
- [47] Crochet, J., Clemens, M., and Hertel, T., *Quantum Yield Heterogeneities of Aqueous Single-Wall Carbon Nanotube Suspensions*. *J. Am. Chem. Soc.* **129** (2007) 8058-8059.
- [48] Carlson, L. J., Maccagnano, S. E., Zheng, M., Silcox, J., and Krauss, T. D., *Fluorescence Efficiency of Individual Carbon Nanotubes*. *Nano Lett.* **7** (2007) 3698-3703.
- [49] Tsyboulski, D. A., Rocha, J. R., Bachilo, S. M., Cagnet, L., and Weisman, R. B., *Structure-Dependent Fluorescence Efficiencies of Individual Single-Walled Carbon Nanotubes*. *Nano Lett.* **7** (2007) 3080-3085.
- [50] Ju, S., Kopcha, W. P., and Papadimitrakopoulos, F., *Brightly Fluorescent Single-Walled Carbon Nanotubes via an Oxygen-Excluding Surfactant Organization*. *Science* **323** (2009) 1319-1323.

- [51] Duque, J. G., Pasquali, M., Cognet, L., and Lounis, B., *Environmental and Synthesis-Dependent Luminescence Properties of Individual Single-Walled Carbon Nanotubes*. *ASC Nano* **3** (2009) 2153-2156.
- [52] Cherukuri, T. K., Tsyboulski, D. A., and Weisman, R. B., *Length- and Defect-Dependent Fluorescence Efficiencies of Individual Single-Walled Carbon Nanotubes*. *ASC Nano* **6** (2012) 843-850.
- [53] Kiowski, O., Jester, S., Lebedkin, S., Jin, Z., Li, Y., and Kappes, M. M., *Photoluminescence Spectral Imaging of Ultralong Single-Walled Carbon Nanotubes: Micromanipulation-Induced Strain, Rupture, and Determination of Handedness*. *Phys. Rev. B* **80** (2009) 075426.
- [54] Heller, D. A., Mayrhofer, R. M., Baik, S., Grinkova, Y. V., Usrey, M. L., and Strano, M. S., *Concomitant Length and Diameter Separation of Single-Walled Carbon Nanotubes*. *J. Am. Chem. Soc.* **126** (2004) 14567-14573.
- [55] Fagan, J. A., Simpson, J. R., Bauer, B. J., De, P. L., Becker, M. L., Chun, J., Migler, K. B., Hight Walker, A. R., and Hobbie, E. K., *Length-Dependent Optical Effects in Single-Wall Carbon Nanotubes*. *J. Am. Chem. Soc.* **129** (2007) 10607-10612.
- [56] Ziegler, L. D., *On the Difference Between Resonance Raman Scattering and Resonance Fluorescence in Molecules: An Experimental View*. *Acc. Chem. Res.* **27** (1994) 1-8.
- [57] Tu, X., Manohar, S., Jagota, A., and Zheng, M., *DNA Sequence Motifs for Structure-Specific Recognition and Separation of Carbon Nanotubes*. *Nature* **460** (2009) 250-253.
- [58] Huang, H., Kajiura, H., Maruyama, R., Kadono, K., and Noda, K., *Relative Optical Absorption of Metallic and Semiconducting Single-Walled Carbon Nanotubes*. *J. Phys. Chem. B* **110** (2006) 4686-4690.
- [59] Rocha, J. R., Bachilo, S. M., Ghosh, S., Arepalli, S., and Weisman, R. B., *Efficient Spectrofluorimetric Analysis of Single-Walled Carbon Nanotube Samples*. *Anal. Chem.* **83** (2011) 7431-7437.
- [60] Huang, J., Zhang, Q., Zhao, M., and Wei, F., *A Review of the Large-Scale Production of Carbon Nanotubes: The Practice of Nanoscale Process Engineering*. *Chin. Sci. Bull.* **57** (2012) 157-166.
- [61] Ying, L. S., bin Mohd Salleh, M. A., bin Mohamed Yusoff, H., Rashid, S. B. A., and bin Abdul Razak, J., *Continuous Production of Carbon Nanotubes – A Review*. *Journal of Industrial and Engineering Chemistry* **17** (2011) 367-376.
- [62] Raty, J., Gygi, F., and Galli, G., *Growth of Carbon Nanotubes on Metal Nanoparticles: A Microscopic Mechanism from Ab Initio Molecular Dynamics Simulations*. *Phys. Rev. Lett.* **95** (2005) 096103.

- [63] Nikolaev, P., Bronikowski, M. J., Bradley, R. K., Rohmund, F., Colbert, D. T., Smith, K. A., and Smalley, R. E., *Gas-Phase Catalytic Growth of Single-Walled Carbon Nanotubes from Carbon Monoxide*. Chem. Phys. Lett. **313** (1999) 91-97.
- [64] Bronikowski, M. J., Willis, P. A., Colbert, D. T., Smith, K. A., and Smalley, R. E., *Gas-Phase Production of Carbon Single-Walled Nanotubes from Carbon Monoxide via the HiPco Process: A Parametric Study*. J. Vac. Sci. Technol. A **19** (2001) 1800-1805.
- [65] Meyer-Plath, A., Orts-Gil, G., Petrov, S., Oleszak, F., Maneck, H., Dörfel, I., Haase, O., Richter, S., and Mach, R., *Plasma-Thermal Purification and Annealing of Carbon Nanotubes*. Carbon **50** (2012) 3934-3942.
- [66] NanoIntegris, *Unsorted Purified SWNTS*, <http://nanointegris.com/our-products/unsorted-purified-swnts-superpuretubes-and-puretubes/> (2018) [Online; accessed 20-april-2018].
- [67] Dumlich, H., Gegg, M., Hennrich, F., and Reich, S., *Bundle and Chirality Influences on Properties of Carbon Nanotubes Studied with van der Waals Density Functional Theory*. Phys. Status Solidi B **248** (2011) 2589-2592.
- [68] Rinkiö, M., Johansson, A., Paraoanu, G. S., and Törmä, P., *High-Speed Memory from Carbon Nanotube Field-Effect Transistors with High- κ Gate Dielectric*. Nano Lett. **9** (2009) 643-647.
- [69] Dekker, C., *Carbon Nanotubes as Molecular Quantum Wires*. Phys. Today **52** (1999) 22-28.
- [70] Cui, J., Yang, D., Zeng, X., Zhou, N., and Liu, H., *Recent Progress on the Structure Separation of Single-Wall Carbon Nanotubes*. Nanotechnology **28** (2017) 452001.
- [71] Hersam, M. C., *Progress Towards Monodisperse Single-Walled Carbon Nanotubes*. Nat. Nanotechnol. **3** (2008) 387-394.
- [72] Hou, P. X., Li, W. S., Zhao, S. Y., Li, G. X., Shi, C., Liu, C., and Cheng, H. M., *Preparation of Metallic Single-Wall Carbon Nanotubes by Selective Etching*. ASC Nano **8** (2014) 7156-7162.
- [73] Bhattacharyya, K., Suda, Y., Okita, A., Saito, T., Ozeki, A., Maekawa, M., Takayama, J., Sugawara, H., and Sakai, Y., *Is the Diameter or Chirality Distribution of Single-Walled Carbon Nanotubes Selected in the Synthesis Process?* J. Nanosci. Nanotechnol. **9** (2009) 1897-1903.
- [74] Wang, H., Yuan, Y., Wei, L., Goh, K., Yu, D., and Chen, Y., *Catalysts for Chirality Selective Synthesis of Single-Walled Carbon Nanotubes*. Carbon **81** (2015) 1-19.

- [75] Zhang, F., Hou, P. X., Liu, C., Wang, B. W., Jiang, H., Chen, M. L., Sun, D. M., Li, J. C., Cong, H. T., Kauppinen, E. I., and Cheng, H. M., *Growth of Semiconducting Single-Wall Carbon Nanotubes with a Narrow Band-Gap Distribution*. Nat. Commun. **7** (2016) 11160.
- [76] Bachilo, S. M., Balzano, L., Herrera, J. E., Pompeo, F., Resasco, D. E., and Weisman, R. B., *Narrow (n,m)-Distribution of Single-Walled Carbon Nanotubes Grown Using a Solid Supported Catalyst*. J. Am. Chem. Soc. **125** (2003) 11186-11187.
- [77] Liu, J., Wang, C., Tu, X., Liu, B., Chen, L., Zheng, M., and Zhou, C., *Chirality-Controlled Synthesis of Single-Wall Carbon Nanotubes Using Vapour-Phase Epitaxy*. Nat. Commun. **3** (2012) 1199.
- [78] Sanchez-Valencia, J., Dienel, T., Gröning, O., Shorubalko, I., Mueller, A., Jansen, M., Amsharov, K., Ruffieux, P., and Fasel, R., *Controlled Synthesis of Single-Chirality Carbon Nanotubes*. Nature **512** (2014) 61-64.
- [79] Arnold, M. S., Green, A. A., Hulvat, J. F., Stupp, S. I., and Hersam, M. C., *Sorting Carbon Nanotubes by Electronic Structure Using Density Differentiation*. Nat. Nanotechnol. **1** (2006) 60-65.
- [80] Zheng, M., Jagota, A., Strano, M. S., Santos, A. P., Barone, P., Chou, S. G., Diner, B. A., Dresselhaus, M. S., Mclean, R. S., Onoa, G. B., Samsonidze, G. G., Semke, E. D., Usrey, M., and Walls, D. J., *Structure-Based Carbon Nanotube Sorting by Sequence-Dependent DNA Assembly*. Science **302** (2003) 1545-1548.
- [81] Yomogida, Y., Tanaka, T., Zhang, M., Yudasaka, M., Wei, X., and Kataura, H., *Industrial-Scale Separation of High-Purity Single-Chirality Single-Wall Carbon Nanotubes for Biological Imaging*. Nat. Commun. **7** (2016) 12056.
- [82] Liu, H., Tanaka, T., Urabe, Y., and Kataura, H., *High-Efficiency Single-Chirality Separation of Carbon Nanotubes Using Temperature-Controlled Gel Chromatography*. Nano Lett. **13** (2013) 1996-2003.
- [83] Marcaccio, M., and Paolucci, F., *Making and Exploiting Fullerenes, Graphene, and Carbon Nanotubes* (Springer-Verlag, Berlin, Heidelberg, Germany, 2014).
- [84] Pénicaud, A., Dragin, F., Pécastaings, G., He, M., and Anglaret, E., *Concentrated Solutions of Individualized Single Walled Carbon Nanotubes*. Carbon **67** (2014) 360-367.
- [85] Thathan, P., Raffaele, M., and Geckeler, K. E., *Carbon Nanotubes in the Liquid Phase: Addressing the Issue of Dispersion*. Small **8** (2012) 1299-1313.
- [86] Wenseleers, W., Vlasov, I. I., Goovaerts, E., Obraztsova, E. D., Lobach, A. S., and Bouwen, A., *Efficient Isolation and Solubilization of Pristine Single-Walled Nanotubes in Bile Salt Micelles*. Adv. Funct. Mater. **14** (2004) 1105-1112.

- [87] Petit, P., Mathis, C., Journet, C., and Bernier, P., *Tuning and Monitoring the Electronic Structure of Carbon Nanotubes*. Chem. Phys. Lett. **305** (1999) 370-374.
- [88] Davis, V. A., Parra-Vasquez, A., Green, M. J., Rai, P. K., Behabtu, N., Prieto, V., Booker, R. D., Schmidt, J., Kesselman, E., Zhou, W., Fan, H., Adams, W. W., Hauge, R. H., Fischer, J. E., Cohen, Y., Talmon, Y., Smalley, R. E., and Pasquali, M., *True Solutions of Single-Walled Carbon Nanotubes for Assembly into Macroscopic Materials*. Nat. Nanotechnol. **4** (2009) 830-834.
- [89] Girifalco, L. A., Hodak, M., and Lee, R. S., *Carbon Nanotubes, Buckyballs, Ropes, and a Universal Graphitic Potential*. Phys. Rev. B **62** (2000) 13104-13110.
- [90] Strano, M. S., Moore, V., Miller, M. K., Allen, M. J., Haroz, E., Kittrell, C., Hauge, R., and Smalley, R. E., *The Role of Surfactant Adsorption During Ultrasonication in the Dispersion of Single-Walled Carbon Nanotubes*. I. Nanosci. Nanotechnol. **3** (2003) 81-86.
- [91] Bahr, J. L., Mickelson, E. T., Bronikowski, M. J., Smalley, R. E., and Tour, J. M., *Dissolution of Small Diameter Single-Wall Carbon Nanotubes in Organic Solvents?* Chem. Commun. (2001) 193-194.
- [92] Shimizu, M., Fujii, S., Tanaka, T., and Kataura, H., *Effects of Surfactants on the Electronic Transport Properties of Thin-Film Transistors of Single-Wall Carbon Nanotubes*. J. Phys. Chem. C **117** (2013) 11744-11749.
- [93] Leeds, J. D., Fourkas, J. T., and YuHuang, W., *Achieving Ultrahigh Concentrations of Fluorescent Single-Walled Carbon Nanotubes Using Small-Molecule Viscosity Modifiers*. Small **9** (2013) 241-247.
- [94] Priya, B. R., and Byrne, H. J., *Investigation of Sodium Dodecyl Benzene Sulfonate Assisted Dispersion and Debundling of Single-Wall Carbon Nanotubes*. J. Phys. Chem. C **112** (2008) 332-337.
- [95] Blanch, A. J., Lenehan, C. E., and Quinton, J. S., *Parametric Analysis of Sonication and Centrifugation Variables for Dispersion of Single Walled Carbon Nanotubes in Aqueous Solutions of Sodium Dodecylbenzene Sulfonate*. Carbon **49** (2011) 5213-5228.
- [96] Vaisman, L., Wagner, H. D., and Marom, G., *The Role of Surfactants in Dispersion of Carbon Nanotubes*. Adv. Colloid Interface Sci. **128-130** (2006) 37-46.
- [97] Fernandes, R. M. F., Abreu, B., Claro, B., Buzaglo, M., Regev, O., Furó, I., and Marques, E. F., *Dispersing Carbon Nanotubes with Ionic Surfactants under Controlled Conditions: Comparisons and Insight*. Langmuir **31** (2015) 10955-10965.
- [98] Yao, Y., Luo, S., and Liu, T., *Determination of the Length, Diameter, Molecular Mass, Density and Surfactant Adsorption of SWCNTs in Dilute Dispersion by Intrinsic Viscosity, Sedimentation, and Diffusion Measurements*. Macromolecules **47** (2014) 3093-3100.

- [99] Jiang, L., Gao, L., and Sun, J., *Production of Aqueous Colloidal Dispersions of Carbon Nanotubes*. *J. Colloid Interface Sci.* **260** (2003) 89-94.
- [100] Shi, Y., Ren, L., Gao, H., and Yang, B., *Optimization Conditions for Single-Walled Carbon Nanotubes Dispersion*. *JSEMAT* **3** (2013) 6-12.
- [101] Moore, V. C., Strano, M. S., Haroz, E. H., Hauge, R. H., Smalley, R. E., Schmidt, J., and Talmon, Y., *Individually Suspended Single-Walled Carbon Nanotubes in Various Surfactants*. *Nano Lett.* **3** (2003) 1379-1382.
- [102] Blanch, A. J., Lenehan, C. E., and Quinton, J. S., *Optimizing Surfactant Concentrations for Dispersion of Single-Walled Carbon Nanotubes in Aqueous Solution*. *J. Phys. Chem. B* **114** (2010) 9805-9811.
- [103] Yurekli, K., Mitchell, C. A., and Krishnamoorti, R., *Small-Angle Neutron Scattering from Surfactant-Assisted Aqueous Dispersions of Carbon Nanotubes*. *J. Am. Chem. Soc.* **126** (2004) 9902-9903.
- [104] Yang, K., Yi, Z., Jing, Q., Yue, R., Jiang, W., and Lin, D., *Sonication-Assisted Dispersion of Carbon Nanotubes in Aqueous Solutions of the Anionic Surfactant SDBS: The Role of Sonication Energy*. *Chinese Sci. Bull.* **58** (2013) 2082-2090.
- [105] Attal, S., Thiruvengadathan, R., and Regev, O., *Determination of the Concentration of Single-Walled Carbon Nanotubes in Aqueous Dispersions Using UV-Visible Absorption Spectroscopy*. *Anal. Chem.* **78** (2006) 8098-8104.
- [106] Mokka, A., *Preparation of HiPco Suspension*. Experimental report, University of Jyväskylä, Finland (2012).
- [107] NanoIntegris, *HiPco® Single-Wall Carbon Nanotubes*. Technical Datasheet, NanoIntegris Technologies, Inc., Canada (2018).
- [108] Maruyama, S., *1D DOS (van Hove Singularity)*, http://www.photon.t.u-tokyo.ac.jp/~maruyama/kataura/1D_DOS.html (2018) [Online; accessed 13-june-2018].
- [109] Dr. Hielscher, *UP200S / UP400S*. Instruction Manual, Hielscher Ultrasonics GmbH, Germany (2007).
- [110] Beckman Coulter, *Type 70.1 Ti Rotor Manual*. Instruction Manual, Beckman Coulter, Inc., U.S.A. (2014).
- [111] Hielscher, T., *Ultrasonic Production of Nano-Size Dispersions and Emulsions*, <https://arxiv.org/ftp/arxiv/papers/0708/0708.1831.pdf> (2007) [Online; accessed 25-june-2018].
- [112] Kuwahara, S., Sugai, T., and Shinohara, H., *Determining Exact Molar Absorbance Coefficients of Single-Wall Carbon Nanotubes*. *Phys. Chem. Chem. Phys.* **11** (2009) 1091-1097.

- [113] Shtein, M., Pri-bar, I., and Regev, O., *A Simple Solution for the Determination of Pristine Carbon Nanotube Concentration*. *Analyst* **138** (2013) 1490-1496.
- [114] Oyama, Y., Saito, R., Sato, K., Jiang, J., Samsonidze, G. G., Grüneis, A., Miyauchi, Y., Maruyama, S., Jorio, A., Dresselhaus, G., and Dresselhaus, M. S., *Photoluminescence Intensity of Single-Wall Carbon Nanotubes*. *Carbon* **44** (2006) 873-879.
- [115] Yang, B., Ren, L., Li, L., Tao, X., Shi, Y., and Zheng, Y., *The Characterization of the Concentration of the Single-Walled Carbon Nanotubes in Aqueous Dispersion by UV-Vis-NIR Absorption Spectroscopy*. *Analyst* **138** (2013) 6671-6676.
- [116] Rance, G. A., Marsh, D. H., Nicholas, R. J., and Khlobystov, A. N., *UV-Vis Absorption Spectroscopy of Carbon Nanotubes: Relationship Between the π -Electron Plasmon and Nanotube Diameter*. *Chem. Phys. Lett.* **493** (2010) 19-23.
- [117] Kuwahara, S., Kuwahara, Y., and Shinohara, H., *Quantitative Analysis of Isolated Single-Wall Carbon Nanotubes with Their Molar Absorbance Coefficients*. *J. Nanomater.* **2014** (2014) 262940.
- [118] Ashleigh, T. B., Courtois, F., Schaerli, Y., Fischlechner, M., Abell, C., Hollfelder, F., and Huck, W. T. S., *Microdroplets in Microfluidics: An Evolving Platform for Discoveries in Chemistry and Biology*. *Angew. Chem. Int. Ed.* **49** (2010) 5846-5868.
- [119] Thorsen, T., Roberts, R. W., Arnold, F. H., and Quake, S. R., *Dynamic Pattern Formation in a Vesicle-Generating Microfluidic Device*. *Phys. Rev. Lett.* **86** (2001) 4163-4166.
- [120] Collins, D. J., Neild, A., deMello, A., Liu, A., and Ai, Y., *The Poisson Distribution and Beyond: Methods for Microfluidic Droplet Production and Single Cell Encapsulation*. *Lab Chip* **15** (2015) 3439-3459.
- [121] Casadevall, S., and deMello, A., *Droplet Microfluidics: Recent Developments and Future Applications*. *Chem. Commun.* **47** (2011) 1936-1942.
- [122] Allhoff, F., Lin, P., and Moore, D., *What is Nanotechnology and why does it Matter?: From Science to Ethics* (Wiley-Blackwell, Chichester, West Sussex, United Kingdom, 2009).
- [123] Gu, H., Duits, M. H. G., and Mugele, F., *Droplets Formation and Merging in Two-Phase Flow Microfluidics*. *Int. J. Mol. Sci.* **12** (2011) 2572-2597.
- [124] Thiam, A. R., Bremond, N., and Bibette, J., *Breaking of an Emulsion under an AC Electric Field*. *Phys. Rev. Lett.* **102** (2009) 188304.
- [125] Bruus, H., *Theoretical Microfluidics*. Lecture notes, Department of Micro and Nanotechnology, Technical University of Denmark, Denmark (2006).

- [126] Wuest, W., *Strömung durch Schlitz- und Lochblenden bei kleinen Reynolds-Zahlen*. Arch. Appl. Mech. **22** (1954) 357-367.
- [127] Beer, N. R., Rose, K. A., and Kennedy, I. M., *Observed Velocity Fluctuations in Monodisperse Droplet Generators*. Lab Chip **9** (2009) 838-840.
- [128] Adzima, B. J., and Velankar, S. S., *Pressure Drops for Droplet Flows in Microfluidic Channels*. J. Micromech. Microeng. **16** (2006) 1504-1510.
- [129] Wong, H., Radke, C. J., and Morris, S., *The Motion of Long Bubbles in Polygonal Capillaries. Part 1. Thin Films*. J. Fluid Mech. **292** (1995) 71-94.
- [130] Vanapalli, S. A., Banpurkar, A. G., van den Ende, D., Duits, M. H., and Mugele, F., *Hydrodynamic Resistance of Single Confined Moving Drops in Rectangular Microchannels*. Lab Chip **9** (2009) 982-990.
- [131] Day, P., Manz, A., and Zhang, Y., *Microdroplet Technology: Principles and Emerging Applications in Biology and Chemistry* (Springer, New York, NY, USA, 2012).
- [132] Tadros, T. F., *Emulsion Formation and Stability* (Wiley-VCH Verlag GmbH & Co. KGaA, Weinheim, Germany, 2013).
- [133] Mason, T. G., *New Fundamental Concepts in Emulsion Rheology*. Curr. Opin. Colloid In. **4** (1999) 231-238.
- [134] Israelachvili, J., *The Science and Applications of Emulsions – An Overview*. Colloid. Surface. A **91** (1994) 1-8.
- [135] Jin, F., Balasubramaniam, R., and Stebe, K. J., *Surfactant Adsorption to Spherical Particles: The Intrinsic Length Scale Governing the Shift from Diffusion to Kinetic-Controlled Mass Transfer*. J. Adhes. **80** (2004) 773-796.
- [136] Griffin, W. C., *Calculation of HLB Values of Non-Ionic Surfactants*. J. Soc. Cosmet. Chem. **5** (1954) 249-256.
- [137] Chemmunique, *The HLB System: A Time-Saving Guide to Emulsifier Selection* (ICI Americas Inc., Wilmington, DE, USA, 1980).
- [138] Huibers, P. D. T., and Shah, D. O., *Evidence for Synergism in Nonionic Surfactant Mixtures: Enhancement of Solubilization in Water-in-Oil Microemulsions*. Langmuir **13** (1997) 5762-5765.
- [139] Xu, J. H., Li, S. W., Tan, J., Wang, Y. J., and Luo, G. S., *Controllable Preparation of Monodisperse O/W and W/O Emulsions in the Same Microfluidic Device*. Langmuir **22** (2006) 7943-7946.

- [140] Li, W., Nie, Z., Zhang, H., Paquet, C., Seo, M., Garstecki, P., and Kumacheva, E., *Screening of the Effect of Surface Energy of Microchannels on Microfluidic Emulsification*. *Langmuir* **23** (2007) 8010-8014.
- [141] Shui, L., van den Berg, A., and Eijkel, J. C. T., *Interfacial Tension Controlled W/O and O/W 2-phase Flows in Microchannel*. *Lab Chip* **9** (2009) 795-801.
- [142] Wacker, J., Louis, G., Razaname, C., Parashar, V. K., and Gijs, M. A. M., *Exotic Droplets Formed in Microfluidic Chips with Uniform Wettability*. *Microelectron. Eng.* **88** (2011) 1891-1893.
- [143] Opawale, F. O., and Burgess, D. J., *Influence of Interfacial Properties of Lipophilic Surfactants on Water-in-Oil Emulsion Stability*. *J. Colloid Interface Sci.* **197** (1998) 142-150.
- [144] Tenje, M., Fornell, A., Ohlin, M., and Nilsson, J., *Particle Manipulation Methods in Droplet Microfluidics*. *Anal. Chem.* **90** (2018) 1434-1443.
- [145] Chu Liang-Yin, Utada Andrew S., Shah Rhutesh K., Kim Jin-Woong, and Weitz David A., *Controllable Monodisperse Multiple Emulsions*. *Angew. Chem. Int. Ed.* **119** (2007) 9128-9132.
- [146] Li, Z., Leshansky, A. M., Pismen, L. M., and Tabeling, P., *Step-Emulsification in Nanofluidic Device*. *Lab Chip* **15** (2015) 1023-1031.
- [147] Malloggi, F., Pannacci, N., Attia, R., Monti, F., Mary, P., Willaime, H., Tabeling, P., Cabane, B., and Poncet, P., *Monodisperse Colloids Synthesized with Nanofluidic Technology*. *Langmuir* **26** (2010) 2369-2373.
- [148] Weinmeister, R., Freeman, E., Eperon, I. C., Stuart, A. M., and Hudson, A. J., *Single-Fluorophore Detection in Femtoliter Droplets Generated by Flow Focusing*. *ASC Nano* **9** (2015) 9718-9730.
- [149] Sahin, S., Bliznyuk, O., Rovalino Cordova, A., and Schroën, K., *Microfluidic EDGE Emulsification: The Importance of Interface Interactions on Droplet Formation and Pressure Stability*. *Sci. Rep.* **6** (2016) 26407.
- [150] Tarchichi, N., Chollet, F., and Manceau, J., *New Regime of Droplet Generation in a T-shape Microfluidic Junction*. *Microfluid. Nanofluid.* **14** (2013) 45-51.
- [151] Gupta, A., Murshed, S. M. S., and Kumar, R., *Droplet Formation and Stability of Flows in a Microfluidic T-junction*. *Appl.Phys.Lett.* **94** (2009) 164107.
- [152] Bai, L., Fu, Y., Zhao, S., and Cheng, Y., *Droplet Formation in a Microfluidic T-junction Involving Highly Viscous Fluid Systems*. *Chem. Eng. Sci.* **145** (2016) 141-148.

- [153] Lee, W., Walker, L. M., and Anna, S. L., *Role of Geometry and Fluid Properties in Droplet and Thread Formation Processes in Planar Flow Focusing*. *Phys. Fluids* **21** (2009) 032103.
- [154] Anna, S. L., Bontoux, N., and Stone, H. A., *Formation of Dispersions Using "Flow Focusing" in Microchannels*. *Appl. Phys. Lett.* **82** (2003) 364-366.
- [155] Fu, T., Ma, Y., Funfschilling, D., and Li, H. Z., *Bubble Formation and Breakup Mechanism in a Microfluidic Flow-Focusing Device*. *Chem. Eng. Sci.* **64** (2009) 2392-2400.
- [156] Fu, T., Wu, Y., Ma, Y., and Li, H. Z., *Droplet Formation and Breakup Dynamics in Microfluidic Flow-Focusing Devices: From Dripping to Jetting*. *Chem. Eng. Sci.* **84** (2012) 207-217.
- [157] Beer, N. R., Rose, K. A., and Kennedy, I. M., *Monodisperse Droplet Generation and Rapid Trapping for Single Molecule Detection and Reaction Kinetics Measurement*. *Lab Chip* **9** (2009) 841-844.
- [158] Schlicht, B., and Zagnoni, M., *Droplet-Interface-Bilayer Assays in Microfluidic Passive Networks*. *Sci. Rep.* **5** (2015) 9951.
- [159] Arayanarakool, R., *Toward Single Enzyme Analysis in a Droplet-based Micro and Nanofluidic System*. Ph.D. thesis, MESA+ Institute for nanotechnology, University of Twente, Netherlands (2012).
- [160] Abbyad, P., Dangla, R., Alexandrou, A., and Baroud, C. N., *Rails and Anchors: Guiding and Trapping Droplet Microreactors in Two Dimensions*. *Lab Chip* **11** (2011) 813-821.
- [161] Huebner, A., Bratton, D., Whyte, G., Yang, M., deMello, A. J., Abell, C., and Hollfelder, F., *Static Microdroplet Arrays: a Microfluidic Device for Droplet Trapping, Incubation and Release for Enzymatic and Cell-Based Assays*. *Lab Chip* **9** (2009) 692-698.
- [162] Srisa-Art, M., deMello, A. J., and Edel, J. B., *High-Efficiency Single-Molecule Detection within Trapped Aqueous Microdroplets*. *J. Phys. Chem. B* **114** (2010) 15766-15772.
- [163] Schmitz, C. H. J., Rowat, A. C., Koster, S., and Weitz, D. A., *Dropspots: A Picoliter Array in a Microfluidic Device*. *Lab Chip* **9** (2009) 44-49.
- [164] Zhu, Y., and Fang, Q., *Analytical Detection Techniques for Droplet Microfluidics – A Review*. *Anal. Chim. Acta* **787** (2013) 24-35.
- [165] Lin, B., *Microfluidics: Technologies and Applications* (Springer-Verlag, Berlin, Heidelberg, Germany, 2011).

- [166] Tan, Y., Fisher, J. S., Lee, A. I., Cristini, V., and Lee, A. P., *Design of Microfluidic Channel Geometries for the Control of Droplet Volume, Chemical Concentration, and Sorting*. *Lab Chip* **4** (2004) 292-298.
- [167] Teste, B., Jamond, N., Ferraro, D., Viovy, J., and Malaquin, L., *Selective Handling of Droplets in a Microfluidic Device Using Magnetic Rails*. *Microfluid. Nanofluid.* **19** (2015) 141-153.
- [168] Link, D. R., Grasland-Mongrain Erwan, Agnes, D., Flavie, S., Zhengdong, C., Galder, C., Manuel, M., and Weitz, D. A., *Electric Control of Droplets in Microfluidic Devices*. *Angew. Chem. Int. Edit.* **45** (2006) 2556-2560.
- [169] Kwang, W. O., and Chong, H. A., *A Review of Microvalves*. *J. Micromech. Microengineering.* **16** (2006) 13-39.
- [170] Baroud, C. N., Delville, J. P., Gallaire, F., and Wunenburger, R., *Thermocapillary Valve for Droplet Production and Sorting*. *Phys. Rev. E.* **75** (2007) 046302.
- [171] Li, P. C. H., and Harrison, D. J., *Transport, Manipulation, and Reaction of Biological Cells On-Chip Using Electrokinetic Effects*. *Anal. Chem.* **69** (1997) 1564-1568.
- [172] Wang, M. M., Tu, E., Raymond, D. E., Yang, J. M., Zhang, H., Hagen, N., Dees, B., Mercer, E. M., Forster, A. H., Kariv, I., Marchand, P. J., and Butler, W. F., *Microfluidic Sorting of Mammalian Cells by Optical Force Switching*. *Nat. Biotechnol.* **23** (2004) 83-87.
- [173] Baroud, C. N., de Saint Vincent, M R, and Delville, J., *An Optical Toolbox for Total Control of Droplet Microfluidics*. *Lab Chip* **7** (2007) 1029-1033.
- [174] Franke, T., Abate, A. R., Weitz, D. A., and Wixforth, A., *Surface Acoustic Wave (SAW) Directed Droplet Flow in Microfluidics for PDMS Devices*. *Lab Chip* **9** (2009) 2625-2627.
- [175] Ding, X., Lin, S. S., Kiraly, B., Yue, H., Li, S., Chiang, I., Shi, J., Benkovic, S. J., and Huang, T. J., *On-Chip Manipulation of Single Microparticles, Cells, and Organisms Using Surface Acoustic Waves*. *PNAS* **109** (2012) 11105.
- [176] Sciambi, A., and Abate, A. R., *Accurate Microfluidic Sorting of Droplets at 30 kHz*. *Lab Chip* **15** (2015) 47-51.
- [177] Jubery, T. Z., Srivastava, S. K., and Prashanta, D., *Dielectrophoretic Separation of Bioparticles in Microdevices: A Review*. *Electrophoresis* **35** (2014) 691-713.
- [178] Baret, J., *Surfactants in Droplet-Based Microfluidics*. *Lab Chip* **12** (2012) 422-433.

- [179] Debon, A. P., Wootton, R. C. R., and Elvira, K. S., *Droplet Confinement and Leakage: Causes, Underlying Effects, and Amelioration Strategies*. *Biomicrofluidics* **9** (2015) 024119.
- [180] Graczyk, M., Balaz, M., Linke, H., and Maximov, I., *Fabrication of Bottle-Shaped Nanochannels in Fused Silica Using a Self-Closing Effect*. *Microelectron. Eng.* **97** (2012) 173-176.
- [181] Feng, Y., Zhou, Z., Ye, X., and Xiong, J., *Passive Valves Based on Hydrophobic Microfluidics*. *Sensor. Actuat. A-Phys.* **108** (2003) 138-143.
- [182] Fukuyama, M., and Hibara, A., *Microfluidic Selective Concentration of Microdroplet Contents by Spontaneous Emulsification*. *Anal. Chem.* **87** (2015) 3562-3565.
- [183] Zang, E., Brandes, S., Tovar, M., Martin, K., Mech, F., Horbert, P., Henkel, T., Figge, M. T., and Roth, M., *Real-Time Image Processing for Label-Free Enrichment of Actinobacteria Cultivated in Picolitre Droplets*. *Lab Chip* **13** (2013) 3707-3713.
- [184] Iliescu, C., Taylor, H., Avram, M., Miao, J., and Franssila, S., *A Practical Guide for the Fabrication of Microfluidic Devices Using Glass and Silicon*. *Biomicrofluidics* **6** (2012) 016505.
- [185] Giri, B., *Laboratory Methods in Microfluidics* (Elsevier, Amsterdam, Netherlands, 2017).
- [186] Lin, C., Lee, G., Lin, Y., and Chang, G., *A Fast Prototyping Process for Fabrication of Microfluidic Systems on Soda-Lime Glass*. *J. Micromech. Microeng.* **11** (2001) 726-732.
- [187] Van Toan, N., Toda, M., and Ono, T., *An Investigation of Processes for Glass Micromachining*. *Micromachines* **7** (2016) 51.
- [188] Rojas, L., Norarat, R., Napari, M., Kivistö, H., Chienthavorn, O., and Whitlow, H. J., *Lithographic Fabrication of Soda-Lime Glass Based Microfluidics*. *Nucl. Instrum. Meth. B* **306** (2013) 296-298.
- [189] Tay, F. E. H., Iliescu, C., Jing, J., and Miao, J., *Defect-Free Wet Etching Through Pyrex Glass Using Cr/Au Mask*. *Microsyst. Technol.* **12** (2006) 935-939.
- [190] Iliescu, C., Jing, J., Tay, F. E. H., Miao, J., and Sun, T., *Characterization of Masking Layers for Deep Wet Etching of Glass in an Improved HF/HCl Solution*. *Surf. Coat. Tech.* **198** (2005) 314-318.
- [191] Bu, M., Melvin, T., Ensell, G. J., Wilkinson, J. S., and Evans, A. G. R., *A New Masking Technology for Deep Glass Etching and its Microfluidic Application*. *Sensor. Actuat. A-Phys.* **115** (2004) 476-482.

- [192] Mao, P., and Han, J., *Fabrication and Characterization of 20 nm Planar Nanofluidic Channels by Glass-Glass and Glass-Silicon Bonding*. *Lab Chip* **5** (2005) 837-844.
- [193] Rodriguez, I., Spicar-Mihalic, P., Kuyper, C. L., Fiorini, G. S., and Chiu, D. T., *Rapid Prototyping of Glass Microchannels*. *Anal. Chim. Acta* **496** (2003) 205-215.
- [194] P Abgrall, a. A., *Lab-on-Chip Technologies: Making a Microfluidic Network and Coupling it into a Complete Microsystem – A Review*. *J. Micromech. Microengineering* **17** (2007) 15-49.
- [195] Thiénot, E., Domingo, F., Cambril, E., and Gosse, C., *Reactive Ion Etching of Glass for Biochip Applications: Composition Effects and Surface Damages*. *Microelectron. Eng.* **83** (2006) 1155-1158.
- [196] Iliescu, C., Chen, B., and Miao, J., *On the Wet Etching of Pyrex Glass*. *Sensor. Actuat. A-Phys.* **143** (2008) 154-161.
- [197] Park, J. H., Lee, N. E., Lee, J., Park, J. S., and Park, H. D., *Deep Dry Etching of Borosilicate Glass Using SF₆ and SF₆/Ar Inductively Coupled Plasmas*. *Microelectron. Eng.* **82** (2005) 119-128.
- [198] Kolari, K., *Deep Plasma Etching of Glass With a Silicon Shadow Mask*. *Sensor. Actuat. A-Phys.* **141** (2008) 677-684.
- [199] Ronggui, S., and Righini, G. C., *Characterization of Reactive Ion Etching of Glass and its Applications in Integrated Optics*. *J. Vac. Sci. Technol. A* **9** (1991) 2709-2712.
- [200] Leech, P. W., *Reactive Ion Etching of Quartz and Silica-Based Glasses in CF₄/CHF₃ Plasmas*. *Vacuum* **55** (1999) 191-196.
- [201] Li, X., Abe, T., and Esashi, M., *Deep Reactive Ion Etching of Pyrex Glass Using SF₆ Plasma*. *Sensor. Actuat. A-Phys.* **87** (2001) 139-145.
- [202] Metwalli, E., and Pantano, C. G., *Reactive Ion Etching of Glasses: Composition Dependence*. *Nucl. Instrum. Meth. B* **207** (2003) 21-27.
- [203] Ichiki, T., Sugiyama, Y., Ujiie, T., and Horiike, Y., *Deep Dry Etching of Borosilicate Glass Using Fluorine-Based High-Density Plasmas for Microelectromechanical System Fabrication*. *J. Vac. Sci. Technol. B* **21** (2003) 2188-2192.
- [204] Spierings, G A C M, *Wet Chemical Etching of Silicate Glasses in Hydrofluoric Acid Based Solutions*. *J. Mater. Sci.* **28** (1993) 6261-6273.
- [205] Kang, J. K., and Musgrave, C. B., *The Mechanism of HF/H₂O Chemical Etching of SiO₂*. *J. Chem. Phys.* **116** (2002) 275-280.

- [206] Li, M., Li, W. H., Zhang, J., Alici, G., and Wen, W., *A Review of Microfabrication Techniques and Dielectrophoretic Microdevices for Particle Manipulation and Separation*. J. Phys. D **47** (2014) 063001.
- [207] Thermo Scientific, *Chemical Compatibility Guide*, <http://sevierlab.vet.cornell.edu/resources/Chemical-Resistance-Chart-Detail.pdf> (2012) [Online; accessed 19-june-2018].
- [208] Chen, Q., Milanese, D., Chen, Q., Ferraris, M., and Righini, G. C., *Fabrication and Direct Bonding of Photosensitive Multicomponent Silicate Glasses for Lossless Planar Waveguide Splitters*. J. Non-Cryst. Solids **354** (2008) 1230-1234.
- [209] Turner, T., and Casnedi, P., *Novel Bonding Technology Improves Optical Assemblies*. Euto Photonics **18** (2013) 27-29.
- [210] Chen, Q., Chen, Q., Milanese, D., and Ferraris, M., *Thermal Assisted Direct Bonding Between Structured Glasses for Lab-on-Chip Technology*. Microsyst. Technol. **15** (2009) 1873.
- [211] Renberg, B., Sato, K., Tsukahara, T., Mawatari, K., and Kitamori, T., *Hands on: Thermal Bonding of Nano- and Microfluidic Chips*. Microchim. Acta **166** (2009) 177-181.
- [212] Martinez-Duarte Rodrigo, *Microfabrication Technologies in Dielectrophoresis Applications – A Review*. Electrophoresis **33** (2012) 3110-3132.
- [213] Zhang, B., Dong, Q., Korman, C. E., Li, Z., and Zaghloul, M. E., *Flexible Packaging of Solid-State Integrated Circuit Chips with Elastomeric Microfluidics*. Sci. Rep. **3** (2013) 1098.
- [214] Shafiee, H., Caldwell, J. L., Sano, M. B., and Davalos, R. V., *Contactless Dielectrophoresis: a New Technique for Cell Manipulation*. Biomed. Microdevices **11** (2009) 997-1006.
- [215] Huang, Y., Qiu, H., Wang, F., Pan, L., Tian, Y., and Wu, P., *Effect of Annealing on the Characteristics of Au/Cr Bilayer Films Grown on Glass*. Vacuum **71** (2003) 523-528.
- [216] Kenrick, P. S., *Grain Boundary Diffusion Effects in Films of Gold on Chromium*. Nature **217** (1968) 1249-1251.
- [217] Roth, A., *Vacuum Sealing Techniques* (American Institute of Physics, Woodbury, NY, USA, 1994).
- [218] Fredrickson, C. K., and Fan, Z. H., *Macro-to-Micro Interfaces for Microfluidic Devices*. Lab Chip **4** (2004) 526-533.
- [219] Temiz, Y., Lovchik, R. D., Kaigala, G. V., and Delamarche, E., *Lab-on-a-Chip Devices: How to Close and Plug the Lab?* Microelectron. Eng. **132** (2015) 156-175.

- [220] Yang, Z., and Maeda, R., *Socket with Built-in Valves for the Interconnection of Microfluidic Chips to Macro Constituents*. *J. Chromatogr. A* **1013** (2003) 29-33.
- [221] Zhen, Y., and Ryutaro, M., *A World-to-Chip Socket for Microfluidic Prototype Development*. *Electrophoresis* **23** (2002) 3474-3478.
- [222] Fluigent, *Microfluidic Dead Volume*, <https://www.fluigent.com/expertises/microfluidic-volume-definitions/> (2018) [Online; accessed 21-june-2018].
- [223] Fritzsche, F. S. O., Kortmann, H., Lonczynski, J., Blank, L. M., and Schmid, A., *Pressure-Resistant and Reversible On-Tube-Sealing for Microfluidics*. *Microfluid. Nanofluid.* **10** (2011) 679-684.
- [224] Ji, H., Chen, G., Yang, J., Hu, J., Song, H., and Zhao, Y., *A Simple Approach to Fabricate Stable Superhydrophobic Glass Surfaces*. *Appl. Surf. Sci.* **266** (2013) 105-109.
- [225] Netzer, L., Iscovici, R., and Sagiv, J., *Adsorbed Monolayers Versus Langmuir-Blodgett Monolayers – Why and How? I: From Monolayer to Multilayer by Adsorption*. *Thin Solid Films* **99** (1983) 235-241.
- [226] Detlev, B., and Martin, L., *Surface Modification in Microchip Electrophoresis*. *Electrophoresis* **24** (2003) 3595-3606.
- [227] Dolník Vladislav, *Wall Coating for Capillary Electrophoresis on Microchips*. *Electrophoresis* **25** (2004) 3589-3601.
- [228] Huang, T. T., Mosier, N. S., and Ladisch, M. R., *Surface Engineering of Microchannel Walls for Protein Separation and Directed Microfluidic Flow*. *J. Sep. Science* **29** (2006) 1733-1742.
- [229] Mutin, P. H., Guerrero, G., and Vioux, A., *Hybrid Materials from Organophosphorus Coupling Molecules*. *J. Mater. Chem.* **15** (2005) 3761-3768.
- [230] Lessel, M., Bäumchen, O., Klos, M., Hähl, H., Fetzer, R., Paulus, M., Seemann, R., and Jacobs, K., *Self-Assembled Silane Monolayers: An Efficient Step-by-Step Recipe for High-Quality, Low Energy Surfaces*. *Surf. Interface Anal.* **47** (2015) 557-564.
- [231] Glass, N. R., Tjeung, R., Chan, P., Yeo, L. Y., and Friend, J. R., *Organosilane Deposition for Microfluidic Applications*. *Biomicrofluidics* **5** (2011) 036501.
- [232] Brzoska, J. B., Azouz, I. B., and Rondelez, F., *Silanization of Solid Substrates: A Step Toward Reproducibility*. *Langmuir* **10** (1994) 4367-4373.
- [233] McGovern, M. E., Kallury, K. M. R., and Thompson, M., *Role of Solvent on the Silanization of Glass with Octadecyltrichlorosilane*. *Langmuir* **10** (1994) 3607-3614.

- [234] Silberzan, P., Leger, L., Ausserre, D., and Benattar, J. J., *Silanation of Silica Surfaces. A New Method of Constructing Pure or Mixed Monolayers*. *Langmuir* **7** (1991) 1647-1651.
- [235] Bennès, J., Ballandras, S., and Chérioux, F., *Easy and Versatile Functionalization of Lithium Niobate Wafers by Hydrophobic Trichlorosilanes*. *Appl. Surf. Sci.* **255** (2008) 1796-1800.
- [236] Priest, C., *Surface Patterning of Bonded Microfluidic Channels*. *Biomicrofluidics* **4** (2010) 032206.
- [237] Kawakatsu, T., Kikuchi, Y., and Nakajima, M., *Regular-Sized Cell Creation in Microchannel Emulsification by Visual Microprocessing Method*. *J. Am. Oil Chem. Soc.* **74** (1997) 317-321.
- [238] The Walsworth Group, *Coating Glass Cells with OTS*, <http://walsworth.physics.harvard.edu/publications/ManualOTSGlassCoating.pdf> (2011) [Online; accessed 25-june-2018].
- [239] Guo-hua, X., and Higashitani, K., *Formation of OTS Self-Assembled Monolayer on Glass Surface Investigated by AFM*. *J. Zhejiang. Univ. - Sc. A* **1** (2000) 162-170.
- [240] Zhao, B., Moore, J. S., and Beebe, D. J., *Surface-Directed Liquid Flow Inside Microchannels*. *Science* **291** (2001) 1023-1026.
- [241] Cheng, Y., Zheng, B., Chuang, P., and Hsieh, S., *Solvent Effects on Molecular Packing and Tribological Properties of Octadecyltrichlorosilane Films on Silicon*. *Langmuir* **26** (2010) 8256-8261.
- [242] Duarte, R. d. C., Ongaratto, R., Piovesan, L. A., de Lima, V. R., Soldi, V., Merlo, A. A., and D'Oca, M. G. M., *New N-acylamino Acids and Derivatives from Renewable Fatty Acids: Gelation of Hydrocarbons and Thermal Properties*. *Tetrahedron Lett.* **53** (2012) 2454-2460.
- [243] Marco Rubber & Plastics, *Rubber O-Ring Chemical Compatibility Chart - O-Ring Material Resistance Guide*, <https://www.marcorubber.com/o-ring-chemical-compatibility-chart-1.htm> (2017) [Online; accessed 25-june-2018].
- [244] Ralston, A. W., Hoerr, C. W., and Crews, L. T., *Solubilities of Some Normal Saturated Aliphatic Hydrocarbons*. *J. Org. Chem.* **09** (1944) 319-328.
- [245] Gianluca, E., Michael, K., and Esther, A., *Influence of Fluorinated Surfactant Composition on the Stability of Emulsion Drops*. *Macromol. Chem. Phys.* **218** (2017) 1600365.
- [246] Mazutis, L., Gilbert, J., Lloyd Ung, W., Weitz, D. A., Griffiths, A. D., and Heyman, J. A., *Single-Cell Analysis and Sorting Using Droplet-Based Microfluidics*. *Nat. Protoc.* **8** (2013) 870-891.

- [247] Capdevila, M., Maestro, A., Porras, M., and Gutiérrez, J. M., *Preparation of Span 80/Oil/Water Highly Concentrated Emulsions: Influence of Composition and Formation Variables and Scale-Up*. *J. Colloid Interface Sci.* **345** (2010) 27-33.
- [248] Bashir, S., Solvas, X. C., Bashir, M., Rees, J. M., and Zimmerman, W. B. J., *Dynamic Wetting in Microfluidic Droplet Formation*. *BioChip J.* **8** (2014) 122-128.
- [249] Peltonen, L., Hirvonen, J., and Yliruusi, J., *The Behavior of Sorbitan Surfactants at the Water–Oil Interface: Straight-Chained Hydrocarbons from Pentane to Dodecane as an Oil Phase*. *J. Colloid Interface Sci.* **240** (2001) 272-276.
- [250] Huang, S., Tan, W., Tseng, F., and Takeuchi, S., *A Monolithically Three-Dimensional Flow-Focusing Device for Dormation of Single/Double Emulsions in Closed/Open Microfluidic Systems*. *J. Micromech. Microeng.* **16** (2006) 2336-2344.
- [251] Hashimoto, M., Garstecki, P., Stone, H. A., and Whitesides, G. M., *Interfacial Instabilities in a Microfluidic Hele-Shaw Cell*. *Soft Matter* **4** (2008) 1403-1413.
- [252] Porras, M., Solans, C., González, C., and Gutiérrez, J. M., *Properties of Water-in-Oil (W/O) Nano-Emulsions Prepared by a Low-Energy Emulsification Method*. *Colloid. Surface. A* **324** (2008) 181-188.
- [253] Croda, *Span and Tween*, <http://chemagent.ru/prodavtsy/download/849/968/19> (2010) [Online; accessed 25-june-2018].
- [254] Mańczyński, A., Góral, M., Wiśniewska-Gocłowska, B., Skrzecz, A., and Shaw, D., *Mutual Solubilities of Water and Alkanes*. *Monatsh. Chem.* **134** (2003) 633-653.
- [255] Tsonopoulos, C., *Thermodynamic Analysis of the Mutual Solubilities of Hydrocarbons and Water*. *Fluid Phase Equilib.* **186** (2001) 185-206.
- [256] Agresti, J. J., Antipov, E., Abate, A. R., Ahn, K., Rowat, A. C., Baret, J., Marquez, M., Klibanov, A. M., Griffiths, A. D., and Weitz, D. A., *Ultrahigh-Throughput Screening in Drop-Based Microfluidics for Directed Evolution*. *PNAS* **107** (2010) 4004-4009.
- [257] Glawdel, T., Elbuken, C., and Ren, C. L., *Droplet Formation in Microfluidic T-junction Generators Operating in the Transitional Regime. II. Modeling*. *Phys. Rev. E.* **85** (2012) 016323.
- [258] de Menech, M., Garstecki, P., Jousse, F., and Stone, H. A., *Transition from Squeezing to Dripping in a Microfluidic T-shaped Junction*. *J. Fluid Mech.* **595** (2008) 141-161.
- [259] Link, D. R., Anna, S. L., Weitz, D. A., and Stone, H. A., *Geometrically Mediated Breakup of Drops in Microfluidic Devices*. *Phys. Rev. Lett.* **92** (2004) 054503.

- [260] Ahn, K., Kerbage, C., Hunt, T. P., Westervelt, R. M., Link, D. R., and Weitz, D. A., *Dielectrophoretic Manipulation of Drops for High-Speed Microfluidic Sorting Devices*. *Appl. Phys. Lett.* **88** (2006) 024104.
- [261] Fu, A. Y., Chou, H., Spence, C., Arnold, F. H., and Quake, S. R., *An Integrated Microfabricated Cell Sorter*. *Anal. Chem.* **74** (2002) 2451-2457.
- [262] He, M., Edgar, J. S., Jeffries, G. D. M., Lorenz, R. M., Shelby, J. P., and Chiu, D. T., *Selective Encapsulation of Single Cells and Subcellular Organelles into Picoliter- and Femtoliter-Volume Droplets*. *Anal. Chem.* **77** (2005) 1539-1544.
- [263] Cetin, B., and Li, D., *Dielectrophoresis in Microfluidics Technology*. *Electrophoresis* **32** (2011) 2410-2427.
- [264] Kang, K. H., Kang, Y., Xuan, X., and Li, D., *Continuous Separation of Microparticles by Size with Direct Current-Dielectrophoresis*. *Electrophoresis* **27** (2006) 694-702.
- [265] Bennett, D. J., Khusid, B., James, C. D., Galambos, P. C., Okandan, M., Jacqmin, D., and Acrivos, A., *Combined Field-Induced Dielectrophoresis and Phase Separation for Manipulating Particles in Microfluidics*. *Appl. Phys. Lett.* **83** (2003) 4866-4868.
- [266] The Engineering ToolBox, *Dielectric Constants of Common Liquids*, https://www.engineeringtoolbox.com/liquid-dielectric-constants-d_1263.html (2008) [Online; accessed 3-July-2018].
- [267] Sugiura, S., Kuroiwa, T., Kagota, T., Nakajima, M., Sato, S., Mukataka, S., Walde, P., and Ichikawa, S., *Novel Method for Obtaining Homogeneous Giant Vesicles from a Monodisperse Water-in-Oil Emulsion Prepared with a Microfluidic Device*. *Langmuir* **24** (2008) 4581-4588.
- [268] Ghosh, P., *Interfacial Tension*. Lecture notes, Department of Chemical Engineering, Indian Institute of Technology Guwahati, India (2014).
- [269] van Buuren, A. R., Marrink, S. J., and Berendsen, H. J. C., *A Molecular Dynamics Study of the Decane/Water Interface*. *J. Phys. Chem.* **97** (1993) 9206-9212.
- [270] Wu, T., Hirata, K., Suzuki, H., Xiang, R., Tang, Z., and Yomo, T., *Shrunk to Femtolitre: Tuning High-Throughput Monodisperse Water-in-Oil Droplet Arrays for Ultra-Small Micro-Reactors*. *Appl. Phys. Lett.* **101** (2012) 074108.
- [271] Bibette, J., and Leal-Calderon, F., *Surfactant-Stabilized Emulsions*. *Curr. Opin. Colloid In.* **1** (1996) 746-751.
- [272] Courtois, F., Olguin, L. F., Whyte, G., Theberge, A. B., Huck, W. T. S., Hollfelder, F., and Abell, C., *Controlling the Retention of Small Molecules in Emulsion Microdroplets for Use in Cell-Based Assays*. *Anal. Chem.* **81** (2009) 3008-3016.

- [273] Moerner, W. E., Shechtman, Y., and Wang, Q., *Single-Molecule Spectroscopy and Imaging over the Decades*. Faraday Discuss. **184** (2015) 9-36.
- [274] Srisa-Art, M., deMello, A. J., and Edel, J. B., *High-Throughput DNA Droplet Assays Using Picoliter Reactor Volumes*. Anal. Chem. **79** (2007) 6682-6689.
- [275] Dittrich, P. S., and Manz, A., *Single-Molecule Fluorescence Detection in Microfluidic Channels – The Holy Grail in μ TAS?* Anal. Bioanal. Chem. **382** (2005) 1771-1782.
- [276] Srisa-Art, M., deMello, A. J., and Edel, J. B., *High-Throughput Confinement and Detection of Single DNA Molecules in Aqueous Microdroplets*. Chem. Commun. (2009) 6548-6550.
- [277] Kang, D., Monsur Ali, M., Zhang, K., Pone, E. J., and Zhao, W., *Droplet Microfluidics for Single-Molecule and Single-Cell Analysis in Cancer Research, Diagnosis and Therapy*. TrAC Trend. Anal. Chem **58** (2014) 145-153.
- [278] Huang, W., Wang, Y., and Wang, Z., *Fluorescence Detection of Single DNA Molecules*. J. Fluoresc. **25** (2015) 1267-1277.
- [279] Fu, A. Y., Spence, C., Scherer, A., Arnold, F. H., and Quake, S. R., *A Microfabricated Fluorescence-Activated Cell Sorter*. Nat. Biotechnol. **17** (1999) 1109-1111.
- [280] Najah, M., Griffiths, A. D., and Ryckelynck, M., *Teaching Single-Cell Digital Analysis Using Droplet-Based Microfluidics*. Anal. Chem. **84** (2012) 1202-1209.
- [281] Zhao, Y., Chen, D., Yue, H., French, J. B., Rufo, J., Benkovic, S. J., and Huang, T. J., *Lab-on-a-Chip Technologies for Single-Molecule Studies*. Lab Chip **13** (2013) 2183-2198.
- [282] Barnes, M. D., Ng, K. C., Whitten, W. B., and Ramsey, J. M., *Detection of Single Rhodamine 6G Molecules in Levitated Microdroplets*. Anal. Chem. **65** (1993) 2360-2365.
- [283] Lan, F., Haliburton, J. R., Yuan, A., and Abate, A. R., *Droplet Barcoding for Massively Parallel Single-Molecule Deep Sequencing*. Nat. Commun. **7** (2016) 11784.
- [284] Andor, *iDus Spectroscopy Cameras*, <http://www.andor.com/scientific-cameras/idus-spectroscopy-cameras#prettyPhoto> (2017) [Online; accessed 5-July-2018].
- [285] Väärämäki, M. J., *Yksiseinämaisten hiilinanoputkien elektroninen spektroskopia ja sen hyödyntäminen mikrofluidistisissa laitteistoissa*. M.Sc. thesis, Department of Chemistry, University of Jyväskylä, Finland (2014).

- [286] Piruska, A., Nikcevic, I., Lee, S. H., Ahn, C., Heineman, W. R., Limbach, P. A., and Seliskar, C. J., *The Autofluorescence of Plastic Materials and Chips Measured under Laser Irradiation*. *Lab Chip* **5** (2005) 1348-1354.
- [287] Clark, R. N., Swayze, G. A., Leifer, I., Livo, K. E., Kokaly, R., Hoefen, T., Lundeen, S., Eastwood, M., Green, R. O., Pearson, N., Sarture, C., McCubbin, I., Roberts, D., Bradley, E., Steele, D., Ryan, T., Dominguez, R., and the Airborne Visible/Infrared Imaging Spectrometer (AVIRIS) Team, *A Method for Quantitative Mapping of Thick Oil Spills Using Imaging Spectroscopy* (U.S. Geological Survey, Reston, VA, USA, 2010).
- [288] KSV, *Sigma 703*. Instruction Manual, KSV Instruments Ltd., Finland (1995).
- [289] The Engineering ToolBox, *Surface Tension of Water in Contact with Air*, https://www.engineeringtoolbox.com/water-surface-tension-d_597.html (2004) [Online; accessed 11-July-2018].
- [290] Basu Ray, G., Chakraborty, I., Ghosh, S., and Moulik, S. P., *A Critical and Comprehensive Assessment of Interfacial and Bulk Properties of Aqueous Binary Mixtures of Anionic Surfactants, Sodium Dodecylsulfate, and Sodium Dodecylbenzenesulfonate*. *Colloid Polym. Sci.* **285** (2007) 457-469.

APPENDIXES

Appendix A

Preparation of CNT dispersion

deionized water (dH₂O): 10 mL

sodium dodecyl benzenesulfonate (SDBS): 100 mg (1 % w/w)

1. Place the reagents into a ~15 mL glass vial.
2. Sonicate in bath-type sonicator until all the SDBS dissolves.
3. From now on, the temperature of the solution/dispersion should not exceed room temperature as the process can fail.

single-walled carbon nanotubes (HiPco™): 5 mg (0.05 % w/w)

4. Add HiPco™ to the SDBS solution.
5. Sonicate in finger-type sonicator, the vial submerged in icy water bath.
6. Set continuous regime with low delivered power and calculate time for the proportional delivered energy of 28 kJ·mL⁻¹

for dr. Hielscher UP200S ultrasonic processor with 3 mm Ti tip

- cycle: 1
- amplitude: 20 % (delivered power ~6.5 W)
- time: 12 h (for 10 mL volume)

7. Transfer the dispersion to the centrifuge tubes and run the pre-centrifugation at 20 °C in centrifugal field 13 200g for 1 hour.

for Beckman-Coulter Optima L-90K Ultracentrifuge with 70.1 Ti Rotor

- 12 000 RPM

8. Carefully collect the supernatant and dispose the precipitate according to waste management rules.
9. Transfer the supernatant to the centrifuge tubes and run the centrifugation at 20 °C in centrifugal field 82 700g for 4 hours.

for Beckman-Coulter Optima L-90K Ultracentrifuge with 70.1 Ti Rotor
 - 30 000 RPM

10. Carefully collect ~80 % of the supernatant and dispose the precipitate according to waste management rules.
11. Filter the final CNT dispersion through $\leq 1.2 \mu\text{m}$ pore size membrane filter.
12. Characterize the CNT dispersion. To compare the results with results reported in the thesis use settings from FIGURE A 1 – FIGURE A 3.

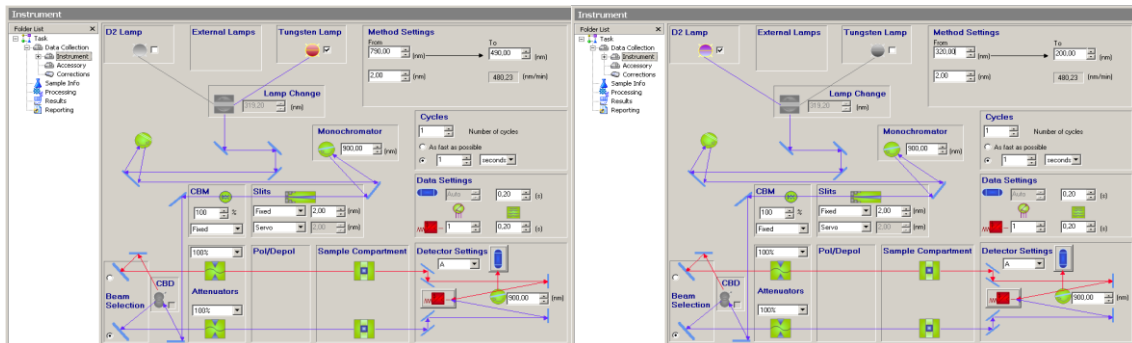


FIGURE A 1: Settings for characterization of CNT dispersion VIS absorption (left) and π -plasmon absorption (right) measured with Perkin Elmer Lambda 850 spectrometer.

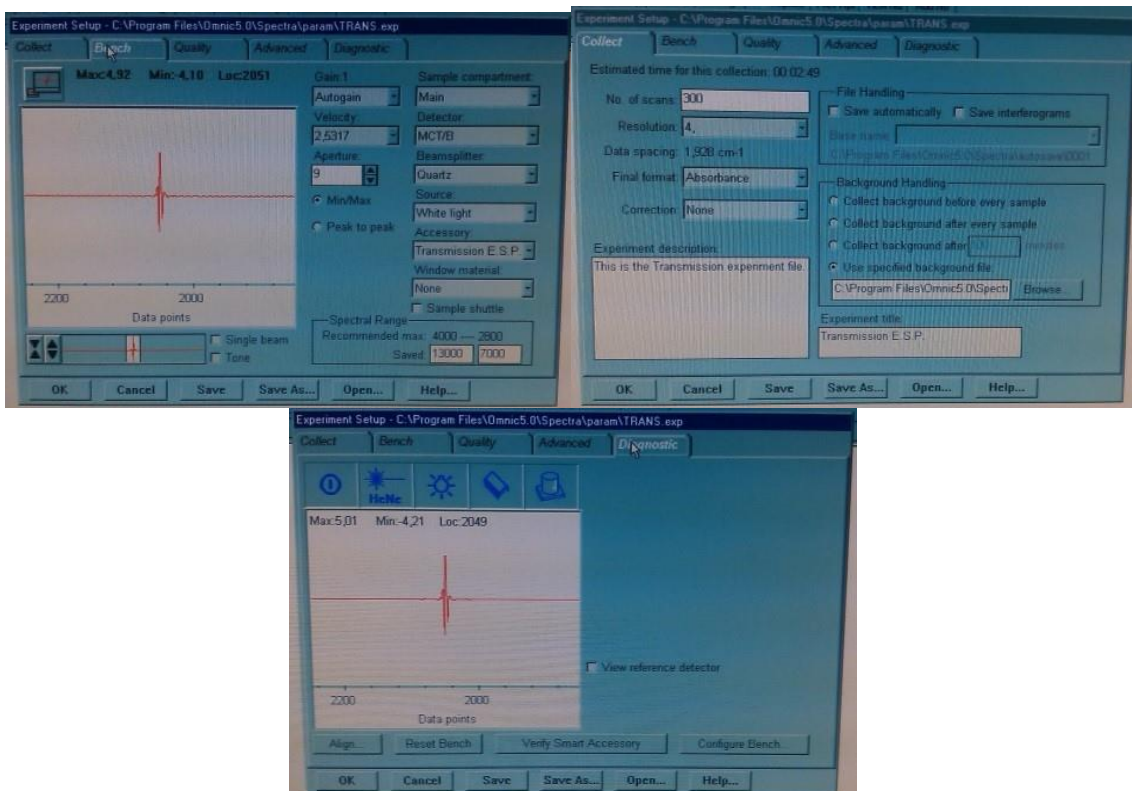


FIGURE A 2: Settings for characterization of CNT dispersion NIR absorption measured with FTIR Nicolet Magna-IR 760 ESP Spectrometer.

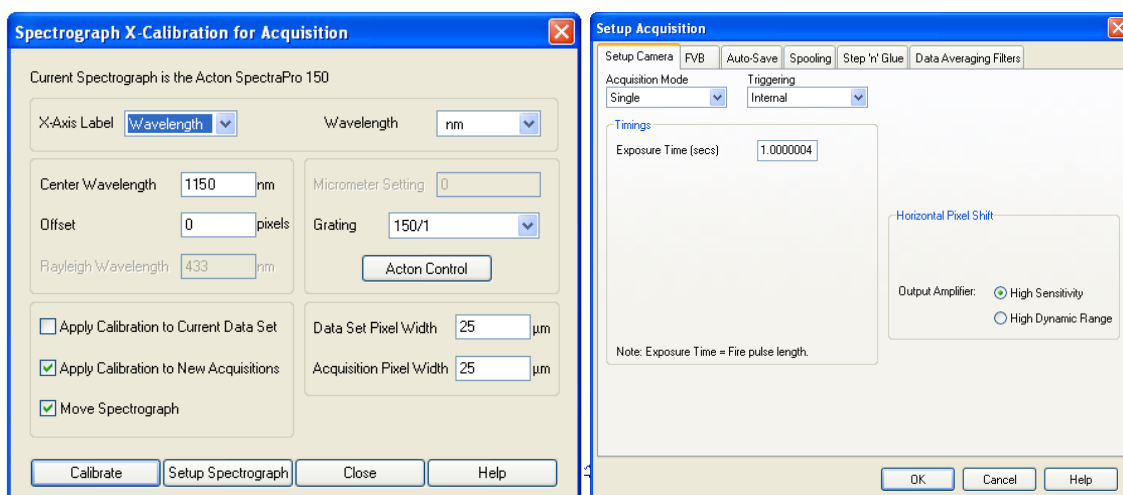


FIGURE A 3: Settings for characterization of CNT dispersion NIR fluorescence measured with home-build fluorescence setup.

13. Store in fridge. An additional filtration through 1.2 or 0.45 μm membrane filter is recommended prior to use.

Reducing SDBS content in CNT dispersion (optional)

14. Dilute freshly prepared CNT dispersion with dH₂O to the required SDBS concentration (the original concentration is 1 % w/w).

15. Shake thoroughly to homogenize the mixture.

16. Transfer the supernatant to the centrifuge tubes and run the centrifugation at 20 °C in centrifugal field 450 000g for 4 hours.

for Beckman-Coulter Optima L-90K Ultracentrifuge with 70.1 Ti Rotor

- 70 000 RPM

17. Carefully collect the precipitate (*sic!*). Attempt to collect as little volume as possible (200 – 300 μm). Dispose the supernatant according to waste management rules.

18. Place the collected precipitate in a glass vial and homogenize in bath-type sonicator for 30 min.

19. Filter the final CNT dispersion through ≤ 1.2 μm pore size membrane filter

20. Characterize the CNT dispersion. To compare the results with results reported in the thesis use settings from FIGURE A 1 – FIGURE A 3.

21. Store at 4 °C. An additional filtration through 1.2 or 0.45 μm membrane filter is recommended prior to use.

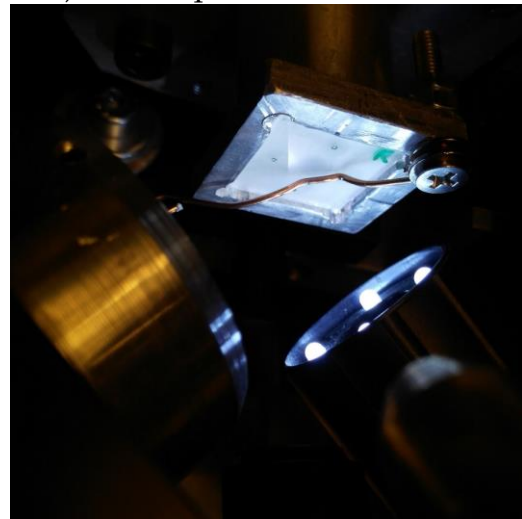
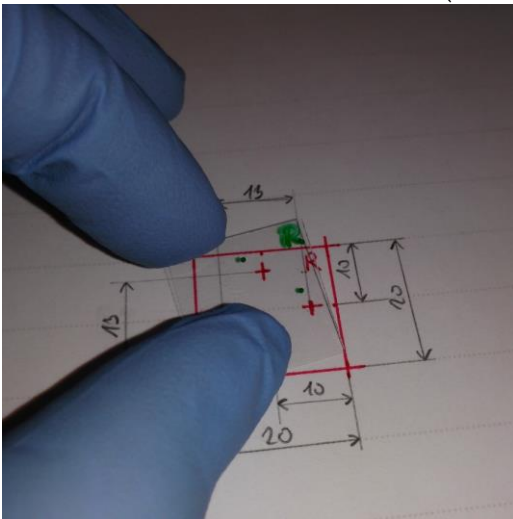
Appendix B

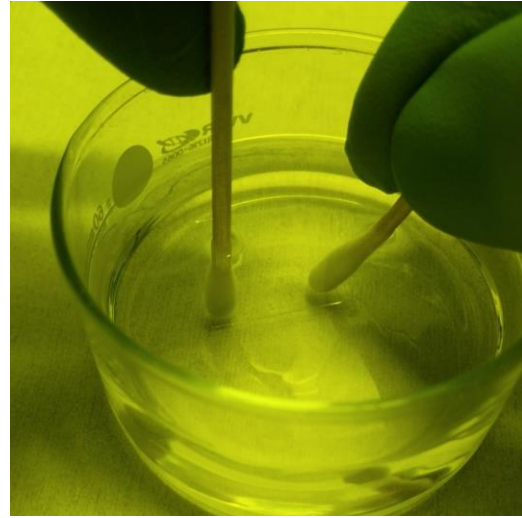
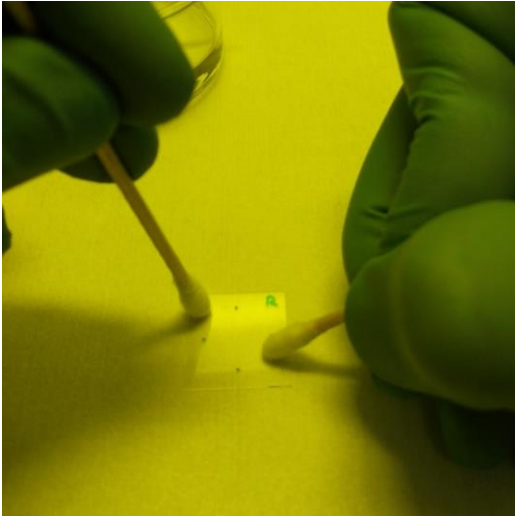
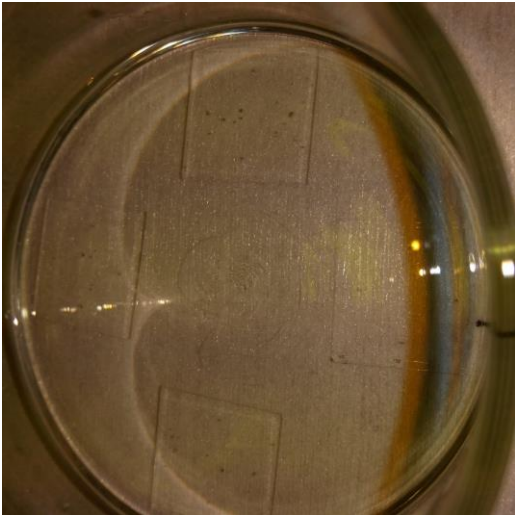
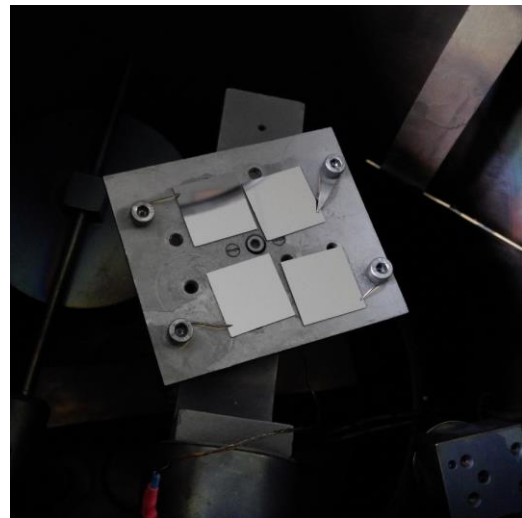
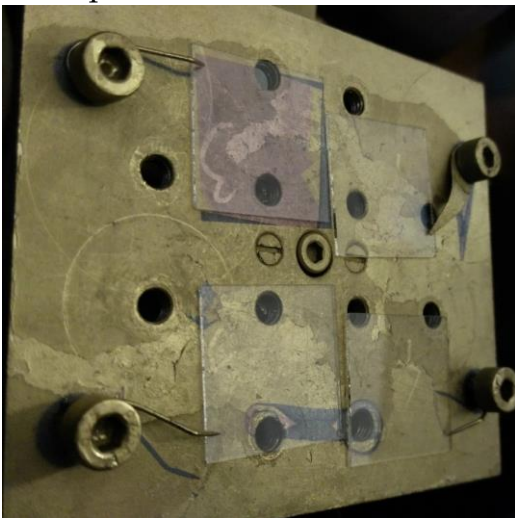
Microfluidic chip manufacture protocol

This protocol describes the manufacture of the most complex microfluidic device developed in this work. For simpler devices, one or several steps may be omitted.

LaserLab:

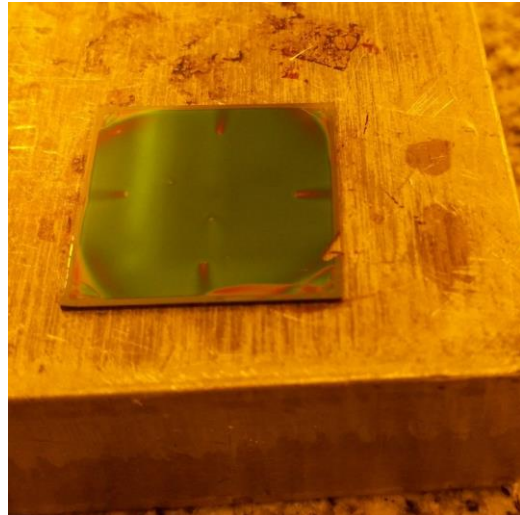
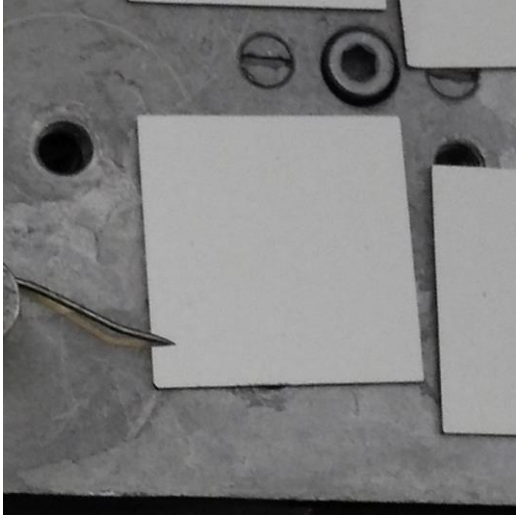
1. Drill holes to Menzel-Gläser (20 x 20 mm², #5) coverslips.¹



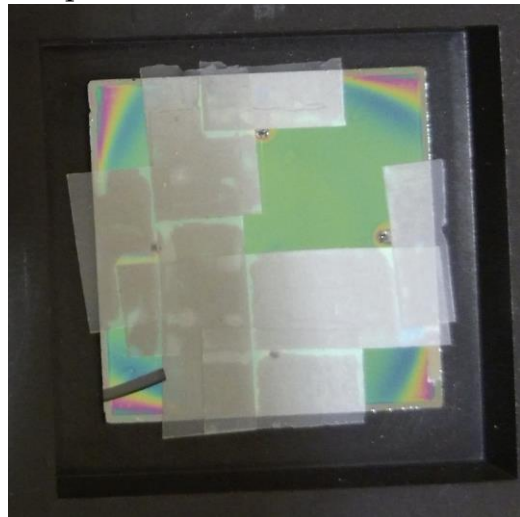
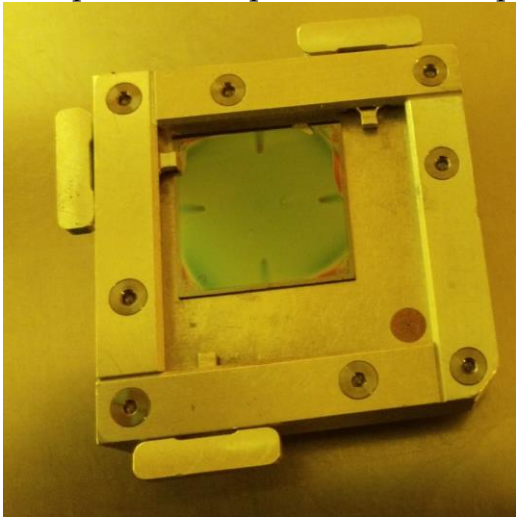
CleanRoom:**2. Clean drilled glasses.²****3. Activate glass surface.³ 🕒*****4. Evaporate 80 nm Cr.⁴**

* The 🕒 symbol means that the planning of the particular step is time-critical.

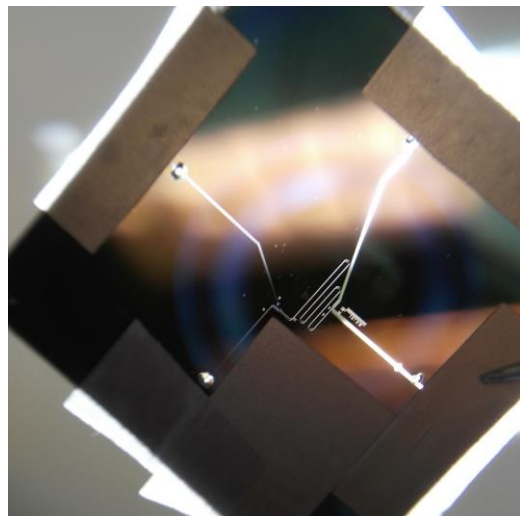
5. Spin coat PMMA A4 950 eBeam resist.⁵



6. Expose, develop, hardbake, and protect – deep channels.⁶



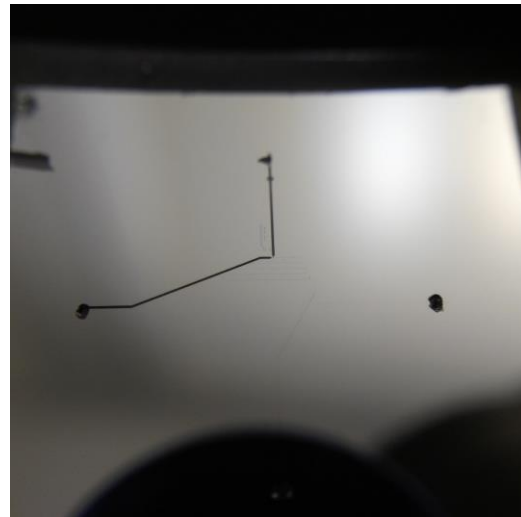
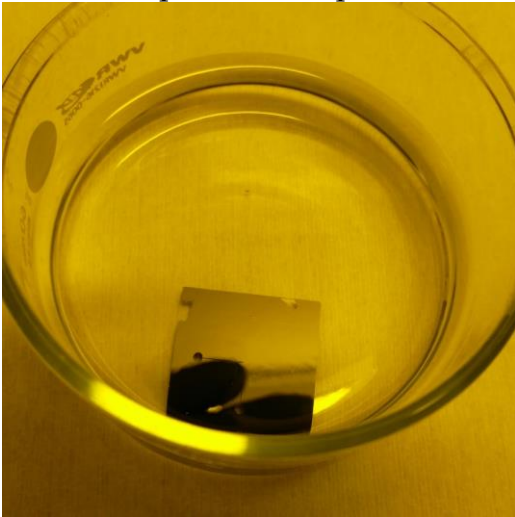
7. Etch Cr through PMMA mask.⁷



8. Etch glass through Cr mask.⁸



9. Remove protective tape and PMMA.⁹



10. Spin coat PMMA A4 950 eBeam resist.¹⁰ ☹️ (see p. 5 above)

11. Expose, develop, and protect – shallow channels.¹¹ (see p. 6 above)

12. Etch Cr through PMMA mask.¹² (see p. 7 above)

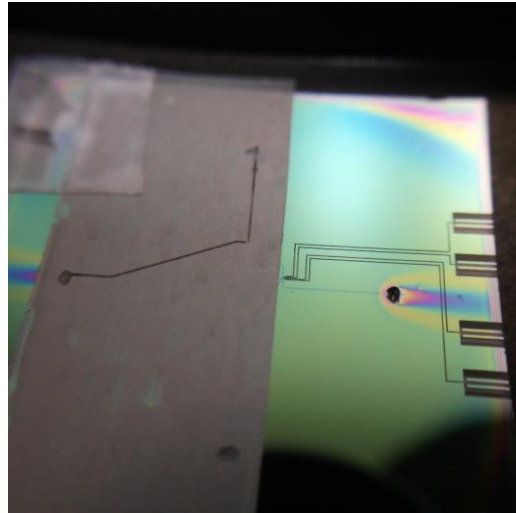
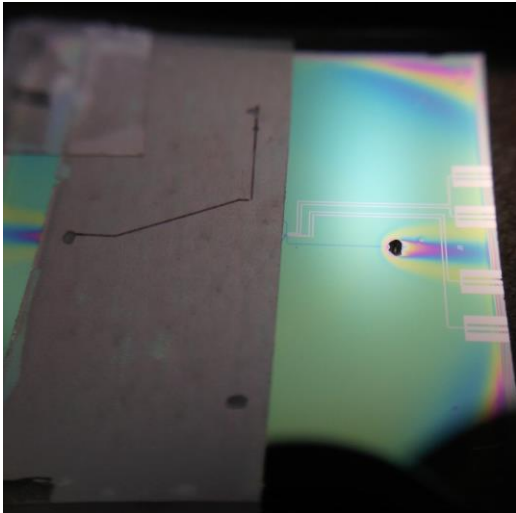
13. Etch glass through Cr mask.¹³ (see p. 8 above)

14. Remove protective tape and PMMA.¹⁴ (see p. 9 above)

15. Spin coat PMMA A4 950 eBeam resist.¹⁵ ☹️ (see p. 5 above)

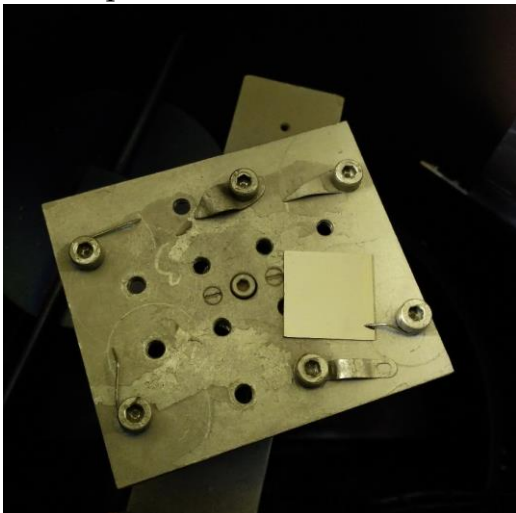
16. Expose, develop, hardbake, and protect – electrodes.¹⁶ (see p. 6 above)

17. Etch Cr through PMMA mask.¹⁷ ([see p. 7 above](#))

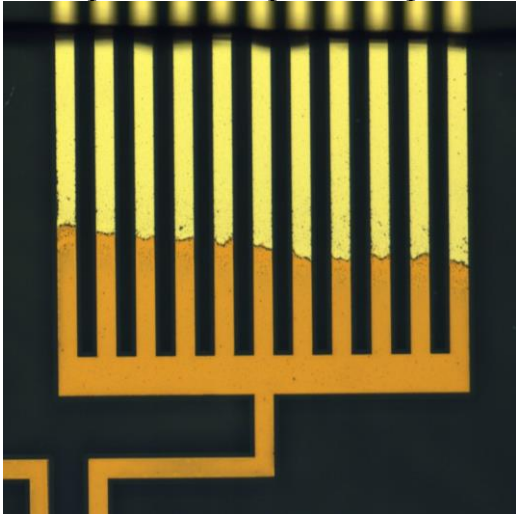


18. Etch glass through Cr mask.¹⁸ ([see p. 8 above](#))

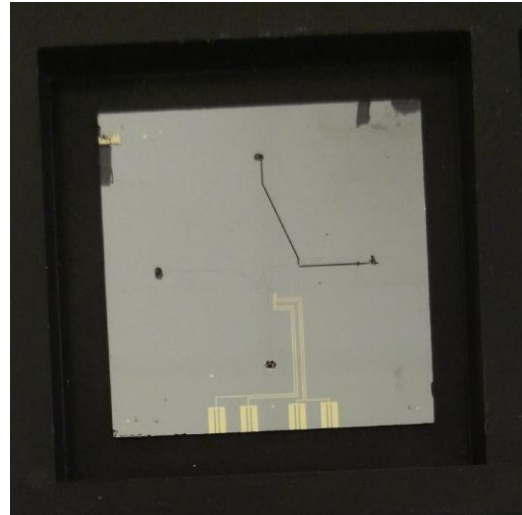
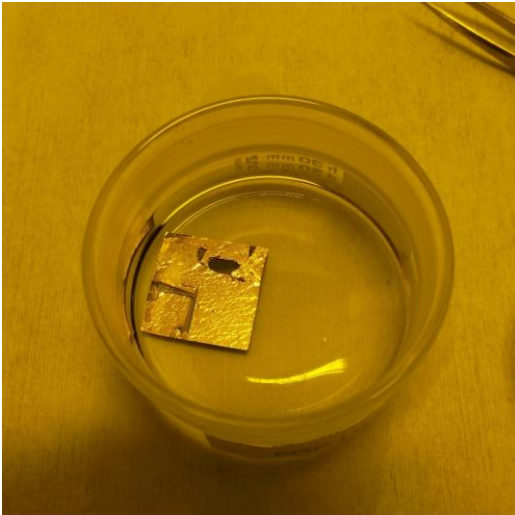
19. Evaporate 50 nm SiO₂ + 4 nm Ti + 50 nm Au.¹⁹



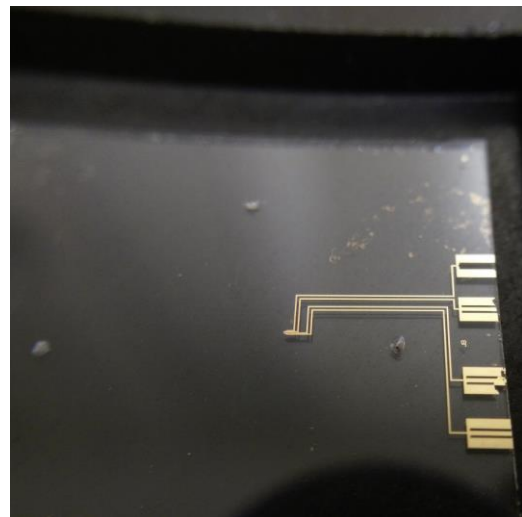
20. Tape electrode pads. Evaporate 4 nm Ti + 50 nm SiO₂.²⁰



21. Remove tape and lift-off.²¹



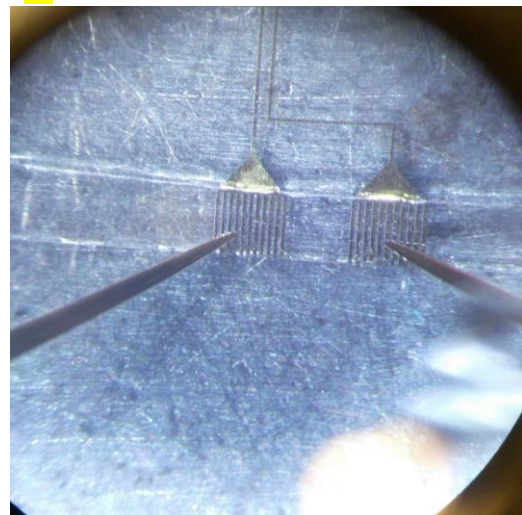
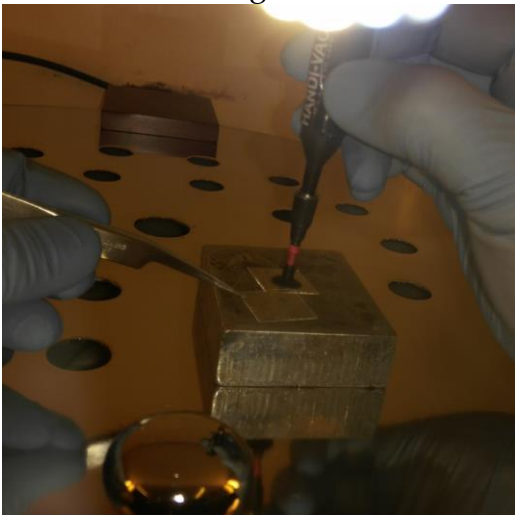
22. Remove Cr mask.²²

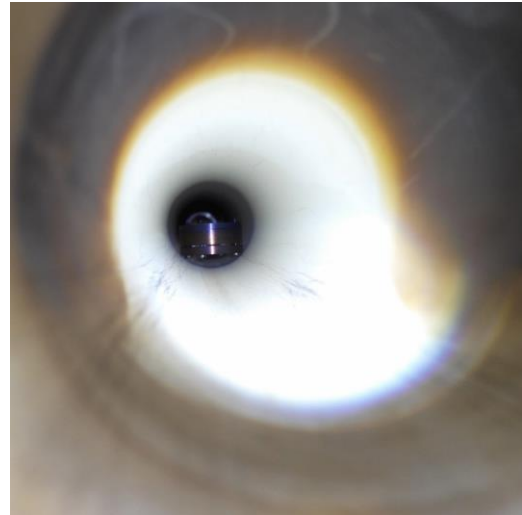


23. Clean cover glass.²³ ([see p. 2 above](#))

24. Activate glass surface.²⁴ 😊 ([see p. 3 above](#))

25. Assemble the glasses. Check electrodes.²⁵ 😊



26. TADB.²⁶ 📷

Microfluidic chip silinization protocol (optional)

This protocol describes the hydrophobic surface treatment suitable for W/O droplet-based microfluidic experiments with hydrocarbon oil continuous phase.

CleanRoom:

27. Terminate the TADB process. Check electrodes.²⁷ 📷 ([see p. 25 above](#))

MicrofluidicLab:

28. Assemble the new chip to the microfluidic holder.²⁸
29. Shortly fill the chip with dH₂O. Dry with N₂ flow.²⁹
30. Prepare fresh OTS solution.³⁰
31. Run OTS solution through the channels.³¹
32. Push the OTS solution out of the channels.³²
33. Run IPA through the channels.³³
34. Remove the chip from microfluidic holder and immerse it in IPA.³⁴
35. Thoroughly clean both the holder and the chip with IPA.³⁵
36. Blow the holder and wipe the chip dry.³⁶
37. Assemble the chip back to microfluidic holder.³⁷
38. Clean the channels with repeated IPA and N₂ flushes.³⁸
39. Anneal the hydrophobic layer.³⁹
40. CHIP IS READY!⁴⁰

¹ Mark the position of the holes according to the MF holder. Protect glass surface from laser induced debris with plastic duct tape. 2000 – 2200 excimer laser pulses should be sufficient. Remove duct tape.

² Process 4 drilled pieces together to save time. Put the glass on the CR sheet and clean both sides with cotton tips and acetone. Focus on the holes surrounding. Do not be afraid to use pressure. Repeat in cup with boiling acetone using only cotton tips. Rinse with acetone. Sonicate in fresh boiling acetone for 3 min. Rinse with acetone. Rinse with IPA. Blow dry with N₂.

³ **Perform activation right before metal evaporation.** Treat in Piranha (H₂O₂:H₂SO₄ – 1:3) at 80 °C for at least 1 hour. Occasionally help the bubbles from the glass surface away. Rinse with dH₂O. Be sure that the Piranha is properly washed away also from the holes. Sonicate for 5 min in dH₂O. Rinse with dH₂O. Blow dry with N₂ (including the holes). Put the glasses on 160 °C hot plate for 3 min to remove adsorbed water.

⁴ The Cr mask needs to come from the side, where drilling laser came out. Place all 4 glasses on the rotational stage. Pay special attention to the cleanliness of the Cr crucible. Clean new pieces of Cr by sonicating them in boiling acetone (5 min) + rinsing with IPA. Be careful about any possible contamination. Align stage axis with the crucible axis as the stage arm is wobbly. During the evaporation set evaporation angle 0°, slow rotation, and evaporation speed 0.8 - 1.0 Å·s⁻¹. Check the Cr mask quality with microscope in DF mode. Do not use samples with poor Cr mask quality.

⁵ **Perform spin coating right before eBeam lithography.** Blow possible dust away with N₂. Put the sample on 160 °C hot plate for 3 min to remove possible water (pre-bake). Cool the sample down on the cleanest Al block. Blow again with N₂. Place the sample on the spin coater stage. Set spin coating program with 500 RPM for PMMA spreading (10 s) and 3000 RPM for spin coating (60 s). Pipette the PMMA during the spreading phase. After the full sequence is ready, put the sample on 160 °C hot plate for 2 min to remove the solvent (post-bake). Cool the sample down on the cleanest Al block. Check the PMMA quality with microscope in DF mode. If the PMMA quality is poor, remove PMMA by sonicating the sample in boiling acetone (1 min) + rinsing with acetone and IPA and repeat the spin coating process. PMMA tends to degrade with time, adsorb water and create bubbles in the spin coated layer during post-bake. If bubbles appear in the PMMA layer many times in a row, it is time to mix new PMMA.

⁶ Expose the pattern from GDSII database. Carefully consider the underetching while designing your patterns (1 µm of the depths widens the channels by 1 µm to both sides). Scratch the PMMA underneath the clamp properly to avoid charging (and drifting) of the sample. Follow sample position from the figure. Find a circular particle with ø50 nm for Write Field alignment. Manipulate the sample only by the place where PMMA was scratched from now on. Develop in 'Developer 1' for 40 s and stop by IPA. Blow dry with N₂. Check if everything is exposed and developed as desired with microscope. For etching of deep (≥3 µm) or large (≥2 µm) structures, hardbake the PMMA on a hot plate at 200 °C for 2 hours. Protect the areas of the sample without exposed structures as good as possible with plastic duct tape. Do not cover the alignment marks in the corners.

⁷ Mix Nichrome etchant and dH₂O – 1:3. Always prepare fresh mixture as the etch rate and quality decreases with used solution. Put sample in the cup and stir gently. The Cr should be completely removed on exposed places in 45 – 90 s. Rinse properly with dH₂O. Blow dry with N₂. Check with microscope. Tape the alignment marks in the corners.

⁸ Mix (HF:HCl – 12:1) solution and dH₂O – 1:5 in HDPE beaker. Put sample in and stir vigorously. It takes 94 s to etch 1 µm away (always use fresh mixture, as the etch rate and quality decreases with time). Rinse properly with dH₂O. Sonicate in dH₂O for 3 min to remove etching products. Rinse properly with dH₂O. Blow dry with N₂. Check with microscope. Tested up to 6 µm depth.

⁹ Peel the protective tape away. Sonicate the sample in boiling acetone for 1 min. Rinse with acetone. Sonicate the sample in fresh boiling acetone for 1 min again. Rinse with acetone, rinse with IPA. Blow dry with N₂.

¹⁰ **Perform spin coating right before eBeam lithography.** Blow possible dust away with N₂. Put the sample on 160 °C hot plate for 3 min to remove possible water (pre-bake). Cool the sample down on the cleanest Al block. Blow again with N₂. Place the sample on the spin coater stage. Set

spin coating program with 500 RPM for PMMA spreading (10 s) and 1000 RPM for spin coating (120 s). Pipette the PMMA during the spreading phase. After the full sequence is ready, put the sample on 160 °C hot plate for 2 min to remove the solvent (post-bake). Cool the sample down on the cleanest Al block. Check the PMMA quality with microscope in DF mode.

¹¹ Expose the pattern from GDSII database. Carefully consider the underetching while designing your patterns (1 μm of the depths widens the channels by 1 μm to both sides). Scratch the PMMA underneath the clamp properly to avoid charging (and drifting) of the sample. Follow sample position from the figure. Find a circular particle with ø50 nm for Write Field alignment. Develop in 'Developer 1' for 40 s and stop by IPA. Blow dry with N₂. Check if everything is exposed and developed as desired with microscope. For etching of fine structures (<2 μm), hardbake is not recommended. Protect the areas of the sample without exposed structures as good as possible with plastic duct tape.

¹² Mix Nichrome etchant and dH₂O – 1:3. Always prepare fresh mixture as the etch rate and quality decreases with used solution. Put sample in the cup and stir gently. The Cr should be completely removed on exposed places in 45 – 90 s. Rinse properly with dH₂O. Blow dry with N₂. Check with microscope.

¹³ Mix (HF:HCl – 12:1) solution and dH₂O – 1:5 in HDPE beaker. Put sample in and stir vigorously. It takes 94 s to etch 1 μm away (always use fresh mixture, as the etch rate and quality decreases with time). Rinse properly with dH₂O. Sonicate in dH₂O for 3 min to remove etching products. Rinse properly with dH₂O. Blow dry with N₂. Check with microscope.

¹⁴ Peel the protective tape away. Sonicate the sample in boiling acetone for 1 min. Rinse with acetone. Sonicate the sample in fresh boiling acetone for 1 min again. Rinse with acetone, rinse with IPA. Blow dry with N₂.

¹⁵ Perform spin coating right before eBeam lithography. Blow possible dust away with N₂. Put the sample on 160 °C hot plate for 3 min to remove possible water (pre-bake). Cool the sample down on the cleanest Al block. Blow again with N₂. Place the sample on the spin coater stage. Set spin coating program with 500 RPM for PMMA spreading (10 s) and 1000 RPM for spin coating (120 s). Pipette the PMMA during the spreading phase. After the full sequence is ready, put the sample on 160 °C hot plate for 2 min to remove the solvent (post-bake). Cool the sample down on the cleanest Al block. Check the PMMA quality with microscope in DF mode.

¹⁶ Expose the pattern from GDSII database. Carefully consider the underetching while designing your patterns (1 μm of the depths widens the channels by 1 μm to both sides). Scratch the PMMA underneath the clamp properly to avoid charging (and drifting) of the sample. Follow sample position from the figure. Find a circular particle with ø50 nm for Write Field alignment. Develop in 'Developer 1' for 40 s and stop by IPA. Blow dry with N₂. Check if everything is exposed and developed as desired with microscope. For etching of deep (≥3 μm) or large (≥2 μm) structures, hardbake the PMMA on a hot plate at 200 °C for 2 hours. Protect the areas of the sample without exposed structures as good as possible with plastic duct tape

¹⁷ Mix Nichrome etchant and dH₂O – 1:3. Always prepare fresh mixture as the etch rate and quality decreases with used solution. Put sample in the cup and stir gently. The Cr should be completely removed on exposed places in 45 – 90 s. Rinse properly with dH₂O. Blow dry with N₂. Check with microscope.

¹⁸ Mix (HF:HCl – 12:1) solution and dH₂O – 1:5 in HDPE beaker. Put sample in and stir vigorously. It takes 94 s to etch 1 μm away (always use fresh mixture, as the etch rate and quality decreases with time). Rinse properly with dH₂O. Sonicate in dH₂O for 3 min to remove etching products. Rinse properly with dH₂O. Blow dry with N₂. Check with microscope.

¹⁹ Place the sample on the rotational stage. Use crucible marked 'Au for Microfluidics' and 'SiO₂ for Microfluidics', not the common ones. Clean new pieces of Au/SiO₂ by sonicating them in boiling acetone (5 min) + rinsing with IPA. Be careful about any possible contamination. Align stage axis with the crucible axis as the stage arm is wobbly. During the evaporation set evaporation angle 0°, slow rotation, and evaporation speed 0.8 - 1.0 Å·s⁻¹.

²⁰ Vent the chamber. Cover the very ends of the electrode pads with plastic duct tape. Align stage axis with the crucible axis as the stage arm is wobbly. During the evaporation set evaporation angle 0°, slow rotation, and evaporation speed 0.8 - 1.0 Å·s⁻¹.

²¹ Peel the protective tape away. Sonicate the sample in boiling acetone for 1 min. Rinse with acetone. Sonicate the sample in fresh boiling acetone for 1 min again. Repeat until there is no electrode material in undesired areas. Rinse with acetone, rinse with IPA. Blow dry with N₂.

²² Mix Nichrome etchant and dH₂O – 1:3. Always prepare fresh mixture as the etch rate and quality decreases with used solution. Put sample in the cup and stir gently. The Cr should be completely removed in 3 – 5 min. Be sure, there is no Cr left behind. The process can be accelerated by changing the etchant for a fresh one or by elevating the temperature to 60 °C. Rinse properly with dH₂O. Blow dry with N₂. Check with microscope. It is crucial to remember the patterned side of the sample from this moment on as it is very difficult to see after Cr removal.

²³ Put the cover glass on the CR sheet and clean both sides with cotton tips and acetone. Do not be afraid to use pressure. Repeat in cup with boiling acetone using only cotton tips. Rinse with acetone. Sonicate in fresh boiling acetone for 3 min. Rinse with acetone. Rinse with IPA. Blow dry with N₂.

²⁴ **Glass surface activation, assembling, TADB and silinization have to be performed in uninterrupted sequence.** (Ideal way is to start about 2PM, make thermal bonding overnight and silinize in the next morning.) Treat the cover glass in Piranha (H₂O₂:H₂SO₄ – 1:3) at 80 °C for at least 1 hour. Occasionally help the bubbles from the glass surface away. Rinse with dH₂O. Threat the channel glass in room temperature Piranha for no more than 10 min. Rinse with dH₂O. Sonicate the glasses upright for 3 min in fresh dH₂O. Rinse with fresh dH₂O. Sonicate the glasses upside down for 3 min in fresh dH₂O. Rinse with fresh dH₂O. Sonicate the glasses upright for 3 min in fresh dH₂O. Rinse with fresh dH₂O. Put bot the glasses to a glass cup filled with fresh dH₂O. (You can also put tips of the tweezers to Piranha to clean them and sonicate them with the glasses to prepare them for very delicate assembling.)

²⁵ This step is very sensitive to any kind of possible contamination. Use face mask and work in laminar flow box with front glass in lower position. Remember to keep both pieces of glass with side to-be-bonded pointing up. Rinse the glasses with dH₂O and blow dry with N₂. Place glasses to hot plate at 160 °C for 2 min. Put glasses on the cleanest Al block to cool them down. Properly blow the glasses with N₂. Use Handi-Vac pen to hold cover glass from the outer side (the side not to be assembled). Hold channel glass down on the aluminium block very close to the glass edge using tweezers or utilize the vacuum stage. Carefully place the cover glass to the center of the channel glass and press firmly. Remove Handi-Vac pen and press both glasses together with your thumb against the Al block to remove all visible Newton rings. Use all power you have, it is safe. Properly connected glasses become clear as a single piece of glass. Place assembled chip to hot plate at 160 °C for 2 min. If it is impossible to remove Newton rings, split the glasses by scalpel blade, sonicate as previously and try again. (If you fail at first, don't give up, some practice is required until you get the hang of things.) Check the conductivity of the electrode loops.

²⁶ Blow possible dirt particles from stainless TADB holder away using N₂ gun. Place assembled chip to the holder with inlet holes down. Load the chip with stainless weights and put it to the furnace. Set slow N₂ flow in the furnace. Set temperature ramp 5 °C·min⁻¹ from room temperature (20 °C) up to 585 °C, keep 2 hours at 585 °C and let cool down naturally (~3 °C·min⁻¹). Run the stirring process of the [\[3\(CHCl₃\)+2\(CCl₄\)\]_{H₂O}](#) (see endnote 30) solution overnight.

²⁷ Wait until the temperature drops below 100 °C. Take the microfluidic chip out of the furnace and remove it from the holder. Check the conductivity of the electrode loops.

²⁸ Take the chip out of CleanRoom. Touch the chip only with gloves before it is assembled into the microfluidic holder. Be sure that all the O-rings in the holder are Viton® as the NBR O-rings will cause the destruction of the channels. Assemble the chip to the holder and check the proper position and contact area with the O-rings.

²⁹ Introduce dH₂O to the chip and wait until all the channels are filled. Push the dH₂O away and dry the chip with flow of N₂. The presence of water adsorbed on the channel surface is crucial for the silinization process, however, any visible presence of water in the channels will reliably lead to irreversible clogging of the chip during the silinization. It is worth to spend extra 10 min on drying here than destroy the chip and spend several days on making a new one.

³⁰ Mix fresh OTS solution. Mix 1 000 µL of hexadecane, 150 µL of CCl₄, 50 µL of water saturated solution of [\[3\(CHCl₃\)+2\(CCl₄\)\]_{H₂O}, and 10 µL of OTS solution straight to the Fluiwell vial. Close the cap to prevent contact with air humidity and mix well.](#)

-
- ³¹ Insert oil inlet tube to the OTS solution and water inlet tube to another vial with IPA. Use the Peltier cooler to cool the whole holder to 16 – 17 °C. Introduce the OTS solution to the chip. If the whole chip is to be silinized, let the OTs solution to enter all the channels, keep only small gas bubble at the water inlet hole by adjusting the pressure in the IPA vial. If the water inlet channel cannot be silinized, do not let the OTS solution to enter that channel and set the pressures so, that gas bubbles are pushed into the flow of the OTS solution elsewhere. The volume of gas in the tube connected to IPA vial is sufficient for the whole silinization process. Maintain the OTS flow at 2 000 mbar for 1 hour.
- ³² Turn the pressure in OTS vial off and set the pressure in IPA vial to 2 000 mbar. Let the gas to push as much of the OTS solution out of the channel as possible (~5 min).
- ³³ By opening the vent on the holder, bypass the gas and let IPA to enter the channels. The cooling can be turned off now. Rinse the channels with IPA for ~10 min.
- ³⁴ Stop the pressure. Disassemble the chip from the holder and immerse it immediately to already prepared cup with IPA. Try to avoid drying of IPA carrying OTS solution leftovers on the chip surface.
- ³⁵ Thoroughly flush the holder with IPA using syringe. Use cotton sticks to carefully rub the surface of the chip. Focus on the surrounding of the inlet holes as they often possess OTS solution leftovers. Be careful not to push those leftovers to the inlet/outlet holes. A jet stream of IPA from syringe with needle can be used to clean the inlet/outlet holes.
- ³⁶ Blow the holder dry with N₂. Wipe the chip dry using a sheet/cloth which does not leave fibers behind. An eyeglass cleaning cloths, cleanroom sheets, lens or screen wipes serves well.
- ³⁷ Touch the chip only with gloves before it is assembled into the microfluidic holder. Assemble the chip to the holder and check the proper position and contact area with the O-rings.
- ³⁸ Run IPA through the channels for ~5 min. Push IPA away and dry the channels with N₂. Repeat the sequence until the channels are absolutely clean and dry.
- ³⁹ Remove the chip from the holder and put it on a hot plate. Anneal the OTS SAM at 200 °C for 2 hours.
- ⁴⁰ The chip is ready for microfluidic experiments. For common fluids (water, n-decane) NBR O-rings are sufficient. For different fluids/solvents, the compatibility of the O-rings must be considered. The OTS layer is stable for months when stored in ambient air conditions.

Appendix C

Supplementary movies

Online movie folder: <https://jyx.jyu.fi/handle/123456789/51290>

Supplementary movie M1

Title: M1_Microfluidics_for_CNT

Link: <https://jyx.jyu.fi/handle/123456789/58966>

Description: High-frequency droplet production in step-emulsification microfluidic device. The abrupt change in channel cross section causes creation of the droplets. The closely-packed droplets automatically order in hexagonal pattern.

Created: 3.2.2017

Chip: no. 26, silinized

Continuous phase: n-decane (3 % w/w SPAN 80) 3 000 mbar

Disperse phase: dH₂O 3 000 mbar

Field of view: 425x320 μm²

Playback speed: 1x

Supplementary movie M2

Title: M2_Microfluidics_for_CNT

Link: <https://jyx.jyu.fi/handle/123456789/58967>

Description: Droplet production in flow-focusing microfluidic device. The droplets are cut off from the water phase flow by pressure of oil from the side channels. The movement of the droplets proves laminar flow in the device.

Created: 25.4.2016

Chip: no. 18, silinized

Continuous phase: n-decane (3 % w/w SPAN 80) 500 mbar

Disperse phase: dH₂O 250 mbar

Field of view: 425x320 μm²

Playback speed: 1x

Supplementary movie M3

Title: M3_Microfluidics_for_CNT

Link: <https://jyx.jyu.fi/handle/123456789/58971>

Description: Droplet production in T-junction microfluidic device. The droplets are cut off from the water phase flow by pressure of oil. The droplets confined in the channel proceed at the same speed as the continuous phase.

Created: 28.2.2018

Chip: DEP-T3, silinized

Continuous phase: n-decane (3 % w/w SPAN 80) 800 mbar

Disperse phase: dH₂O 845 mbar

Field of view: 115x65 μm²

Playback speed: 0.25x

Supplementary movie M4

Title: M4_Microfluidics_for_CNT

Link: <https://jyx.jyu.fi/handle/123456789/58972>

Description: Size and frequency of the droplets produced in T-junction as a function of continuous and disperse phase pressure ratio.

Created: 25.-27.10.2017

Chip: DEP-T12, silinized

Continuous phase: n-decane (3 % w/w SPAN 80) 1 000 mbar

Disperse phase: dH₂O 1 039 – 1 085 mbar

Field of view: 115x65 μm²

Playback speed: 1x/time-lapse

Supplementary movie M5

Title: M5_Microfluidics_for_CNT

Link: <https://jyx.jyu.fi/handle/123456789/58973>

Description: the features of the sorting junction. Pressure balancer helps to equilibrate the pressure difference created by the presence of a droplet. The transition from shallow to deep channel mediates the transition from free to confined regime. The droplets are separated in the sorting junction according to the flow rate ratio.

Created: 13.10.2017

Chip: DEP-T13, silinized

Continuous phase: n-decane (1 % w/w SPAN 80) 750 mbar

Disperse phase: dH₂O 843 mbar

Field of view: 240x180 μm²

Playback speed: 1x

Supplementary movie M6

Title: M6_Microfluidics_for_CNT

Link: <https://jyx.jyu.fi/handle/123456789/58974>

Description: the hydrodynamic trap holds an incoming droplet until the arrival of following droplet. The previous droplet leaves the trap in very rapid manner.

Created: 22.3.2018

Chip: DEP-T18, silinized

Continuous phase: n-decane (3 % w/w SPAN 80) 600 mbar

Disperse phase: dH₂O 665 mbar

Field of view: 143x107 μm²

Playback speed: 0.0625x

Supplementary movie M7

Title: M7_Microfluidics_for_CNT

Link: <https://jyx.jyu.fi/handle/123456789/59018>

Description: a comparison of two designs of a droplet trap. While the droplet exchange is mediated by direct droplet contact in the symmetric design, a short continuous phase plug mediated the droplet exchange in the asymmetric design.

Created: 3.11.2017

Chip: DEP-T13, silinized

Continuous phase: n-decane (1 % w/w SPAN 80) N/A mbar

Disperse phase: sample O_1:30_cent N/A mbar

Field of view: 90x90 μm²

Playback speed: 1x

Supplementary movie M8

Title: M8_Microfluidics_for_CNT

Link: <https://jyx.jyu.fi/handle/123456789/59019>

Description: a comparison of two sorting strategies. While the shallow channel guides the droplets more precisely to the sorting point, the confined droplets are more vulnerable to coalescence and break-up. The deep channel lowers the positioning precision; however, the droplets are more stable.

Created: 20.11. & 27.11.2017

Chip: DEP-T12, silinized & DEP-T14, silinized

Continuous phase: n-decane (1 % w/w SPAN 80) 1 000 mbar & 1 250 mbar

Disperse phase: dH₂O 1 079 mbar & 1 320 mbar

Field of view: 500x378 μm² & 330x250 μm²

Playback speed: 1x & 1x

Supplementary movie M9

Title: M9_Microfluidics_for_CNT

Link: <https://jyx.jyu.fi/handle/123456789/59020>

Description: the droplets in contact coalesce when exposed to DEP field.

Created: 9.10.2017

Chip: DEP-T13, silinized

Continuous phase: n-decane (1 % w/w SPAN 80) 750 mbar

Disperse phase: dH₂O 843 mbar

Field of view: 250x188 μm²

Playback speed: 1x

Supplementary movie M10

Title: M10_Microfluidics_for_CNT

Link: <https://jyx.jyu.fi/handle/123456789/59021>

Description: Droplets are preferentially directed to the channel with higher flow rate in the passive sorting junction. When the droplets are exposed to DEP field, the DEP force pull them to the narrower channel.

Created: 4.7.2017

Chip: DEP-T4, silinized

Continuous phase: n-decane (3 % w/w SPAN 80) 1 000 mbar

Disperse phase: dH₂O 1 050 mbar

Field of view: 91x68 μm²

Playback speed: 1x

Supplementary movie M11

Title: M11_Microfluidics_for_CNT

Link: <https://jyx.jyu.fi/handle/123456789/59022>

Description: the subtle solubility of water in n-decane causes leaking of the droplet content. If the n-decane flows by static droplets, it carries the water slowly away up to the total disappearance of the droplets.

Created: 30.3.2017

Chip: no. 18, silinized

Continuous phase: n-decane (3 % w/w SPAN 80) 1 200 mbar

Disperse phase: dH₂O (1 % w/w SDBS) 1 450 mbar

Field of view: 395x296 μm²

Playback speed: time-lapse

Supplementary movie M12

Title: M12_Microfluidics_for_CNT

Link: <https://jyx.jyu.fi/handle/123456789/59023>

Description: the droplets exchanging in the trap causes visible scattering of the laser beam focused on the droplet. The obvious change of laser light intensity can be used for detection of droplet exchange.

Created: 28.11.2017

Playback speed: 1x

Supplementary movie M13

Title: M13_Microfluidics_for_CNT

Link: <https://jyx.jyu.fi/handle/123456789/59024>

Description: Compared to pure water, the CNT dispersion has much lower interfacial tension at the dispersion – glass interface due to the presence of SDBS surfactant. Since the behavior of microfluidic system in the confined regime is driven by liquid – solid interfacial tension, the droplet formation and droplet propagation are unstable and unpredictable.

Created: 1Left – 28.2.2018, 1Right – 28.2.2018, 2Left – 20.6.2017, 2Right – 7.7.2017

Chip: DEP-T3, silinized

Continuous phase: n-decane (3 % w/w SPAN 80) 1Left – 800 mbar, 1Right – 800 mbar, 2Left – 700 mbar, 2Right – 650 mbar

Disperse phase: dH₂O 1Left – 845 mbar, 2Left – 700 mbar; dH₂O (1 % w/w SDBS) 1Right – 765 mbar, 2Right – 650 mbar

Field of view: 1Left, 1Right – 111x83 μm²; 2Left, 2Right – 105x79 μm²

Playback speed: 1x

Supplementary movie M14

Title: M14_Microfluidics_for_CNT

Link: <https://jyx.jyu.fi/handle/123456789/59025>

Description: the CNT dispersion with low SDBS content allows stable droplet formation but leads to fast formation of CNT plugs in the hydrophobic channels. The selective channel surface treatment allows long-term stable functionality of the microfluidic system.

Created: 5.4.2018

Chip: DEP-T18, selectively silinized

Continuous phase: n-decane (3 % w/w SPAN 80) 600 mbar

Disperse phase: sample B (low SDBS) 655 mbar

Field of view: 167x125 μm²

Playback speed: time-lapse